Study of surface plasmon optical waves for sensing applications

Tarlis, Aggelos

Award date:
2007

Awarding institution:
University of Bath

Study of Surface Plasmon Optical Waves for Sensing Applications

Aggelos Tarlis

A thesis submitted for the degree of Doctor of Philosophy

University of Bath

Department of Electronic and Electrical Engineering

January 2007

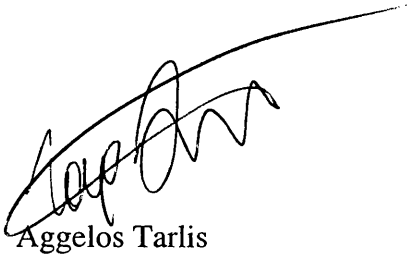

Aggelos Tarlis

ProQuest LLC
789 East Eisenhower Parkway
P.O. Box 1346
Ann Arbor, MI 48106-1346

Summary

The aim of this thesis is to investigate the electromagnetic properties of Surface Plasmon Waves (SPWs) for developing optical biosensors. This is performed by studying the SPW modal properties in various waveguide arrangements. It is shown that multilayer structures can sustain SPWs that have the potential to exhibit significantly reduced modal losses and subwavelength operation allowing them to be used for biological microscopy and sensing.

SPW excitation in prism coupled waveguide arrangements is also analysed by applying the Transmission Line (T-L) theory. It is shown that the T-L analysis can reduce any multilayer structure into a two section T-L circuit offering a clear physical insight of the nature of the contribution of each of the structure's layers to the overall phenomenon. Results present that the SPW excitation seen as a 'dip' in the power reflection coefficient of the structure is an impedance matching condition satisfied only when lossy metal films are involved. Following that, theoretical analysis and experimental demonstration of SPW excitation in such arrangements with the use of non-ideal optical sources having spectrally broad and divergent output beam is also given. The results indicate that SPW excitation at longer wavelengths becomes more sensitive to the divergence angle and spectral width of the optical source. However, such sources show a significant potential for replacing the traditionally used for such purposes gas lasers.

Moreover, SPW lossless propagation and subwavelength operation is theoretically achieved with the use of dielectric media with optical gain that counterbalance the metal losses. If such optically active dielectric films are used in SPW prism coupled structures, then the SPW "dip" in the power reflection coefficient of the structure becomes very narrow and the system sensitivity increases. Furthermore, the reflected signal exceeds unity indicating that the metal losses have been overcompensated by the optical gain.

Finally, it is shown that SPWs in addition to the enhancement that can provide to the intensity of weak scattered signals from particles, can also control and make more directive the far field radiation of such particles which are modeled as dipole antennas. Hence, a significantly increased collection of scattered signals can be realised.

Acknowledgments

I would like to thank my supervisor Dr. J. Sarma for his continuous support, discussions, patience and big parties during this PhD period. His courage dealing with me has also to be highlighted. Many thanks also belong to Dr. F. Causa for her valuable discussions, help and advice.

I have to thank Delia, Nicola, Liam and mr Woo for not only coping with me into the same office for such a long period but also introducing me into the tricks of this group apart from providing me with help and support during the ups and downs of the PhD work. Tao Tao, Ken, Lumin, Murphy, Giovanni, Xizi Chen and Lin Ma are also thanked for the cheerful and exciting times they offered to me.

E2V Technologies, Chelmsford, UK is acknowledged for financial support. In particular I have to thank Dr. B.P. Allen and Dr. R. Gilbert for their discussions and ideas.

I cannot forget God and my family for the miraculous continuous support and encouragement that provided to me all this period, surprisingly without any complaints. Million thanks also belong to πατερα Θεοδοσιο, Antoni, Vass, Art, Paul and Yannis for wasting their valuable time to keep me up during the PhD period.

Finally, I deeply acknowledge all the sunny smiles who either stayed or left my life during this work and especially the two who could not wait for a bit longer.

Contents

Chapter 1 Introduction

Chapter 2 Optical Wave Propagation

Chapter 3 Surface Plasmon Electromagnetic Waves

Chapter 4 Surface Plasmon Wave Excitation

List of Acronyms

Ag	Silver
Al	Aluminium
ATR	Attenuated Total Reflection
Au	Gold
BS	Beam Splitter
CCD	Charge Coupled Device
CMA	Cascaded Matrix Analysis
Cr	Cromium
Cu	Copper
DMD	Dielectric cladding metal guide three layer slab waveguide
Ell	Ellipsometry
FWHM	Full Width Half Maximum
GaAlAs	Gallium Aluminium Arsenide
GaAs	Gallium Arsenide
GaN	Gallium Nitride
Ge	Germanium
HeNe	Helium Neon
IR	Infrared
K-R	Kretschmann – Raether
LED	Light Emitting Diode
LRSPWs	Long Range SPWs
MDM	Metal cladding dielectric guide three layer slab waveguide
NIR	Near IR
OI	Optical Interferometers
pw	Plane wave
PWG	Prism coupled Waveguide
QW	Quantum Well
RM	Resonant Mirrors
RS	Raman Scattering
s/c	Semiconductor
SERS	Surface Enhanced Raman Spectroscopy

SEWs	Surface Electromagnetic Waves
Si	Silicon
SiO_2	Silicon Dioxide (Fused Silica)
SLD	Superluminescent Light Diode
SRSPWs	Short Range SPWs
SPs	Surface Plasmons
SPPs	Surface Plasmon Polaritons
SPR	Surface Plasmon Resonance
SPWs	Surface Plasmon Waves
TE	Transverse Electric
TiO_2	Titanium Dioxide
TIRF	Total Internal Reflection Fluorescence
T-L	Transmission Line
TM	Transverse Magnetic
TR	Total Reflection
T-R	Transverse Resonance
UV	Ultraviolet
VHF	Very High Frequencies
w/g	Waveguide

Chapter 1

Introduction

The increasing need for small, portable, robust and non-invasive sensors which can be used for medical diagnostics [1.1], environmental monitoring [1.2], food safety and bio/chemical interactions, has led the research community to employ optical methods as the detection mechanism [1.3-4]. Optical sensors allow the quantitative determination of one or more of the fundamental characteristics of optical radiation such as intensity, phase, frequency and polarisation. Hence, for sensing applications a change of the activity, the concentration or the spatial distribution of the sample under investigation results in a change in one of the radiation characteristics. Optical techniques such as Resonant Mirrors (RM), Ellipsometry (Ell), Optical Interferometers (OI), Total Internal Reflection Fluorescence (TIRF), Raman Scattering (RS) and Surface Plasmon Resonance (SPR) are very commonly utilised in various sensing applications [1.5]. Particularly, SPR has recently attracted a lot of attention due to the label-free sensing character, the real-time observation of bio/chemical interactions [1.6], the compatibility with different chemical environments and the simple arrangement needed to be implemented [1.7]. In addition, the electromagnetic mechanism producing the SPR phenomenon has recently opened new areas of applications, which will be discussed later.

1.1 Surface Plasmon Waves

The SPR phenomenon is based on the optical excitation of Surface Plasmon Waves (SPWs), which are particular kind of transverse magnetic (TM) polarised electromagnetic surface waves. Throughout this thesis, a surface wave is defined as an electromagnetic wave whose field amplitude decays exponentially across the interface in each medium [1.8]. Other types of surface waves are the well known Zenneck and Sommerfeld waves which are supported at a planar interface between a lossless and absorbing medium at radio frequencies, Figure 1.1a, the Goubau waves which are

similar to Zenneck and Sommerfeld waves but sustained in cylindrical structures, Figure 1.1b, whereas surfaces waves can also be supported in corrugated conducting surfaces, Figure 1.1c, [1.9].

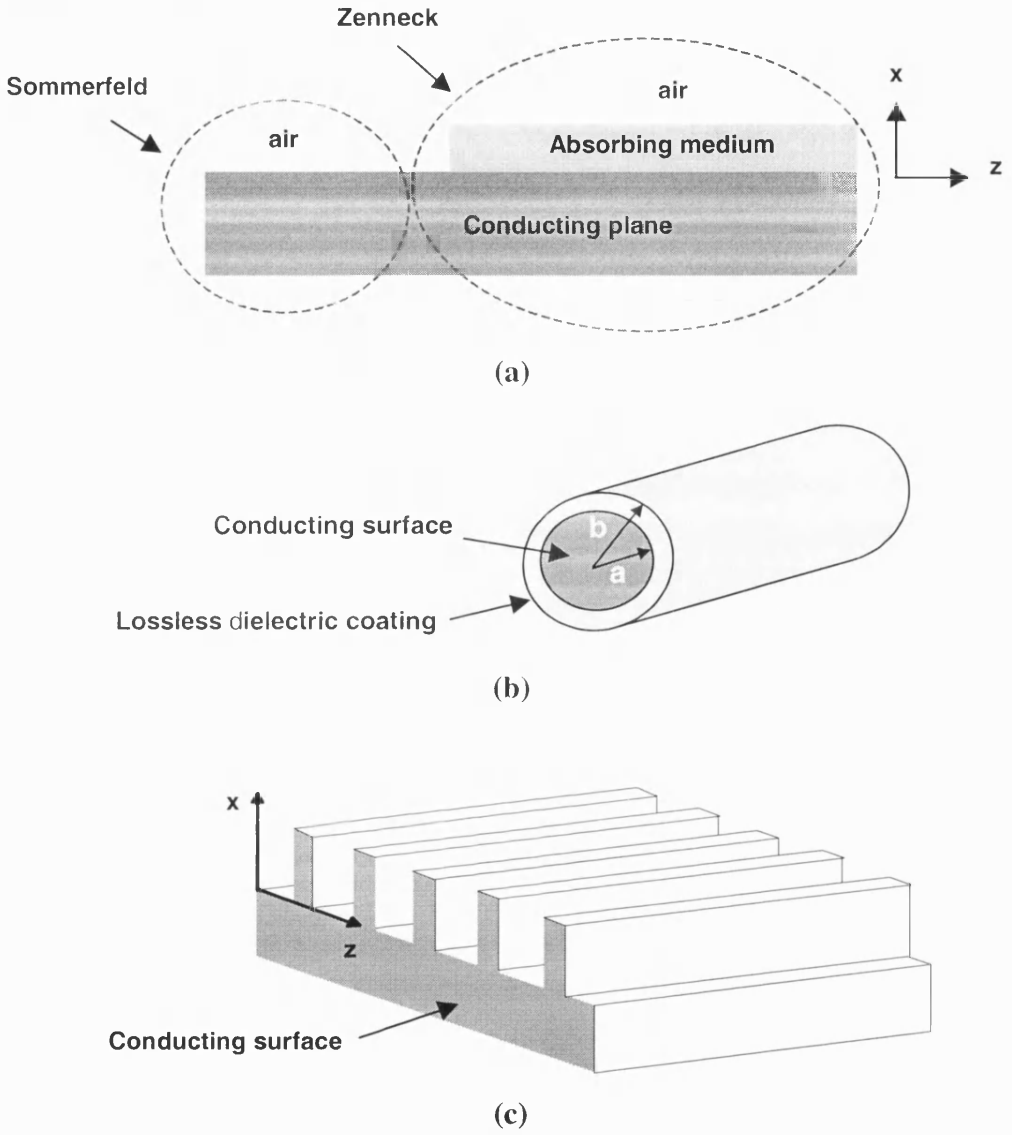

Figure 1.1. Typical surface waves are supported in: a) planar structures (Sommerfeld and Zenneck waves), b) cylindrical configurations (Goubau waves), and c) corrugated surfaces.

Ideal SPWs in particular, known also as Fano waves, can be sustained at a single interface between two media with opposite sign relative permittivity ε, such as a dielectric with $\varepsilon_d = + |\varepsilon_d|$, and an (electrical) plasma with $\varepsilon_m = - |\varepsilon_m|$, [1.10], Figure 1.2. Metals at optical frequencies and Ionosphere at Very High Frequencies (VHF) exhibits plasma characteristics [1.11].

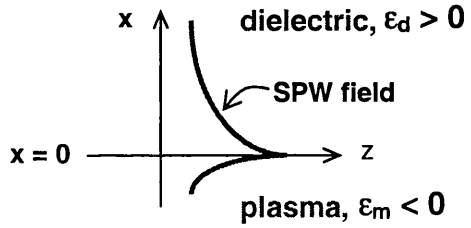

Figure 1.2. Typical SPW field at a single dielectric - (electrical) plasma interface.

The main mechanism of SPWs is the oscillations in the density of the free electrons, referred to as surface plasmons (SPs), that lie within about 20nm of the surface of the metal and produce $\varepsilon_m < 0$ [1.12]. Hence, the electromagnetic fields associated with these oscillations do not extend very far from or into the metal (around 300nm and 25nm respectively). Interactions between electrons and vibrating atoms in the metal cause SPWs to have a finite propagation across the surface and lose power in the form of heat due to usual electrical resistance of metals. Note that SPWs are also referred to as Surface Plasmon Polaritons (SPPs) due to the interaction of SPs with photons [1.13].

It has been almost a century since Wood in 1902 while experimentally studying the reflected spectra of visible light from a grating, observed drops in the intensity over short ranges in wavelength but did not relate the effect to the SPWs [1.14]. Although SPWs have been known as solutions of Maxwell's equations for surface waves propagating in conductors since Sommerfeld in 1909 [1.9], their properties had not been understood until the end of 1950. Later attempts to explain the so called "Wood's anomalies" failed until Ritchie with his work in 1957 made SPWs widely known in the field of surface science [1.15].

The first experimental observation of SPWs came by Turbadar in 1959, who observed a decrease in reflectivity from aluminium films under attenuated total reflection (ATR) with a prismatic structure [1.16]. However, similarly to Wood, Turbadar did not relate the decreased reflectivity to the SPW. The explanation to the results was that "*This effect can be predicted from thin film theory but has not previously been noted*" [1.16]. Same conclusions had already been made by Abeles in 1957 after theoretically analysing the reflectivity for the same structure [1.17].

It was then Otto and Kretschmann with Raether in 1968 the first who finally theoretically related and experimentally established that the minimum in the reflected signal from a prismatic structure under ATR, corresponds to the excitation of SPWs [1.10, 1.18]. The prism arrangements employed for that purpose are the well known "Otto", Figure 1.3a, and "Kretschmann - Raether" (K-R), Figure 1.3b.

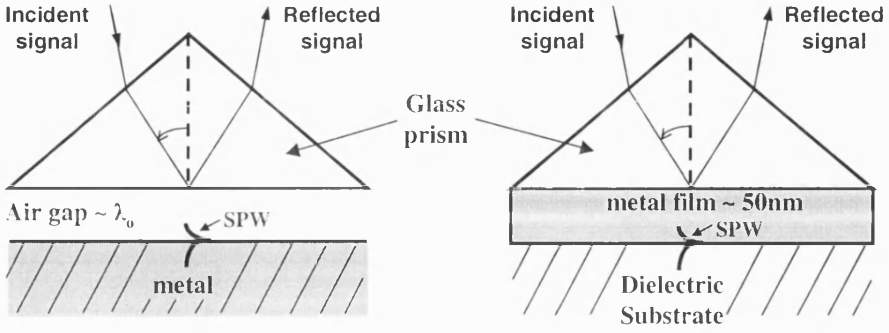

Figure 1.3. SPW prism coupled arrangements: a) Otto, and b) Kretschmann – Raether.

The only difference between the two prism structures is the air gap (typically of the order of free space (vacuum) wavelength λ_o) between the prism and the metal film in the Otto configuration, unlike the K-R system where the metal is directly deposited onto the prism. As Raether reports, the Otto arrangement can be employed for surfaces that need not to be damaged or touched by the prism a very important issue when studying for example surface phonon polaritons on single crystal surfaces [1.10]. Between the two prism configurations, the K-R seems to be the most popular for various applications since the Otto structure requires precise adjustment of the air gap thickness. Other optical techniques/arrangements that have the potential to be employed for SPW excitation involve the use of diffraction gratings [1.10, 1.13], textured surfaces [1.12], and end-fire excitation [1.19-20].

Since the era of Ritchie, there has been a large research interest in studying slab or finite width single and multiple dielectric - metal interface structures with linear or non-linear media capable of supporting SPWs [1.10, 1.19, 1.21-26]. Multiple single interface SPWs structures can support "symmetric-like" and "antisymmetric-like" SPWs with respect to their field distribution [1.19, 1.23]. Symmetric SPWs are referred to as "Long Range SPWs" (LRSPWs), due to the reduced modal losses (extended propagation distance) compared to the antisymmetric SPWs which are known as "Short Range SPWs" (SRSPWs) [1.10]. Hence, symmetric SPWs have become very attractive for use

in various applications [1.26-28]. Excitation of SPWs in small metal particles have also attracted a lot of interest due to the very strong optical field intensity that is produced in such structures compared to flat surfaces configurations [1.29-30].

1.2 SPW applications

The high field localisation and strong optical field intensity of SPWs compared to other surface waves [1.31], allows SPWs to be involved in a broad range of applications, from fundamental physics to optical systems. Therefore, it has become very common recently to refer to the area of photonics based on the use of SPWs as "*Plasmonics*" [1.13]. Some of the most interesting plasmonic applications are briefly discussed in this section.

1.2.1 Sensors

As mentioned in section 1.1, SPR (based on SPW excitation) is commonly employed in the area of optical sensors for biological/chemical detection. A typical SPR arrangement is based most of the times on the K-R prism coupler, Figure 1.3b, rather than on the Otto, Figure 1.3a, which requires precise adjustment of the air gap thickness.

In a K-R arrangement, Figure 1.4a, by considering TM polarised signals, SPW excitation relies on monitoring the field intensity I_R of the reflected signal in terms of the incident angle θ_i (angle scanning) or wavelength λ_o (spectral scanning) [1.32]. For the angle scanning method, a source signal with field intensity I_s impinges onto the prism - metal interface at different θ_i while λ_o is kept constant. In the spectral method however, θ_i is kept fixed and λ_o varies. In both techniques, at a specific angle $\theta_i = \theta_{spw}$ or wavelength $\lambda_o = \lambda_{spw}$, $I_R \rightarrow 0$ which indicates that SPW excitation is sustained at the metal – dielectric substrate interface, Figure 1.4b. The position of θ_{spw} or λ_{spw} is very sensitive to changes in the relative permittivity of the substrate dielectric, hence the operation of the system as a biological or chemical sensor.

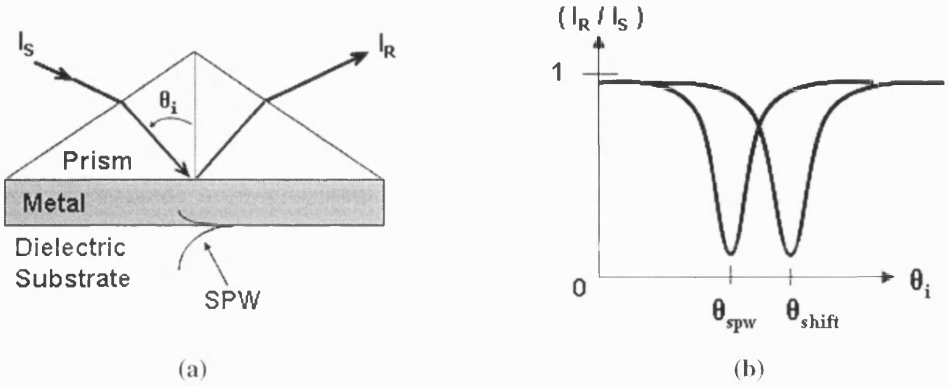

Figure 1.4. a) K-R prism coupler , b) angle scanning SPW excitation.

If a K-R SPW configuration is to be used as a biosensor, then with reference to Figure 1.4a the metal film is coated with a chemo/bio-responsive layer with a typical thickness between 5-8nm. That layer has to be smaller than the penetration depth of the SPW field inside the dielectric substrate which is around 300-400nm, [1.33]. Such a layer usually consists of biomolecular recognition elements for example antibodies which have the potential to react and bind with specific antigens, [1.34]. If an analyte sample containing such antigens is injected into the substrate area and passes over the biomolecular layer, the antigens may bind with the antibodies of the layer. As a consequence, a modification of the coverage of the metal with the biomolecular layer occurs (increase of layer thickness) which causes also a change into the refractive index δn_s of the substrate. That refractive index change alters the properties of the SPW which is now excited at a different angle $\theta_{shift} = (\theta_{spw} + \delta\theta)$, Figure 1.4b, where $\delta\theta$ is due to δn_s, [1.35]. A typical shift of 0.001^o in the SPW excitation angle corresponds to a 10^{-5} change in refractive index, when the substrate refractive index is in the range of 1.33-1.4, and describes a change in the surface coverage of the biomolecular layer of around 10 pg/mm^2 , [1.36].

Following that procedure, biologists and chemists can detect and analyse different biological/chemical substances. The first attempt to utilise SPWs for biosensing applications was made by Liedberg et al. in 1983, where a K-R prism coupler was used to detect the anaesthetic gas halothen by recording refractive index changes in a silicon-glycol copolymer deposited onto the metal film [1.37]. Since then, SPR biosensors have been applied in a variety of applications such as immunosensing [1.38] and drug discovery [1.34].

Some of the benefits employing SPR sensors in bio/chemical detection as reported by [1.34] are presented in Table 1.1.

SPR advantages
Lack of labelling requirements allows for the analysis of almost all biomolecular systems
Real time characterisation
Reaction equilibrium is not disturbed during measurements
Stability of immobilised ligand can be monitored
SPR can be used in qualitative formats such as screening and as a biophysical tool
Automated instruments provide reproducible analyses
Low amounts of materials required

Table 1.1. SPR advantages for biosensing [1.35].

The main limiting factor however in SPR biosensors, is that the analytes under detection must have a sufficient mass (> 2000 daltons) to cause a significant change in θ_{spw} or λ_{spw} [1.33].

Most of the commercial SPR biosensors are based on the K-R prism configuration. Attempts have also been made to utilise optical waveguide structures, but their sensitivity was found to be much less compared to the prism arrangements [1.38]. Among the various SPR companies, Table 1.2, Biacore and Texas Instruments (TI) are the leaders of the corresponding market [1.39-41].

SPR Manufacturer	System
Biacore (Uppsala, Sweden)	BIAcore
Affinity Sensors (Franklin, MA)	IASys
Nippon Laser Electronics (Hokkaido, Japan)	SPR-670
Artificial Sensing Instruments (Zurich, Switzerland)	OWLS
IBIS Technologies BV(Enschede, The Netherlands)	IBIS
Texas Instruments (Dallas, TX)	TISPR
Aviv (Lakewood, NJ)	PWR-400
Bio Tul AG (Munich, Germany)	Kinomics
Quantech Ltd (Eagan, MN)	FasTraQ

Table 1.2. Commercial SPR systems, [1.42].

1.2.2 Surface Enhanced Raman Spectroscopy (SERS)

An optical phenomenon that has seen an incredible boost due to the use of SPWs is the Raman Scattering (RS), which is widely used in molecular spectroscopy [1.32]. When an optical signal with frequency f is incident on a Raman active molecule, then the molecule is polarised and is subjected to an internal motion such as vibration or rotation of frequency f_m. The scattered signal from the molecule has then three frequency components: f, $f_- = (f - f_m)$ and $f_+ = (f + f_m)$, where f_+ and f_- are known as 'Stokes' and 'anti – Stokes' respectively [1.43]. Both f_+ and f_- are very weak since only 1 in 10^{11} incident photons exchange energy with the Raman active molecule [1.44].

Until 1976 it was believed that the weak Raman scattered signals can be enhanced only by employing a high power optical source or increasing the number of scattering molecules, [1.44]. Fleischmann in 1974, [1.45], observed intense RS from pyridine adsorbed onto a roughened silver electrode but could not explain the effect. It was believed at that time that the extra - ordinary enhanced Raman signal was due to the increase in the electrode surface area and as a consequence in the increased number of adsorbed molecules, [1.46].

However, JeanMaire and Van Duyne with Albrecht and Creighton showed in 1977 that rough silver surfaces in the vicinity of an illuminated particle, can enhance the weak Raman scattered signals from the particle by a factor ranging from 10^4 to 10^6 [1.46]. The more intense Raman signal was then related to electromagnetic mechanisms such as the enhancement of the local to the surface field intensity due to polarisation effects.

Such an enhanced RS signal can be observed only in structures that support SPWs, can become very strong especially with rough metal surfaces and metal particles compared to flat surfaces and is known as Surface Enhanced Raman Scattering (SERS) [1.46]. According to Metiu and Das [1.46], "*Large signal enhancements are produced when the structure absorbs the photon and localises it. Gratings and flat surfaces (in the ATR configuration) absorb the photon and 'store' the electromagnetic energy into the surface plasmon; this is delocalised in the direction parallel to the surface but localised in the perpendicular one. This increases the electromagnetic energy density near the surface. A sphere localises the photon, by surface plasmon excitation, in all directions and the resulting concentration of electromagnetic energy is larger than that produced*

by a grating". As a consequence, the amount of the RS enhancement significantly depends on the morphology of the SPW structure employed. Hence, it has been found that closely spaced metal features as in aggregated colloids or cold-deposited films can provide a sufficiently strong RS signal of the order of 10^{14} [1.47].

1.2.3 Subwavelength optics

An important feature of SPWs is that under certain conditions they can exhibit subwavelength operation i.e. have an extremely short effective (modal) wavelength λ_{eff} and very tight field which are not restricted by the diffraction limit, as it happens with "conventional" surface waves [1.13]. As a consequence, SPWs have the potential of manipulating light in nanoscale dimensions structures allowing the design of optical circuits. At the present days, electronic components such as transistors have dimensions of the order of 50nm which sometimes do not allow the use of other connectors for transferring signals, such as optical fibres (~ 1000nm diameter), to be introduced due to the incompatibility in the size and technology [1.48]. SPWs can on the other hand easily operate under such environments and this has led in the development of SPW based optical modulators, switches, interferometers, capacitors and inductors [1.49-50].

Another application of the SPW subwavelength operation is found in microscopy where the diffraction limit of conventional lenses prevents the detection of small amounts of molecules in cellular concentrations. As Knoll first reported in 1988, if SPW fields are used to illuminate interfacial structures in microscopy, high contrast without loss of spatial resolution can be obtained. This is due to the high sensitivity SPWs have to small thickness variations of thin layers, [1.51]. Following Knoll's approach, Smolyaninov and co-workers in 2005 experimentally demonstrated a far-field microscope with nanometer-scale resolution [1.52].

1.2.4 Enhanced light transmission

It has also been shown that the use of SPWs can increase the transmission of light when excited in flat thin metal films with nanoholes. Ebbessen et al. in 1998 reported that if light impinges on a metal film (~200nm thick) which contains an array of nanoholes (~150nm diameter, $\lambda_0 / 2$ separation), then more than the amount of light falling on each hole is transmitted on the other side of the film which is opposed to what the diffraction

theory describes [1.53]. The answer to the problem was found in SPWs. As the light falls onto the film, due to the holes couples to SPWs and under certain conditions, a SPW standing wave is formed. If the maxima of this wave coincide with the positions of the holes, then the amplitude of the generated fields inside the film is enhanced and more than the expected light is transmitted on the other side.

It has also been found that if a single subwavelength aperture surrounded by periodic structures on both metal film's sides is made, then the transmitted light can be beamed rather than diffracted, Figure 1.5, [1.54]. This suggests that a well directed source of light can be generated using a subwavelength aperture which can potentially be employed in magneto-optic data storage [1.13].

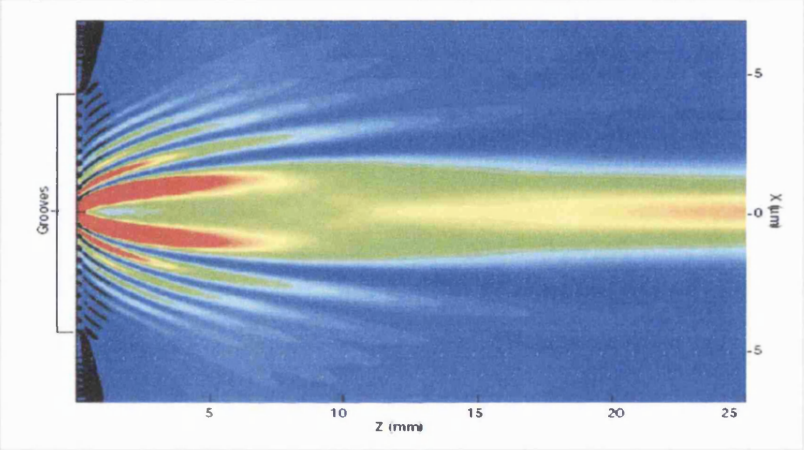

Figure 1.5. Output beam from a metallic subwavelength aperture surrounded by periodic grooves [1.54].

1.2.5 Metamaterials

A combination of both practical and fundamental physics applications involving plasmonics has been studied recently in the design of the so-called "perfect lens". The concept was developed by Pendry in 2000 by exploring a neglected idea made by Veselago in 1967 [1.55-56]. This new type of lens was found to be capable of focusing features far smaller than the wavelength of light, including small molecules. The mechanism is based on a category of materials referred to as "*metamaterials*" which can have both negative relative permittivity ($\epsilon < 0$, due to the support of SPs) and relative permeability ($\mu < 0$). Hence, the refractive index of the material defined as $n = \sqrt{\varepsilon\mu}$, becomes negative allowing negative refraction to occur which is the concept of the "perfect lens" operation [1.57].

1.2.6 Other applications

Finally, SPWs have also been employed in various other practical applications such as: holography [1.58], wavelength filters [1.59], long wavelength semiconductor lasers (λ_o ~ 17 - 19μm) [1.60-61], optical polarisers [1.62], or to improve fluorescence collection efficiency [1.63]. Fundamental physics have also been studied with SPWs such as non-linear effects due to the local heating developed by SPW excitation, optical phase conjugation through pulsed laser excitation of thermal gratings in Ag films, or pulsed excitation of SPWs to probe the dynamics of thin metal films (e.g. electron relaxation rates and phonon decay times), [1.62].

1.3 Thesis layout

This thesis studies and analyses SPWs in the context of optical guided electromagnetic waves in various structures. The involvement of SPWs for light scattering purposes is also examined. Hence, chapter 2 provides the basic electromagnetic concepts that will be used throughout this thesis and examines optical wave propagation in different media. The frequency dependent relative permittivity is also studied.

The main scope of chapter 3 is to review the modal properties of SPWs supported in single and multiple interface dielectric - metal guides, and wherever is possible to provide a comparison with conventional dielectric guides. In addition, a computational model to solve multilayer waveguide structures consisted of media with complex permittivities where for example SPWs can be supported is also presented.

In chapter 4, the theory of Transmission Lines is introduced as an alternative technique to the cascaded matrix analysis for examining intricate multilayer prism coupled arrangements, as it has the advantage of significantly simplifying such structures and also providing direct and simple interpretation of the response of the system. The emphasis of this study is to provide a simple yet rigorous design tool for analysing SPW excitation in prism coupled structures.

Experimental demonstration of SPW and conventional dielectric wave excitation in prism coupled waveguide arrangements is presented in chapter 5. The use of optical

sources with spectrally broad and divergent output optical beam when employed for SPW excitation is also given followed by simulation and experimental results.

In chapter 6, the use of optically active media in SPW configurations to compensate for the usual high metal losses and provide SPW lossless and subwavelength operation is discussed. The study is performed for the SPW structures of chapter 3 and extended in some of the prism coupled SPW arrangements of chapter 4, which can be potentially employed for sensing applications.

SPWs have also been used for enhancing weak scattered signals from particles as for example in Raman scattering. Hence, chapter 7 studies the basic electromagnetic mechanism behind this signal enhancement phenomenon. In addition, it is suggested that the use of SPWs can be employed to alter the far field radiation pattern from an array of particles, modelled as dipole antennas, and make it more directive.

Finally, conclusions and suggestions for possible future works are drawn in chapter 8.

References

[1.1] www.sensorsmag.com/articles/0397/acoustic/main.shtml

[1.2] M.P. Marco, D. Barcelo, "Enviromental applications of analytical biosensors", Meas. Sci. Technol. 7 (1996), p. 1547.

[1.3] K. Amos, "Sensor market goes global", InTech, www.isa.org, June 1999, p.40.

[1.4] A.F. Collings, F. Caruso, "Biosensors: recent advances", Rep. Prog. Phys. 60 (1997), p.1397-1445.

[1.5] A. Brecht, G. Gauglitz, "Optical probes and transducers", Biosensors & Bioelectronics vol.10 (1995), p.923.

[1.6] P. James, "SPR Technology in the analysis of biomolecular binding events", Innovations in Pharmaceutical Technology, http://www.iptonline.com/articles/public/IPTNINE30NoPrint.pdf

[1.7] J.M. McDonnell, "Surface plasmon resonance: towards an understanding of the mechanisms of biological molecular recognition", Current Opinion in Chemical Biology, 2001, 5:572-577.

[1.8] F. Yang, J. R. Sambles, G. W. Bradberry, "Long-range surface modes supported by thin films," Phys. Rev. B 44, p.5855-5872, 1991.

[1.9] R.E. Collin, "Field Theory of Guided Waves", IEEE Press, 2nd Edition (1991).

[1.10] H. Raether, "Surface Plasmons on Smooth and Rough Surfaces and on Gratings", vol.111, Springer Tracts in Modern Physics, Springer-Verlag, 1988.

[1.11] E. Hecht, "Optics", Addison Wesley, 3rd edition, 1998, p.130.

[1.12] B. Barnes, R.Sambles, Physics World, vol.19, no.1, p.17, January 2006.

[1.13] W.L. Barnes, A. Dereux, T. W. Ebbesen, "Surface plasmon subwavelength optics", Nature, vol.424, no.14, pp.824-830, 14 August 2003.

[1.14] R.W. Wood, "On a remarkable case of uneven distribution of light in a diffraction grating spectrum", Baltimore, June 2nd 1902.

[1.15] R.H. Ritchie, "Plasma Losses by Fast Electrons in Thin Films", Physical Review, vol.106, no.5, June 1st 1957, p.874.

[1.16] T. Turbadar, "Complete Absorption of Light by Thin Metal Films", 4 September 1958, published in Journal of Modern Optics in 1964 as "Complete Absorption of Plane Polarised Light by Thin Metal Films", vol.11, no.3, July 1964, p.207.

[1.17] F. Abeles, "Optical properties of thin absorbing films", Journal of the Optical Society of America, vol. 47, issue 6, p.473.

[1.18] A. Otto, "Excitation of Nonradiative Surface Plasma Waves in Silver by the Method of Frustrated Total Reflection", Zeitschrift fur Physik 216, p.398 (1968)

[1.19] J.J. Burke, G.I. Stegeman, T. Tamir, "Surface-polariton-like waves guided by thin, lossy metal films", Phys. Rev. B, vol.33, no. 8, pp.5186-5201, 15 April 1986.

[1.20] G.I. Stegeman, R.F. Wallis, A.A. Maradudin, "Excitation of surface Plasmon polaritons by end-fire coupling", optics Letters, vol.8, no.7, July 1983, p.386.

[1.21] P. Berini, "Plasmon polariton waves guided by thin lossy metal films of finite width: bound modes of symmetric structures", Phys. Rev. B 61, p.10484-10503, 2000.

[1.22] R. Charbonneau, P. Bierini, E. Berolo, E. Lisicka-Shrzek, "Experimental observation of plasmon polariton waves supported by a thin metal film of finite width", Optics Letters, vol.25, no.11, 1 June 2000, pp.844-846.

[1.23] B.Prade, J.Y.Vinet and A.Mysyrowicz, "Guided optical waves in planar heterostructures with negative dielectric constant", Phys. Rev. B, vol.44, no.24, p.13556, 15 December 1991.

[1.24] B. Prade, J.Y. Vinet, "Guided Optical Waves in Fibers With Negative Dielectric Constant", Journal of Lightwave Technology, vol.12, no.1, January 1994, p.6.

[1.25] I.V. Shadrivov, A.A. Shukhorukov, Y.S. Kivshar, A.A. Zharov, A.D. Boardman, P. Egan, "Nonlinear surface waves in left-handed materials", Physical Review E 69, p.016617-1, 2004.

[1.26] O. Hugon, P. Benech, H. Gagnaire, "Surface plasmon chemical/biological sensor in integrated optics", Sensors and Actuators B,51, (1998), p.316.

[1.27] M.J. Jory, G.W. Bradberry, P.S. Cann, J.R. Sambles, "A surface-plasmon-based optical sensor using acousto-optics", Meas. Sci. Technol. 6, (1995), pp.1193-1200.

[1.28] R. Charbonneau, N. Lahoud, G. Mattiussi, P. Berini, "Demonstration of integrated optics elements based on long-ranging surface plasmon polaritons", Optics Express, vol.13, no.3, 7 February 2005, p.977.

[1.29] S.A. Maier, "Plasmonics – Towards Subwavelength Optical Devices", Current Nanoscience, 2005, 1, p.17-22.

[1.30] S. Kawata, "Near-field optics and surface plasmon polaritons", Springer Verlag, 2001.

[1.31] W. H. Weber, G. W. Ford, "Optical electric-field enhancement at a metal surface arising from surface-plasmon excitation", Optics Letters, vol.6, no.3, pp.122-124, March 1981.

[1.32] J. Homola, S.S. Yee, G. Gauglitz, "Surface plasmon resonance sensors: review", Sensors and Actuators B, vol.54, no.1, pp.3-15, 25 January 1999.

[1.33] http://www.xantec.com/html/spr.html

[1.34] D.G. Myszka, R.L. Rich, "Implementing surface plasmon resonance biosensors in drug discovery", PSTT, vol.3, no.9, September 2000, p.310.

[1.35] J. Homola, "Present and future of surface Plasmon resonance biosensors", Anal. Bioanal. Chem. vol.377, 2003, p.528.

[1.36] G. Canziani, W. Zhang, D. Cines, A. Rux, S. Willis, G. Cohen, R. Eisenberg, I. Chaiken, "Exploring Biomolecular Recognition Using Optical Biosensors", Methods, vol.19, 1999, p.253.

[1.37] B. Liedberg, C. Nylander, I. Lundstrom, "Biosensing with surface plasmon resonance – how it all started", Biosensors and Bioelectronics, vol.10, no.8, pp.i-ix, 1995.

[1.38] P.B. Daniels, J.K. Deacon, M.J. Eddowes, D.G. Pedley, "Surface Plasmon Resonance Applied to Immunosensing", Sensors and Actuators, 15 (1988), p.11.

[1.39] www.biacore.com

[1.40] www.ibis-spr.nl

[1.41] www.ti.com/spr

[1.42] J. Hodgson, "Light, Angles, Action: Instruments for label-free, real-time monitoring of intermolecular interactions", Bio/technology, vol.12, January 1994, p.31.

[1.43] F. H. Read, "Electromagnetic Radiation", John Wiley & Sons, 1980.

[1.44] "Surface-enhanced Raman effect", Physics Today, April 1980, p.18.

[1.45] A. Campion, P. Kambhampati, "Surface-enhanced Raman scattering", Chemical Society Reviews, vol.27, p.241, 1998.

[1.46] M. Moskovits, "Surface-enhanced spectroscopy", Reviews of Modern Physics, vol.57, no.3, part I, July 1985, p.783.

[1.47] S. Nie, S.R. Emory, Science 275, 1102 (1997).

[1.48] E. Ozbay, "Plasmonics: Merging Photonics and Electronics at Nanoscale Dimensions", Science, vol.311, no.13, pp.189-193, January 2006.

[1.49] S.I.Bozhevolnyl, V.M.Shalaev, "Nanophotonics with Surface Plasmons – Part I", Photonics Spectra, January 2006, p.58.

[1.50] N. Engheta, A. Salandrino, A. Alu, "Circuit Elements at Optical Frequencies: Nanoinductors, Nanocapacitors, and Nanoresistors", Phys. Rev. Letters, vol.95, no.9, pp.095504, 23 August 2005.

[1.51] B. Rothenhausler, W. Knoll, "Surface-plasmon microscopy", Nature, vol.332, 14 April 1988, p.615.

[1.52] I. I. Smolyaninov, "A far-field optical microscope with nanometre-scale resolution based on in-plane surface plasmon imaging", J. Opt. A: Pure Appl. Opt., vol.7, no.2, pp.S165–S175, February 2005.

[1.53] T. W. Ebbesen, H. J. Lezec, H. F. Ghaemi, T. Thio, P. A. Wolff, "Extraordinary optical transmission through sub-wavelength hole arrays", Nature, vol.391, pp.667–669, February 1998.

[1.54] L. Martin-Moreno, F.J. Garcia-Vidal, H.J. Lezec, A. Degiron, T.W. Ebbessen, "Theory of highly Directional Emission from a Single Subwavelength Aperture Surrounded by Surface Corrugations", Physical Review Letters vol.90, no.16, p.167401-1, 25 April 2003

[1.55] J.B. Pendry, "Negative Refraction Makes a Perfect Lens", Physical Review Letters, vol.85, no.18, 30 October 2000, p.3966.

[1.56] V.G. Veselago, "The electrodynamics of substances with simultaneously negative values of ε and μ", Soviet Physics Uspekhi, vol.10, no.4, pp.509-514, January - February, 1968.

[1.57] J.B. Pendry, "Negative refraction", Contemporary Physics, vol.45, no.3, May - June 2004, pp.191-202.

[1.58] G.P. Wang, T. Sugiura, S. Kawata, "Holography with surface-plasmon-coupled waveguide modes", Applied Optics, vol.40, no.22, 1 August 2001, pp.3649-3653.

[1.59] Y. Wang, "Wavelength selection with coupled surface plasmon waves", Applied Physics Letters, vol.82, no.24, p.4385, 16 June 2003.

[1.60] A. Tredicucci, C. Gmachl, F. Capasso, A.L. Hutchinson, D.L. Sivco, A.Y, Cho, "Single-mode surface plasmon laser", Applied Physics Letters, vol.76, no.16, p.2164, 17 April 2000.

[1.61] R. Colombelli, F. Capasso, C.Gmachl, A.L.Hutchinson, D.L. Sivco, A. Tredicucci, M.C. Wanke, A.M. Sergent, A.Y. Cho, "Far-infrared surface-plasmon quantum-

cascade lasers at 21.5 μm and 24 μm wavelengths", Appl. Phys. Lett., vol.78, no.18, p.2620, 30 April 2001.

[1.62] J.R. Sambles, G.W. Bradbery, F. Yang, "Optical excitation of surface plasmons: an introduction", Contemporary Physics, vol.32, no.3, pp.173-183, 1991.

[1.63] J.R. Lakowicz, "Radiative decay engineering 3. Surface plasmon-coupled directional emission", Analytical Biochemistry, vol.324 (2004), pp.153–169.

Chapter 2

Optical Wave Propagation

This chapter provides the fundamental electromagnetic theory and analyses the propagation of a plane wave through different material in order to familiarise the reader with some of the basic concepts that will be used throughout this thesis. Emphasis is also given in the differences between dielectric media and metals through the study of the corresponding frequency dependent relative permittivities.

2.1 Maxwell's Equations

Electromagnetic wave propagation in a linear, isotropic, homogeneous medium having time harmonic dependent fields of the form

$$\tilde{\underline{F}}(x,y,z,t) = \underline{F}(x,y,z)\exp[+j\omega t] \tag{2.1}$$

where x, y, z denote the use of a cartesian co-ordinate system, [Appendix A], ω and t are both real and positive representing angular frequency and time respectively, $j = \sqrt{-1}$ and $\underline{F}$ is a complex vector, can be described by Maxwell's equations [2.1]:

$$\begin{aligned} \nabla \times \underline{E} &= -j\omega \underline{B} \\ \nabla \times \underline{H} &= \underline{J} + j\omega \underline{D} \\ \nabla \cdot \underline{D} &= \rho \\ \nabla \cdot \underline{B} &= 0 \end{aligned} \tag{2.2}$$

∇ is a vector differential operator depending of the spatial co-ordinates [Appendix A]; $\underline{E}$ and $\underline{H}$ are the electric and magnetic field vectors respectively; $\underline{D}$ and $\underline{B}$ are the electric displacement and the magnetic flux vectors respectively; ρ is the free charge density; $\underline{J} = \underline{J}_S + \underline{J}_C$ is the total electric current density flowing inside the medium, made of the contribution of the current source, $\underline{J}_S$, and the conductive current, $\underline{J}_C$. $\underline{E}$, $\underline{H}$, $\underline{B}$, $\underline{D}$ and J_C are related to each other as [2.1]:

$$\underline{D} = \varepsilon_o \varepsilon \underline{E} \tag{2.3}$$

$$\tilde{\underline{B}} = \hat{\mu}\tilde{\underline{H}} \tag{2.4}$$

$$\tilde{\underline{J}} = \sigma\tilde{\underline{E}} \tag{2.5}$$

where σ is the material conductivity; $\hat{\mu} = \mu_o \mu$ where $\mu_o = 4\pi\times10^{-7}\,(\mathrm{H/m})$ is the free space (vacuum) magnetic permeability and μ is the relative magnetic permeability; $\varepsilon_o = 8.854\times10^{-12}\,(\mathrm{F/m})$ is the free space permittivity (dielectric constant) and ε is the relative permittivity of the medium which is in general complex and related to the refractive index n as

$$\varepsilon = n^2 \tag{2.6}$$

Throughout this thesis Maxwell's equations, eqn.(2.2), are solved for non-magnetic ($\mu = +1$), source and charge free media ($\underline{J}_S = 0$, $\tilde{\rho} = 0$).

2.2 The Wave Equation

By rearranging Maxwell's equations, eqn.(2.2), it is possible to obtain the wave equation for the electric and the magnetic fields in the cartesian co-ordinates, [Appendix A], [2.1]:

$$\nabla^2\underline{E} + k_o^2\varepsilon\underline{E} = \left[\frac{\partial^2}{\partial x^2} + \frac{\partial^2}{\partial y^2} + \frac{\partial^2}{\partial z^2} + k_o^2\varepsilon\right]\underline{E} = 0 \tag{2.7}$$

$$\nabla^2\underline{H} + k_o^2\varepsilon\underline{H} = \left[\frac{\partial^2}{\partial x^2} + \frac{\partial^2}{\partial y^2} + \frac{\partial^2}{\partial z^2} + k_o^2\varepsilon\right]\underline{H} = 0 \tag{2.8}$$

where $k_o^2 = \omega^2\varepsilon_o\mu_o = [2\pi/\lambda_o]^2$, and λ_o is the free space wavelength. The following compact notation will be introduced: $\partial_x^2 = \frac{\partial^2}{\partial x^2}$, $\partial_y^2 = \frac{\partial^2}{\partial y^2}$ and $\partial_z^2 = \frac{\partial^2}{\partial z^2}$. Equations (2.7) and (2.8) produce six scalar equations describing the six components of the electromagnetic field. Which one of eqns.(2.7) and (2.8) is used depends on the convenience of the particular problem. If for example the wave equation in $\underline{E}$ is used then $\underline{H}$ is obtained from Maxwell's equations, eqns.(2.2).

2.3 Poynting Vector

The power flow out of a surface carried by an electromagnetic wave is described by the Poynting vector [2.1, 2.2],

$$\tilde{\underline{S}} = \tilde{\underline{E}} \times \tilde{\underline{H}} \tag{2.9}$$

which provides the direction and magnitude of this power flow per unit area at any point in space. Note that there is no power flow in the vicinity of a system of static charges that has electric field but no magnetic, and in the case of a perfect conductor where there is a zero tangential electric field component.

Since however $\tilde{\underline{S}}$, eqn.(2.9), has very rapid time variation it is more convenient to calculate the corresponding instantaneous quantity. Hence, by rearranging Maxwell's equations, eqn.(2.2), for a surface A and volume V of concern, as it is given in [2.1], the following equation is obtained:

$$\oint_A \left(\underline{E} \times \underline{H}^*\right) \cdot d\underline{A} = -\int_V \sigma \underline{E} \cdot \underline{E}^* \, dV - j\omega \int_V \left[\mu \underline{H} \cdot \underline{H}^* - \varepsilon \underline{E} \cdot \underline{E}^*\right] dV \tag{2.10}$$

where $\underline{E}^*$ and $\underline{H}^*$ are the complex conjugates of $\underline{E}$ and $\underline{H}$ respectively.

The first integral on the right side of eqn.(2.10) represents power loss in the conduction current. Thus the real part of the complex Poynting flow on the left side can be related to this power loss as:

$$\underline{S} = \frac{1}{2} \mathrm{Re}\left\{\underline{E} \times \underline{H}^*\right\} \tag{2.11}$$

where Re{ } defines the real part of $\underline{S}$ which is measured in (Watts / m^2) . The amount of total power carried by the electromagnetic wave can then be evaluated as [2.1],

$$P = \oint_A \underline{S} \, dA \tag{2.12}$$

and is given in Watts.

The second integral on the right of eqn.(2.10) is proportional to the difference between average stored magnetic energy in the volume V and average stored electric energy. Hence, the imaginary part of eqn.(2.10) is

$$\mathrm{Im}\left\{\oint_A \left(\underline{E} \times \underline{H}^*\right) \cdot dA\right\} = 4\omega\left(U_{Eav} - U_{Hav}\right) \tag{2.13}$$

where U_{Eav} and U_{Hav} are the average stored energy in the electric and magnetic fields. Thus the imaginary part of the Poynting flow through the surface can be thought of as reactive power.

2.4 Plane Wave Propagation

Propagation of an electromagnetic wave in different media can easily be studied by considering a plane wave (pw). By assuming a cartesian co-ordinate system with x, y and z being the three axes, a pw is defined as a wave with no field variation in the plane perpendicular to the direction of propagation. If the wave propagation is along the z – direction, hence there is no field variation in the x - y plane, thus $\partial_x^2 = \partial_y^2 \equiv 0$ in the wave equations, eqns.(2.7-8),

$$\frac{d^2\underline{E}(z)}{dz^2} + k_o^2 \varepsilon \underline{E}(z) = 0 \tag{2.14}$$

$$\frac{d^2\underline{H}(z)}{dz^2} + k_o^2 \varepsilon \underline{H}(z) = 0 \tag{2.15}$$

If the refractive index n is in general complex of the form $n = n_R - jn_I$, then the corresponding relative permittivity ε becomes, eqn.(2.6),

$$\varepsilon = (n_R - jn_I)^2 = (n_R^2 - n_I^2) - j2n_R n_I = \varepsilon_R - j\varepsilon_I \tag{2.16}$$

For this pw Maxwell's equations, eqns.(2.2), give $E_z = H_z \equiv 0$. In this case the non-zero field components are E_y, H_x, E_x and H_y, where E_y is related only to H_x and E_x only to H_y.

By considering the set H_y and E_x, and solving eqn.(2.15), then

$$\begin{aligned} H_y(z) &= A_f \exp[-jk_o n z] \\ &= A_f \exp[-jk_o n_R z]\exp[-k_o n_I z] \end{aligned} \tag{2.17}$$

where A_f is the field amplitude. Equation (2.17) shows that the wave will propagate with a propagation constant

$$\beta_R = k_o n_R \tag{2.18}$$

and a decay / growth rate (depending on the sign of n_I)

$$\beta_I = k_o n_I \tag{2.19}$$

The characteristic wave impedance Z_w is

$$Z_w = \frac{E_x}{H_y} = Z_{vac} \frac{n_R + jn_I}{n_R^2 + n_I^2} \tag{2.20}$$

where

$$Z_{vac} = \sqrt{\frac{\mu_o}{\varepsilon_o}} = 120\pi\,(\Omega) \approx 377\,(\Omega) \tag{2.21}$$

is the free space wave impedance.

The corresponding time averaged Poynting vector component considering only H_y and E_x is, eqn.(2.11),

$$S_z(z) = \frac{1}{2} \mathrm{Re}\left\{ Z_{vac} \frac{n_R}{n_R^2 + n_I^2} |A_f|^2 \exp[-2k_o n_I z] \right\} \tag{2.22}$$

where it shows that there is only power flow along the direction of the wave propagation when $n_R \neq 0$.

The characteristics of the pw propagating in different refractive index media will be studied and discussed in sections 2.4.1-3.

2.4.1 Wave propagation in real refractive index media

Consider that $n = n_R > 0$ and $\varepsilon = \varepsilon_R > 0$, which represents a lossless dielectric medium. Hence H_y, eqn.(2.17), becomes

$$H_y(z) = A_f \exp[-jk_o n_R z] \tag{2.23}$$

describing a forward travelling wave along the positive z direction, having a real (resistive) and positive wave impedance, eqn.(2.20),

$$Z_w = \frac{Z_{vac}}{n_R} \tag{2.24}$$

and power flow as given by eqn.(2.22), in the direction of the wave propagation

$$S_z(z) = \frac{Z_{vac}}{2n_R} |A_f|^2 \tag{2.25}$$

2.4.2 Wave propagation in imaginary refractive index media

When $n = -jn_I$ then $\varepsilon = -|\varepsilon_R| < 0$, and eqn.(2.17) takes the form

$$H_y(z) = A_f \exp[-k_o n_I z] \tag{2.26}$$

with Z_w and S_z both being purely imaginary (reactive), eqns.(2.20) and (2.22),

$$Z_w = +j\frac{Z_{vac}}{n_I} \tag{2.27}$$

$$S_z(z) = +j\frac{Z_{vac}}{2n_I}|A_f|^2 \exp[-2k_o n_I z] \tag{2.28}$$

If $n_I > 0$ eqn.(2.26) describes an exponential decaying wave along the positive z direction having a decay depth Δ,

$$\Delta = \frac{1}{k_o n_I} \tag{2.29}$$

The $n_I > 0$ case corresponds to a pw wave propagating in a free electron (lossless) metal [2.3]. When $n_I < 0$, eqn.(2.26) represents an exponential growing wave in the positive z direction.

2.4.3 Wave propagation in complex refractive index media

Consider now $n = n_R - jn_I$, and ε is as given in eqn.(2.16). Hence H_y, eqn.(2.17), Z_w, eqn.(2.20), and S_z, eqn.(2.22), become,

$$H_y(z) = A_f \exp[-jk_o n_R z]\exp[-k_o n_I z] \tag{2.30}$$

$$Z_w = Z_{vac}\frac{n_R}{n_R^2 + n_I^2} + jZ_{vac}\frac{n_I}{n_R^2 + n_I^2} \tag{2.31}$$

$$S_z(z) = \frac{Z_{vac}}{2}\frac{n_R}{n_R^2 + n_I^2}|A_f|^2 \exp[-2k_o n_I z] \tag{2.32}$$

a) $n_R > 0$ and $n_I > 0$

This n condition is a combination of the cases described in sections (2.4.1-3). Hence, now, eqn.(2.30) represents an attenuated forward travelling wave along the positive z direction, which propagates until S_z, eqn.(2.32), decays to 1/e (~37%) of the initial value at a distance

$$z = L_Z = [2k_o n_I]^{-1} \tag{2.33}$$

If $n_I > n_R > 0$ then $\varepsilon = -|\varepsilon_R| - j|\varepsilon_I|$, describing a lossy metal at optical frequencies. When however $n_R > n_I > 0$, then $\varepsilon = |\varepsilon_R| - j|\varepsilon_I|$, which characterises a lossy dielectric medium. Although both n cases yield the same pw characteristics, the difference is that dielectrics have $\beta_R > \beta_I > 0$ whereas metals give $\beta_I > \beta_R > 0$, hence a smaller Δ, eqn.(2.29), and a shorter L_Z, eqn.(2.33).

b) $n_R > 0$ and $n_I < 0$

In this case eqn.(2.30) describes an exponentially growing forward travelling wave along the positive z direction with H_y, Z_w and S_z as given by eqns.(2.30-2).

Let $|n_I| < |n_R|$ with $\varepsilon = |\varepsilon_R| + j|\varepsilon_I|$, which describes a dielectric medium with optical gain g as found from eqn.(2.32),

$$g = 2k_o|n_I| \tag{2.34}$$

similar to that employed in semiconductor optical sources such as Laser Diodes and Light Emitting Diodes (LEDs) [2.4].

A summary of the plane wave field characteristics studied for different refractive index $n = n_R - j\,n_I$ cases is presented in Table 2.1.

n_R	n_I	$\varepsilon = n^2$	$H_y(z)$	S_z	Z_w
> 0	= 0	$\varepsilon = \varepsilon_R > 0$	Propagating	Purely real	Purely real
= 0	< 0	$\varepsilon = -\|\varepsilon_R\| < 0$	Decaying	Purely imaginary (reactive)	Prurely imaginary (reactive)
= 0	> 0	$\varepsilon = -\|\varepsilon_R\| < 0$	Growing	Reactive (purely imaginary)	Reactive (negative)
> 0	< 0	$\varepsilon = \|\varepsilon_R\| - j\|\varepsilon_I\|$ or $\varepsilon = -\|\varepsilon_R\| - j\|\varepsilon_I\|$	Oscillatory decaying	Partly reactive - real (lossy)	Partly reactive - real
> 0	> 0	$\varepsilon = \|\varepsilon_R\| + j\|\varepsilon_I\|$	Oscillatory growing	Partly reactive - real (optical gain)	Partly reactive - real

Table 2.1. Plane wave field parameters for various n.

2.5 Frequency dependent permittivity

The response of a dielectric medium to an external electromagnetic field is largely determined by the behaviour of electrons that are bound to the atomic nuclei by quasi-elastic forces. In a conducting medium (such as a metal), unlike in a dielectric, not all the electrons are bound to the atoms. Some move between the molecules and are said to be free electrons, to distinguish them from the other electrons that are bound to the atoms, just as in a dielectric. In the absence of an external electromagnetic field, the free electrons move in a random manner and hence they do not give rise to a net current flow. When an external field is applied the free electrons acquire an additional velocity and their motion becomes more orderly, even though occasionally the electrons still collide with the (essentially stationary) atoms. This more orderly motion of the electrons gives rise to the induced current flow. This electron process can be described by the equation of electron motion for displacement r [2.1],

$$\frac{d^2\underline{r}}{dt^2} + \omega_\tau \frac{d\underline{r}}{dt} + \omega_o^2 \underline{r} = -\frac{e}{m^*}\underline{E}_{ap} \tag{2.35}$$

where ω_τ is the collision frequency between the electrons and the atoms given by, [2.5],

$$\omega_\tau = \frac{e}{\mu_e m^*} \tag{2.36}$$

μ_e is the electron mobility, ω_o is related to bonding forces between the electrons and the atomic nuclei, e corresponds to the electron charge, m^* is the electron effective mass; $\underline{E}_{ap} = \underline{E}\exp[+j\omega t]$ is the plane wave applied electric field. Assuming that the displacement and the electric field are in phasor form, eqn.(2.5) has then a solution [2.1],

$$\underline{r} = \frac{-(e/m^*)\underline{E}_{ap}}{(\omega_o^2 - \omega^2) + j\omega\omega_\tau} \tag{2.37}$$

which describes a periodic motion which gives rise to a current in the medium. If there is a n_e density of free electrons, the current density $\underline{J}$, eqn.(2.5), is given as [2.3]

$$\underline{J} = -n_e e \underline{v} \tag{2.38}$$

where v is the velocity of an electron and can be found by differentiating eqn.(2.37) with respect to time t,

$$\underline{v} = \frac{d\underline{r}}{dt} = \frac{-(e/m^*)\underline{E}_{ap}}{(\omega_o^2 - \omega^2) + j\omega\omega_\tau} j\omega \tag{2.39}$$

Hence, by using eqn.(2.39) into eqn.(2.38), it is possible to obtain,

$$\underline{J} = \frac{n_e (e^2/m^*)\underline{E}_{ap}}{(\omega_o^2 - \omega^2) + j\omega\omega_\tau} j\omega \tag{2.40}$$

But since $\underline{J} = \sigma \underline{E}_{ap}$, eqn.(2.5), and assuming no restoring forces present ($\omega_o = 0$) then

$$\sigma = \frac{\varepsilon_o \omega_p^2}{\omega_\tau + j\omega} \tag{2.41}$$

where

$$\omega_p^2 = \frac{n_e e^2}{\varepsilon_o m^*} \tag{2.42}$$

is the plasma frequency. In general, $m^* = k m_e$ where m_e is the electron mass and $k \approx 1$ for metals [2.3], whereas for dielectrics such as GaAs and Si is 0.067 and 0.26 respectively [2.5].

For a source free, $\underline{J}_S$ = 0, and charge free, $\rho = 0$, medium, Maxwell's equations, eqn.(2.2), give

$$\begin{aligned} \hat{\varepsilon} &= \varepsilon_o \left[\varepsilon - j\left(\frac{\sigma}{\omega\varepsilon_o}\right)\right] \\ &= \varepsilon_o \varepsilon_c \end{aligned} \tag{2.43}$$

where ε is a real quantity and describes contribution from the bound electrons of the medium. By using σ as given by eqn.(2.41) in eqn.(2.43), ε_c can be rewritten as

$$\begin{aligned} \varepsilon_c &= \varepsilon - \frac{\omega_p^2}{\omega^2 + \omega_\tau^2} - j\frac{\omega_p^2 \omega_\tau}{\omega(\omega^2 + \omega_\tau^2)} \\ &= \varepsilon_R - j\varepsilon_I \end{aligned} \tag{2.44}$$

At high frequencies ($\omega \rightarrow \infty$), $\sigma \rightarrow 0$, eqn.(2.41), hence $\varepsilon_c = \varepsilon = n_R^2$, eqn.(2.16), describing a lossless dielectric. If however $\omega \rightarrow 0$ (dc conditions), σ becomes, eqn.(2.41),

$$\sigma_{dc} = \frac{\varepsilon_o \omega_p^2}{\omega_\tau} \tag{2.45}$$

and ε_c, eqn.(2.43), is written as

$$\varepsilon_c = \varepsilon - j\frac{\omega_p^2}{\omega\omega_\tau} \tag{2.46}$$

Since at such frequencies $\left|\frac{\omega_p^2}{\omega\omega_\tau}\right| >> |\varepsilon|$, ε_c, eqn.(2.43), can be given as

$$\varepsilon_c \approx -j\frac{\omega_p^2}{\omega\omega_\tau} \tag{2.47}$$

which is the case of a perfect conductor [2.6]. For this case, n can be written as

$$n = \frac{\sqrt{2}}{2}\frac{\omega_p}{\sqrt{\omega\omega_\tau}} - j\frac{\sqrt{2}}{2}\frac{\omega_p}{\sqrt{\omega\omega_\tau}} \tag{2.48}$$

For dielectric media $\varepsilon > 0$, hence eqn.(2.44) describes a lossy dielectric material which for the range of frequencies

$$\omega^2 < \left(\frac{\omega_p^2}{\varepsilon}\right) - \omega_\tau^2 \tag{2.49}$$

can give $\varepsilon_R < 0$ (e.g. heavily doped s/c) which is beyond the Infrared (IR) spectrum regime.

If eqn.(2.44) describes a (lossy) metal, then $\varepsilon = 1$ [2.3], so that

$$\varepsilon_c = 1 - \frac{\omega_p^2}{\omega^2 + \omega_\tau^2} - j\frac{\omega_p^2\,\omega_\tau}{\omega\left(\omega^2 + \omega_\tau^2\right)} = \varepsilon_R - j\varepsilon_I \tag{2.50}$$

giving $\varepsilon_R < 0$ for $\omega^2 < \omega_p^2$ as typically $\omega_p^2 >> \omega_\tau^2$. Noble metals like gold (Au), silver (Ag), aluminium (Al) and copper (Cu), have $\omega_p \approx 56.5\times10^{14}\,s^{-1}$ in the ultra violet (UV) frequency region [2.7] and $\omega_\tau \approx 10^{14}\,s^{-1}$ [2.3]. If an ideal (lossless) metal is considered, then $\omega_\tau \to 0$ (i.e. probability of collision very small and losses are neglected), and eqn.(2.50) gives

$$\varepsilon_c = \left[1 - \left(\frac{\omega_p}{\omega}\right)^2\right] = \varepsilon_R \tag{2.51}$$

In that case, the metal is expected to behave essentially as a dielectric [2.3]. A typical variation of ε_R and ε_I of Al, Cu, Ag and Au as a function of the wavelength λ_o is presented in Figure 2.1 for the optical spectrum regime. Note that the values of ε_R and ε_I for the studied metals have been taken from [2.8].

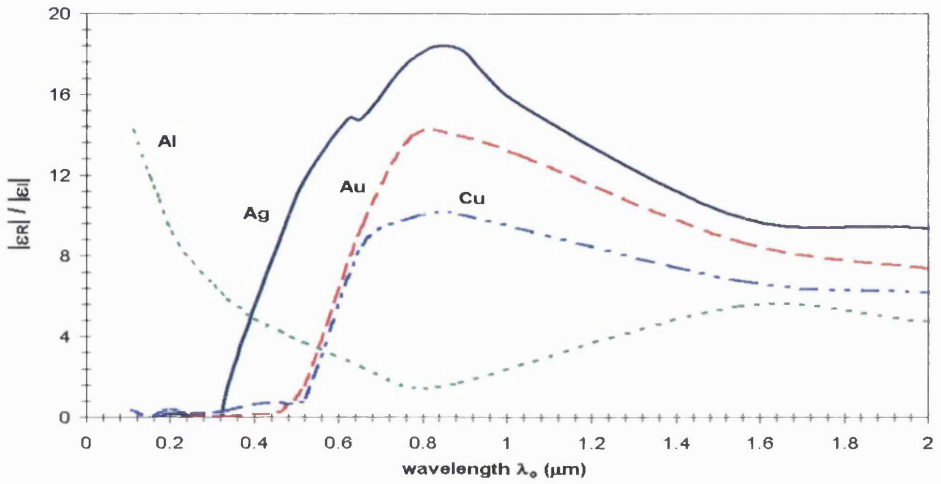

Figure 2.1. Variation of $|\epsilon_R| / |\epsilon_I|$ as a function of wavelength for Ag, Au, Al and Cu in the optical spectrum regime. Data have been obtained from [2.8].

Among the different metals, Al for $\lambda_o < 0.4\mu m$, and Ag for $\lambda_o > 0.4\mu m$ offer the highest $\left(|\varepsilon_R|/|\varepsilon_I|\right)$ ratio, 16 and 20 respectively. As it is well known, metals are widely used as coatings on surfaces or as mirrors due to their high reflectivity. Hence, the larger the $\left(|\varepsilon_R|/|\varepsilon_I|\right)$ ratio, the better reflectivity is provided by a metal surface. Here reflectivity is defined as the ratio between the reflected field intensity I_R from an air – metal interface, of a signal with field intensity I_S that impinges at a normal incident angle to that interface, inset of Figure 2.2, and is given as, [2.1],

$$\frac{I_R}{I_S} = \left|\frac{\sqrt{\varepsilon_m} - \sqrt{\varepsilon}}{\sqrt{\varepsilon_m} + \sqrt{\varepsilon}}\right|^2 = \left|\frac{\sqrt{-|\varepsilon_R| - j|\varepsilon_I|} - \sqrt{\varepsilon}}{\sqrt{-|\varepsilon_R| - j|\varepsilon_I|} + \sqrt{\varepsilon}}\right|^2 \qquad (2.52)$$

where $\varepsilon_m = -|\varepsilon_R| - j|\varepsilon_I|$ is the metal relative permittivity and $\varepsilon = 1$ is the corresponding relative permitivity of the air. Hence, for a large $\left(|\varepsilon_R|/|\varepsilon_I|\right)$ ratio eqn.(2.52) gives $\left(I_R / I_S\right) \to 1$. The reflectivity for the air – metal interface of the inset of Figure 2.2 when Ag, Au, Al and Cu are used as a function of the wavelength λ_o, is presented in Figure 2.2.

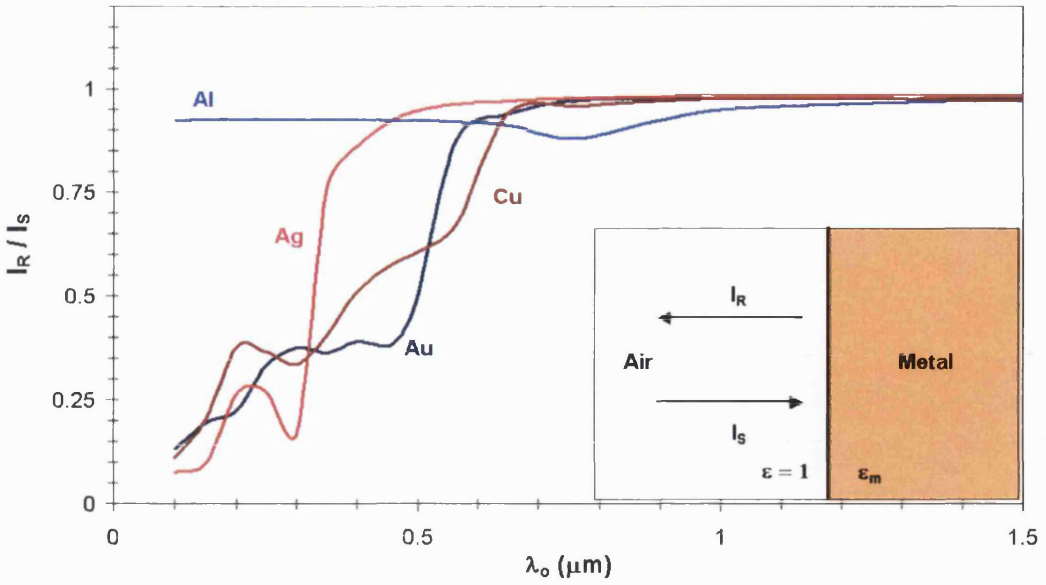

Figure 2.2. Reflectivity from an air – metal interface as a function of wavelength, for Au, Ag, Al and Cu metals.

Hence, for $\lambda_o > 0.7\mu m$, all metals exhibit $(I_R / I_S) \approx 1$, whereas when $\lambda_o < 0.7\mu m$, only Al yields unity reflectivity unlike Ag, Au and Cu which approach transparent conditions i.e. $(I_R / I_S) \rightarrow 0$. The results for $\lambda_o < 0.5\mu m$ are due to the fact that only Al has a high $\left(|\varepsilon_R|/|\varepsilon_I|\right)$ ratio (>1) in that spectrum regime unlike Au, Ag and Cu which give $\left(|\varepsilon_R|/|\varepsilon_I|\right) < 1$, Figure 2.1.

2.6 Conclusions

This chapter has studied the propagation of a plane electromagnetic wave in different refractive index media and showed that such a wave has a purely reactive wave impedance and Poynting vector when propagating in a negative relative permittivity medium. Lossless media represented by real relative permittivity, have real such parameters indicating unattenuated wave propagation. Metals at optical frequencies and heavily doped dielectrics in the THz frequency range, have been shown to exhibit negative relative permittivity. This behaviour was shown by studying the corresponding frequency dependent relative permittivity.

References

[2.1] S. Ramo, J.R. Whinnery, T. Van Duzer, "Fields and Waves in Communication Electronics", John Wiley & Sons, 3rd edition (1994)

[2.2] L.D. Landau, E.M. Lifshitz, "Electrodynamics ofContinuous Media", Volume 8 of Course of Theoretical Physics, Pergamon Press, (1975).

[2.3] M. Born, E. Wolf, "Principles of Optics", Pergamon Press, 6th edition, 1986.

[2.4] J. Wilson, J.F.B. Hawkes, "Optoelectronics: An Introduction", Prentice-Hall International Series In Optoelectronics, 1983.

[2.5] J. Singh, "Semiconductor Devices, Basic Principles", John Wiley & Sons, 2001.

[2.6] A. Ishimaru, "Electromagnetic wave propagation, radiation, and scattering", Prentice Hall, 1991.

[2.7] P. Yeh, "Optical Waves in Layered Media", John Wiley & Sons, 1988.

[2.8] E.D. Palik, "Handbook of optical constants of solids", Academic Press (1985).

Chapter 3

Surface Plasmon Electromagnetic Waves

It is well known that confined optical propagation can be obtained by dielectric guides consisted of at least 3 layers (e.g. optical fibers). However, it is also possible to have electromagnetic waves propagating at a single interface formed by a dielectric and a metal, known as Surface Plasmon Waves (SPWs). Hence, this chapter will review the SPW modal properties at single and multiple dielectric - metal interface structures. An "in-house" developed mathematical model for solving multilayer waveguide structures with complex permittivity media will also be presented.

3.1 Single interface Surface Waves

Consider the planar interface of Figure 3.1, formed by two media with relative permittivities $\varepsilon_1 = \varepsilon_{1R} - j\varepsilon_{1I}$ and $\varepsilon_2 = \varepsilon_{2R} - j\varepsilon_{2I}$, for $x > 0$ and $x < 0$ respectively. Both media are non-magnetic, with relative permeability $\mu = 1$. If there is no field variation along y, the time harmonic dependent fields of the structure will be of the form $\tilde{F}(x,y,z,t) = F(x)\exp[j(\omega t - \beta z)]$, with ω and t real and positive; β is in general complex while F(x) describes the transverse field variation.

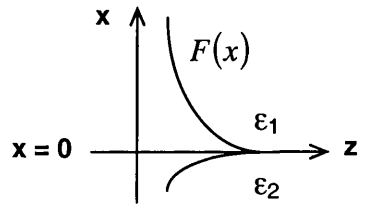

Figure 3.1. Typical schematic of confined optical propagation at single interface.

The wave equation in each medium assuming no field variation along y ($\partial_y^2 \equiv 0$) is then, eqn.(2.7-8),

$$\frac{d^2F(x)}{dx^2} + \left(k_o^2 \varepsilon_q - \beta^2\right)F(x) = 0 \qquad (3.1)$$

where q = 1, 2 corresponds to the two media.

For confined (bound) propagation it is necessary that when $|x| \to \infty$ then $F(x) \to 0$. As a consequence, the solution of eqn.(3.1) should be

$$F(x) = \begin{cases} A_1 \exp[-k_{x1} x], & x \geq 0 \\ A_2 \exp[+k_{x2} x], & x \leq 0 \end{cases} \tag{3.2}$$

where A_1, A_2 are field amplitudes in each region and k_{x1}, k_{x2} are the corresponding transverse propagation constants related to β as,

$$k_{xq}^2 = \beta^2 - k_o^2 \varepsilon_q \tag{3.3}$$

Since k_{xq} and β are in general complex of the form $k_{xq} = k_{xq(R)} - jk_{xq(I)}$ and $\beta = \beta_R - j\beta_I$, for confined wave propagation, it is required that $\beta_R, \beta_I > 0$ and $k_{xq(R)}, k_{xq(I)} > 0$.

A schematic of electromagnetic bound propagation is given in Figure 3.1. In general, electromagnetic waves providing optical confined propagation are known as Surface Electromagnetic Waves (SEWs), [3.1].

3.1.1 TE Surface Waves

With reference to the structure of Figure 3.1, consider TE polarised waves. Such waves can be best described by the electric field component $\tilde{E}_y(x,y,z,t) = E_y(x) \exp[+j(\omega t - \beta z)]$, where ω, β, t have been defined in section 3.1.

By considering confined propagation and following the procedure described in section 3.1, E_y will be of the form given by eqn.(3.2), while from Maxwell's equations, eqn.(2.2), the other non-zero field components are H_z and H_x, [Appendix B.1]. As a consequence, the continuity of the tangential fields, E_y and H_z at the interface x = 0 gives the dispersion equation

$$k_{x1} + k_{x2} = 0 \tag{3.4}$$

which shows that confined optical electromagnetic propagation cannot be sustained at a single interface when TE wave propagation is considered [3.2].

3.1.2 TM Surface Waves

When TM wave propagation is studied for the structure of Figure 3.1, it is best to start the analysis by using the magnetic field component $\tilde{H}_y(x,y,z,t) = H_y(x)\exp[+j(\omega t - \beta z)]$. Hence, by considering no field variation along y, and following the analysis given in section 3.1 for confined propagation, H_y will have the same form as F(x), eqn.(3.2).

The other non-zero field components of the structure obtained from Maxwell's equations, eqn.(2.2), E_z and E_x, are of the form

$$E_x(x) = \begin{cases} \dfrac{\beta}{\omega\varepsilon_o\varepsilon_1} A_1 \exp[+k_{x1}x], & x \geq 0 \\ \dfrac{\beta}{\omega\varepsilon_o\varepsilon_2} A_2 \exp[-k_{x2}x], & x \leq 0 \end{cases} \tag{3.5}$$

$$E_z(x) = \begin{cases} j\dfrac{k_{x1}}{\omega\varepsilon_o\varepsilon_1} A_1 \exp[-k_{x1}x], & x \geq 0 \\ -j\dfrac{k_{x2}}{\omega\varepsilon_o\varepsilon_2} A_2 \exp[+k_{x2}x], & x \leq 0 \end{cases} \tag{3.6}$$

The continuity of the tangential electric and magnetic field components H_y and E_z at the interface x = 0 can give the dispersion equation,

$$\frac{k_{x1}}{\varepsilon_1} + \frac{k_{x2}}{\varepsilon_2} = 0 \tag{3.7}$$

from which [3.3],

$$\beta = k_o\sqrt{\frac{\varepsilon_1\varepsilon_2}{\varepsilon_1+\varepsilon_2}} = \beta_R - j\beta_I \tag{3.8}$$

and

$$k_{xq} = k_o\sqrt{\frac{-\varepsilon_q^2}{\varepsilon_1+\varepsilon_2}} = k_{xq(R)} - jk_{xq(I)} \tag{3.9}$$

where q = 1, 2.

Equations (3.7-9) are studied for different ε_1, ε_2 combinations to examine the single interface structure of Figure 3.1 for bound (surface) electromagnetic waves.

a) $\varepsilon_1 = \varepsilon_{1R} > 0$, $\varepsilon_2 = \varepsilon_{2R} > 0$

Under this condition, eqn.(3.7) cannot be satisfied and confined wave propagation cannot be provided for any ε_1, ε_2 combination.

b) $\varepsilon_1 = \varepsilon_{1R} > 0$, $\varepsilon_2 = -|\varepsilon_{2R}| < 0$

The fact that now $\varepsilon_2 = -|\varepsilon_{2R}| < 0$ allows eqn.(3.7) to be satisfied, having a longitudinal propagation constant β, eqn.(3.8),

$$\beta = \beta_R = k_o \sqrt{\frac{\varepsilon_{1R}|\varepsilon_{2R}|}{\varepsilon_{1R} - |\varepsilon_{2R}|}} \tag{3.10}$$

and a transverse propagation k_{xq}, eqn.(3.9),

$$k_{xq} = k_{xq(R)} = k_o \sqrt{\frac{-\varepsilon_q^2}{\varepsilon_1 - |\varepsilon_{2R}|}} \tag{3.11}$$

which are satisfied only for $|\varepsilon_{2R}| > \varepsilon_{1R}$. Optical surface waves with such features are known as "*Fano*" waves and excited at interfaces between dielectrics and ideal (lossless) metals [3.1].

c) $\varepsilon_1 = \varepsilon_{1R} > 0$, $\varepsilon_2 = \varepsilon_{2R} - j\varepsilon_{2I}$, $|\varepsilon_{2R}| >> |\varepsilon_{2I}|$

A complex ε_2 with $|\varepsilon_{2R}| >> |\varepsilon_{2I}|$ leads to a complex $\beta = \beta_R - j\beta_I$, eqn.(3.8), which has a real term

$$\beta_R \approx k_o \sqrt{\varepsilon_{1R}} \left[\frac{\varepsilon_{2R}(\varepsilon_{1R} + \varepsilon_{2R}) + \varepsilon_{2I}^2}{(\varepsilon_{1R} + \varepsilon_{2R})^2 + \varepsilon_{2I}^2} \right]^{1/2} \tag{3.12}$$

and an imaginary term

$$\beta_I \approx \frac{k_o \sqrt{\varepsilon_{1R}}}{2\left[(\varepsilon_{2R} + \varepsilon_{1R})^2 + \varepsilon_{2I}^2\right]} \frac{\varepsilon_{1R}\,\varepsilon_{2I}}{\left[\varepsilon_{2R}(\varepsilon_{2R} + \varepsilon_{1R}) + \varepsilon_{2I}^2\right]^{1/2}} \tag{3.13}$$

As a consequence, k_{xq}, eqn.(3.9), is complex resulting into oscillating decaying fields into both media. From eqns.(3.12-13), confined propagation can be obtained when:

- $\varepsilon_{2R} > \varepsilon_{2I} > 0$ which corresponds to a surface wave between a lossless and an absorbing dielectric, or
- $\varepsilon_{2R} < 0$ and $\varepsilon_{2I} > 0$, which corresponds to lossy Fano waves known as "*Surface Plasmon Waves*" (SPWs) [3.1].

d) $\varepsilon_1 = \varepsilon_{1R} > 0$, $\varepsilon_2 = \varepsilon_{2R} - j\varepsilon_{2I}$, $\varepsilon_{2I} >> \varepsilon_{2R} > 0$.

This case corresponds to the well known Zenneck waves, [3.3], supporting at an interface between a lossless dielectric with relative permittivity $\varepsilon_1 = \varepsilon_{1R} > 0$ and a highly conductive medium with relative permittivity $\varepsilon_2 = \varepsilon_{2R} - j\varepsilon_{2I} \approx -j\varepsilon_{2I}$, eqn.(2.47), which have a complex β, eqn.(3.8), with a real term described by

$$\beta_R \approx \frac{k_o}{2}\sqrt{\frac{\varepsilon_{2I}^2 \varepsilon_{1R}}{\varepsilon_{1R}^2 + \varepsilon_{2I}^2}} \tag{3.14}$$

and an imaginary by,

$$\beta_I \approx \frac{k_o}{2}\sqrt{\frac{\varepsilon_{1R}^3}{\varepsilon_{1R}^2 + \varepsilon_{2I}^2}} \tag{3.15}$$

The derivation of β_R and β_I for the above studied cases is given in Appendix B.2.

Table 3.1 summarises the combinations between ε_1 and ε_2 which give a confined (surface) wave propagation at the single interface structure of Figure 3.1, when $\varepsilon_{1I} = 0$.

ε_{1R}	ε_{2R}	ε_{2I}	**Types of Surface Waves**
> 0	**> 0**	**= 0**	No surface waves
> 0	**> 0**	**> 0**	Confined propagation with lossy dielectric media
> 0	**< 0**	**= 0**	Fano waves
> 0	**< 0**	**> 0**	SPWs
> 0	**= 0**	**> 0**	Zenneck waves

Table 3.1. Types of surface waves for different ε_1, ε_2 combinations.

Among all the different SEWs briefly introduced in this section, our studies in this thesis will focus in the analysis of ideal and lossless SPWs in multilayer structures, due

to the large number of applications that they are recently involved into, such as biosensing and nanoscale optical components.

3.2 Ideal (lossless) SPWs – Fano waves

Assume the structure of Figure 3.1, where medium 2 ($x < 0$) is an ideal metal with relative permittivity $\varepsilon_2 = \varepsilon_m = -|\varepsilon_{mR}|$, and medium 1 ($x > 0$) a lossless dielectric with relative permittivity $\varepsilon_1 = \varepsilon_{1R} > 0$. Following the analysis of section 3.1.2, the structure can support Fano waves (ideal SPWs) only for TM wave propagation as no TE surface wave can be sustained in a single interface guide, section 3.1.1. The non-zero Fano field components are then: H_y, E_x and E_z. Because the metal is ideal, $\beta = \beta_R > 0$, eqn.(3.10), $k_{x1} = k_{x1(R)} > 0$, eqn.(3.11). and $k_{x2} = k_{xm} = k_{xm(R)} > 0$.

Hence, the dispersion equation for the Fano waves of the structure is, eqn.(3.7),

$$k_{x1(R)} = \frac{\varepsilon_1}{|\varepsilon_{mR}|} k_{xm(R)} \tag{3.16}$$

which describes a straight line with slope $(\varepsilon_1 / |\varepsilon_{mR}|)$, instead of a tangent / cotagent - like function obtained for a three layer dielectric slab waveguide [Appendix C, eqn.(C.17-18)]. By subtracting $k^2_{x1(R)}$ from $k^2_{xm(R)}$, eqn.(3.11), the normalized frequency, w, of the guide is evaluated,

$$k^2_{xm(R)} - k^2_{x1(R)} = k_o^2(\varepsilon_1 + |\varepsilon_{mR}|) = w^2 \tag{3.17}$$

Equation (3.17) represents a hyperbola with an asymptote of 45° slope, i.e. for $|\varepsilon_{mR}| = \varepsilon_1$. By plotting eqns.(3.16-17) on the same graph, any interception point between the two functions will correspond to a bound mode in the waveguide structure, Figure 3.2.

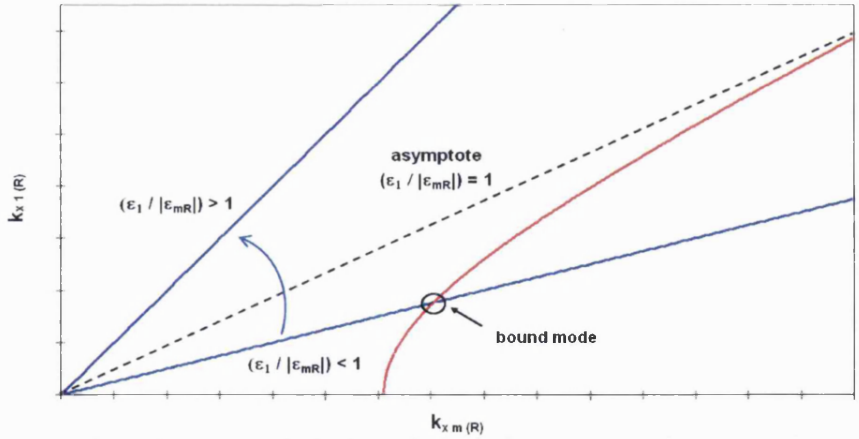

Figure 3.2. Dispersion diagram for Fano waves sustained at a single interface. Blue lines correspond to eqn.(3.16) for different (ϵ_1 / $|\epsilon_{mR}|$) ratios, whereas the red line describes eqn.(3.17); the dotted line is the asymptote of eqn.(3.17).

For the single interface waveguide structure of our studies there is a single interception point between eqn.(3.16) and eqn.(3.17) when $\left(\varepsilon_1 / |\varepsilon_{mR}|\right) < 1$, which corresponds to a Fano mode with β, eqn.(3.10),

$$\beta = \beta_R = k_o \sqrt{\frac{\varepsilon_1 |\varepsilon_{mR}|}{|\varepsilon_{mR}| - \varepsilon_1}} = k_o \sqrt{\varepsilon_{eff}} > k_o \varepsilon_1^{1/2} \qquad (3.18)$$

Any other $|\varepsilon_{mR}|$, ε_1 combination cannot provide a (fully) bound mode, so the effective permittivity of the mode ε_{eff} has to lie beyond ε_1, Table 3.2.

Single interface waveguide fields			
ε_{eff} range	**Dielectric**	**Metal**	**Mode type**
$\varepsilon_{eff} > \varepsilon_1$	Decaying	Decaying	Fano
$0 < \varepsilon_{eff} < \varepsilon_1$	Propagating	Decaying	Semi-bound
$-\varepsilon_1 < \varepsilon_{eff} < 0$	Propagating	Decaying	Semi-bound
$-\lvert\varepsilon_{mr}\rvert < \varepsilon_{eff} < -\varepsilon_1$	Propagating	Decaying	Semi-bound
$\varepsilon_{eff} < -\lvert\varepsilon_{mr}\rvert$	Propagating	Propagating	Not realizable

Table 3.2. Dielectric and metal field behaviour for different ε_{eff}.

By replacing $|\varepsilon_{mR}|$ in eqn.(3.18) with the corresponding frequency dependent expression, eqn.(2.51), it is found that $|\varepsilon_{mR}| > \varepsilon_1$ is only fulfilled for $\omega > \omega_p / \sqrt{\varepsilon_1 + 1}$

(or $\lambda_o < \lambda_p \sqrt{\varepsilon_1 + 1}$), and that β, eqn.(3.18), exhibits only material and not modal dispersion [3.4].

The corresponding transverse propagation k_x in the two media is, eqn.(3.11),

$$k_{xq} = k_{xq(R)} = k_o \sqrt{\frac{\varepsilon_q^2}{|\varepsilon_{mR}| - \varepsilon_1}} \tag{3.19}$$

which shows that the decay depth Δ of the field obtained when $H_y = e^{-1}$, eqn.(3.2), as given by

$$\Delta_q = \mathrm{Re}\left\{k_{x(q)}^{-1}\right\} = \mathrm{Re}\left\{\left(\beta^2 - k_o^2 \varepsilon_q\right)^{-1/2}\right\} \tag{3.20}$$

is shorter inside the metal compared to that in the dielectric. For a typical interface between air ($\varepsilon_1 = 1$) and Ag ($\varepsilon_{mR} = -49$) at $\lambda_o = 1\mu m$, $\beta = 6.35\mu m^{-1}$, $\Delta_1 = 1100nm$ and $\Delta_m = 22nm$. Hence, almost all the field (98%) is in the dielectric while guided by the metal.

The study of eqn.(3.18) reveals some interesting features of Fano waves, such as that β is always larger than that of a plane wave propagating in the dielectric medium, something not feasible for bound modes in dielectric slab guides where β is limited by the higher ε of the structure, [Appendix C, eqn.(C.6)]. Hence, Fano waves always exhibit a smaller phase velocity U_p, compared to that of a plane wave in a dielectric,

$$U_p = \frac{\omega}{\beta_R} = \frac{c}{\sqrt{\varepsilon_1}} \sqrt{\frac{|\varepsilon_{mR}| - \varepsilon_1}{|\varepsilon_{mR}|}} < \frac{c}{\sqrt{\varepsilon_1}} \tag{3.21}$$

The group velocity U_g, of Fano waves is

$$U_g = \frac{\partial \omega}{\partial \beta_R} \tag{3.22}$$

which for $|\varepsilon_{mR}| = (\omega_p / \omega)^2 - 1$, can be rearranged to give, [Appendix B.3],

$$U_g = \frac{\partial \omega}{\partial \beta_R} = \left\{ \frac{\sqrt{\varepsilon_1}}{c} \left(\frac{|\varepsilon_{mR}|}{|\varepsilon_{mR}| - \varepsilon_1} \right)^{1/2} \left[1 + \left(\frac{\omega_p}{\omega} \right)^2 \frac{\varepsilon_1}{|\varepsilon_{mR}| \left(|\varepsilon_{mR}| - \varepsilon_1 \right)} \right] \right\}^{-1} \tag{3.23}$$

that is always positive for $|\varepsilon_{mR}| > \varepsilon_1$.

In practice at long wavelengths $|\varepsilon_{mR}| >> \varepsilon_1$, hence β approaches plane wave conditions with $\beta \rightarrow k_o\sqrt{\varepsilon_1}$, eqn.(3.18). If Fano wave excitation is performed at the UV spectrum regime where it is practically possible that $\varepsilon_1 \approx |\varepsilon_{mR}|$, then $\beta \rightarrow \infty$, eqn.(3.18), leading to very short Δ, eqn.(3.20), and effective wavelength λ_{eff}, where

$$\lambda_{eff} = k_o \frac{\lambda_o}{\beta_R} \tag{3.24}$$

Both Δ and λ_{eff} are desired to be very short to allow Fano waves to be involved in new emerging areas such as sub-wavelength probing and miniaturized optical circuits or structures [3.5]. As a result of the $\beta \rightarrow \infty$ condition, $U_g \rightarrow 0$, eqn.(3.23), and similarly $U_p \rightarrow 0$, eqn.(3.21), which is a well known phenomenon in plasma physics and has to be distinguished from the cut-off condition appearing in the dielectric guides where $U_p \rightarrow \infty$ [3.6]. An infinite U_p describes an electromagnetic wave that is only oscillating in the transverse direction of propagation and not propagating in the longitudinal.

The time averaged Poynting vector $\underline{S}$ of the structure, has non-zero component only along the longitudinal z - direction, eqn.(2.11),

$$S_z(x,z) = \begin{cases} \dfrac{\beta}{2\omega\varepsilon_o\varepsilon_1} |A_1|^2 \exp\left[-2k_{x1(R)}x\right], & x \geq 0 \\ -\dfrac{\beta}{2\omega\varepsilon_o|\varepsilon_{mR}|} |A_2|^2 \exp\left[+2k_{xm(R)}x\right], & x \leq 0 \end{cases} \tag{3.25}$$

From eqn.(3.25), the direction of S_z is along the direction of the wave propagation in the dielectric ($S_z > 0$), but opposite inside the metal ($S_z < 0$), due to $\varepsilon_m < 0$, Figure 3.3.

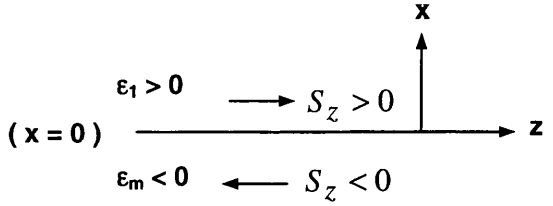

Figure 3.3. Schematic representation of the Poynting vector direction.

Although $S_z < 0$ in the metal resulting in a negative power flow, eqn.(2.6), the total power flow P of the structure, eqn.(2.12), given by

$$P = \frac{\beta}{4\omega\varepsilon_o} |A_1|^2 \left(\frac{1}{k_{x1(R)}\varepsilon_1} - \frac{1}{k_{xm(R)}|\varepsilon_{mR}|} \right) \tag{3.26}$$

is positive for $|\varepsilon_{mR}| > \varepsilon_1$.

Finally, because the intensity of the Fano field described by S_z is maximum at the interface (x = 0), eqn.(3.25), Fano waves are very attractive for examining interface properties e.g. in biological detection [3.7].

3.3 Lossy SPWs

If the metal of the structure of Figure 3.1 (x < 0), is lossy with $\varepsilon_m = -|\varepsilon_{mR}| - j|\varepsilon_{mI}|$ whereas the dielectric remains lossless (x > 0, $\varepsilon_1 = \varepsilon_{1R} > 0$), then a lossy SPW surface wave can be sustained, section 3.1.2. The lossy SPW has similar properties to the Fano wave case studied in section 3.2, but now due to the lossy metal β, eqn.(3.8), and k_{x1} , k_{x2}, eqn.(3.9), are complex with $\beta = \beta_R - j\beta_I$, $k_{x1} = k_{x1(R)} - jk_{x1(I)}$ and $k_{x2} = k_{xm} = k_{xm(R)} - jk_{xm(I)}$. Note that β_R, β_I, $k_{x(R)}$ and $k_{x(I)}$ have to be positive quantities to comply with confined propagation. Due to the imaginary part of β and k_{x1}, k_{x2}, the SPWs have oscillating decaying fields instead of purely decaying as for the Fano waves. Note that typical metals at the visible / IR wavelength regime have $|\varepsilon_{mR}| >> |\varepsilon_{mI}|$, hence $\beta_R > \beta_I > 0$ as derived by eqns.(3.12 – 13). An example of β_R and β_I variation for the lossy SPW as a function of wavelength is shown in Figure 3.4.

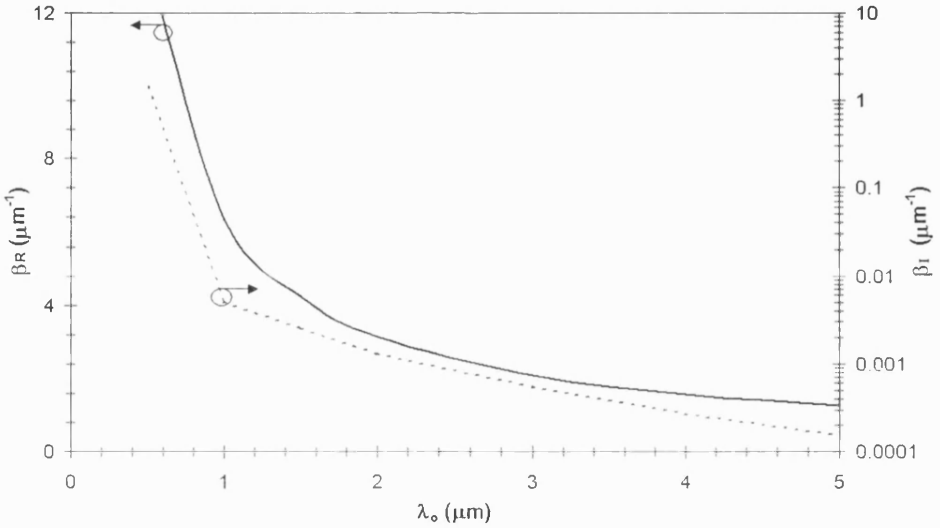

Figure 3.4. Wavelength dependence of β_R and β_I for an SPW at a typical Au - air interface.

While Fano waves yield $\beta_R \to \infty$ for $|\varepsilon_{mR}| \approx \varepsilon_1$, for the same condition however, SPWs give,

$$\beta_R \approx k_o \frac{2\varepsilon_1 + |\varepsilon_{mI}|}{2\sqrt{2}\sqrt{|\varepsilon_{mI}|}} \tag{3.27}$$

$$\beta_I \approx k_o \frac{2\varepsilon_1 - |\varepsilon_{mI}|}{2\sqrt{2}\sqrt{|\varepsilon_{mI}|}} \tag{3.28}$$

which show that $\beta_R \approx \beta_I$, hence very high modal losses which lead to a very short longitudinal propagation constant as it will be shown later in this section. Figure 3.5 shows the variation of β_R and β_I as a function of ε_1 for a dielectric – Au interface at $\lambda_o = 633\text{nm}$.

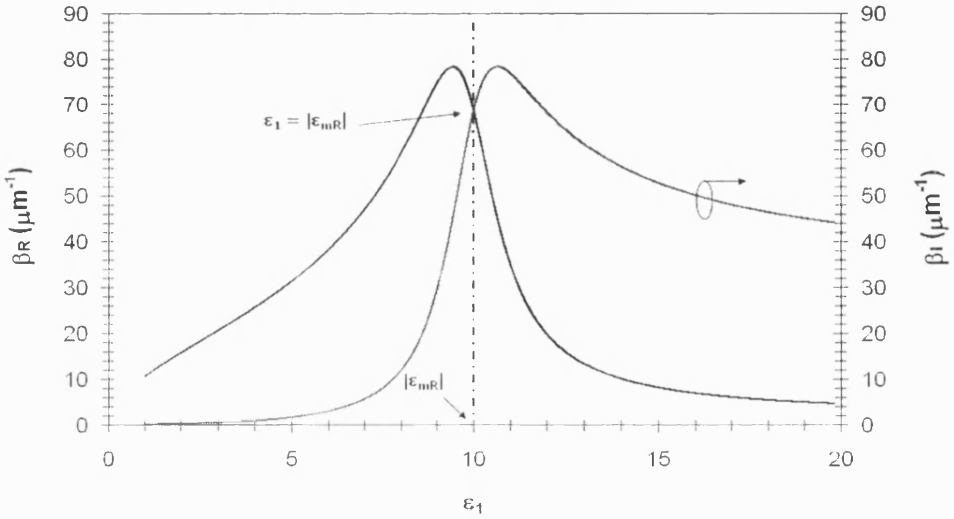

Figure 3.5. β_R and β_I variation as a function of ε_1 when ε_m = - 9.9 - j 1.04 and λ_o = 633nm.

It is clearly shown on the graph that when $|\varepsilon_{mR}| \approx \varepsilon_1$ a high β_R is obtained but at the expense of a high β_I as $\beta_R \approx \beta_I$, and with a much smaller magnitude compared to the ideal metal case (Fano Waves).

Unlike the Fano waves where there is power flow only along the direction of the wave propagation z, eqns.(3.25), SPWs have an additional Poynting vector component in the transverse direction x, S_x, due to the presence of $\varepsilon_{mI} \neq 0$. Hence, the full set of the Poynting vector components derived from eqn.(2.11), for the single dielectric – (lossy) metal interface are:

Dielectric (x $\geq$ 0) :

$$S_z(x,z) = |A_1|^2 \frac{\beta_R}{2\omega\varepsilon_1} \exp(-2k_{x1(R)}x)\exp(-2\beta_I z)$$

$$S_x(x,z) = -|A_1|^2 \frac{k_{x1(I)}}{2\omega\varepsilon_1} \exp(-2k_{x1(R)}x)\exp(-2\beta_I z) \qquad (3.29)$$

Metal (x $\leq$ 0) :

$$S_z(x,z) = -\frac{|A_2|^2}{\varepsilon_{mR}^2 + \varepsilon_{mI}^2} \frac{\beta_R|\varepsilon_{mR}| - \beta_I|\varepsilon_{mI}|}{2\omega} \exp(2k_{xm(R)}x)\exp(-2\beta_I z)$$

$$S_x(x,z) = \frac{|A_2|^2}{2\omega} \frac{k_{xm(R)}|\varepsilon_{mI}| + k_{xm(I)}|\varepsilon_{mR}|}{\varepsilon_{mR}^2 + \varepsilon_{mI}^2} \exp(2k_{xm(R)}x)\exp(-2\beta_I z) \qquad (3.30)$$

Similarly to the Fano waves, SPWs have $S_z > 0$ in the dielectric and $S_z < 0$ in the metal, unlike S_x where $S_x < 0$ in the dielectric and $S_x > 0$ in the metal.

Due to the metal losses however, SPWs propagate for a finite distance L_z in the longitudinal direction of propagation z, until the field intensity S_z reaches 1/e (37%) of its initial amplitude. This distance is given by, [3.8],

$$L_z = [2\beta_1]^{-1} \tag{3.31}$$

A way to extend L_z is to operate at long wavelengths due to the reduced metal losses but at the expense of a less tight field (large decay depth Δ_1), Figure 3.6, which also gives a less intense optical field.

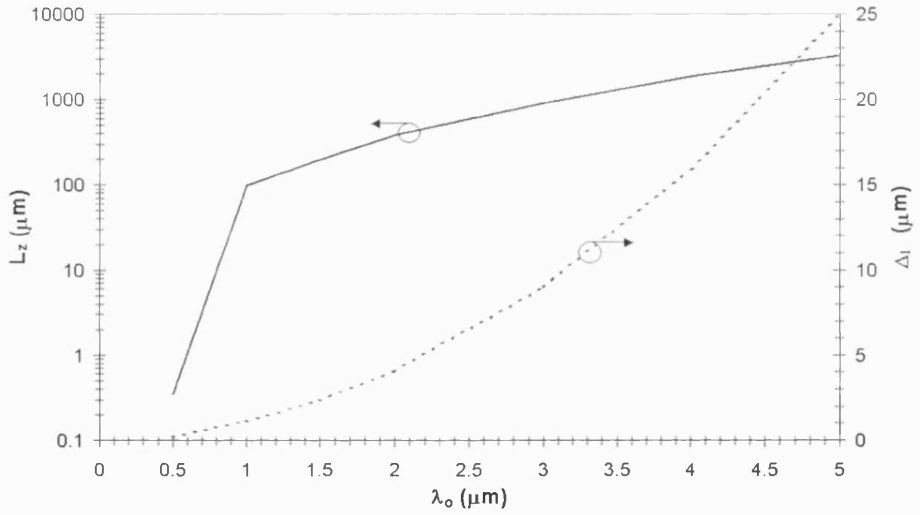

Figure 3.6. Wavelength dependence of SPW dielectric decay depth Δ_1 and propagation distance L_z at an Au - air interface. Note that L_z is in logarithmic scale.

An alternative option is the use of low ε_1 media since β_1 is proportional to $|\varepsilon_{m1}|$, eqn.(3.13), [3.9]. The problem however with this approach is that there is limited number of materials with such properties. In addition, when SPWs are involved in sensing applications the dielectric is usually a water type solution with $\varepsilon_1 \approx 1.77$ which does not allow large flexibility. Another suggestion for increasing L_Z (decrease β_1) is to use multiple dielectric – metal interface structures or introduce optically active media with optical gain g > 0, [3.10-11]. The potential positive effect of these approaches on L_Z will be discussed in section 3.4 and in chapter 6.

3.4 SPWs in multilayer waveguide structures

So far, a single dielectric - metal interface structure capable of supporting SPWs has been studied for providing the basic theory of SPWs. However, as mentioned in section 3.3, the detrimental effect of the usually large metal losses leads to a very short SPW longitudinal propagation distance. To overcome this problem, it has been suggested that multiple dielectric – metal interface structures can be used. Hence, in this section multiple dielectric - metal interface SPW waveguide structures will be analysed. The study will be performed for two 3 - layer slab waveguide arrangements: a) a metal guide with dielectric cladding (DMD) and b) a dielectric guide with metal cladding (MDM).

3.4.1 DMD structure

Consider the three layer slab guide of Figure 3.7, where the cladding media have relative permittivity ε_1, ($x \geq +b$), and ε_3, ($x \leq 0$) respectively, while the guiding region, ($-b \leq x \leq +b$), which is of width $h = (2b)$, has relative permittivity ε_2.

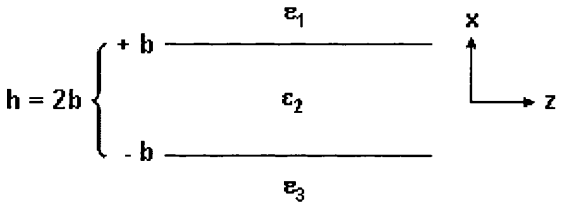

Figure 3.7. Typical three layer slab waveguide structure. For a DMD configuration: $\varepsilon_1 > \varepsilon_2 > 0$ and $\varepsilon_2 = \varepsilon_m = -|\varepsilon_{mR}| - j|\varepsilon_{mI}|$, with $|\varepsilon_{mR}| >> |\varepsilon_{mI}|$.

Let the structure of Figure 3.7 be a DMD arrangement where ε_1 and ε_2 are both real with $\varepsilon_1 > \varepsilon_2 > 0$ and correspond to a lossless dielectric, while $\varepsilon_2 = \varepsilon_m = -|\varepsilon_{mR}| - j|\varepsilon_{mI}|$ with $|\varepsilon_{mR}| >> |\varepsilon_{mI}|$ describes a lossy metal in the optical frequency regime.

The analysis of this structure has shown that TE confined waves cannot be sustained, whereas TM wave propagation allows only the support of SPWs [3.4]. By assuming no field variation along y, it is possible to solve the wave equation, eqn.(2.8), for the H_y magnetic component:

$$H_y(x) = \begin{cases} A_1 \exp(-k_{x1}\, x), & x \geq +b \\ A_m \cosh(k_{xm}\, x) + B_m \sinh(k_{xm}\, x), & -b \leq x \leq +b \\ A_3 \exp(+k_{x3}\, x), & x \leq -b \end{cases} \qquad (3.32a)$$

Hence, the remaining non-zero TM field components as derived by Maxwell's equations, eqn.(2.2), are

$$E_z(x) = \begin{cases} \dfrac{k_{x1}}{\omega\varepsilon_o\varepsilon_1} A_1 \exp(-k_{x1}\,x), & x \geq +b \\ \dfrac{k_{xm}}{\omega\varepsilon_o\varepsilon_m}\left[A_m \sinh(k_{xm}\,x) + B_m \cosh(k_{xm}\,x)\right], & -b \leq x \leq +b \\ -\dfrac{k_{x3}}{\omega\varepsilon_o\varepsilon_3} A_3 \exp(+k_{x3}\,x), & x \leq -b \end{cases} \qquad (3.32b)$$

$$E_x(x) = \begin{cases} \dfrac{\beta}{\omega\varepsilon_o\varepsilon_1} A_1 \exp(-k_{x1}\,x), & x \geq +b \\ \dfrac{\beta}{\omega\varepsilon_o\varepsilon_m}\left[A_m \cosh(k_{xm}\,x) + B_m \sinh(k_{xm}\,x)\right], & -b \leq x \leq +b \\ \dfrac{\beta}{\omega\varepsilon_o\varepsilon_3} A_3 \exp(+k_{x3}\,x), & x \leq -b \end{cases} \qquad (3.32c)$$

where k_{x1}^2, k_{xm}^2 and k_{x3}^2 are described by eqn.(3.3) as,

$$k_{x1}^2 = \beta^2 - k_o^2\varepsilon_1 \qquad (3.33)$$

$$k_{xm}^2 = \beta^2 - k_o^2\varepsilon_m \qquad (3.34)$$

$$k_{x3}^2 = \beta^2 - k_o^2\varepsilon_3 \qquad (3.35)$$

and A_1, A_m, B_m and A_3 are the field amplitudes in the relevant media. For an ideal metal guide ($\varepsilon_{mI} = 0$), the fields are purely hyperbolic sine / cosine inside the metal film and exponentially decaying in the dielectric regions with $k_{xq} = k_{xq(R)} > 0$, (q = 1, 2 = m, 3). If a lossy metal ($\varepsilon_{mI} \neq 0$) is involved, then the fields are oscillatory decaying in the cladding whereas a mixture of both hyperbolic sine / cosine and sine / cosine – like fields exist inside the metal film, where now $k_{xq} = k_{xq(R)} - jk_{xq(I)}$ with $k_{xq(R)}$, $k_{xq(I)} > 0$.

From the continuity of the tangential field components E_z and H_y at the interfaces $x = \pm b$, the dispersion equation of the structure is obtained [3.9],

$$\tanh(k_{xm}\,h) = -\frac{[k_{x1}\,k_{xm}\,\varepsilon_m\,\varepsilon_3 + k_{xm}\,k_{x3}\,\varepsilon_1\,\varepsilon_m]}{[k_{x1}\,k_{x3}\,\varepsilon_m^2 + k_{xm}^2\varepsilon_1\,\varepsilon_3]} \tag{3.36}$$

For an infinitely thick metal film ($h \to \infty$ and $\tanh(k_{xm}\,h) \to 1$), eqn.(3.36) becomes

$$(k_{x1}\,\varepsilon_m + k_{xm}\,\varepsilon_1)(k_{x3}\,\varepsilon_m + k_{xm}\,\varepsilon_3) = 0 \tag{3.37}$$

representing single interface SPWs propagating along the ε_1 - ε_m and ε_3 - ε_m interfaces for $|\varepsilon_{mR}| > \varepsilon_1 > \varepsilon_3 > 0$, with properties as discussed in sections 3.2-3.

If the metal film has a finite thickness h, the two single interface SPWs may couple to each other and produce symmetric and antisymmetric-like SPWs with respect to their field distributions. Here the definition of antisymmetric is for SPWs with H_y exhibiting a zero inside the metal film unlike the symmetric which does not [3.9], Figure 3.8.

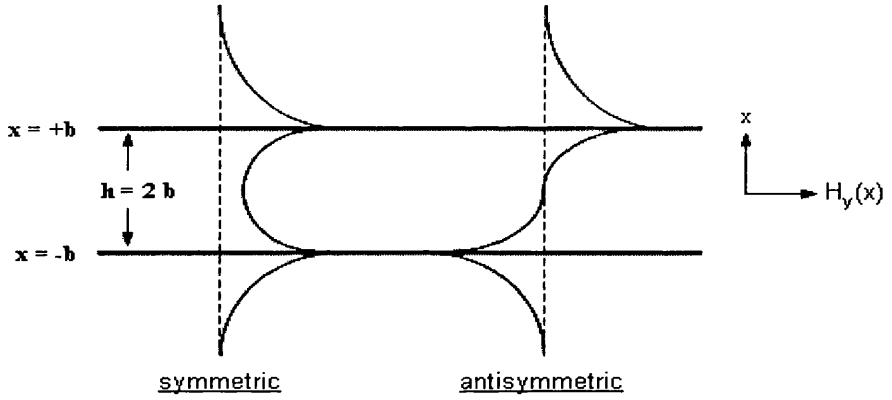

Figure 3.8. Symmetric and antisymmetric SPW field patterns.

It is important to mention here that now β is a function of h and can be obtained by solving the dispersion equation, eqn.(3.36), either numerically or graphically. A computational model for numerically solving such multilayer structures has been developed and will be presented in section 3.5. Note that all the waveguide arrangements analysed in this thesis are solved with the use of this model.

To analyse the available SPW modes of the DMD guide, consider for simplicity a symmetric structure with $\varepsilon_3 = \varepsilon_1$ and $k_{x1}^2 = k_{x3}^2$, eqns.(3.33, 3.35). Hence, eqn.(3.36) can split in two equations describing the antisymmetric, eqn.(3.38), and the symmetric - like SPW, eqn.(3.39), [3.4]

$$\tanh\left(\frac{k_{xm}h}{2}\right) = -\frac{\varepsilon_1 k_{xm}}{\varepsilon_m k_{x1}} \tag{3.38}$$

$$\tanh\left(\frac{k_{xm}h}{2}\right) = -\frac{\varepsilon_m k_{x1}}{\varepsilon_1 k_{xm}} \tag{3.39}$$

The normalized frequency w of the structure following the procedure given in section 3.2, is

$$u^2 - v^2 = w^2 \tag{3.40}$$

where $u^2 = b^2 k_{xm}^2$, $v^2 = b^2 k_{x1}^2$ and $w^2 = b^2 k_o^2 (\varepsilon_1 - \varepsilon_m)$.

The SPW modal properties of the DMD guide will now be examined by studying eqns.(3.38-9) when $\varepsilon_1 < |\varepsilon_{mR}|$ and $\varepsilon_1 \geq |\varepsilon_{mR}|$.

a) $|\varepsilon_{mR}| > \varepsilon_1$

Under this condition, eqns.(3.38-39) show that the DMD structure can sustain only two SPW modes: an antisymmetric (fundamental mode) and a symmetric [3.4, 3.9]. Note here the fundamental mode exhibits the highest β_R in the structure. Unlike the conventional dielectric slab guides in which only the fundamental mode (symmetric) has no cut-off, [Appendix C, Figure C.3], in a DMD structure both SPWs exhibit no cut-off. Between the two SPWs however, the symmetric exhibits smaller β_I and therefore longer L_z, eqn.(3.31), compared to the antisymmetric. Due to that property, the symmetric SPW is referred to as "Long Range SPWs" (LRSPWs) whereas the antisymmetric as "Short Range SPWs" (SRSPWs) [3.1]. LRSPWs are of great interest in biological sensing due to the longer interaction length they provide with the sample under probing, [3.9]. SRSPWs however have the advantage of a very high β_R as the thickness h of the metal film is reduced, offering the potential for subwavelength probing applications due to the very short decay depth Δ, eqn.(3.20), and effective modal wavelength λ_{eff}, eqn.(3.24). If h increases, both SPWs become degenerate and exhibit single dielectric – metal interface features [3.12]. An example showing the above SPW modal features is given in Figure 3.9 where β_R and β_I for the symmetric and antisymmetric SPWs are analysed as a function of the metal thickness h.

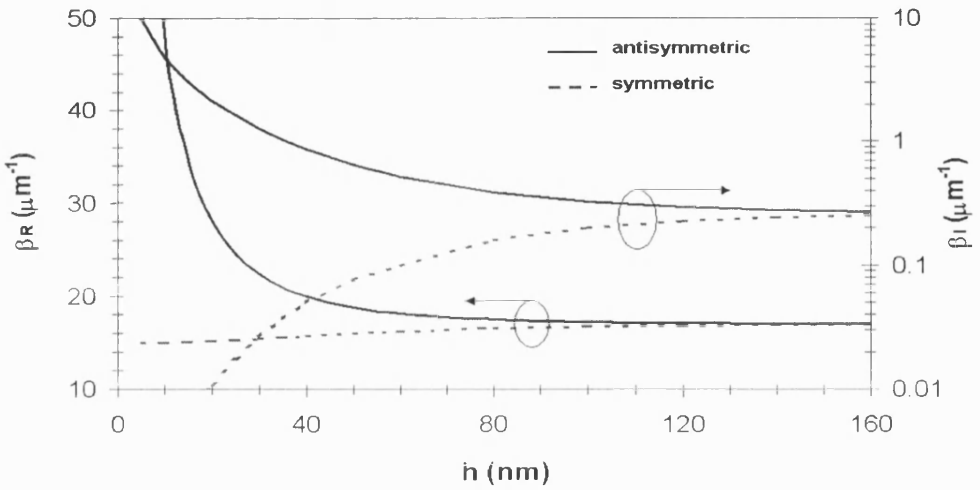

Figure 3.9. Variation of symmetric (dashed line) and antisymmetric (solid line) SPW β_R and β_I as a function of the metal film thickness h, for $\varepsilon_1 = 2.25$, $\varepsilon_m = -9.9 - j\,1.04$ (Au) and $\lambda_o = 633$nm. Note that β_I is in logarithmic scale.

The Poynting vector, eqn.(2.11), of the structure considering an ideal metal has the same characteristics with the single interface SPW structure, section 2.2. Hence, there is only one Poynting vector component in the longitudinal direction of propagation z, S_z, that is positive in the dielectric and negative in the metal. For a lossy metal, there is also a component in the x direction, S_x, indicating power dissipation in the transverse direction. The total power flow for the antisymmetric, P_{ant}, and the symmetric, P_{sym}, for the simple ideal metal case ($\varepsilon_{mI} = 0$) is, eqn.(2.12),

$$P_{ant} = \frac{|B_m|^2 \beta}{2\omega\varepsilon_o}\left\{\frac{\sinh^2(k_{xm}b)}{\varepsilon_1 k_{x1}} - \frac{1}{\varepsilon_m}\left[\frac{\sinh(k_{xm}h)}{2k_{xm}} - b\right]\right\} \tag{3.41}$$

$$P_{sym} = \frac{|B_m|^2 \beta}{2\omega\varepsilon_o}\left\{\frac{\cosh^2(k_{xm}b)}{\varepsilon_1 k_{x1}} - \frac{1}{\varepsilon_m}\left[\frac{\sinh(k_{xm}h)}{2k_{xm}} + b\right]\right\} \tag{3.42}$$

both P_{ant} and P_{sym} are positive for the $|\varepsilon_{mR}| > \varepsilon_1$ case.

b) $\varepsilon_1 \geq |\varepsilon_{mR}|$

Although a single dielectric – metal interface can support bound SPW only if $\varepsilon_1 < |\varepsilon_{mR}|$, eqn.(3.18), the finite thickness metal film of the DMD structure allows

SPWs to be sustained even when $\varepsilon_1 \geq |\varepsilon_{mR}|$, [3.4]. Unlike the $|\varepsilon_{mR}| > \varepsilon_1$ case, section 3.4.1a, where only one symmetric and one antisymmetric SPW are supported by the DMD guide, when $\varepsilon_1 \geq |\varepsilon_{mR}|$ only two symmetric SPWs exist and not any antisymmetric. The two SPWs have an upper cut-off thickness h = h_{co}, which for the simple case of an ideal metal is obtained by combining eqns.(3.39) and (3.40) and considering that when cut-off happens then $\beta^2 = k_o^2 \varepsilon_1$, [Appendix D.2, eqn.(D.11)],

$$h_{co} > \left\{ \log_e \left[\frac{\varepsilon_1 + |\varepsilon_{mR}|}{\varepsilon_1 - |\varepsilon_{mR}|} \right] \right\} \frac{1}{k_o \left(\varepsilon_1 + |\varepsilon_{mR}| \right)^{1/2}} \tag{3.43}$$

As h is reduced the fundamental SPW yields an increased β_R at an expense of high losses (short L_z), whereas the lower order SPW has a β_R that remains constant for any h and exhibit less modal losses (longer L_z). An example of β_R and β_I SPW modal variation as a function of the metal thickness h for the two symmetric SPWs is given in Figure 3.10 for ε_1 = 12.25, ε_m = -9.9 - j 1.04 (Au) and λ_o = 633nm.

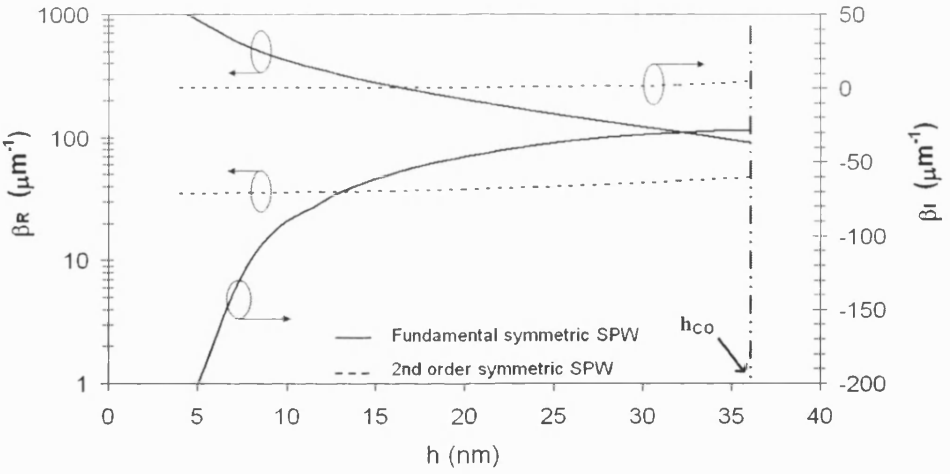

Figure 3.10. Variation of the fundamental symmetric (solid line) and 2nd order symmetric (dashed line) SPW β_R and β_I as a function of the metal film thickness h, for ε_1 = 12.25, ε_m = -9.9 - j 1.04 (Au) and λ_o = 633nm. Note that β_R is in logarithmic scale.

The evaluation of the total power flow for the two symmetric modes from eqn.(3.42), shows that the fundamental SPW has $P_{sym} < 0$ whereas the lower order, $P_{sym} > 0$. A negative power flow however, corresponds to a negative SPW group velocity [3.4, 3.13]. Note now that this negative group velocity is not only because of the material

dispersion due to the metal, but also because of modal dispersion. Figure 3.11 presents a dispersion diagram (ω - β_R) for the DMD structure of this section assuming that $\varepsilon_1 = 12.25$ and $\varepsilon_m = -9.9 - j\ 1.04$ are frequency independent i.e. not dispersive, for a metal film thickness h = 15nm.

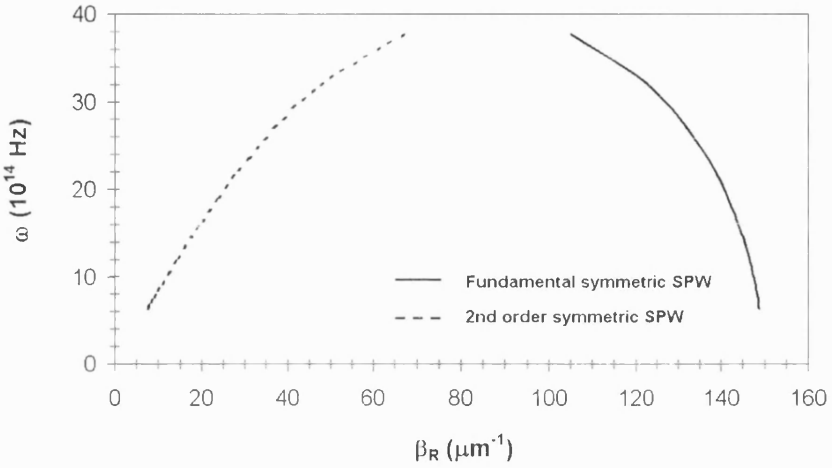

Figure 3.11. Dispersion diagram (ω - β_R) for the fundamental (solid line) and 2nd order (dashed line) symmetric SPWs of the DMD structure for $\varepsilon_1 = 12.25$, $\varepsilon_m = -9.9 - j\ 1.04$ and metal film thickness h = 15nm.

It is clear from Figure 3.11 that the fundamental symmetric SPW exhibits a negative group velocity even if the materials of the DMD guide are not dispersive. Negative group velocities are also encountered in semiconductors for optical-phonon branches or near the top of the conduction bands. Since that SPW has also a positive phase velocity, eqn.(3.17), therefore such waves can be classified as a backward traveling waves [3.13-14]. This result can also be seen in Figure 3.10, where β_1 for the fundamental SPW is negative which indicates that the wave is propagating backwards.

3.4.2 MDM structure

With reference to the structure of Figure 3.7 consider now a MDM guide, where the cladding regions (for $x \geq +b$ and $x \leq -b$) are metals with complex relative permittivities $\varepsilon_1 = \varepsilon_{m1}$ and $\varepsilon_3 = \varepsilon_{m3}$, whereas the guide region ($-b \leq x \leq +b$) is a lossless dielectric with a real relative permittivity $\varepsilon_2 > 0$. For the simplicity of the calculations, a symmetric structure will be considered here with $\varepsilon_{m1} = \varepsilon_{m2} = \varepsilon_m = -|\varepsilon_{mR}| - j|\varepsilon_{mI}|$.

Unlike the DMD configuration where only TM bound waves are supported, the MDM structure can sustain both TE and TM confined propagation [3.4]. Since however the scope of this thesis is to study modal features of SPWs which only exist for TM waves, therefore the analysis of TE wave propagation will not be considered here.

The search for bound solutions for the magnetic field component H_y of the structure through the wave equation by assuming no field variation along y, eqn.(2.8), reveals that two types of waves can be sustained in the structure: the "conventional" waves obtained in metal cladding dielectric guides when $\beta_R^2 < k_o^2 \varepsilon_2$ and the SPWs for $\beta_R^2 > k_o^2 \varepsilon_2$, Figure 3.12, [3.4].

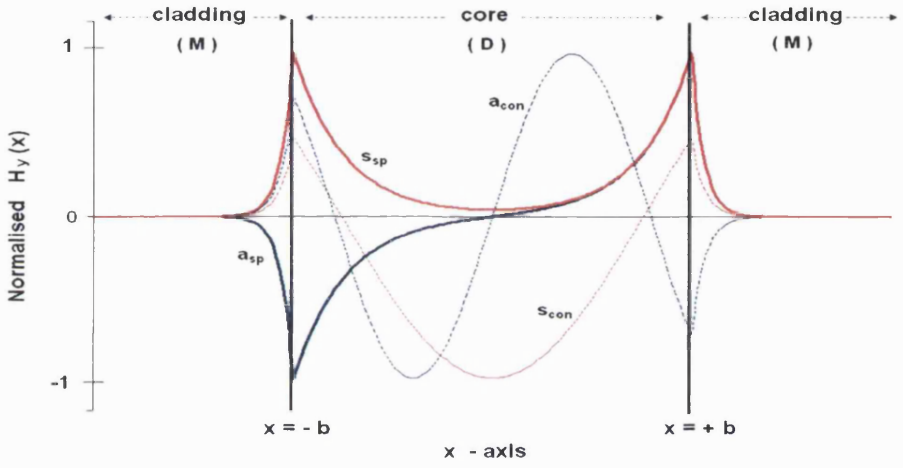

Figure 3.12. Symmetric and antisymmetric normalized H_y field variation for SPWs and conventional waves. a_{sp}: antisymmetric SPW, s_{sp}: symmetric SPW, a_{con}: antisymmetric conventional, s_{con}: symmetric conventional.

As shown in Figure 3.12, SPWs have maximum field amplitude at the interfaces x $= \pm$ b of the structure, while conventional waves inside the guide region ($-b \leq x \leq +b$). Hence, this is why SPWs are widely used to probe interfaces compared to conventional waves, [3.15].

In this thesis however, only the SPWs will be studied. As a consequence the non-zero SPW field components of the structure are H_y, E_z and E_x which are described by eqns.(3.32) by considering a symmetric guide with: $\varepsilon_1 = \varepsilon_3 = \varepsilon_m$, $\varepsilon_m = \varepsilon_2$, $k_{x1} = k_{x3} = k_{xm}$, $k_{xm} = k_{x2}$, $A_1 = A_3 = A_m$, $A_m = A_2$ and $B_m = B_2$. The

transverse propagations constants k_{x1} and k_{xm} are given by eqns.(3.33-34) whereas the symmetric and the antisymmetric SPW dispersion equations from eqns.(3.38-39).

Similarly to the DMD guide case, the SPW modal properties of the MDM structure will be examined by studying the SPW dispersion equations, eqns.(3.38-39), for $\varepsilon_1 < |\varepsilon_{mR}|$ and $\varepsilon_1 \geq |\varepsilon_{mR}|$.

a) $\varepsilon_1 < |\varepsilon_{mR}|$

For $\varepsilon_1 < |\varepsilon_{mR}|$, a symmetric (fundamental) and an antisymmetric SPW can be supported. Between the two modes the symmetric exhibits the less losses (LRSPWs) and exhibits no cut-off in comparison to the antisymmetric which has higher losses (SRSPWs) and an upper cut-off thickness h_{co}. As the dielectric film thickness h is reduced, the symmetric SPW yields now a high β_R compared to the antisymmetric SPW. However, when h is very thick the two modes become degenerate, and the interfaces of the structure approach single dielectric - metal interface conditions. Results of an example showing the variation of β_R and β_I as a function of the dielectric film thickness for the two SPWs, is given in Figure 3.13.

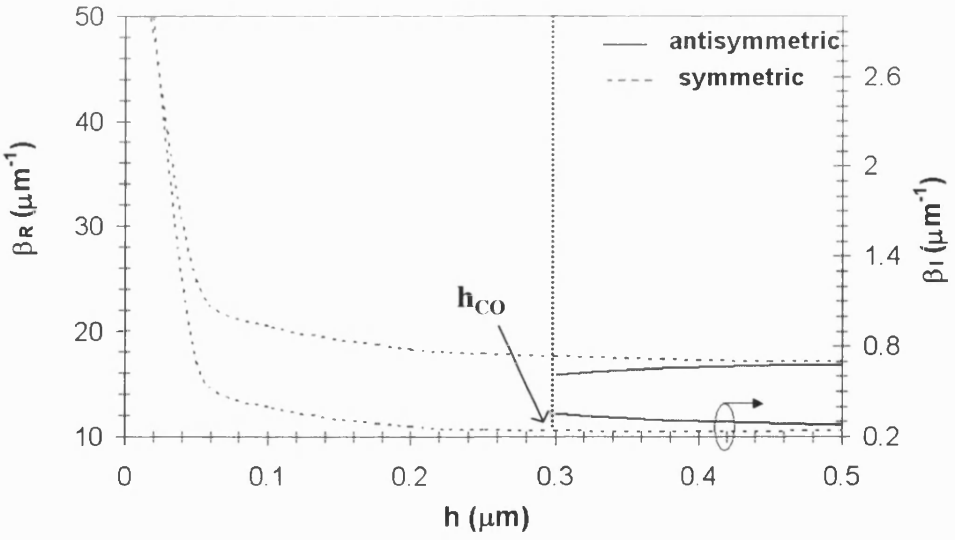

Figure 3.13. Variation of β_R and β_I as a function of the dielectric film thickness h for a symmetric (dashed line) and an antisymmetric (solid line) SPW for ε_m = - 9.9 - j 1.04, ε_2 = 2.25 and λ_o = 633nm.

For an ideal metal, the total Poynting vector, eqn.(2.11), as derived for the DMD structure has a component only along the z direction which is also the case for the MDM guide when $\varepsilon_1 = \varepsilon_3 = \varepsilon_m$, $\varepsilon_m = \varepsilon_2$, $k_{x1} = k_{x3} = k_{xm}$, $k_{xm} = k_{x2}$,

$A_1 = A_3 = A_m$, $A_m = A_2$ and $B_m = B_2$, which gives P_{sym}, eqn.(3.42), and P_{ant}, eqn.(3.41), positive when $\varepsilon_2 < |\varepsilon_{mR}|$.

b) $\varepsilon_1 \geq |\varepsilon_{mR}|$

In that case the MDM guide can support only one antisymmetric SPW exhibiting an upper cut-off thickness and not any symmetric. When h decreases, both β_R and β_I of the SPW increase in magnitude, allowing the mode to be used for subwavelength applications at the expense of high modal losses. Results of an example studying β_R and β_I variation as a function of h for the antisymmetric SPW is given in Figure 3.14.

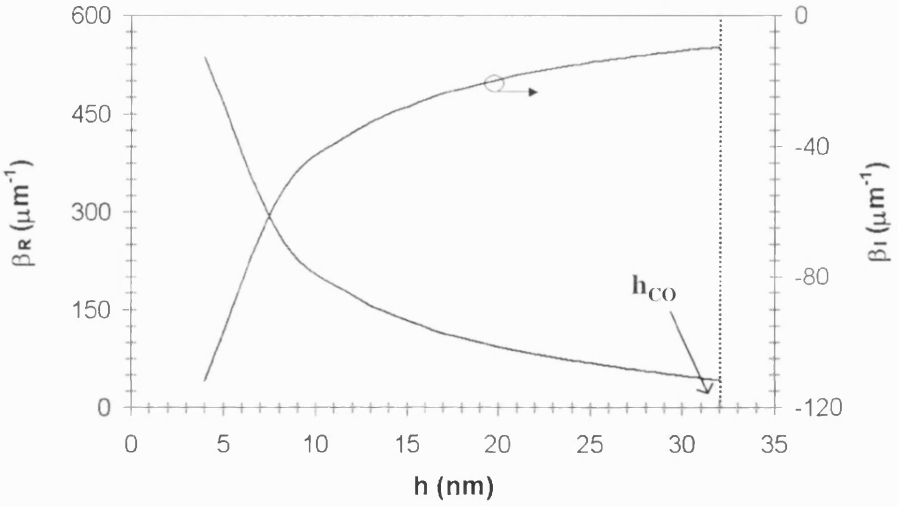

Figure 3.14. Variation of β_R and β_I for an antisymmetric SPW as a function of the dielectric film thickness h when ε_2 =12.25, ε_m = - 9.9 - j 1.04 and λ_0 = 633nm.

The numerical study of the total power flow as found from eqn.(3.41-42) when $\varepsilon_1 = \varepsilon_3 = \varepsilon_m$, $\varepsilon_m = \varepsilon_2$, $k_{x1} = k_{x3} = k_{xm}$, $k_{xm} = k_{x2}$, $A_1 = A_3 = A_m$, $A_m = A_2$ and $B_m = B_2$, reveals that $P_{ant} < 0$ which corresponds to a negative group velocity [3.4, 3.13]. Because the SPW phase velocity is then positive, eqn.(3.21), the SPW is considered to be a backward traveling wave, which is also represented by a negative β_I in Figure 3.14.

A summary of the SPW modal properties for the different waveguide arrangements studied in this chapter is presented in Table 3.3.

	$\lvert\varepsilon_{mR}\rvert > \varepsilon_1$	$\varepsilon_1 \geq \lvert\varepsilon_{mR}\rvert$
Single interface	▪ 1 SPW ▪ positive total power flow	no SPWs
DMD	▪ 1 antisymmetric SPW (fundamental) ▪ 1 symmetric SPW ▪ both SPWs no cut-off ▪ symmetric less lossy ▪ no conventional waves	▪ 2 symmetric SPWs ▪ fundamental symmetric => backward traveling wave ▪ both SPWs high modal losses ▪ no conventional waves
MDM	▪ 1 symmetric SPW (fundamental) ▪ 1 antisymmetric SPW ▪ symmetric no cut-off, less lossy ▪ sustain conventional waves	▪ 1 antisymmetric SPW ▪ negative total power flow ▪ high modal losses ▪ upper cut-off thickness

Table 3.3. SPW modal properties in different waveguide structures.

As a conclusion, with reference to the structure of Figure 3.7, a three layer slab optical waveguide can sustain different types of electromagnetic waves depending on the combination between the relative permittivities ε_1, ε_2 and ε_3 and the range of β solutions.

Hence, if $\varepsilon_2 > 0$ and $\varepsilon_1 = \varepsilon_3 < 0$, this case corresponds to a metal cladding dielectric guide, section 3.4.2, where it is possible to have:

a) for $\beta^2 > k_o^2 \varepsilon_2$, SPWs, Figure 3.15a,

b) for $\beta^2 < k_o^2 \varepsilon_2$, conventional bound modes, Figure 3.15b.

For a purely dielectric slab structure with $\varepsilon_2 > \varepsilon_1 > \varepsilon_3 > 0$, [Appendix C], there are three possibilities:

a) for $k_o^2 \varepsilon_1 < \beta^2 < k_o^2 \varepsilon_2$ the usual conventional bound modes are obtained, Figure 3.15b,

b) for $k_o^2 \varepsilon_3 < \beta^2 < k_o^2 \varepsilon_1$, a semi-bound semi-continuum mode is obtained, Figure 3.15d,

c) for $0 < \beta^2 < k_o^2 \varepsilon_3$, a fully continuum mode is provided, Figure 3.15f.

Finally, for a dielectric cladding metal guide arrangement, section 3.4.1, with $\varepsilon_2 < 0$ and $\varepsilon_1 > \varepsilon_3 > 0$, it is possible to have:

a) for $\beta^2 > k_o^2 \varepsilon_1$, SPWs are obtained, Figure 3.15a,

b) for $k_o^2 \varepsilon_3 < \beta^2 < k_o^2 \varepsilon_1$, a semi – SPW mode is sustained, Figure 3.15c,

c) for $0 < \beta^2 < k_o^2 \varepsilon_3$, a fully continuum mode is realized, Figure 3.15e.

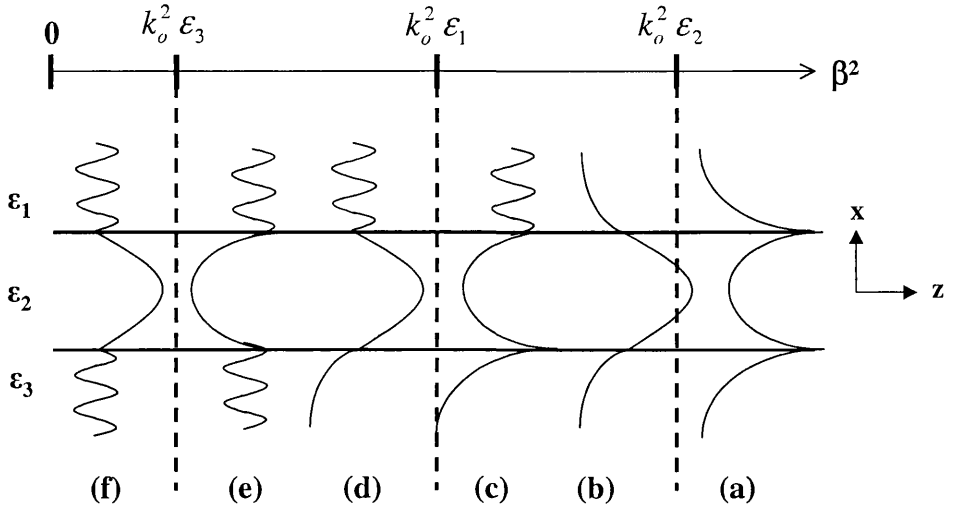

Figure 3.15. Modes in a three layer slab optical waveguide as a function of β^2.

Finally, the above summary shows that the main difference between SPWs and conventional waves is that SPWs can have $\beta^2 \to \infty$ unlike conventional waves where $\beta^2 < k_o^2 \varepsilon_2$ i.e. limited by the relative permittivity of the guiding region.

3.5 Solving multilayer waveguide structures

It is well known that optical slab waveguide structures consisting of up to three layers, and have either real or complex relative permittivity $\varepsilon_C = \varepsilon_R - j\varepsilon_I$, can easily be examined for surface waves (bound modes). This can be done by seeking for the correct solution for the longitudinal propagation constant β, which may also be complex and of the form $\beta = \beta_R - j\beta_I$, when solving the corresponding dispersion equation of the structure either graphically or numerically [3.2]. If however, β is to be sought in more than three layer configurations, the dispersion equation becomes very complicated and

the range for the acceptable β_R and β_I solutions cannot be easily defined. Hence, the use of high level mathematical numerical algorithms is essential [3.16-18].

To avoid the use of such complicated procedures, a simplified algorithm has been developed here. The model is based on the assumption that the media of the multilayer structure have ε_C with $|\varepsilon_R| >> |\varepsilon_I|$ which provides $|\beta_R| >> |\beta_I|$ as it is the case for the SPWs, section 3.3.

Any multilayer waveguide structure has in general a complex dispersion equation $\mathcal{D}$ of the form

$$\mathcal{D}(\beta_R, \beta_I) = \mathcal{D}_R(\beta_R, \beta_I) + j\,\mathcal{D}_I(\beta_R, \beta_I) = 0 \tag{3.44}$$

where $\mathcal{D}_R$ and $\mathcal{D}_I$ are the real and imaginary parts of $\mathcal{D}$ given as a function of β_R and β_I.

Equation (3.44) is in general a transcendental equation which in principle can be easily solved as a system of two equations

$$\mathcal{D}_R(\beta_R, \beta_I) = 0 \tag{3.45}$$

$$\mathcal{D}_I(\beta_R, \beta_I) = 0 \tag{3.46}$$

with two unknown variables β_R and β_I, by employing well known mathematical techniques [3.19].

The only problem however that needs to be tackled, is the range in which β_R and β_I should lie for bound mode solutions. It is well known that in a lossless guide (where all media have $\varepsilon_I = 0$) bound modes have $\beta_I = 0$, hence then the range for acceptable β_R solutions is given by solving the wave equation, eqn.(2.7-8) for the corresponding waveguide structure, [Appendix C gives an example for a 3-layer structure]. The difficulties however arise even if one of the waveguide media has $\varepsilon_I \neq 0$, which will then give $\beta_I \neq 0$. As a consequence, apart from defining a range for β_R solutions, it is necessary now to set also a corresponding range for β_I which for some cases is very difficult to be done, hence the full complex plane has to be searched.

To overcome this complication, it is suggested here that the problem is split into two parts: a) when all media have $\varepsilon_I = 0$ (purely lossles waveguide), and b) when at least one medium has $\varepsilon_I \neq 0$. It is also assumed that the analysis will be valid for the case where $|\varepsilon_R| >> |\varepsilon_I|$ so that $|\beta_R| >> |\beta_I|$.

If all media have $\varepsilon_I = 0$, then $\mathcal{D} = \mathcal{D}_{lossless}$ of the structure, eqn.(3.44), is either purely real or imaginary (depends on the way is derived) and is satisfied for a number of $\beta_{(q)} = \beta_{R(q)}$ solutions for surface waves, where q = 1, 2, ..Q corresponds to the number of available surface modes in the waveguide. Let for the sake of simplicity that $\mathcal{D}_{lossless} = \mathcal{D}_R$ is real and mode 1 is used which has $\beta_{(1)} = \beta_{R(1)}$, lies in the range defined by the wave equation, [Appendix C, eqn.(C.6)], and obtained by well known and commonly mathematical algorithms.

When at least one of the structure media has $\varepsilon_I \neq 0$, the dispersion equation $\mathcal{D}$ is complex $\mathcal{D} = \mathcal{D}_C = \mathcal{D}_{CR} + j\mathcal{D}_{CI}$ and for surface waves is satisfied for a number of complex $\beta = \beta_C$ solutions of the form $\beta_{C(q)} = \beta_{CR(q)} - j\beta_{CI(q)}$ when

$$\mathcal{D}_{CR} = 0 \tag{3.47}$$

$$\mathcal{D}_{CI} = 0 \tag{3.48}$$

Since it has been assumed that $|\varepsilon_R| >> |\varepsilon_I|$, hence $\varepsilon_I \neq 0$ produces a small perturbation to $\beta_{R(q)}$ so that $\beta_{CR(q)} = \beta_{R(q)} + \delta\beta_{CR(q)}$ where $|\delta\beta_{CR(q)}| << |\beta_{R(q)}|$, and also $|\beta_{CR(q)}| >> |\beta_{CI(q)}|$.

As a consequence, $\mathcal{D}_C$ can then be solved employing an iteration procedure until eqns.(3.47-48) are simultaneously zero. By following the assumptions made in this section ($|\varepsilon_R| >> |\varepsilon_I|$ and $|\beta_{CR(q)}| >> |\beta_{CI(q)}|$), the iteration process for $\mathcal{D}_C$ will have starting values for $\beta_{CR(q)} = \beta_{R(q)}$ and $\beta_{CI(q)} = \Delta$, where Δ is very small number and close to zero. Hence, by increasing or decreasing $\beta_{CR(q)}$ and $\beta_{CI(q)}$ by small steps $\Delta\beta_{CR}$ and $\Delta\beta_{CI}$ respectively, it is possible to satisfy eqns.(3.47-48) and obtain a set of $\beta_{CR(q)}$ and $\beta_{CI(q)}$ solutions for surface (bound) modes. The model has been tested for

correct operation with material from the literature as it is presented in Appendix E. The flow diagram of this algorithm is presented in Figure 3.16.

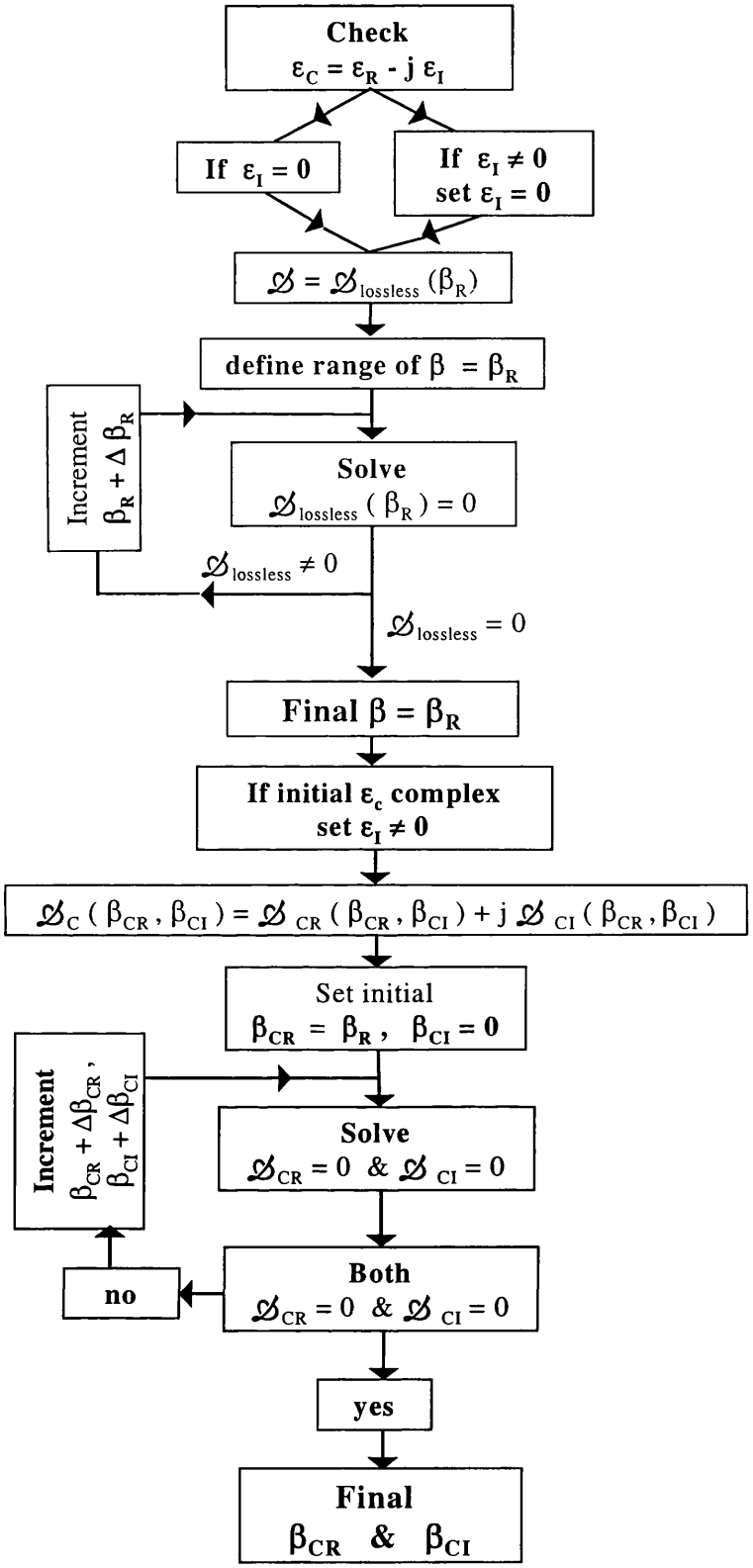

Figure 3.16. Flow diagram for numerically solving multilayer waveguide structures.

3.6 Conclusions

In this chapter the modal properties of SPWs supported by single and multiple dielectric – metal interface waveguide structures have been reviewed. It has been shown that SPWs exhibit high modal losses as a consequence of the typically large metal losses, which make them have a short longitudinal propagation distance. By comparison, SPWs supported in multilayer waveguide structures can have significantly reduced modal losses and exhibit very large longitudinal propagation constant which leads to very short transverse decay depth and effective wavelength. Hence, SPWs have the potential to be involved in subwavelength applications or long length sensing interactions. It has also been found that SPWs may yield a negative total power flow due to a negative group velocity.

Finally, an "in-house" developed mathematical algorithm for solving multilayer waveguide structures with complex relative permittivity media where SPWs can be sustained, has also been presented and tested for its correct operation.

References

[3.1] F. Yang, J. R. Sambles, G. W. Bradberry, "Long-range surface modes supported by thin films," Phys. Rev. B 44, p.5855-5872, 1991.

[3.2] P. Yeh, "Optical Waves in Layered Media", John Wiley & Sons, 1988.

[3.3] A. Ishimaru, "Electromagnetic wave propagation, radiation, and scattering", Prentice Hall, 1991.

[3.4] B. Prade, J.Y. Vinet and A. Mysyrowicz, "Guided optical waves in planar heterostructures with negative dielectric constant", Phys. Rev. B, vol.44, no.24, p.13556, 15 December 1991.

[3.5] W.L. Barnes, "Surface plasmon-polariton length scales: a route to sub-wavelength optics", J. Opt. A: Pure Appl. Opt., vol.8, no.4, pp.S87-93, April 2006.

[3.6] A.D. Boardman, "Electromagnetic Surface Modes", John Wiley & Sons, 1982, p.143.

[3.7] W. Knoll, "Interfaces and thin films as seen by bound electromagnetic waves", Ann. Rev. Phys. Chem., vol.49, pp.565-634, 1998.

[3.8] H. Raether, "Surface Plasmons on Smooth and Rough Surfaces and on Gratings", vol.111, Springer Tracts in Modern Physics, Springer-Verlag, 1988.

[3.9] J.J. Burke, G.I. Stegeman, T. Tamir, "Surface-polariton-like waves guided by thin, lossy metal films", Phys. Rev. B, vol.33, no. 8, pp.5186-5201, 15 April 1986.

[3.10] A.Tarlis, J.Sarma, "Surface Plasmon Waves in Multilayers with Loss / Gain", XXVIII URSI General Assembly, New Delhi, India, 23-29 October 2005.

[3.11] A.Tarlis, J.Sarma, F.Causa, S.Maier, "Losses and Gains with Surface Plasmon Waves", SIOE'06 "Semiconductors and Integrated Optoelectronics Conference", University of Cardiff, Wales, 21-23 March 2006.

[3.12] J. Homola, "Present and future of surface plasmon resonance biosensors", Anal. Bioanal. Chem.(2003), vol.377, no.3, p.528.

[3.13] P. Tournois, V. Laude, "Negative group velocities in metal-film optical waveguides", Optics Communications, vol.137, pp.41-45, 15 April 1997.

[3.14] S. Ramo, J.R. Whinnery, T. Van Duzer, "Fields and Waves in Communication Electronics", John Wiley & Sons, 3rd edition (1994).

[3.15] O. Parriaux, G. Voirin, "Plasmon Wave versus Dielectric Waveguiding for surface Wave sensing", Sensors and Actuators, A21 – A23 (1990), p.1137.

[3.16] E. Anemogiannis, E. Glytsis, "Multilayer Waveguides: Efficient Numerical Analysis of General Structures", Journal of Lightwave Technology, vol.10 no.10, October1992, p.1344

[3.17] E.K. Sharma, M.P. Singh, P.C. Kendall, "Exact Multilayer Waveguide Design Including Absorbing or Metal Layers", Electronics Letters, 28th February 1991, vol.27 no.5, p.408

[3.18] M.R. Ramadas, E. Garmire, A. Ghatak, K. Thyagarajan, M.R. Shenoy, "Analysis of absorbing and leaky planar waveguides: a novel method", Optics Letters, vol.14 no.7, 1 April 1989, p.376

[3.19] "Roots of one or more transcendental equations", NAG Fortran Library Manual, Mark 14, vol.1, Foreword – D01, The Numerical Algorithms Group Limited, 1st edition, 1990.

Chapter 4

Surface Plasmon Wave Excitation

In chapter 3, SPW modal properties in different waveguide structures were presented and analysed. In this chapter however, prism couplers will be studied as a mean for SPW excitation. The analysis will use the well known theory of electrical transmission lines to describe the SPW excitation phenomenon in various prism coupled waveguide structures instead of the commonly applied cascaded matrix analysis.

4.1 Surface Wave Excitation

The analysis of the SPW modal properties in chapter 3 has taken into account that SPWs had been excited by end-fire excitation, i.e. shining light in the longitudinal z direction. In some cases however, end-fire excitation is difficult to be used for example if the dimensions of the waveguide structures are below the light diffraction limit, such as is the case for SPW excitation. An alternative approach is to shine light from the top of the structure, provided that this is not perfectly flat [4.1], which can be done by employing grating and prism couplers or make the surface rough.

Prism coupling is a very attractive and convenient wave excitation method in terms of fabrication, operation, apparatus involved and theoretical analysis, and has the advantage of allowing mode selectivity [4.2]. A drawback of this method is that the maximum allowable longitudinal propagation constant β of the guided modes is limited by the prism materials. Grating couplers have the potential of a high β and can also offer compact structures, but require complicated theoretical analysis and precise fabrication [4.3]. This thesis however, will study only the prism couplers and analyse their use for SPW excitation.

4.2 Plane wave – Cascaded Matrix Analysis

It is well known that guided wave excitation in a prism coupled waveguide arrangement is realised by monitoring the field intensity of the reflected signal I_R from the prism coupler, as a function of the incident angle θ_i at which the input signal with field intensity I_S impinges onto the prism.

The most commonly used analysis for modeling I_R from any multilayer prism coupled structure, is the well known plane wave, cascaded matrix analysis (CMA) [4.4]. With CMA, the study of I_R is performed by examining the field reflection coefficient Γ of the corresponding structure.

Consider the prism coupled structure of Figure 4.1 consisted of n layers (n = 1,2,...,N) , where a $(TM)_z$ or $(TE)_z$ polarised plane wave with field intensity I_S is incident at an angle θ_i, at the interface x = 0. Here, a $(TM)_z$ polarised wave has the electric field parallel to the plane of incidence (poi) x – z, whereas a $(TE)_z$ wave has the electric field normal to the poi, [4.4]. The n^{th}-layer of the structure has thickness d_n and, in general, a complex relative permittivity, ε_n. The layers 1 and N are semi-infinite and $\varepsilon_1 = \varepsilon_p$ will be assumed real and positive (to represent the experimental situation for prism excitation).

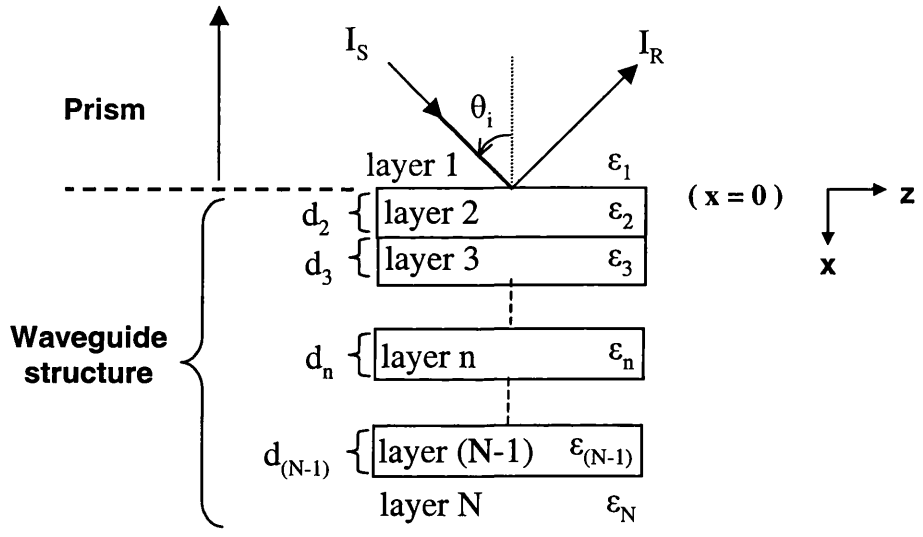

Figure 4.1. Multilayer prism coupled waveguide structure.

Let the time harmonic dependent total field in each medium, assuming no field variation along y, be of the form

$$\begin{aligned}\tilde{F}_{(n)}(x,y,z,t) &= F_{(n)}(x)\exp[+j(\omega t - k_{z(n)} z)] \\ &= \{A_n \exp[-jk_{x(n)} x] + B_n \exp[+jk_{x(n)} x]\}\exp[+j(\omega t - k_{z(n)} z)]\end{aligned} \tag{4.1}$$

where A_n and B_n are the field amplitudes in the n^{th} medium and $k_{z(n)}$, $k_{x(n)}$ the corresponding longitudinal and transverse propagation constants. To simplify the analysis consider that for $(TM)_z$ polarized plane waves $\tilde{F}$ corresponds to the magnetic field component $\tilde{H}_y$, whereas for $(TE)_z$ waves to the electric field component $\tilde{E}_y$. From Maxwell's equations the non-zero $(TM)_z$ field components are $\tilde{H}_y$, $\tilde{E}_z$ and $\tilde{E}_x$, whereas for $(TE)_z$ are $\tilde{E}_y$, $\tilde{H}_x$ and $\tilde{H}_x$. The detailed analysis is given in Appendix F.1-2.

The requirement of field matching across any interface for all z in either polarisations, requires k_z to be the same in every layer, [Appendix F, eqn.(F.11)],

$$k_{z(n-1)} = k_{z(n)} = \beta = k_o \sqrt{\varepsilon_1} \sin\theta_i \tag{4.2}$$

Equation (4.2) is purely real since ε_1 is purely real and the incident signal is an infinite propagating plane wave, whereas $k_{x(n)}$ is in general complex, [Appendix F.3], different in each medium and related to β, eqn.(4.2), as:

$$k_{x(n)}^2 = k_o^2 \varepsilon_n - \beta^2 \tag{4.3}$$

From the continuity of the tangential field components E_z and H_y for $(TM)_z$ or E_y and H_z for $(TE)_z$ fields, at every interface of the structure, the field reflection coefficient Γ of the structure is, [Appendix F.1-2, eqn.(F.22)],

$$\Gamma = \frac{B_1}{A_1} \tag{4.4}$$

where A_n and B_n are found by

$$\begin{pmatrix} A_1 \\ B_1 \end{pmatrix} = \begin{pmatrix} M_{11} & M_{12} \\ M_{21} & M_{22} \end{pmatrix} \begin{pmatrix} A_N \\ B_N \end{pmatrix} \tag{4.5}$$

The matrix elements M_{11}, M_{12}, M_{21} and M_{22} for $(TM)_z$ and $(TE)_z$ polarised signals are defined in Appendix F.1. Equation (4.4) describes the ratio between the incident and

the reflected field amplitudes A_1 and B_1 respectively, assuming that $B_N = 0$, i.e. there is no reflected signal in the N layer [4.4].

From eqn.(4.5) it is also possible to evaluate the field transmission coefficient T of the structure, which relates the incident field amplitude A_1 with the transmitted field amplitude in the N medium, A_N, as:

$$T = \frac{A_N}{A_1} \tag{4.6}$$

Equation (4.5) can be used to examine any interface of the multilayer prism coupled structure as,

$$T_n = \frac{A_{n+1}}{A_n} \tag{4.7}$$

In this thesis the field transmission coefficient T as described by eqn.(4.6) will be used, unless it is explicitly indicated otherwise.

4.3 Transmission Line analysis of multilayer prism coupled structures

The study of Γ, eqn.(4.4), and T, eqn.(4.6), for analyzing optical wave excitation and propagation in multilayer prism coupled waveguide structures by employing CMA, section 4.2, provides a satisfactory description of the response of such system. However, it is often desirable to have a rigorous analysis procedure that also provides better physical interpretation of the various optical phenomena occurring in the structure. This requirement can be satisfied by implementing the transmission line (T-L) analysis. T-L uses the transverse characteristic impedance and the well known theory of transmission lines [4.5-8] to reduce the model for the multilayer structure to a simple two line circuit [4.9] so that the condition for mode excitation is clearly recognised. In addition, a far better physical insight is obtained of the nature of the contribution by each of the layers to the overall electromagnetic phenomenon.

4.3.1 Basic Transmission Line (T-L) Theory

The theory of electromagnetic wave propagation on transmission lines is well established [4.6-7] and it is also well known that the electromagnetic field equations can be rigorously written in terms of the T-L equations (sometimes referred to as the

Generalised Telegraphist's Equations), [4.10-11]. The basic T-L equation of primary interest here is the impedance Z_{in} seen at the input of a T-L which has a characteristic impedance, Z_0, propagation constant, γ, length, d, and is terminated by an impedance Z_L. From T-L theory, [4.6-7]

$$Z_{in} = Z_0 \left[\frac{Z_L + Z_0 \tanh(\varphi)}{Z_0 + Z_L \tanh(\varphi)} \right] \tag{4.8}$$

where $\varphi = \gamma d$, the electrical length of the line. Note that in general Z_0, γ, φ and Z_L are complex.

4.3.2 T-L Representation of Fields in Multiple Layers

The multilayer structure of Figure 4.2a can be represented as a T-L network, Figure 4.2b, where the $(TM)_z$ and $(TE)_z$ polarised transverse (x-directed) impedances for the n^{th} layer are, [Appendix F.1, eqn.(F.12)], [4.6-7],

$$\text{TM:} \quad Z_{0x(n)} = \frac{-E_{z(n)}}{H_{y(n)}} = \frac{k_{x(n)}}{k_o \varepsilon_n} \tag{4.9}$$

$$\text{TE:} \quad Z_{0x(n)} = \frac{-E_{y(n)}}{H_{z(n)}} = \frac{k_o}{k_{x(n)}} \tag{4.10}$$

Note that all characteristic impedances Z_{0x} are normalised with respect to $Z_{vac} \approx 377\ (\Omega)$, eqn.(2.21).

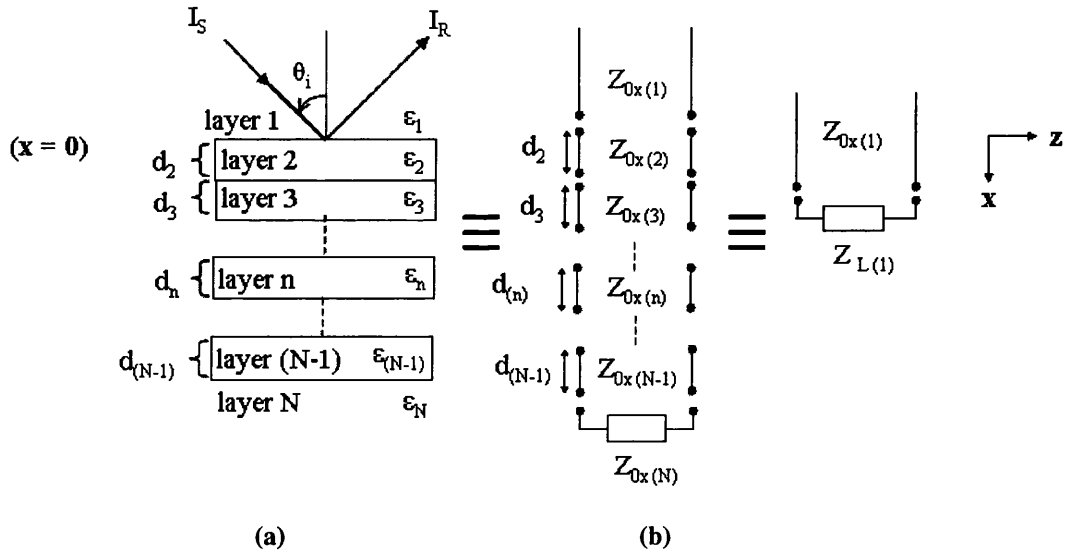

Figure 4.2. Multilayer prism coupled waveguide structure, (a), represented as a T-L network, (b).

Conventional T-L theory, eqn.(4.8), can be applied to find the input impedance by 'looking along' $x > 0$ from the $x = 0$ plane (interface between layers 1 and 2) in to the cascade of transmission lines (layers, $n = 2, 3 \ldots N-1, N$); by considering two layers at a time, starting with layers N and N-1, and progress upwards to thus obtain the "load" impedance $Z_{L(1)}$. Operating in this way on layers N-1 and N, the cascade of T-Ls will be reduced to $1 \leq n \leq N-2$ with the $(N-2)^{th}$ T-L terminated by a load

$$Z_{L(N-2)} = Z_{0x(N-1)}\left[\frac{Z_{L(N-1)} + Z_{0x(N-1)}\tanh(\varphi_{(N-1)})}{Z_{0x(N-1)} + Z_{L(N-1)}\tanh(\varphi_{(N-1)})}\right] \tag{4.11}$$

where $Z_{L(N-1)} = Z_{0x(N)}$ and the electrical length φ of the structure is, [Appendix F],

$$\begin{aligned}\varphi_{(N-1)} &= \gamma_{N-1}\, d_{(N-1)} \\ &= +jk_{x(N-1)}\, d_{(N-1)}\end{aligned} \tag{4.12}$$

Continued application of this process will end with the semi-infinite T-L with characteristic impedance, $Z_{0x(1)}$, terminated by the load impedance, $Z_{L(1)}$, that will have been obtained from the above process, Figure 4.2b.

The field reflection coefficient for the incident wave due to the load $Z_{L(1)}$, terminating the semi-infinite T-L is then, [4.6-7],

$$\Gamma = \frac{Z_{L(1)} - Z_{0x(1)}}{Z_{L(1)} + Z_{0x(1)}} \tag{4.13}$$

which corresponds to the reflection coefficient obtained by CMA, eqn.(4.4), [4.4].

The fraction of the incident power that is reflected is $|\Gamma|^2$, [4.6], and the condition for maximum power transfer to the load is $|\Gamma|^2 \rightarrow 0$. As eqn.(4.13) shows, this condition is achieved when $Z_{L(1)} = Z_{0x(1)}$, (impedance matching) [4.5, 4.8]. The power reflection coefficient $|\Gamma|^2$ is what will be presented in the numerical examples in this section and also used in other chapters where the intensity of the reflected signal needs to be represented, unless explicitly indicated otherwise. It is this conveniently obtained final representation of the multilayer structure as given by eqn.(4.13) in terms of just two impedances that provides the ready 'insight' in to the resulting characteristics to be expected due to the multilayer structure.

The corresponding field transmission coefficient T of the T-L network for n = 2,3,..,N can be derived by, [4.7],

$$T = \left[\frac{2Z_{0x(2)}}{Z_{0x(2)} + Z_{0x(1)}} \frac{2Z_{0x(3)}}{Z_{0x(3)} + Z_{0x(2)}} \cdots \frac{2Z_{0x(n)}}{Z_{0x(n-1)} + Z_{0x(n)}} \cdots \frac{2Z_{0x(N)}}{Z_{0x(N)} + Z_{0x(N-1)}} \right] \times \quad (4.14)$$
$$\times D^{-1} \exp\left[-\varphi_{(2)} - \varphi_{(3)} - \ldots - \varphi_{(n)} - \ldots - \varphi_{(N-1)} \right]$$

where

$$D = \prod_{n=2}^{N} \left[1 - \left(\frac{Z_{0x(n-1)} - Z_{0x(n)}}{Z_{0x(n-1)} + Z_{0x(n)}} \right) \left(\frac{Z_{L(n-1)} - Z_{0x(n)}}{Z_{L(n-1)} + Z_{0x(n)}} \right) \exp\left(-2\varphi_{(n)} \right) \right] \quad (4.15)$$

and $Z_{L(N-1)} = Z_{0x(N)}$, eqn.(4.13). Note that $|T|^2$, eqn.(4.6), will be analysed in this thesis, which represents field intensity at the [(N-1) / N] interface of the structure [4.12].

Since the main interest of this section is to describe SPW excitation in prism coupled waveguide structures with the use of the T-L analysis, hence only TM polarised fields will be considered here.

4.4 SPW excitation in a K-R arrangement

The multilayer prism coupled structure of Figure 4.2a is transformed into a K-R arrangement when n = 3, Figure 4.3a, [4.13-14]. The prism, the metal film of thickness $d_2 = d_m$ and the dielectric substrate have relative permittivity, $\varepsilon_1 = \varepsilon_p$ (real), $\varepsilon_2 = \varepsilon_m = -|\varepsilon_{mR}| - j\,|\varepsilon_{mI}|$ and $\varepsilon_3 = \varepsilon_s = +|\varepsilon_{sR}| - j\,|\varepsilon_{sI}|$ respectively, where $\varepsilon_p > |\varepsilon_{sR}| >> |\varepsilon_{sI}|$. The corresponding refractive index of the three media are n_p, $n_m = n_{mR} - j\,n_{mI}$ and $n_s = n_{sR} - j\,n_{sI}$, where $n_p > n_{sR} > n_{sI} > 0$ and $n_{mI} > n_{mR} > 0$.

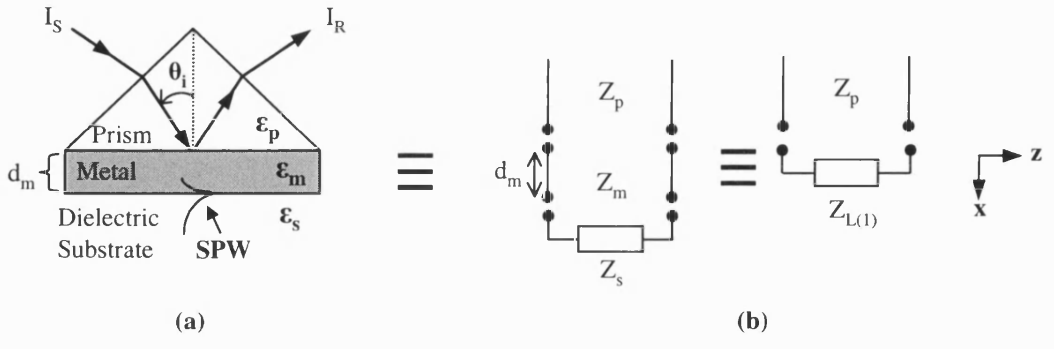

Figure 4.3. K-R prism coupled arrangement, (a), represented as a three section T-L chain, (b).

The K-R coupler can then be represented as a 3-section T-L network, Figure 4.3b,where the prism, metal and substrate have transverse characteristic impedance, eqn.(4.9), $Z_{0x(1)} = Z_p$, $Z_{0x(2)} = Z_m$, and $Z_{0x(3)} = Z_s$ respectively. Use of the electrical length $\varphi_2 = \varphi_m$, eqn.(4.12), yields the lumped load impedance, $Z_{L(1)}$, eqn.(4.11),

$$Z_{L(1)} = Z_m \left[\frac{Z_s + Z_m \tanh(\varphi_m)}{Z_m + Z_s \tanh(\varphi_m)} \right] \tag{4.16}$$

which reduces the T-L network into a 2-section system with field reflection coefficient, eqn.(4.13),

$$\Gamma = \frac{Z_{L(1)} - Z_p}{Z_{L(1)} + Z_p} \tag{4.17}$$

The field transmission coefficient is then, eqns.(4.14)-(4.15),

$$T = \left[\frac{2Z_m}{Z_m + Z_p} \frac{2Z_s}{Z_s + Z_m} \right] \times D^{-1} \exp[-\varphi_s] \tag{4.18}$$

where

$$D = \left[1 - \left(\frac{Z_p - Z_m}{Z_p + Z_m} \right) \left(\frac{Z_s - Z_m}{Z_s + Z_m} \right) \exp(-2\varphi_m) \right] \tag{4.19}$$

The characteristics of $|\Gamma|^2$, eqn.(4.17), and $|T|^2$, eqn.(4.18), for the K-R prism coupler of Figure 4.3, are analysed as a function of the incident angle θ_i for non-ideal ($\varepsilon_{mI} \neq 0$) and ideal ($\varepsilon_{mI} = 0$) metal layers. Results of a numerical example with the parameter values, $\varepsilon_p = 2.25$, $\varepsilon_{sR} = 1$, $\varepsilon_{sI} = 0$, $d_m = 50$nm, $\varepsilon_m = -9.9 - j\ 1.05$ (Au film) [4.15] and $\lambda_o = 633$nm are examined to illustrate the typical features. Note that since an unattenuated propagating wave has been assumed in the prism medium, eqn.(4.2), Z_p will always be real and positive, unlike Z_m and Z_s which can be considered in general to be complex, with $Z_m = Z_{mR} + j\, Z_{mI}$ and $Z_s = Z_{sR} + j\, Z_{sI}$.

4.4.1 Finite thickness metal film (layer)

a) Lossy metal ($\varepsilon_{mi} \neq 0$)

By considering a real (lossy) metal in the K-R coupler of finite thickness d_m, for any θ_i, Z_p is real, eqn.(4.9), and Z_m is complex with $Z_m = Z_{mR} + jZ_{mI}$ where

$$Z_{mR} \approx \frac{1}{n_{mR}^2 + n_{mI}^2}\left[n_{mR}\left(1+|\varepsilon_{mR}|\frac{\varepsilon_1 \sin^2\theta_i}{\varepsilon_{mR}^2+\varepsilon_{mI}^2}\right)^{1/2} + n_{mI}\left(\frac{\varepsilon_{mI}}{2}\frac{\varepsilon_1 \sin^2\theta_i}{\varepsilon_{mR}^2+\varepsilon_{mI}^2}\left(1+|\varepsilon_{mR}|\frac{\varepsilon_1 \sin^2\theta_i}{\varepsilon_{mR}^2+\varepsilon_{mI}^2}\right)^{-1/2}\right)\right] \tag{4.20}$$

$$Z_{mI} \approx \frac{1}{n_{mR}^2 + n_{mI}^2}\left[n_{mI}\left(1+|\varepsilon_{mR}|\frac{\varepsilon_1 \sin^2\theta_i}{\varepsilon_{mR}^2+\varepsilon_{mI}^2}\right)^{1/2} - n_{mR}\left(\frac{\varepsilon_{mI}}{2}\frac{\varepsilon_1 \sin^2\theta_i}{\varepsilon_{mR}^2+\varepsilon_{mI}^2}\left(1+|\varepsilon_{mR}|\frac{\varepsilon_1 \sin^2\theta_i}{\varepsilon_{mR}^2+\varepsilon_{mI}^2}\right)^{-1/2}\right)\right] \tag{4.21}$$

with $Z_{mI} > Z_{mR} > 0$ for a typical metal.

The electrical length φ_m is also complex with $\varphi_m = \varphi_{mR} + j\,\varphi_{mI}$, [Appendix F.3, eqns.(F.39-40)], and φ_{mR} , $\varphi_{mI} > 0$, for typical metals. The transverse impedance of the substrate Z_s, eqn.(4.9), changes from purely real (resistive) for θ_i less than the total reflection angle θ_{TR} between the prism and the substrate, to a purely imaginary (reactive) for $\theta_i > \theta_{TR}$:

$$Z_s = -j\left[\frac{(\varepsilon_p/\varepsilon_s)\sin^2\theta_i - 1}{\varepsilon_p}\right]^{1/2} = -j|Z_{sI}| \tag{4.22}$$

Note that the choice of a negative sign in eqn.(4.22) is to allow exponentially decaying fields in the substrate medium, [Appendix F.3, eqns.(F.35-36)].

Hence, when $\theta_i < \theta_{TR}$, the complex Z_m, φ_m and the real Z_s produce a complex $Z_{L(1)} = Z_{LR(1)} + j\,Z_{LI(1)}$, eqn.(4.16), which makes Γ, eqn.(4.17),

$$\Gamma = \frac{(Z_{LR(1)} - Z_p) + j\,Z_{LI(1)}}{(Z_{LR(1)} + Z_p) + j\,Z_{LI(1)}} \tag{4.23}$$

From eqn.(4.23) it is seen that the resistive load impedance $Z_{LR(1)}$ provides a potential for the incident power to be absorbed into the load at a specific θ_i for the corresponding d_m and λ_o. The maximum power transfer to the load is satisfied when $Z_{LI(1)} \rightarrow 0$ and $Z_{LR(1)} \approx Z_p$. Although eqn.(4.23) has the potential for $\Gamma \approx 0$, for a typical K-R prism coupler employed in sensing applications, this condition cannot easily be achieved realistically as is evident from the results shown in Figure 4.4 for $\theta_i < \theta_{TR}$.

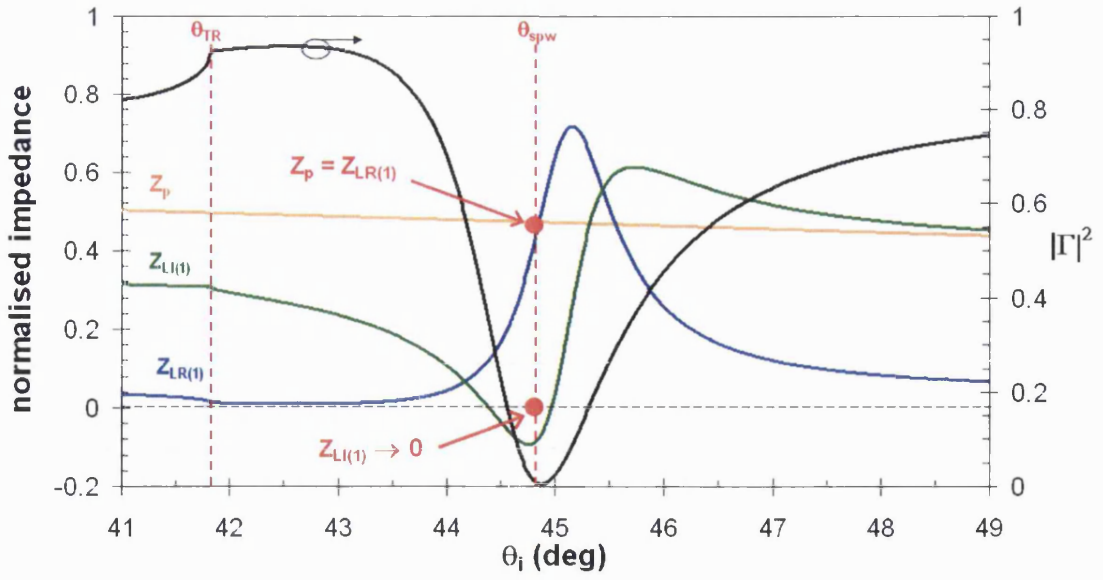

Figure 4.4. Angular variation of Z_p, $Z_{L(1)}$ and $|\Gamma|^2$ for the lossy metal K-R arrangement.

For $\theta_i > \theta_{TR}$ total (internal) reflection conditions occur between the prism and the substrate that leads to an exponentially decaying field in the substrate which, with reference to the T-L representation, corresponds to an imaginary $Z_s = - j |Z_{sI}|$, eqn.(4.22). The other system impedances, Z_p, eqn.(4.9), Z_m, eqns.(4.20-21), and φ_m, remain unaltered leading again to a complex Z_L .

Unlike the $\theta_i < \theta_{TR}$ case, there is now a specific $\theta_i = \theta_{spw}$ at which an impedance matching is achieved between the load and the input section of the T-L system. When the matching occurs, then $|\Gamma|^2 \rightarrow 0$, Figure 4.4 for $\theta_i > \theta_{TR}$, demonstrating SPW excitation at the metal - substrate interface.

In addition to $|\Gamma|^2 \rightarrow 0$ condition for SPW excitation, at $\theta_i = \theta_{spw}$ the field transmission coefficient $|T|^2$ exceeds unity, eqn.(4.18), Figure 4.5. Hence, the result $|T|^2 >> 1$ highlights the very strong optical field intensity that is developed at the metal - substrate interface due to SPW excitation [4.16].

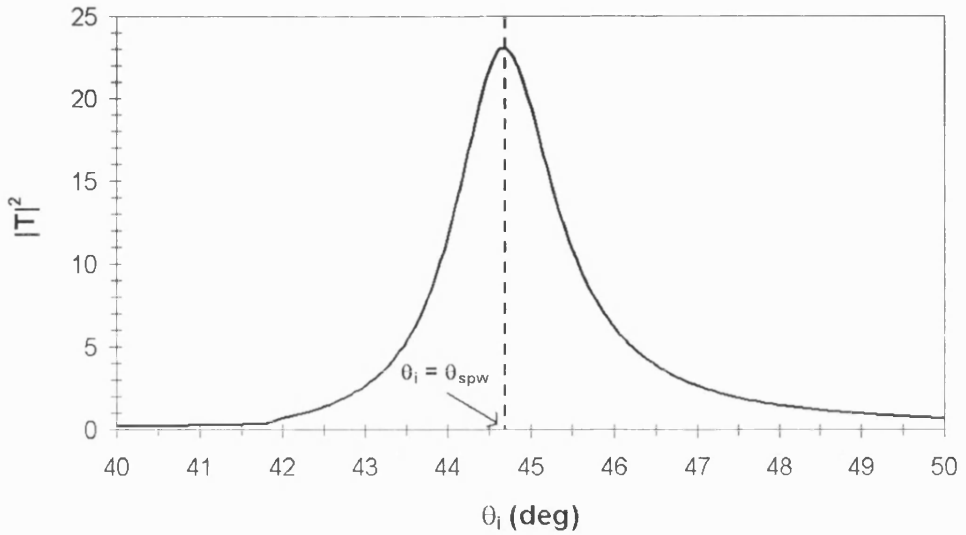

Figure 4.5. Angular variation of $|T|^2$ for the lossy metal K-R prism coupled arrangement.

The excitation of the SPW at the metal – substrate interface can also be viewed in a more direct manner by applying the Transverse Resonance (T-R) condition [4.8]. This technique is an application of the T-L theory to the equivalent circuit of a transverse section of the guiding structure and is applicable in any waveguide that is uniform in the direction of propagation i.e. along z axis. With reference to Figure 4.5 and using the impedance equation given by eqn.(4.9), the T-R condition requires that the sum of the impedances 'looking' from the metal - substrate interface towards the substrate and towards the metal should vanish - that is,

$$Z_m + Z_s = 0 \tag{4.24}$$

which is satisfied if

$$\theta_i = \theta_{spw} = \sin^{-1}\left[\mathrm{Re}\left\{ \left(\frac{\varepsilon_m \varepsilon_s}{\varepsilon_p (\varepsilon_m + \varepsilon_s)} \right)^{1/2} \right\} \right] > \theta_{TR} \tag{4.25}$$

Equation (4.25) can be rearranged to obtain

$$k_o \sqrt{\varepsilon_p} \sin\theta_{spw} = \mathrm{Re}\left\{ k_o \sqrt{\frac{\varepsilon_m \varepsilon_s}{\varepsilon_m + \varepsilon_s}} \right\} \tag{4.26}$$

which corresponds to the well known phase velocity matching criterion between the incident electromagnetic signal and the single interface SPW. The left hand side of eqn.(4.26) represents the longitudinal propagation constant k_z of the incident plane wave signal, eqn.(4.2), whereas the right hand side corresponds to the real part of the

propagation constant for the single interface SPW as described by eqn.(3.8), with $\varepsilon_s = \varepsilon_1$.

The SPW excitation at the metal/substrate interface of the K-R coupler can also be realised by evaluating the reflection coefficient Γ_{ms} at that interface from eqn.(4.13), where $Z_{0x(1)} = Z_m$ and $Z_{L(1)} = Z_s$,

$$\Gamma_{ms} = \frac{Z_s - Z_m}{Z_s + Z_m} \tag{4.27}$$

When the T-R criterion is fulfilled, eqn.(4.24), then, at θ_{spw}, eqn.(4.25), $|\Gamma_{ms}|^2 >> 1$, eqn.(4.27), Figure 4.6, which is an indication of resonance, a well known phenomenon in electrical circuits [4.5].

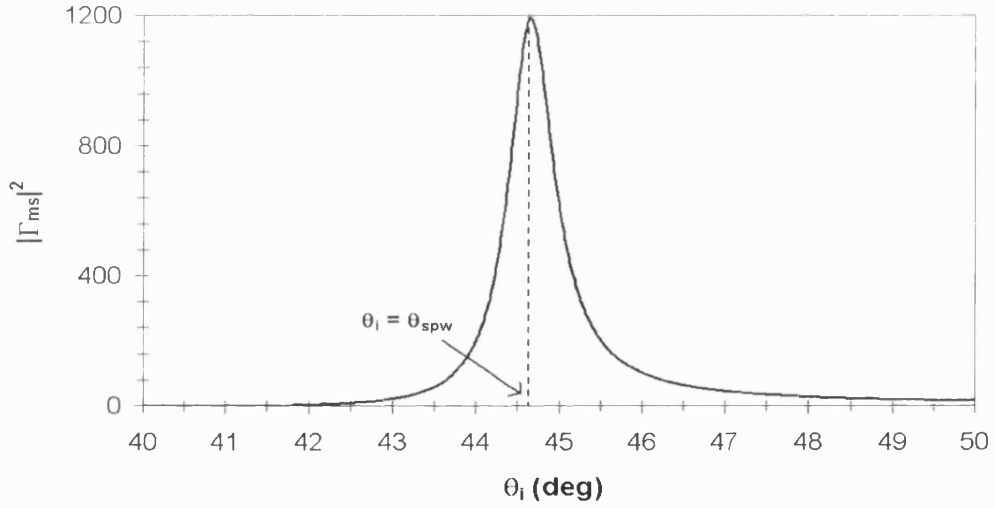

Figure 4.6. Angular variation of $|\Gamma_{ms}|^2$ at the (lossy) metal - dielectric substrate interface of the K-R prism coupler.

The interpretation of SPW excitation in a K-R prism coupled waveguide structure with a lossy metal layer does not readily follow from the cascaded matrix equation for a three-layer system, eqn.(4.4), [4.12]:

$$\Gamma = \frac{\Gamma_{12} + \Gamma_{23} \exp\left[j 2 k_{x(m)} d_m\right]}{1 + \Gamma_{12}\,\Gamma_{23} \exp\left[j 2 k_{x(m)} d_m\right]} \tag{4.28}$$

where

$$\Gamma_{12} = \frac{\varepsilon_p k_{x(m)} - \varepsilon_m k_{x(p)}}{\varepsilon_p k_{x(m)} + \varepsilon_m k_{x(p)}} \tag{4.29}$$

$$\Gamma_{23} = \frac{\varepsilon_m k_{x(m)} - \varepsilon_s k_{x(m)}}{\varepsilon_m k_{x(m)} + \varepsilon_s k_{x(m)}} \tag{4.30}$$

where $k_{x(p)}$, $k_{x(m)}$ and $k_{x(s)}$ are the transverse propagation constants of the field, eqn.(4.3), in the prism, metal and substrate respectively.

Equation (4.28) becomes complicated and does not provide an easy indication of SPW excitation without studying in detail the absorption losses and/or the transmission coefficient of the system [4.17]. The T-L method however, provides a clear and direct physical interpretation of the phenomenon through only the expression for Γ, eqn.(4.17). Note from eqn.(4.23) that Γ depends on only three terms, Z_p, $Z_{LR(1)}$ and $Z_{LI(1)}$, and $\Gamma = 0$ at $\theta_i > \theta_{TR}$ when $Z_{LR(1)} = Z_p$ and $Z_{LI(1)} = 0$. Hence, the condition $\Gamma \rightarrow 0$ which represents SPW excitation, corresponds to impedance matching.

b) Ideal metal ($\varepsilon_{mI} = 0$)

If the metal film of the K-R prism coupler is ideal ($\varepsilon_{mI} = 0$), then Z_p and Z_s exhibit the same θ_i variation as for the lossy metal case. The impedance Z_m of the metal is however now purely imaginary, eqn.(4.9),

$$Z_m = +j\frac{\left[1 + \left(\varepsilon_p / |\varepsilon_{mR}|\right) \sin^2 \theta_i\right]^{1/2}}{n_{mI}} = +j|Z_{mI}| \tag{4.31}$$

The electrical length of the line φ_m is also purely real, $\varphi_m = \varphi_{mR}$, due to the purely decaying fields inside the metal film, [Appendix F.3, eqns.(F.37-38)].

Thus, for $\theta_i < \theta_{TR}$, Z_p and Z_s are real, eqn.(4.9), and Z_m imaginary, eqn.(4.31), so that eqn.(4.16) yields a complex $Z_{L(1)} = Z_{LR(1)} + j\, Z_{LI(1)}$. For the given parameters $Z_{LI(1)} >> Z_{LR(1)}$, hence $|\Gamma|^2$ for the ideal metal case varies similarly to the lossy metal situation, Figure 4.4.

When $\theta_i > \theta_{TR}$, there is a decaying field in the substrate, which with reference to the T-L representation, eqn.(4.9), corresponds to an imaginary $Z_s = -\, j\, |Z_{sI}|$, eqn.(4.22). Under this condition $Z_{L(1)}$, eqn.(4.16), becomes

$$Z_{L(1)} = j\left[\frac{|Z_{mI}| \tanh(\varphi_{mR}) - |Z_{sI}|}{|Z_{mI}| - |Z_{sI}| \tanh(\varphi_{mR})}\right] |Z_{mI}| = j\, Z_{LI(1)} \tag{4.32}$$

a purely reactive load. Thus, as expected for a source terminated by a purely reactive impedance, $|\Gamma|^2 = 1$, eqn.(4.17), [4.13].

Since $|\Gamma|^2 = 1$ for $\theta_i > \theta_{TR}$, SPW excitation cannot be detected as a minimum in $|\Gamma|^2$ because the source presents a resistive impedance while the 'load' is purely reactive for all incident angles. The presence of the SPW at the (ideal) metal - substrate interface for $\theta_i > \theta_{TR}$, can still be recognised by evaluating Γ_{ms}, eqn.(4.27), at this interface. Similarly to the lossy metal case, $|\Gamma_{ms}|^2 > 1$, Figure 4.6, indicating resonance at the same angle θ_{spw}, eqn.(4.25), as described by the T-R condition, eqn.(4.24). Note that now although the excitation of the SPW mode cannot be detected from the reflection coefficient Γ, it still exists in the structure (and has been verified from non-linear optical interactions [4.17]).

4.4.2 Limit cases for the metal film thickness

Interesting results however appear if the metal film thickness is either infinitely thin or thin.

a) Infinitely thin metal film (layer)

If the metal film of the K-R coupler , Figure 4.3a, is now infinitely thin ($d_m \rightarrow 0$) then in the equation for the load impedance of the system $Z_{L(1)}$, eqn.(4.16), $\tanh(\varphi_m) \rightarrow 0$, which gives $Z_{L(1)} = Z_s$ and as a consequence,

$$\Gamma = \frac{Z_s - Z_p}{Z_s + Z_p} \tag{4.33}$$

$$T = \left[\frac{2Z_p}{Z_s + Z_p} \right] \tag{4.34}$$

Hence, the K-R prism coupler, Figure 4.3a, acts as a single interface formed by the prism and the substrate dielectric. Since $\varepsilon_p > \varepsilon_s$, for $\theta_i < \theta_{TR}$, both Z_p and $Z_s = Z_{sR}$ are real representing resistive circuit elements. It is well known then that for TM-polarised waves the Brewster effect takes place, [4.4], at $\theta_i = \theta_B < \theta_{TR}$ which corresponds to an impedance matching between the input and the load, $Z_s = Z_p$, resulting into $|\Gamma|^2 = 0$, eqn.(4.33), and $|T|^2 = 1$, eqn.(4.34).

When however $\theta_i > \theta_{TR}$, Z_s converts to a purely reactive impedance $Z_s = j\, Z_{sI} = -j\, |Z_{sI}|$, eqn.(4.22) which gives $|\Gamma|^2 = 1$, a well known result for T-L systems terminated by a reactive load, indicating total reflection, Figure 4.7.

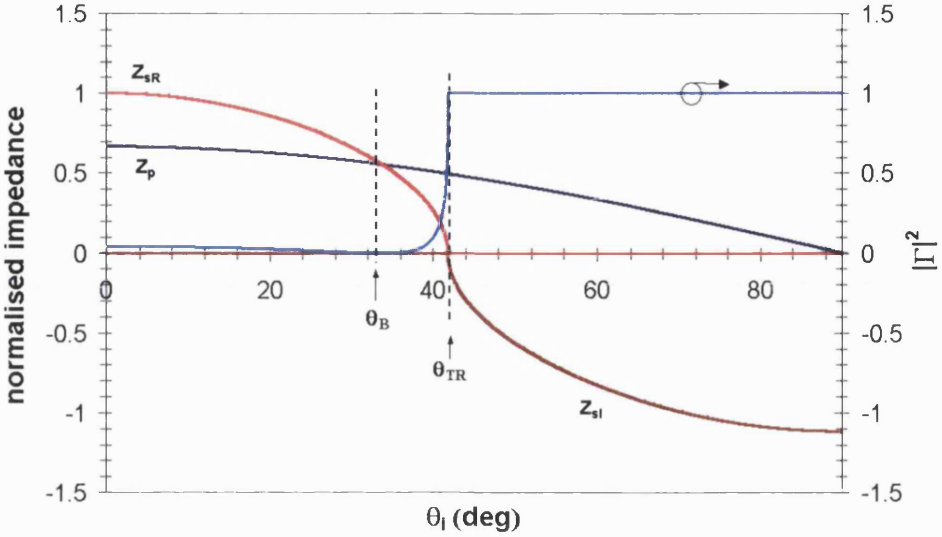

Figure 4.7. Angular variation of $|\Gamma|^2$, Z_p and $Z_s = Z_{sR} + j\, Z_{sI}$, when $d_m \rightarrow 0$ in the K-R prism coupled arrangement of Figure 4.3a.

b) Infinitely thick metal film (layer)

If however the metal film is very thick ($d_m \rightarrow \infty$), then from eqn.(4.16), ($\tanh(\varphi_m) \rightarrow 1$), $Z_{L(1)} = Z_m$ and the K-R prism coupler converts into a single interface formed by the prism and the metal. Under this condition, and if the metal is ideal ($\epsilon_{mI} = 0$), Z_m is purely imaginary, eqn.(4.31), so that $|\Gamma|^2 = 1$ for any θ_i, Figure 4.8a.

For $d_m \rightarrow \infty$, then $T \rightarrow 0$, eqn.(4.17), as a consequence of the reactive (decaying) character of the metal, eqn.(4.31). Hence, $|\Gamma|^2 = 1$ and it is deduced that the metal acts as an ideal mirror, and no power is transmitted into the load of the T-L circuit.

In the case of a lossy metal however, the cascaded matrix (plane-wave) field analysis method becomes more difficult to visualise. By contrast, the T-L analysis still permits a 'physical understanding' of the resulting characteristics even though the detailed expressions are now more complicated. From the derived expressions, it is found that for any θ_i the load impedance is complex, $Z_{L(1)} = Z_m = Z_{mR} + j\, Z_{mI}$, eqns.(4.20-21), with $Z_{mI} > Z_{mR} > 0$. The presence of the resistive load impedance term implies that some

power is absorbed into the load. As a consequence, $|\Gamma|^2 < 1$ which represents a lossy mirror, Figure 4.8b.

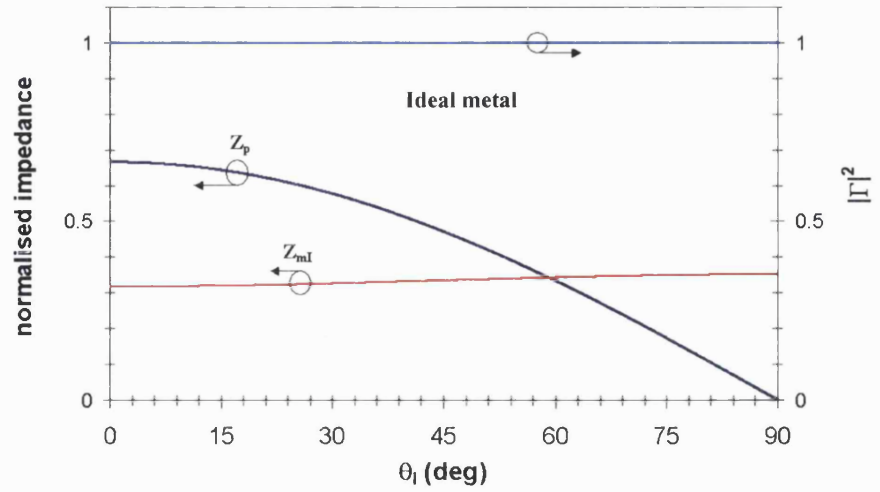

(a)

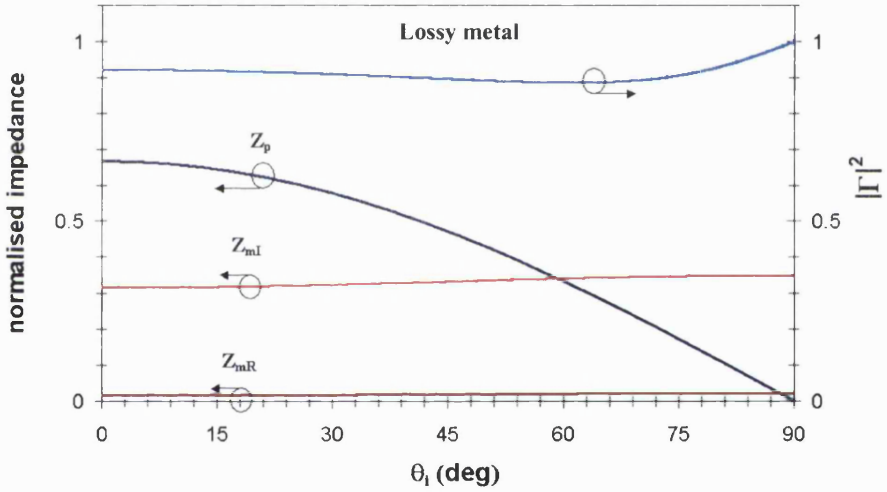

(b)

Figure 4.8. Angular variation of $|\Gamma|^2$, Z_p and $Z_m = Z_{mR} + j\, Z_{mI}$ when $d_m \rightarrow \infty$ in the K-R prism coupled structure of Figure 4.3a for an ideal (a) and lossy (b) metal.

Note that the single dielectric – metal interface obtained from the K-R system when $d_m \rightarrow \infty$ can in principle according to sections 3.2-3, support a SPW mode. The reason why this is not happening now is due to the different wave excitation method that is employed (prism coupler instead of end-fire excitation assumed in sections 3.2-3).

4.5 Four layer prism coupler

The T-L analysis can also be applied to model symmetric and antisymmetric SPW excitation in prism coupled DMD or MDM waveguide configurations, as it is shown in sections 4.5.1 and 4.5.2.

4.5.1 Prism coupled DMD structure

As discussed in section 3.4.1, a symmetric DMD waveguide configuration under TM wave propagation can support an antisymmetric and a symmetric SPW mode. With reference to Figure 4.2 the prism coupled DMD configuration can be represented as a T-L network for n = 4 with $\varepsilon_1 = \varepsilon_p > 0$, $\varepsilon_2 = \varepsilon_s = \varepsilon_{sR} > 0$, $\varepsilon_3 = \varepsilon_m = -|\varepsilon_{mR}| - j\,|\varepsilon_{mR}|$ and $\varepsilon_4 = \varepsilon_s$ to be the relative permittivities of the prism, the lossless dielectric film of thickness $d_2 = d_s$, the lossy metal film of thickness $d_3 = d_m$ and the substrate dielectric respectively, with $|\varepsilon_{mR}| >> |\varepsilon_{mI}|$ and $\varepsilon_p > \varepsilon_s$. From eqn.(4.9), the corresponding transverse impedances are $Z_{0x(1)} = Z_p$, $Z_{0x(2)} = Z_{0x(4)} = Z_s$, and $Z_{0x(3)} = Z_m$, whereas $\varphi_2 = \varphi_s$ and $\varphi_3 = \varphi_m$ are the electrical lengths of the lossless dielectric and the substrate respectively. As a consequence the effective load impedance of the T-L network formed by the dielectric, the metal and the substrate, as described by eqn.(4.11), is

$$Z_{L(1)} = Z_s \left[\frac{Z_{L(2)} + Z_s \tanh(\varphi_s)}{Z_s + Z_{L(2)} \tanh(\varphi_s)} \right] \tag{4.35}$$

Hence, the field reflection and transmission coefficients, Γ and T, of the structure are given by eqns.(4.13-14).

By assuming that the structure has the following parameters: $\varepsilon_p = 3.24$, $\varepsilon_s = 2.25$, $\varepsilon_m = -49.9 - j\,3.85$ (Au film), $d_s = 0.8\mu m$ and $d_m = 47nm$ at $\lambda_o = 1033nm$, results for $|\Gamma|^2$, eqn.(4.13), and $|T|^2$, eqn.(4.14), are presented in Figures 4.9-10.

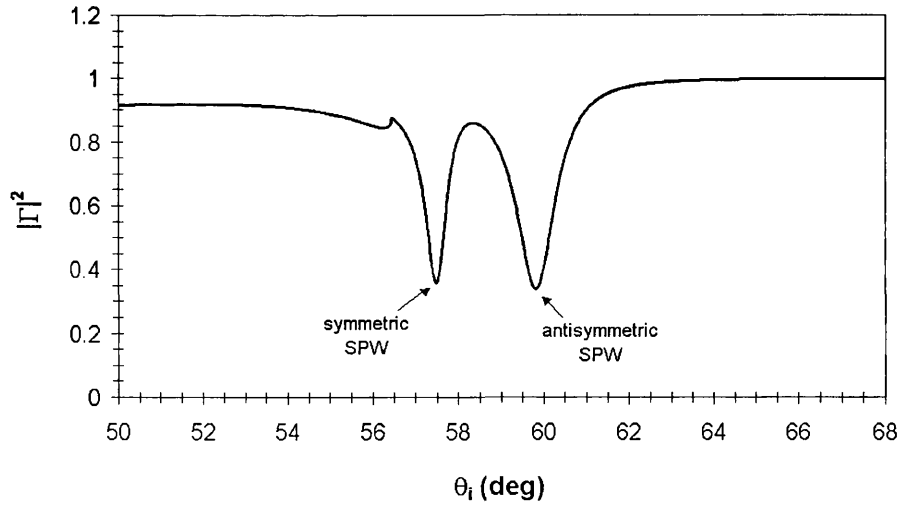

Figure 4.9. Example of symmetric and antisymmetric SPW excitation in a prism coupled DMD structure when monitoring angular variation of $|\Gamma|^2$ from a four section T-L network with $\varepsilon_p = 3.24$, $\varepsilon_s = 2.25$, $\varepsilon_m = -49.9 - j\,3.85$ (Au film), $d_s = 0.8\mu m$ and $d_m = 47nm$ at $\lambda_o = 1033nm$.

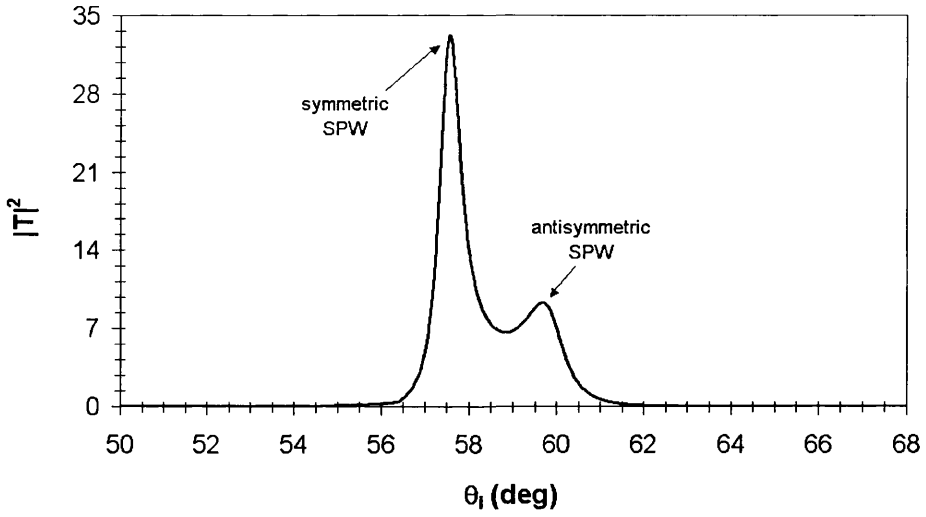

Figure 4.10. Example of symmetric and antisymmetric SPW field intensity in a prism coupled DMD structure when monitoring angular variation of $|T|^2$ from a four section T-L network with $\varepsilon_p = 3.24$, $\varepsilon_s = 2.25$, $\varepsilon_m = -49.9 - j\,3.85$ (Au film), $d_s = 0.8\mu m$ and $d_m = 47nm$ at $\lambda_o = 1033nm$.

Figure 4.9 clearly shows that there are two 'dips' in $|\Gamma|^2$ at $\theta_i \approx 57^o$ and 60^o, which correspond to the symmetric and antisymmetric SPW respectively. The two SPW modes can also be distinguished from the width of their FWHM which for the symmetric is narrower (~ 0.5^o) compared to the antisymmetric (~ 1^o) as a result of the reduced metal losses effect. As a consequence, the evaluation of the field intensity from

$|T|^2$, Figure 4.10, for the symmetric SPW is much higher (~35) in respect to the antisymmetric one (~10).

4.5.2 Prism coupled MDM structure

As shown in section 3.4.2, a MDM waveguide can support both SPWs and conventional modes under TM wave propagation. With reference then to the structure described in section 4.5.1, consider now that the layers 2 and 4 are metal films with thickness $d_2 = d_4 = d_m$ and relative permittivity $\varepsilon_2 = \varepsilon_4 = \varepsilon_m$, whereas layer 3 is a dielectric film with thickness $d_3 = d_s$ and relative permittivity $\varepsilon_3 = \varepsilon_s$.

Let d_m = 32nm and d_s = 1100nm, while the rest of the system parameters have the same values as in section 4.5.1, $|\Gamma|^2$, eqn.(4.13), and $|T|^2$, eqn.(4.14), of the structure are presented in Figures 4.11-12.

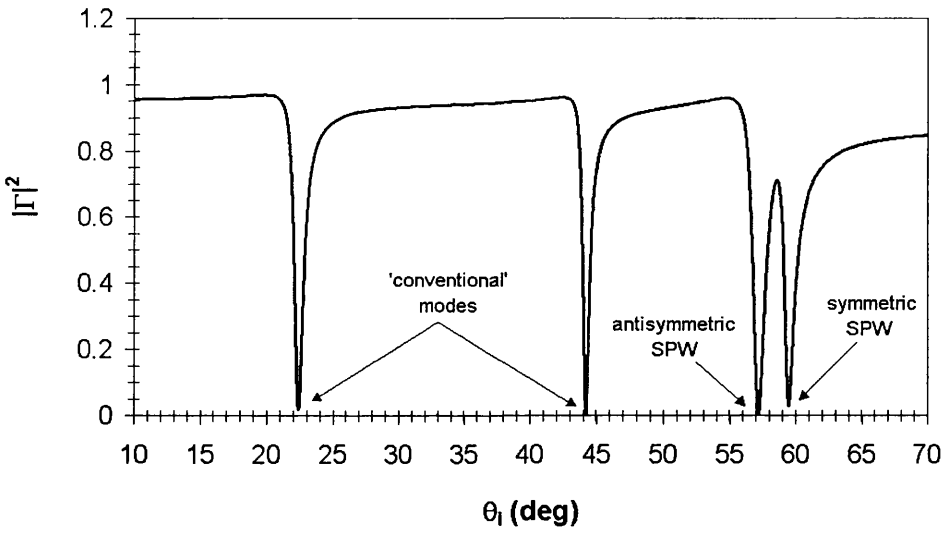

Figure 4.11. Example of SPW and 'conventional' wave excitation in a prism coupled MDM structure when monitoring angular variation of $|\Gamma|^2$ from a four section T-L network with ε_p = 3.24, ε_s = 2.25, ε_m = - 49.9 - j 3.85 (Au film), d_s = 1.1μm and d_m = 32nm at λ_o = 1033nm.

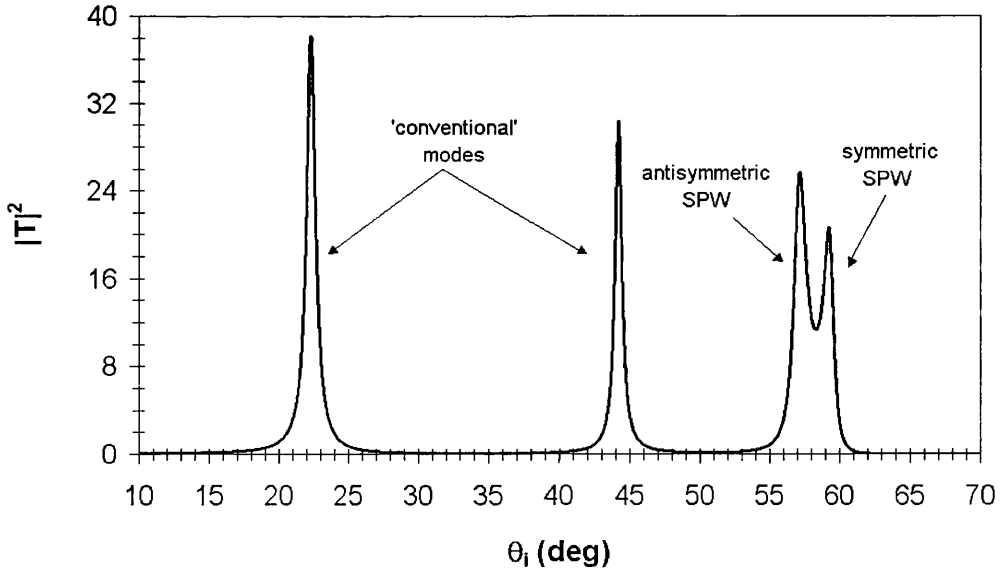

Figure 4.12. Example of SPW and 'conventional' wave field intensity in a prism coupled MDM structure when monitoring angular variation of $|T|^2$ from a four section T-L network with $\varepsilon_p = 3.24$, $\varepsilon_s = 2.25$, $\varepsilon_m = -49.9 - j\,3.85$ (Au film), $d_s = 1.1\mu m$ and $d_m = 32nm$ at $\lambda_o = 1033nm$.

As Figure 4.11 shows, the study of $|\Gamma|^2$ yields two 'dips' at $\theta_i \approx 57^\circ$ and 61° which correspond to antisymmetric and symmetric SPW excitation. By comparison to the prism coupled DMD structure of section 4.5.1, there are now two more 'dips' in $|\Gamma|^2$ at $\theta_i \approx 22^\circ$ and 44°, which represent 'conventional' antisymmetric and symmetric mode excitation. Thicker dielectric films d_s can increase the number of the 'conventional' modes, whereas thinner ones can only allow SPWs to exist. Since SPWs exhibit high losses, hence the larger FWHM compared to the excited 'conventional' waves.

Note now that $|T|^2$ for the 'conventional' modes is larger compared to the that obtained for the SPWs. This result is a consequence mainly of the fact that the SPWs have not been excited properly and not so much because of the large metal losses.

4.6 Metal effects on K-R system sensitivity

As mentioned earlier, section 1.2.1, the K-R prism coupled SPW arrangement has found a widely use as a biological / chemical sensor. The medium that has however an important role when sensing operation is taking place is the metal film. Hence, the

following section will study the effect of the metal layer on the sensitivity of the K-R configuration when operating as a sensor.

4.6.1 SPW excitation angle

One of the most typical uses for a K-R prism coupled arrangement, Figure 4.3, is to operate as a sensor. The concept of the K-R coupler sensing function is to detect changes $\delta\varepsilon_s$ in ε_s which are shown as shifts at the position of the SPW excitation angle θ_{spw}, eqn.(4.25). The sensitivity $\Re$ of θ_{spw}, eqn.(4.25), to respond to $\delta\varepsilon_s$ is an important parameter and is estimated by:

$$\Re = \frac{d\theta_{spw}}{d\left(\sqrt{\varepsilon_s}\right)} = \frac{|\varepsilon_{mR}|}{|\varepsilon_{mR}| - \varepsilon_s}\sqrt{\frac{|\varepsilon_{mR}|}{|\varepsilon_{mR}|(\varepsilon_p - \varepsilon_s) - \varepsilon_p\varepsilon_s}} \tag{4.36}$$

which increases when:

a) $|\varepsilon_{mR}| \rightarrow \varepsilon_s$, or

b) $|\varepsilon_{mR}| \rightarrow \dfrac{\varepsilon_p\,\varepsilon_s}{\varepsilon_p - \varepsilon_s}$

In practice, case (a) can be achieved as the SPW excitation wavelength λ_o approaches the UV spectrum regime, whereas case (b) depends on the combination between ε_p and ε_S. Note however that at long wavelengths since $|\varepsilon_{mR}|$ becomes very large compared to typical ε_p and ε_s, $\Re$ becomes, eqn.(4.36),

$$\Re \approx \sqrt{\frac{1}{(\varepsilon_p - \varepsilon_s)}} \tag{4.37}$$

which indicates that the K-R sensitivity is independent of the choice of the metal. With reference to the K-R coupler of Figure 4.3, Figure 4.13 gives the variation of $\Re$ as a function of the SPW excitation wavelength λ_o for different metals when ε_p = 2.25, ε_s = 1 and d_m = 50nm; the values of ε_m for the various metals have been obtained from [4.15].

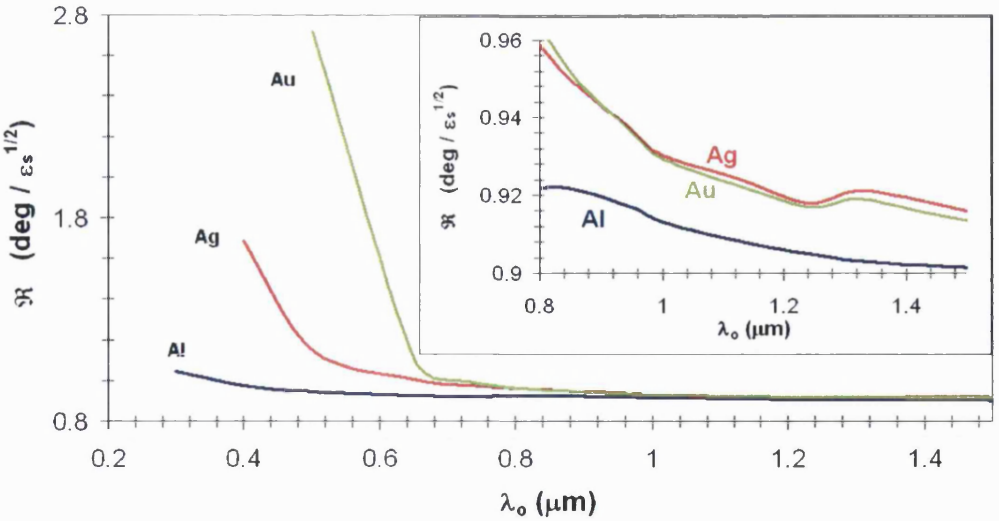

Figure 4.13. Wavelength variation of $\Re$ when using Al, Ag, Au metal films.

Hence, Au provides the highest sensitivity response for $\lambda_o \leq 0.9\mu m$, whereas when $\lambda_o > 0.9\mu m$ all the metals have almost the same $\Re$ as expected from eqn.(4.37).

4.6.2 FWHM

Another factor that affects the resolution sensitivity of the K-R coupler of section 4.6.1 as a sensor is the FWHM of the $|\Gamma|^2$ 'dip' when SPW excitation is observed. This FWHM depends on the metal losses which are represented by the imaginary term ϵ_{mI} in ε_m. As it is presented in Figure 4.14, for the parameters of section 4.6.1, if $|\varepsilon_{mI}| \rightarrow 0$ and d_m is properly adjusted to ensure optimum SPW excitation all the time at a thickness $d_m = d_{opt}$, then the FWHM of $|\Gamma|^2$ becomes extremely narrow. This result clearly indicates that if the metal losses are reduced, then the K-R arrangement can offer a significantly improved resolution sensitivity.

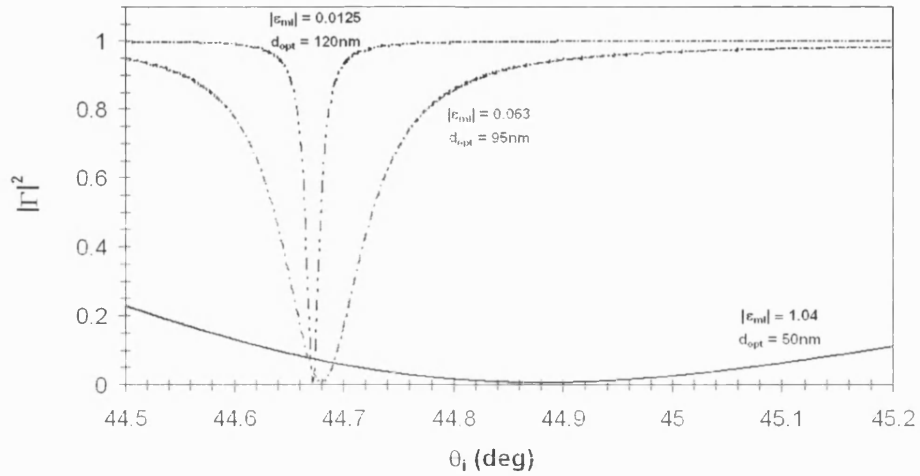

Figure 4.14. Angular variation of $|\Gamma|^2$ for optimum SPW excitation when a) $|\varepsilon_{ml}| = 1.04$ and $d_{opt} = 50nm$, b) $|\varepsilon_{ml}| = 0.063$ and $d_{opt} = 95nm$ and c) $|\varepsilon_{ml}| = 0.0125$ and $d_{opt} = 120nm$.

The above results yield that as $\varepsilon_{ml} \rightarrow 0$ and d_m increases then FWHM $\rightarrow 0$, Figure 4.15. Note however, that if $\varepsilon_{ml} = 0$ then $|\Gamma|^2 = 1$, and the metal thickness is not important, section 4.4.1b.

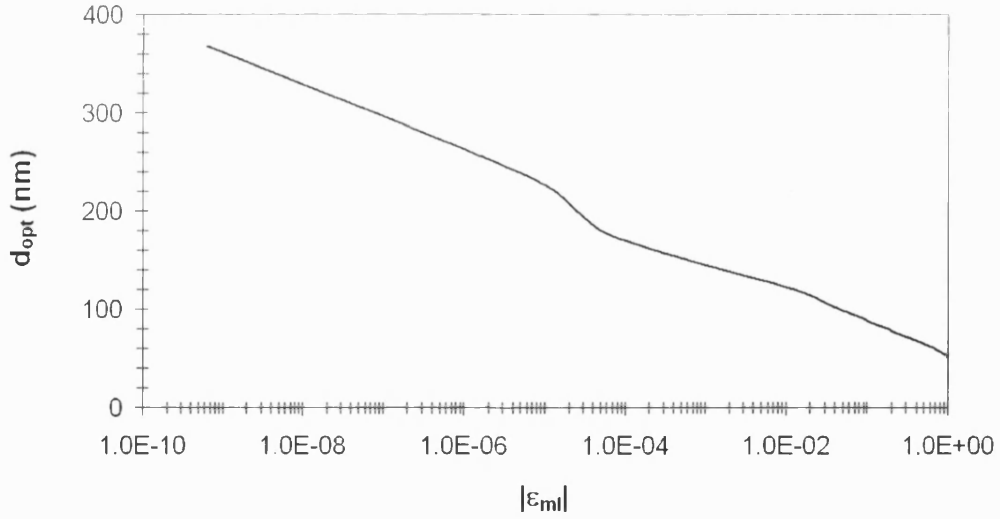

Figure 4.15. Variation of d_{opt} as a function of $|\varepsilon_{ml}|$ for optimum SPW excitation in the K-R prism coupled structure of Figure 4.3a.

In practice however, among the most typical used metals for SPW excitation in a K-R coupler and for the parameters of section 4.6.1, Ag provides the narrower FWHM followed by Au, Cu and Al, Figure 4.16. But, Ag is unstable mechanically, has low adhesion to glass, natural tendency to form discontinuous islands, and oxidises [4.18-19], while Cu and Al have too broad FWHM. Hence, Au appears to be the best

candidate for SPW structures used as sensors as it also offers the highest sensitivity $\Re$, Figure 4.13.

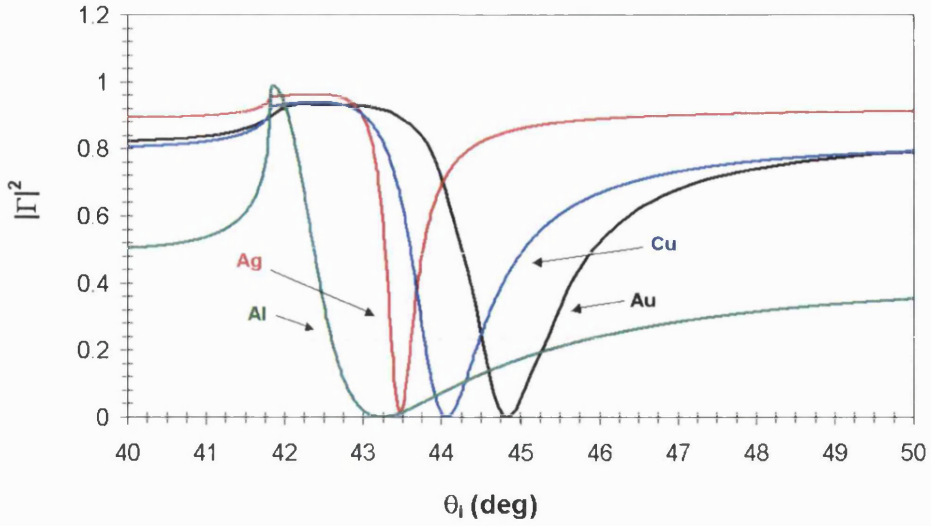

Figure 4.16. Effects of various metals on the FWHM of the 'dip' of $|\Gamma|^2$ at SPW excitation.

4.6.3 SPW excitation and field intensity

Finally, the thickness d_m of the metal film is another parameter that affects SPW excitation as it controls the depth of the 'dip' in $|\Gamma|^2$ which corresponds to the amount of power coupling into the excited SPW, Figure 4.17. Hence, an optimum d_m allows not only better monitoring of θ_{spw}, eqn.(4.25), but also a high SPW field intensity $|T|^2$, eqn.(4.17), compared to the non-optimum conditions making the K-R system more sensitive, Figure 4.18.

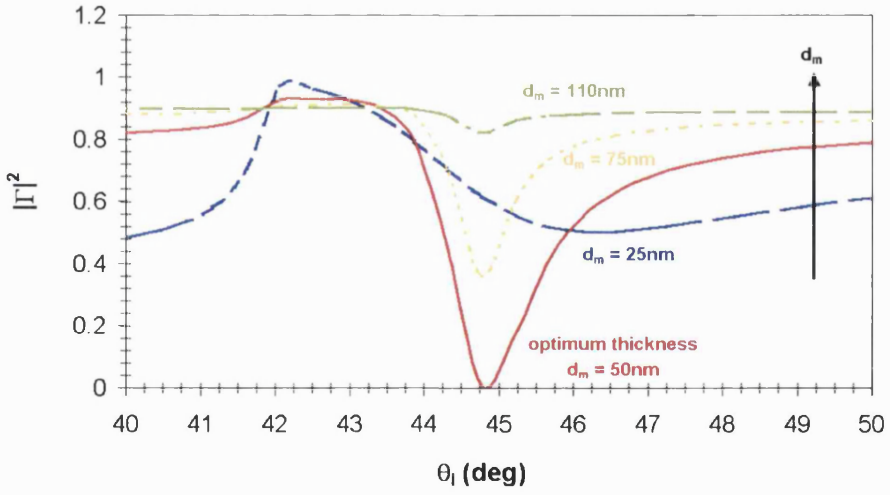

Figure 4.17. Angular variation of $|\Gamma|^2$ for the K-R prism coupled structure of Figure 4.3a for different metal film thickness d_m.

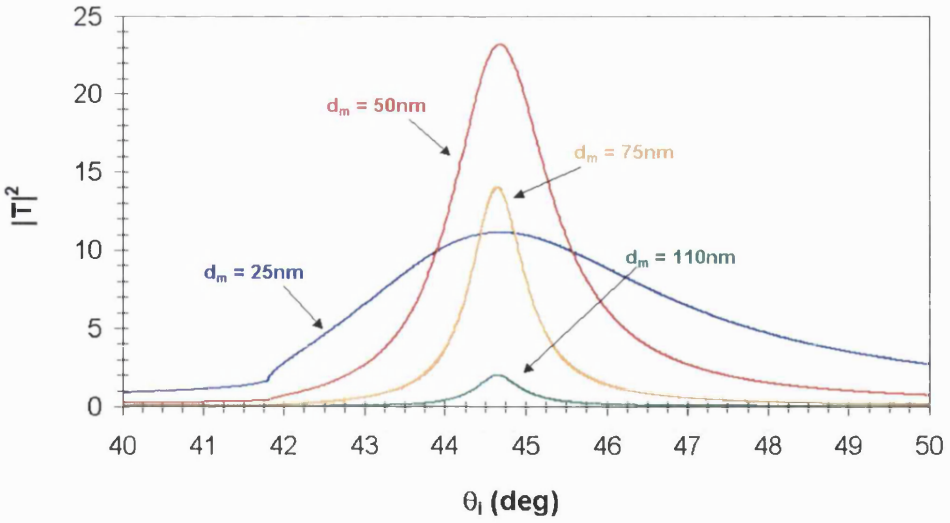

Figure 4.18. Angular variation of $|T|^2$ for the K-R prism coupled structure of Figure 4.3a for different metal film thickness d_m.

4.7 Attenuated and unattenuated wave propagation with prism coupled arrangements

The T-L analysis of prism coupled waveguide structures given in this chapter has considered unattenuated longitudinal (z – directed) wave propagation. This condition however assumes a purely real β, eqn.(4.2), even if media with complex ϵ are involved which is opposed to what was shown in chapter 3 where β is complex, eqn.(3.8). This difference in β is due to the fact that guided wave excitation in the prism coupled structure is introduced from the top of the structure by an incident wave unbounded in the ± z direction. As a consequence, the incident wave continuously provides power into the excited guided wave along the ±z direction and no modal losses are considered. To include the modal losses of the excited wave and have the same results as in chapter 3, it is then necessary to assume a semi-infinite prism in the positive z direction [4.9], Figure 4.19,

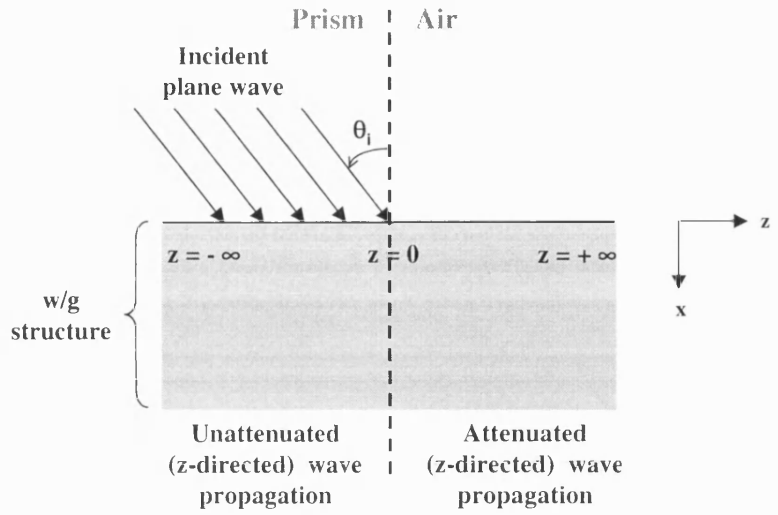

Figure 4.19. Schematic representation of the longitudinal wave propagation (z-directed) in a waveguide structure when a semi-infinite prism coupler is employed for surface wave excitation.

Hence, β inside the excitation area ($-\infty < z \leq 0$) will be considered real, eqn.(4.2), but in the region $z > 0$ where the incident plane wave does not exist, β is assumed complex. Note that the semi-infinite prism coupling approach is widely used for coupling in and out electromagnetic waves at waveguide structure [4.9].

4.8 Conclusions

This chapter has shown that prism coupled SPW structures can be effectively modelled by implementing transmission line analysis instead of the commonly employed cascaded matrix analysis. The application of the transmission line analysis demonstrates that the SPW excitation phenomenon is an impedance matching concept which can be only achieved for lossy metal SPW structures. This technique has also successfully described SPW excitation in prism coupled DMD and MDM structures where apart from SPWs, 'conventional' modes are also realised.

The role of the metal film for increasing the sensitivity of a typical K-R prism coupled arrangement when operating as a sensor has also been studied showing that gold films are the best candidates.

Chapter 4

[4.1] A. Otto, "Excitation of Nonradiative Surface Plasma Waves in Silver by the Method of Frustrated Total Reflection", Zeitschrift fur Physik 216, p.398 (1968)

[4.2] J.J. Burke, G.I. Stegeman, T. Tamir, "Surface-polariton-like waves guided by thin, lossy metal films", Phys. Rev. B, vol.33, no. 8, pp.5186-5201, 15 April 1986.

[4.3] J. Homola, S.S. Yee, G. Gauglitz, "Surface plasmon resonance sensors: review", Sensors and Actuators B, vol.54, no.1, pp.3-15, 25 January 1999.

[4.4] P. Yeh, "Optical Waves in Layered Media", John Wiley & Sons, 1988.

[4.5] R. Chipman, "Theory and Problems of Transmission Lines", Schaum's Outline Series, McGraw-Hill Book Company, 1968, p.139.

[4.6] S. Ramo, J.R. Whinnery, T. Van Duzer, "Fields and Waves in Communication Electronics", John Wiley & Sons, 3rd edition (1994).

[4.7] J.R. Wait, "Electromagnetic Wave Theory", John Wiley & Sons, 1987, p.151.

[4.8] R.E. Collin, "Foundations for Microwave Engineering", McGraw-Hill, 1966, p.64.

[4.9] R.G. Hunsperger, "Integrated Optics: Theory and Technology", 3rd ed., Springer Series in Optical Sciences, 1991, p.96.

[4.10] S.A. Schelkunoff, "Electromagnetic Fields", 1st edition, Blaisdell Publishing Company, 1963, p.150.

[4.11] T. Rozzi, M. Mongiardo, "Open electromagnetic waveguides", IEE Electromagnetic Waves Series 43, The institution of Electrical Engineers London, 1997, p.117.

[4.12] H. Raether, "Surface Plasmons on Smooth and Rough Surfaces and on Gratings", vol.111, Springer Tracts in Modern Physics, Springer-Verlag, 1988.

[4.13] "Transmission Line Analysis of Surface Plasmon Resonance", A.Tarlis, J.Sarma, SIOE'04 "Semiconductors and Integrated Optoelectronics Conference", University of Cardiff, Wales, 5-7 April 2004.

[4.14] "Transmission Line Circuit Representation of Surface Plasmon Waves", A.Tarlis, J.Sarma, F.Causa, International Conference on Nano-Material Synthesis and Integration for Sensors, Electronics, Photonics and Electro-Optics, SPIE Optics East 2006, Boston, USA, (Invited Oral Presentation).

[4.15] E.D. Palik, "Handbook of optical constants of solids", Academic Press (1985).

[4.16] W.H. Weber, G.W. Ford, "Optical electric-field enhancement at a metal surface arising from surface-plasmon excitation", Optics Letters, vol.6, no.3, p.123, March 1981.

[4.17] H.J. Simon, D.E. Mitchell, J.G. Watson, "Surface plasmons in silver films – a novel undergraduate experiment", American Journal of Physics vol.43, no.7, p.630, July 1975.

[4.18] J.W. Sadowski, J. Lekkala, I. Vikholm, "Biosensors based on surface plasmons excited in non-noble metals", Biosensors and Bioelectronics, no.6, 1991, pp.439-444.

[4.19] S.Y. Wu, H.P. Ho, "Sensitivity improvement of the surface plasmon resonance optical sensor by using a gold-silver transducing layer", Proceedings of Electron Devices Meeting 2002, IEEE Hong Kong, p.63.

Chapter 5

Experimental Prism Coupled Surface Wave Excitation

The previous chapter described and applied the T-L model for theoretically analysing prism coupled surface wave excitation and in particular SPW excitation. This chapter however, will demonstrate experimental prism coupled excitation of SPWs and 'conventional' waves at different waveguide arrangements and use them for producing a spatial mode beat effect. In addition, experimental and theoretical analysis of SPW excitation with semiconductor optical sources having spectrally broad and divergent output beam will also be presented and discussed.

5.1 Experimental apparatus

Whereas chapter 4 theoretically studied prism coupled surface wave excitation and in particular SPW excitation, in this chapter experimental demonstration of the phenomenon will be given for both SPWs and 'conventional' waves. The prism coupled waveguide (w/g) arrangement that was employed throughout this chapter is presented in Figure 5.1 and constituted of the following sub-systems:

1) Prism coupler
2) w/g structure
3) Rotating system
4) Optical source
5) Polariser
6) Detector

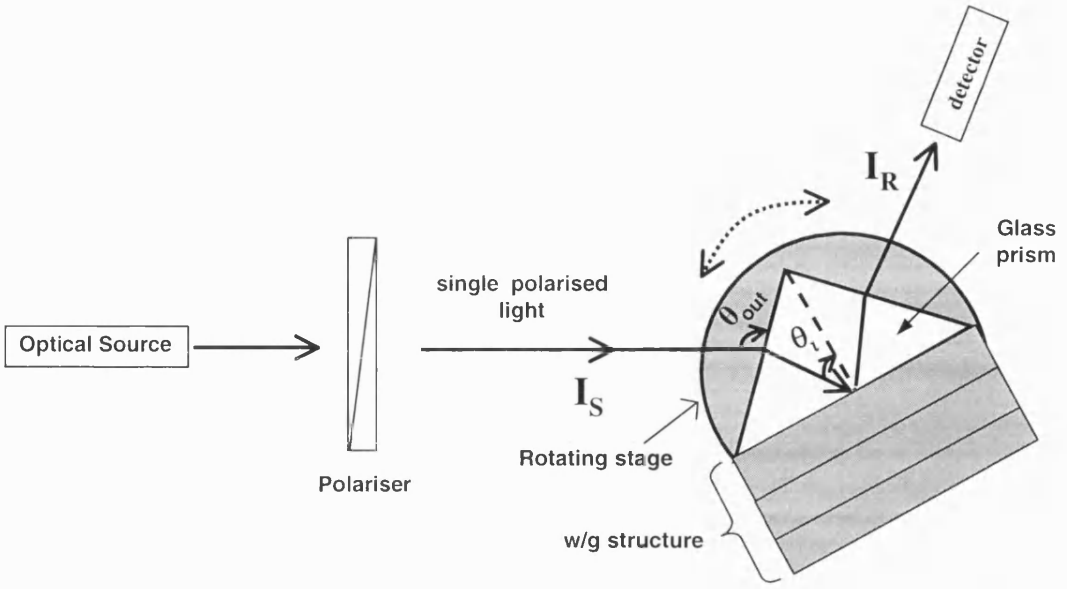

Figure 5.1. Top view of prism coupled surface wave excitation experimental apparatus, where I_S is the intensity of the source signal and I_R of the reflected from the prism.

5.1.1 Prism coupler

The main purpose of the prism coupler as discussed in chapter 4 is to allow impedance matching with the transmission line load of the system. Two types of right angle glass prisms are employed here: a BK7 with relative permittivity $\varepsilon_p \approx 2.25$ and a LSFN9 with $\varepsilon_p \approx 3.43$ [5.1]. In general, it is recommended that a high ε_p prism is used to shift the wave excitation angles to smaller values. This not only provides better mechanical flexibility when rotating the prism, but also allows a larger variety of substances to be detected through the shift of the excitation angle if the system is to be used as a sensor. Note that all the plots in this chapter that examine the field intensity of the reflected signal I_R from the prism for an input source signal with field intensity I_S, will be given as a function of the internal angle of the prism θ_i which is related to the external (rotating) prism angle θ_{out} as:

$$\theta_i = 45 - \sin^{-1}\left[\frac{1}{\sqrt{\varepsilon_p}}\sin(45 - \theta_{out})\right] \tag{5.1}$$

[See Appendix G.1 for the details of the calculation.]

5.1.2 Waveguide structures

Three waveguide (w/g) structures were used in this chapter: a single dielectric – metal (DM) interface for exciting SPWs, Figure 5.2a, a DMD structure, Figure 5.2b, for exciting symmetric and antisymmetric SPWs, and a dielectric guide, Figure 5.2c, for 'conventional' wave excitation.

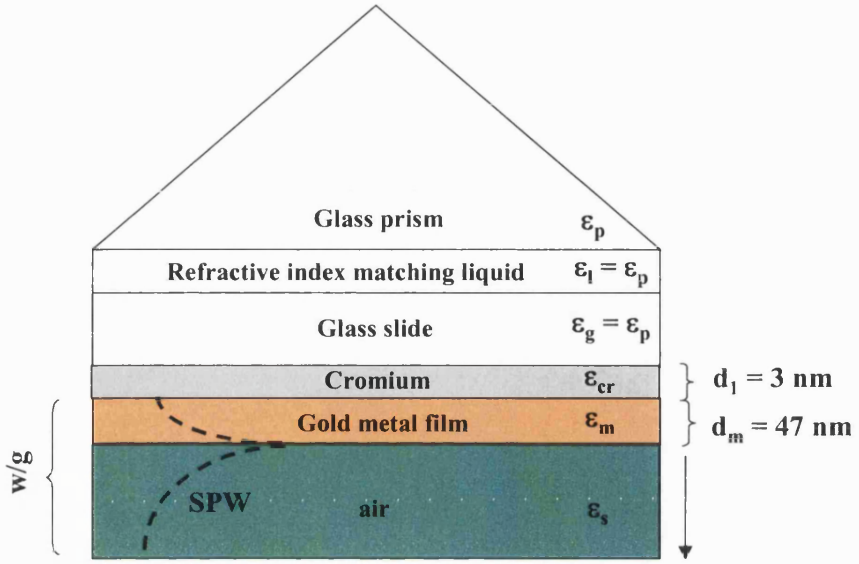

(a)

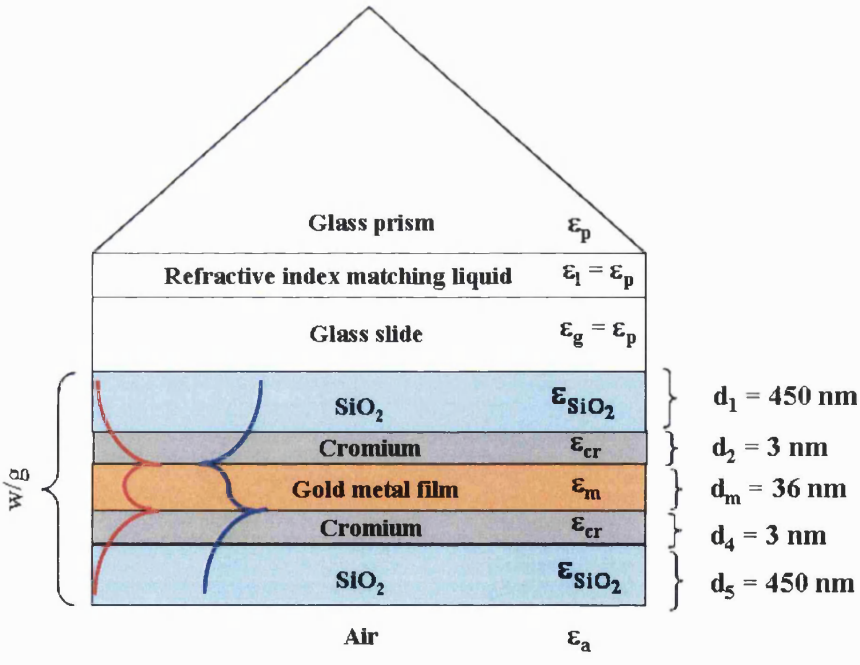

(b)

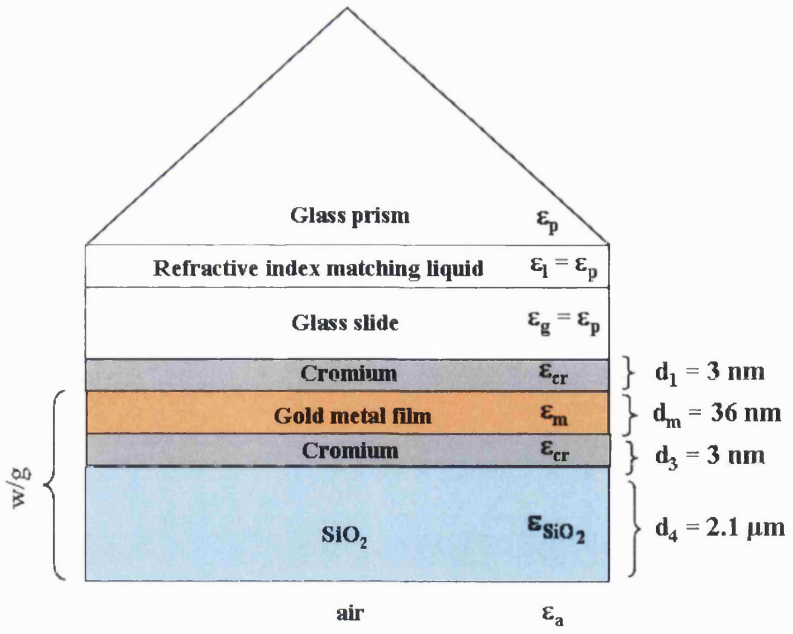

(c)

Figure 5.2. Prism coupled waveguide (PWG) structures for a) single interface SPW excitation, b) symmetric and antisymmetric SPW excitation in a DMD guide, and c) 'conventional' wave excitation.

In the structure of Figure 5.2a, SPW excitation is formed at the air – Au interface, whereas the symmetric and the antisymmetric SPWs are sustained at the SiO_2 – Au – SiO_2 waveguide of Figure 5.2b. The 'conventional' waves are supported at the Au – SiO_2 – Air waveguide of Figure 5.2c, with the SiO_2 film being the guiding region. Note that to avoid damaging the prism, all the w/g structures are deposited on a glass slide with relative permittivity $\varepsilon_g = \varepsilon_p$. In all the prism coupled w/g structures, the use of a 3nm cromium (Cr) layer next to the Au film was necessary to allow adhesion of Au on the glass slide or the SiO_2 film. To avoid any dust particles or glass defects which could produce air gaps between the glass slide and the prism, a refractive index matching liquid with relative permittivity $\epsilon_l = \epsilon_p = \epsilon_g$ had to be introduced between the two media [5.2]. Also, the deposition of the liquid had to be uniform between the prism and the slide to avoid air gaps.

5.1.3 Rotating system

The prism coupled w/g (PWG) systems were clamped on an x - z translating stage and then mounted on a manually rotating stage (RS1) for performing the rotation, Figure

5.3. The purpose of the x – z stage was to align the PWG to rotate concentric with the rotating axis of RS1. Correct alignment was ensured by monitoring the rotation of the PWG with respect to that of RS1 through a CCD camera connected to a monitor.

The detector of the system was placed on an extension arm which was mounted on rotation stage RS2, and the whole system was placed on the same rotating axis as the PWG – RS1 sub-system.

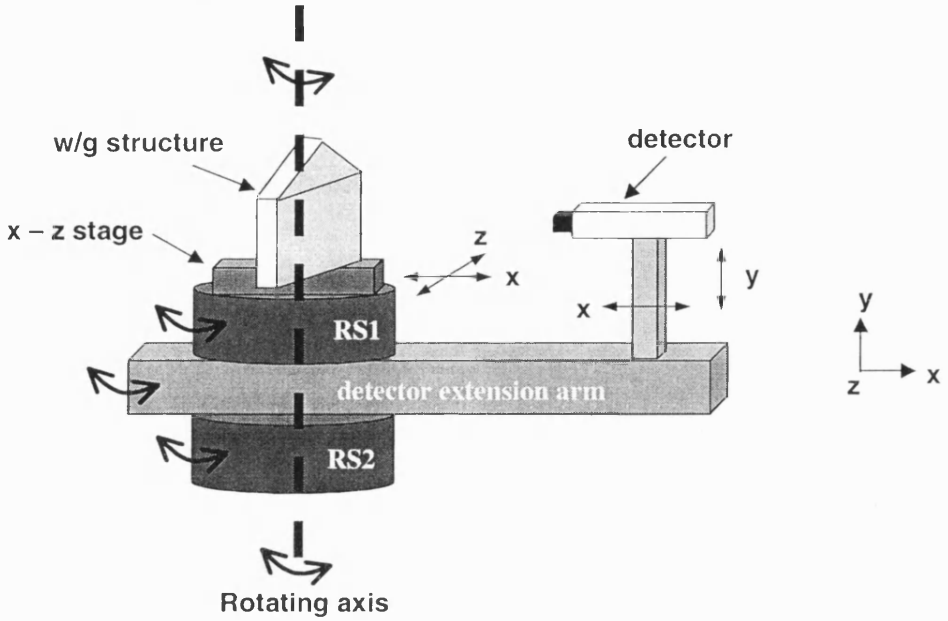

Figure 5.3. Rotating system for a PWG structure.

Note that both RS1 and RS2 had minimum step angle of 0.5°. From a design point of view, due to the manual operation of the system, RS2 is allowed to have worst step angle compared to RS1 which is rotating the PWG.

5.1.4 Optical source

For the excitation of the SPWs and the 'conventional' waves, two different optical sources were used:

a) a commonly employed for such cases commercial gas HeNe Laser [5.3] with peak emission wavelength λ_o = 633nm and output power of 5mW

b) an 'in-house' fabricated Superluminescent Light Diode (SLD) with λ_o = 980nm and maximum optical power of 120mW at 2A injection current (the SLD characteristics are given in Appendix G.2).

The SLD was pulsed driven with 1ms period and 10μs pulse width, unlike the HeNe which was powered directly from the mains (cw operation). The choice of the two sources was made to provide a comparison between commercial gas lasers and 'in-house' fabricated semiconductor optical sources when used for surface wave excitation.

An important parameter for the two sources was the divergent angle $\delta\psi$ of their output beams. As it is shown later in this chapter, a large $\delta\psi$ can smear out the excitation of the surface wave and prevent the system from being used as sensor. The evaluation of $\delta\psi$ can be done by projecting the output beam of the source onto a CCD camera and measure the corresponding spot size at different distances z from the CCD. A schematic of the measurement procedure is illustrated in Figure 5.4.

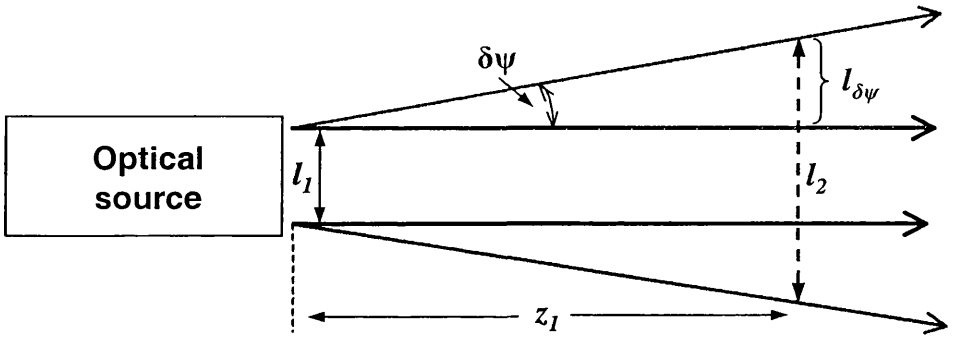

Figure 5.4. Measuring the divergence angle of an optical source.

Hence, $\delta\psi$ is:

$$\delta\psi = \tan^{-1}\left[l_{\delta\psi} / z_1\right] \tag{5.2}$$

where $l_{\delta\psi} = (l_2 - l_1)/2$ and l_1 and l_2 correspond to the diameter of the beam spot at the output of the optical source and at z_1 distance from the source respectively.

To reduce $\delta\psi$ (collimate the beam) as is the need for the highly divergent beam of the SLD [5.4], a collimating lens has to be placed at a distance from the source equal to its focal length [5.3], Figure 5.5.

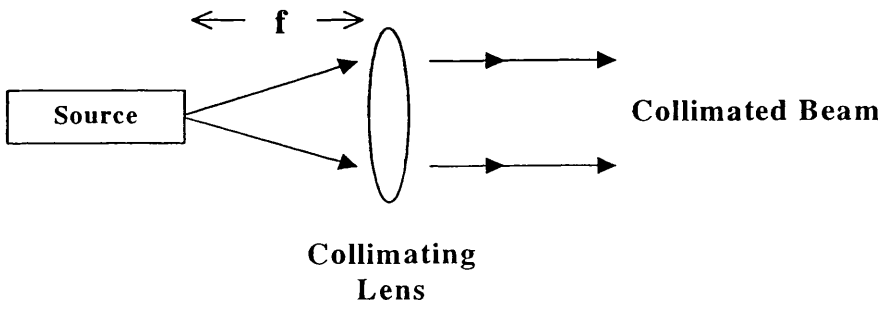

Figure 5.5. Collimating an optical source with a divergent output beam.

5.1.5 Optical polariser

Since both the HeNe and the SLD were not single (linearly) polarised, an optical polariser had to be used after the optical source to ensure only one light polarisation passing, either TE or TM. Since TM polarisation is required for SPW excitation, hence the polariser in all the experiments was set to block TE polarised light, unless otherwise explicitly indicated.

5.1.6 Detector

The detectors were commercially available photodiodes [5.5] operating in either pulsed or cw mode, depending on the optical source employed in the expriment. The circuit diagrams of the two detectors can be found in Appendix G.3.

The performance of the experimental arrangement can be further improved if an optical isolator is used to avoid reflections from the polariser or the lens to the source which can cause instability problems. Finally, a lock-in amplifier (followed by a chopper for the cw source) can increase the sensitivity of the detector if the system is to be used as a sensor.

5.2 SPW excitation in a single interface DM guide

5.2.1 Use of HeNe

By employing the arrangement of Figure 5.1 and the PWG structure of Figure 5.2a, single interface SPW excitation was performed with the use of the HeNe laser. The parameters of the system were: $\varepsilon_p = 2.25$, $\varepsilon_{cr} = -1.096 - j\ 20.7868$ [5.6], $\varepsilon_m = -9.89 - j\ 1.045$, [5.7], and $\varepsilon_s = 1$ (air). The divergent angle $\delta\psi$ of the HeNe output

beam was measured to be 0.06°, following the procedure described in section 5.1.4. Note that since $\delta\psi$ was quite small with respect to the distance between the source from the PWG (z = 1m), there was no need for a collimating lens.

A comparison between experimental and theoretical, eqn.(4.13) for n = 4, monitoring of the normalised I_R with respect to I_S, as a function of the internal prism angle θ_i to observe SPW excitation is presented in Figure 5.5.

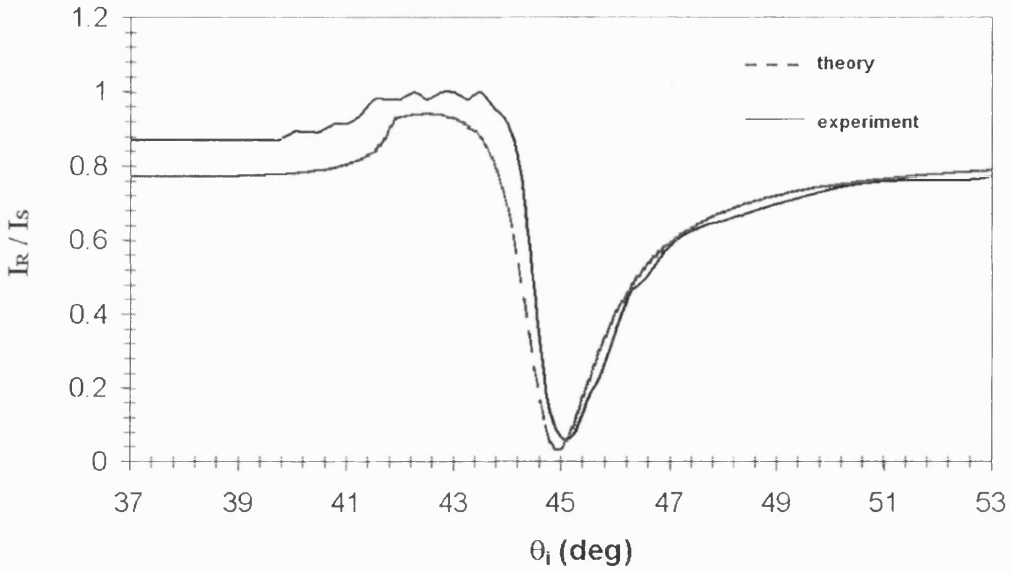

Figure 5.6. Experimental and theoretical results for single interface SPW excitation at the PWG of Figure 5.2a, where $\varepsilon_p = 2.25$, $\varepsilon_{cr} = -1.096 - j\ 20.7868$, $\varepsilon_m = -9.89 - j\ 1.045$, $\varepsilon_s = 1$, $d_1 = 3nm$, $d_m = 47nm$ and using a HeNe laser source with $\lambda_o = 633nm$.

Figure 5.6 shows that there is an agreement between theory and experiment, where the SPW excitation angle θ_{spw}, eqn.(4.25), and the total reflection angle θ_{TR} between the prism and the air are observed at 44.7° and 41.8° respectively.

Any differences between the two results are due to:

- the different actual and theoretical values for the parameters of the system (e.g. relative permittivity and thickness of the media)
- the misalignment of the PWG on RS1
- the manual rotation of the system
- not sufficient angle scanning resolution.

The corresponding theoretical SPW field intensity at the Au – air interface for the above parameters as calculated by $|T|^2$, eqn.(4.14) for n = 4, is presented in Figure 5.7.

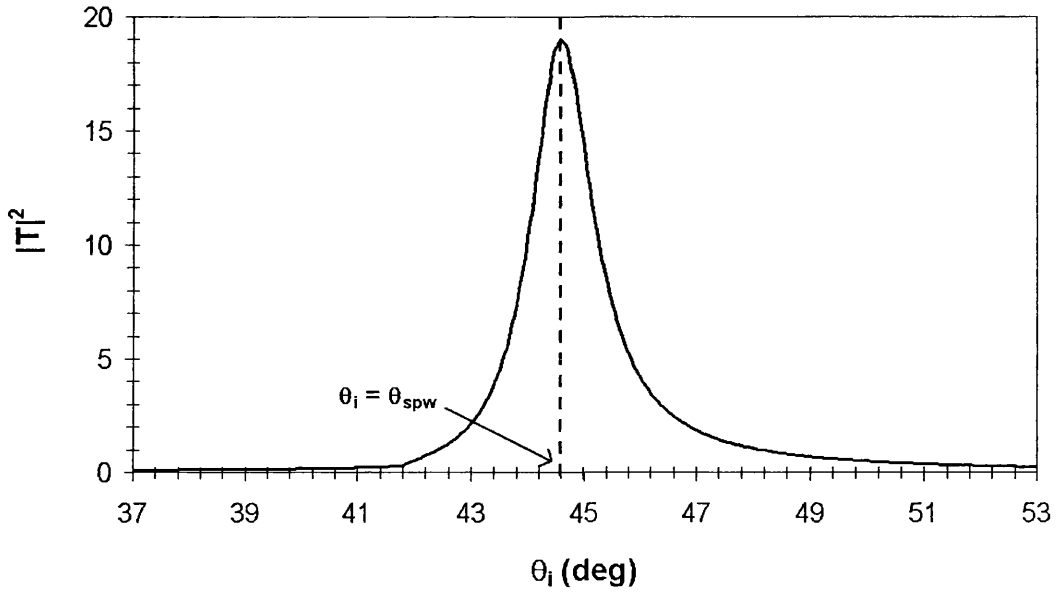

Figure 5.7. Theoretical evaluation of the SPW field intensity $|T|^2$ at the Au – air interface of the PWG structure of Figure 5.2a, for ε_p = 2.25, ε_{cr} = -1.096 - j 20.7868, ε_m = -9.89 - j 1.045, ε_s = 1, d_1 = 3nm, d_m = 47nm and using a HeNe laser source with λ_o = 633nm.

Note that although the described PWG structure of this section is the same as the one theoretically analysed in section 4.4.1, $|T|^2$ evaluated here is less compared to that in Figure 4.5 due to the use of the 3nm cromium film for the experiments.

5.2.2 Use of the SLD

SPW excitation with the use of the SLD was performed in the same PWG structure as for the HeNe case, section 5.2.1. Note now that due to the highly divergent beam of the SLD [Appendix G.2, Figure G.4], a collimating lens was introduced between the source and the polariser, achieving $\delta\psi \approx 0.09^o$.

Due to the different source wavelength of the SLD (λ_o = 980nm) compared to the HeNe (λ_o = 633nm), the relative permittivity of the cromium and the gold film are now ε_m = - 41.8 – j 3.05 [5.7] and ε_{cr} = - 1.12 – j 24.35 [5.6]. The experimental and theoretical, eqn.(4.13) for n = 4, monitoring of the normalised I_R as a function of θ_i to demonstrate SPW excitation with the use of the SLD is given in Figure 5.8.

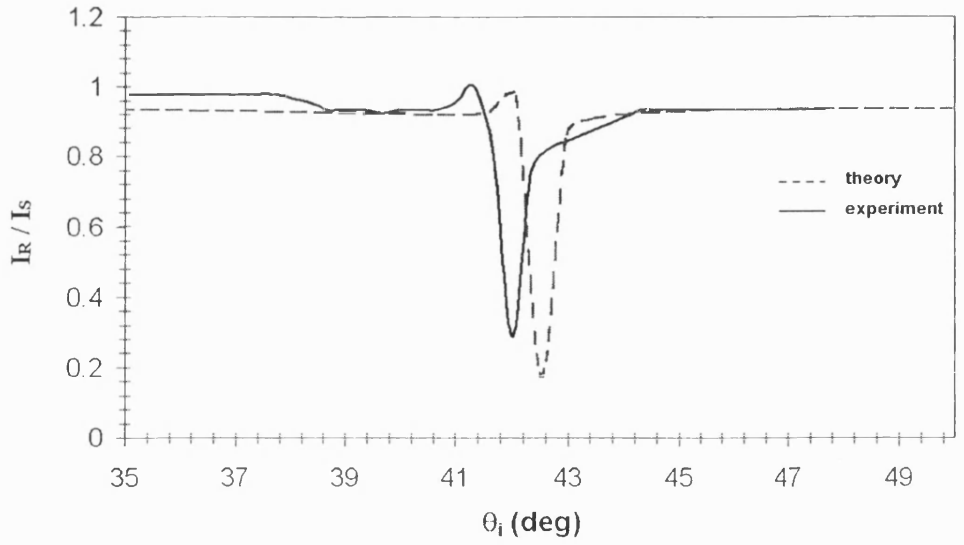

Figure 5.8. Experimental and theoretical results for single interface SPW excitation at the PWG of Figure 5.2a, where $\varepsilon_p = 2.25$, $\varepsilon_{cr} = -1.12 - j\,24.35$, $\varepsilon_m = -41.8 - j\,3.05$, $\varepsilon_s = 1$, $d_1 = 3nm$, $d_m = 47nm$ and using a SLD with $\lambda_o = 980nm$.

The comparison between the theory and experiment are not in such a good agreement now as for the HeNe case, Figure 5.6. However, SPW excitation is still clearly observed at $\theta_{spw} \approx 42^o$ which has now shifted towards to θ_{TR}. This is however an expected result since for SPW excitation occurring at longer λ_o it is known that $|\varepsilon_{mR}| >> \varepsilon_p$ which makes θ_{spw} to be, eqn.(4.25),

$$\theta_{spw} \approx \sin^{-1}\left[\sqrt{\frac{\varepsilon_s}{\varepsilon_p}}\right] \tag{5.3}$$

The differences observed between the theoretical and experimental results are due to the reasons given for the HeNe case, section 5.2.1, and also because the PWG has been designed for optimum SPW excitation at $\lambda_o = 633nm$. In addition, to achieve $I_R \approx 0$, i.e. 100% SPW excitation coupling efficiency, it is necessary that $d_m \approx 40nm$.

The theoretical SPW field intensity as evaluated by $|T|^2$, eqn.(4.14) for $n = 4$, is given in Figure 5.9.

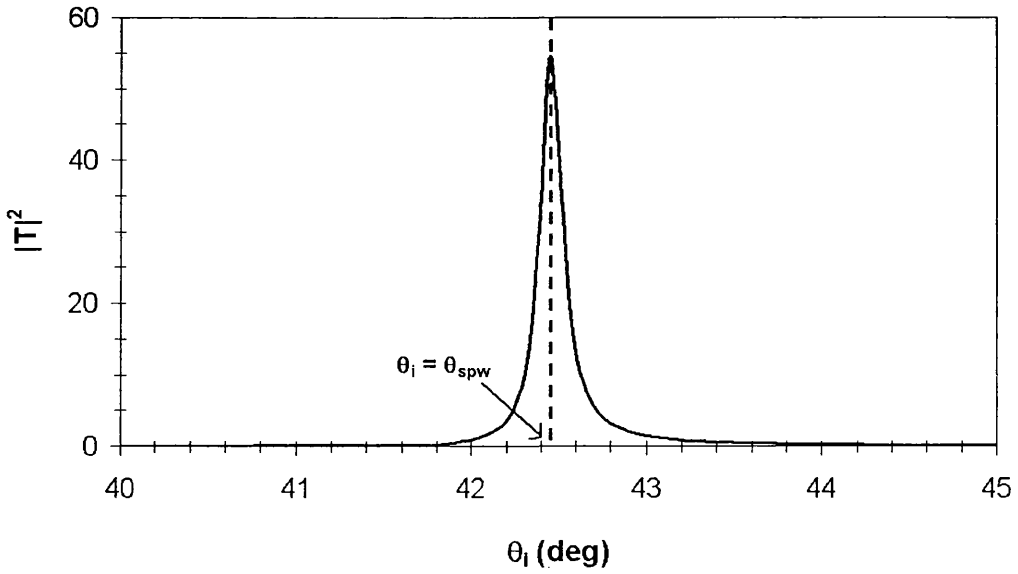

Figure 5.9. Theoretical evaluation of the SPW field intensity $|T|^2$ at the Au – air interface of the PWG structure of Figure 5.2a, when $\varepsilon_p = 2.25$, $\varepsilon_{cr} = -1.12 - j\,24.35$, $\varepsilon_m = -41.8 - j\,3.05$, $\varepsilon_s = 1$, $d_l = 3nm$, $d_m = 47nm$ and using a SLD with $\lambda_o = 980nm$.

The SPW field intensity when the SLD is used is much higher (almost 3 times) compared with the HeNe case, Figure 5.7, as a consequence of the reduced metal losses at longer wavelengths.

5.2.3 SPW excitation: comparison between HeNe and SLD

The comparison of SPW excitation between the two optical sources has demonstrated that the longer the SPW excitation wavelength the narrower the FWHM of the 'dip' of the normalised I_R ($FWHM_{SLD} \approx 0.5^o$; $FWHM_{HeNe} \approx 2^o$). As a consequence, this result improves the SPW sensing resolution capability. Note that to support high sensitivity and resolution measurements, it is necessary to employ high precision automated rotating stages.

In addition, the use of an 'in-house' fabricated semiconductor optical source can well compete with commercial gas laser sources as the HeNe gas Laser, when employed for SPW excitation. Moreover, the compact size and reduced cost of the semiconductor optical sources can easily lead to an integrated SPW system for biosensing or chemical applications.

5.3 SPW excitation in a DMD guide

As discussed in section 3.4.1, the use of a symmetric DMD waveguide structure can support under TM wave propagation only a symmetric and an antisymmetric SPW. In this section experimental demonstration of the excitation of the two SPW modes in such a guide will be given. The PWG configuration employed is that of Figure 5.2b, and the optical source was only the SLD as the HeNe laser could not excite SPW modes for that combination of materials / film thickness. The parameters of the system at $\lambda_o = 980$nm, were: $\varepsilon_p = 3.43$, $d_1 = d_5 = 450$nm, $d_m = 36$nm, $\varepsilon_a = 1$, $\varepsilon_{SiO_2} \approx 2.1$ while ε_m and ε_{cr} had the values given in section 5.2.2. Note that the SLD was used with a collimating lens to achieve a divergent angle of $\delta\psi \sim 0.09^o$. The excitation of the two SPW modes was theoretically, eqn.(4.13) for n = 7, and experimentally observed by monitoring I_R as a function of θ_i , Figure 5.10.

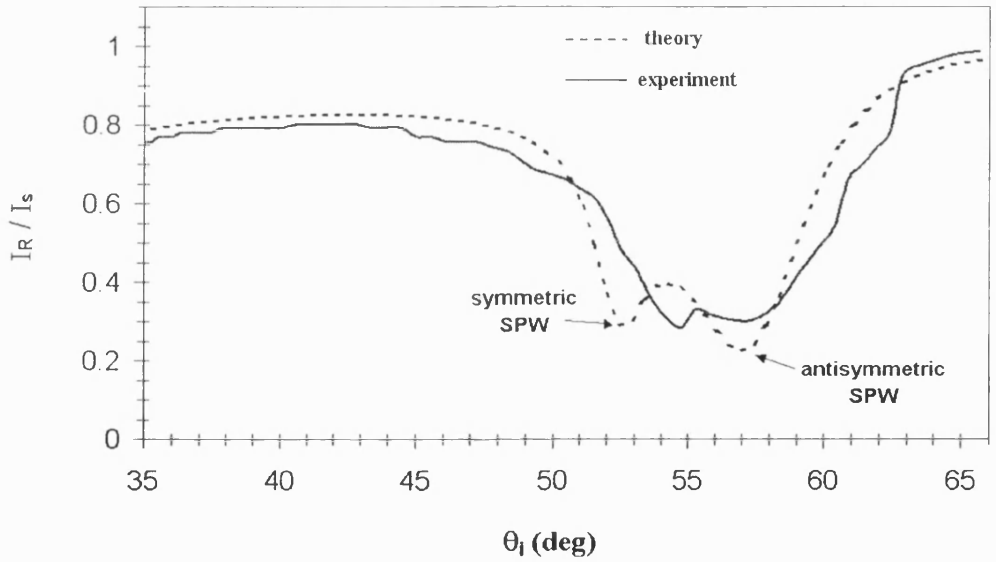

Figure 5.10. Theoretical and experimental observation of symmetric and antisymmetric SPW excitation in the DMD structure of Figure 5.2b, where $\lambda_o = 980$nm, $\varepsilon_p = 3.43$, $d_1 = d_5 = 450$nm, $d_m = 36$nm, $\varepsilon_a = 1$, $\varepsilon_{cr} = -1.12 - j\,24.35$, $d_2 = d_4 = 3$nm, $\varepsilon_{SiO_2} \approx 2.1$ and $\varepsilon_m = -41.8 - j\,3.05$.

Although the experimental observation, solid line, of the excited SPW modes was not as clear as theoretically estimated, dashed line, however, the two SPW modes could still be recognised. The antisymmetric mode corresponded to the 'dip' of (I_R / I_S) occurred at $\theta_i \approx 58^o$, whereas the symmetric was observed at $\theta_i \approx 53^o$. The distinction between the two modes can also be done from the width of the corresponding 'dip'. As discussed in

section 3.4.1, the metal losses contribute more to the antisymmetric mode producing higher modal losses compared to the symmetric, Figure 3.9, and therefore a wider FWHM.

The theoretical field intensity of the two SPW modes at the bottom Au - SiO_2 interface of the prism coupled arrangement as evaluated from $|T|^2$, eqn.(4.14) for n = 7, is given in Figure 5.11.

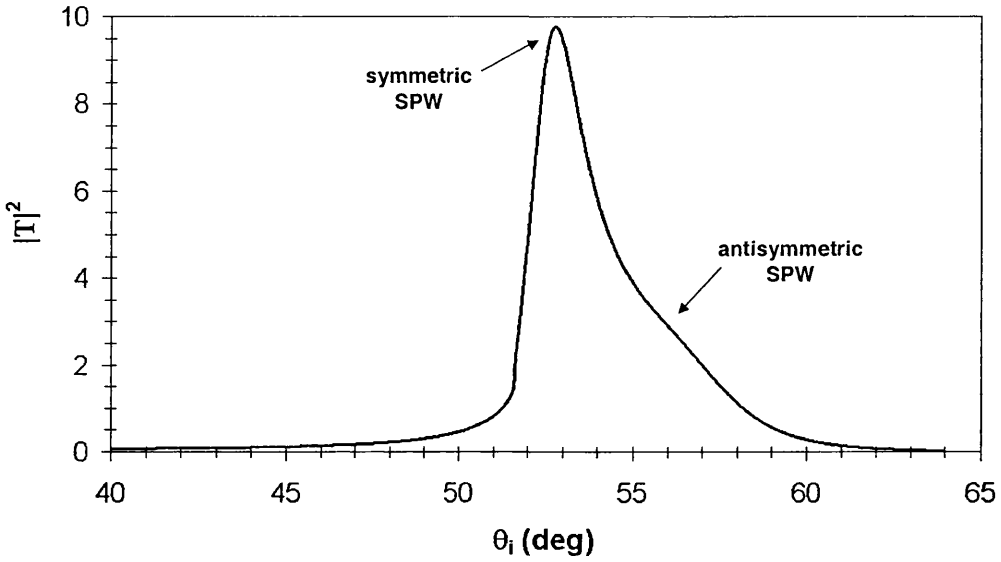

Figure 5.11. Theoretical field intensity, $|T|^2$, calculation of the symmetric and antisymmetric SPWs at the bottom Au - SiO_2 interface of the PWG arrangement of Figure 5.2b, where λ_o = 980nm, ε_p = 3.43, $d_1 = d_5$ = 450nm, d_m = 36nm, ε_a = 1, ε_{cr} = - 1.12 – j 24.35, $d_2 = d_4$ = 3nm, $\varepsilon_{SiO_2} \approx 2.1$ and ε_m = - 41.8 – j 3.05.

The results show that the symmetric SPW exhibits a significantly stronger field intensity compared to the antisymmetric SPW. This is due to the fact that the antisymmetric SPW is more susceptible to the effect of the metal losses of the structure as was discussed in chapter 3 and shown in Figure 3.9. This result can also be seen if the magnitude of the magnetic field component $|H_y(x)|^2$ for the two modes is plotted at their corresponding excitation angles (θ_i = 52.6 and 57°), as it is given in Figure 5.12.

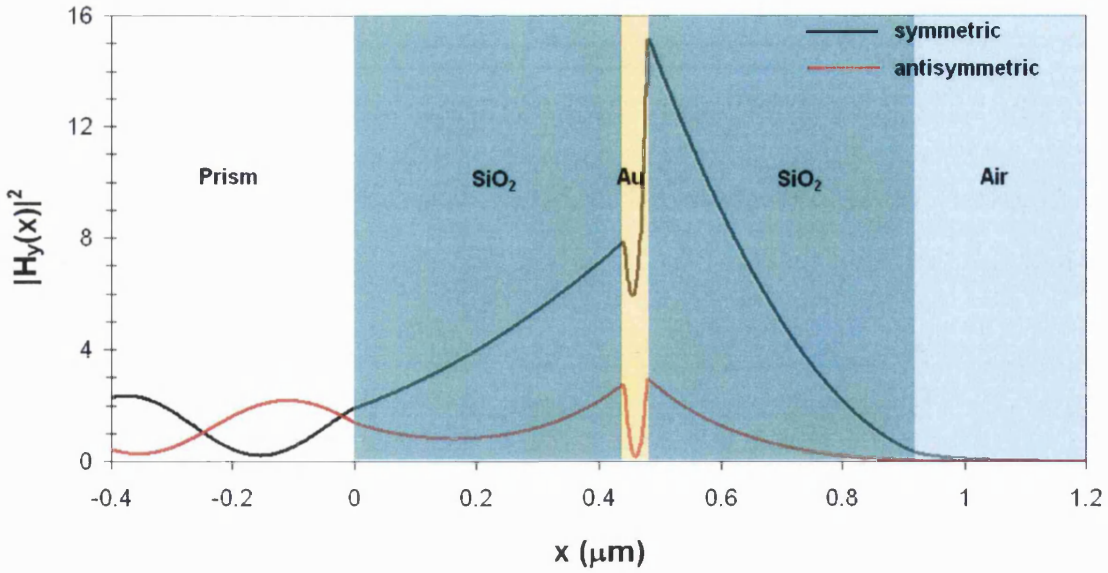

Figure 5.12. $|H_y(x)|^2$ field distribution for the symmetric and the antisymmetric SPW inside the PWG of Figure 5.2b, when θ_i = 52.6 and 57° respectively.

5.4 'Conventional' surface wave excitation

Apart from exciting SPW modes at single and multiple dielectric - metal interfaces, the prism coupler has been also widely used to excite 'conventional' modes. The PWG that was employed is the one shown in Figure 5.2c. The parameters of the system when the HeNe is used were: $\varepsilon_p = 2.25$, $\varepsilon_s = 1$, $\varepsilon_{SiO_2} \approx 2.1$, $d_1 = d_3 = 3$nm, $d_m = 36$nm and $d_4 = 2.1\mu$m, while ε_m and ε_{cr} were as given in section 5.2.1,

Due to the large thickness of the guiding region ($d_4 = 2.1\mu$m) and the relatively short wavelength ($\lambda_o = 633$nm), the highly asymmetric waveguide structure (Au-Cr-SiO_2-Air) was capable of supporting six 'conventional' modes under TM-polarised light as it is theoretically (employing T-L analysis) and experimentally shown in Figure 5.13.

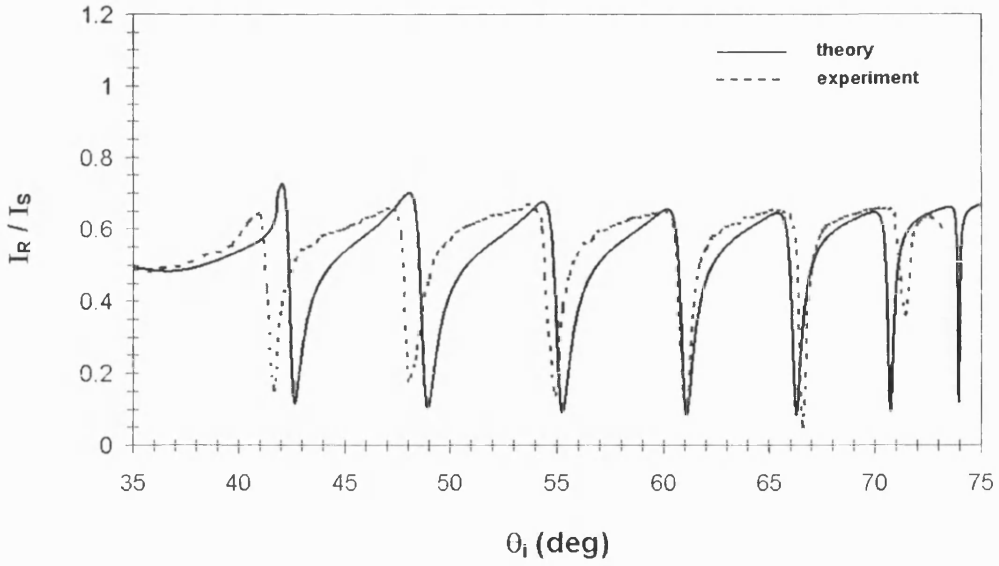

Figure 5.13. Theoretical and experimental excitation of 'conventional' modes in the prism coupled structure of Figure 5.2c, where $\varepsilon_p = 2.25$, $\varepsilon_s = 1$, $\varepsilon_{SiO_2} \approx 2.1$, $d_1 = d_3 = 3nm$, $d_m = 36nm$, $d_4 = 2.1\mu m$, $\varepsilon_{cr} = -1.096 - j\,20.7868$, $\varepsilon_m = -9.89 - j\,1.045$ and $\lambda_o = 633nm$.

Theoretical and experimental results are in a good agreement, and 6 modes are experimentally observed at $\theta_i \approx 72^o$, 67^o, 61^o, 55^o, 48^o and 43^o. The mode theoretically excited at $\theta_i \approx 73.9^o$ corresponds to a symmetric - like 'conventional' mode. The corresponding theoretical field intensity $|T|^2$, eqn.(4.14), for each of the excited modes, calculated at the SiO_2 / air interface is presented in Figure 5.14.

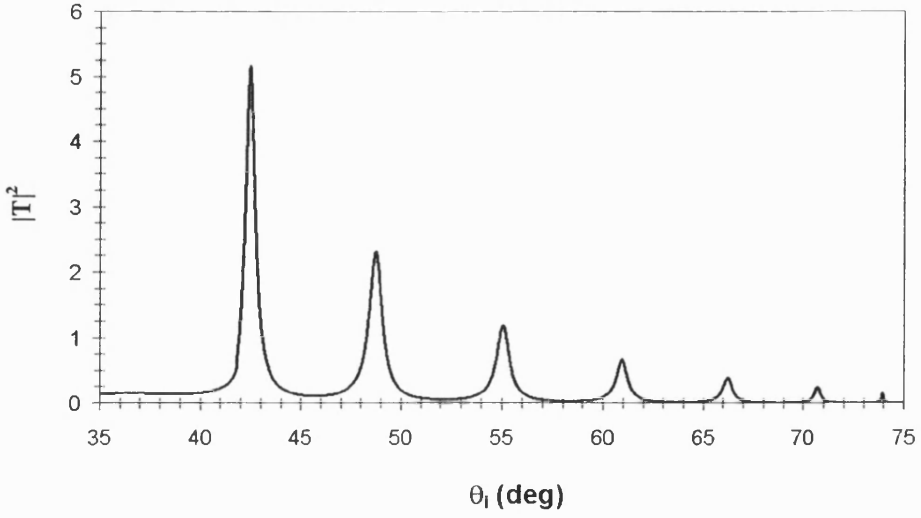

Figure 5.14. Theoretical field intensity, $|T|^2$, calculation of the conventional modes at the bottom SiO_2 – air interface of the PWG arrangement of Figure 5.2c, where $\varepsilon_p = 2.25$, $\varepsilon_s = 1$, $\varepsilon_{SiO_2} \approx 2.1$, $d_1 = d_3 = 3nm$, $d_m = 36nm$, $d_4 = 2.1\mu m$, $\varepsilon_{cr} = -1.096 - j\,20.7868$, $\varepsilon_m = -9.89 - j\,1.045$ and $\lambda_o = 633nm$.

The higher order modes (smaller β due to smaller θ_i, eqn.(4.2)) exhibit a stronger $|T|^2$ compared to the higher order ones, as a consequence of the less confined field inside the guiding region formed by the SiO_2. This result can be seen by plotting the magnitude square of the magnetic field distribution along x, $|H_y(x)|^2$, for the modes theoretically excited at $\theta_i = 42.6^o$, 55.2^o and 73.9^o , Figure 5.15.

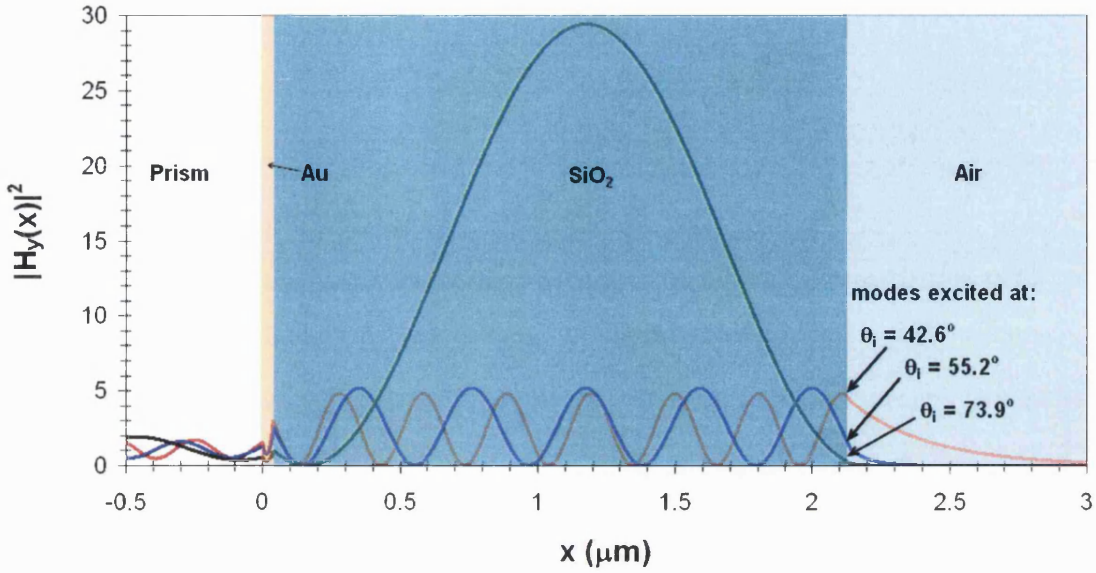

Figure 5.15. $|H_y(x)|^2$ field distribution for the 'conventional' modes of the PWG of Figure 5.2c excited at $\theta_i = 42.6^o$, 55.2^o and 73.9^o.

It is clearly shown in Figure 5.15 that the higher order mode spreads more in the air region giving a higher field intensity at the SiO_2 – air interface compared to the higher order mode which has the highest field intensity inside the guiding region (SiO_2 film).

As it is well known, prism couplers can also be used for exciting 'conventional' modes in optical waveguide structures [5.8]. Recently, however, the excitation of these modes has become quite popular especially in the area of biological / chemical sensing. Until now the main drawback for using 'conventional' modes in sensing was the fact that the maximum field intensity of the excited mode was met inside the guiding region. As a consequence there was no access to the sample under investigation, which was usually placed in the cladding region of the guide, hence the preference to the SPW modes. This constraint has been overcome recently by the use of porous materials such as SiO_2 or TiO_2 which allow absorption of the sample inside the guiding region [5.9].

5.5 Spatial Mode Beat effect

5.5.1 Theory

It is well known that the superposition of two electromagnetic waves with different frequencies and phases can produce a beat effect [5.3]. A similar case can also occur if the two waves have the same frequency but different phase so that only a spatial beat effect can take place.

The spatial beat effect can be described by considering the single interface of Figure 5.16, where two beams (a) and (b) are incident at x = 0 at angles θ_a and θ_b respectively.

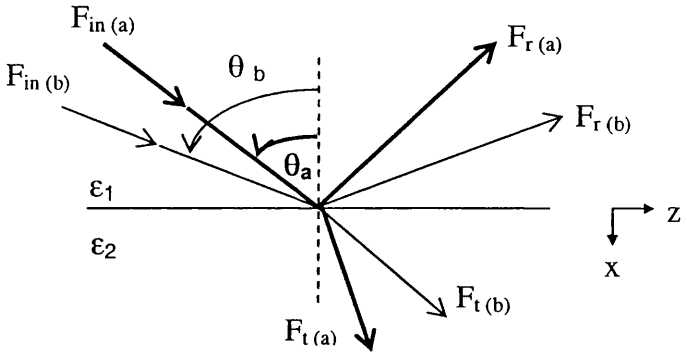

Figure 5.16. Two beams, with different propagation characteristics, incident at a single interface.

The total time dependent field for each of the beams is of the form

$$\tilde{F}_{T(q)}(x,z,t) = F_{T(q)}(x,z)\exp[+j\omega t] \tag{5.4}$$

where q = a, b denoting the two beams. The total field variation in medium 1 (x < 0), omitting the time dependency is

$$\begin{aligned} F_{T(q)}(x,z) &= F_{in(q)}(x,z) + F_{r(q)}(x,z) \\ &= A_{in(q)}\exp\left[-j\left(k_{x1(q)}x + k_{z1(q)}z\right)\right] + A_{r(q)}\exp\left[-j\left(-k_{x1(q)}x + k_{z1(q)}z\right)\right] \end{aligned} \tag{5.5}$$

where F_{in} and F_r are the incident and reflected transverse field variations, A_{in} and A_r are the corresponding field amplitudes and k_{x1}, k_{z1} are the transverse and longitudinal propagation constants respectively given by

$$k_{z1(q)}^2 = k_o^2 \varepsilon_1 \sin^2\theta_q \tag{5.6}$$

$$k_{x1(q)}^2 = k_o^2 \varepsilon_1 - k_{z1(q)}^2 \tag{5.7}$$

The total transmitted field $F_{t(q)}$ from each beam in the second medium ($x > 0$) having relative permittivity ε_2, has the same form as that described by eqn.(5.5), but the reflected field term is now not included. Note that the corresponding transverse and longitudinal propagation constants are therefore k_{x2} and k_{z2} respectively. From the continuity of the fields at $x = 0$,

$$k_{z1(q)} = k_{z2(q)} = \beta_{(q)} \tag{5.8}$$

hence

$$k_{x2(q)}^2 = k_o^2 \varepsilon_2 - \beta_{(q)}^2 \tag{5.9}$$

From the above, the total field resulting from the two incident beams at the interface $x = 0$ is then

$$\begin{aligned} F_{T(a+b)}(x = 0, z,) &= F_{T(a+b)}(x = 0, z) \exp[+ j\omega t] \\ &= \{A_{in(a)} \exp[- j\beta_{(a)} z] + A_{in(b)} \exp[- j\beta_{(b)} z]\} \end{aligned} \tag{5.10}$$

By assuming that the two beams have the same incident amplitude $A_{in(a)} = A_{in(b)} = A$, eqn.(5.10) gives

$$\begin{aligned} \tilde{F}_{T(a+b)}(z, t) &= F_{T(a+b)}(z) \exp[+ j\omega t] \\ &= 2A \exp\left[-j\left(\frac{\beta_{(a)} + \beta_{(b)}}{2}\right)z\right] \cos\left[\left(\frac{\Delta\beta}{2}\right)z\right] \exp[+ j\omega t] \end{aligned} \tag{5.11}$$

where

$$\Delta\beta = \beta_{(a)} - \beta_{(b)} \tag{5.12}$$

Hence, eqn.(5.11) describes a time dependent high frequency propagating wave with propagation constant

$$\beta_{hf} = \frac{\beta_{(a)} + \beta_{(b)}}{2} \tag{5.13}$$

enclosed in a low frequency envelope with propagation constant

$$\beta_{lf} = \frac{\beta_{(a)} - \beta_{(b)}}{2} \tag{5.14}$$

The corresponding total field intensity at $x = 0$ is therefore proportional to

$$F_{T(a+b)}(z)\, F^*_{T(a+b)}(z) = 4A^2 \cos^2\left[\left(\frac{\Delta\beta}{2}\right)z\right] \tag{5.15}$$

where $F^*_{T(a+b)}$ is the complex conjugate of $F_{T(a+b)}$.

Experimentally, it is the field intensity of the spatial beat effect that is observed, eqn.(5.15), which is shown as periodic bright and dark light spots areas at the interface x = 0 of Figure 5.16 which correspond to the maxima and minima of eqn.(5.15). The separation between two consecutive bright spots is equal to the wavelength of the envelope λ_{env} of eqn.(5.15), low frequency term, which is

$$\lambda_{env} = \frac{2\pi}{\Delta\beta} \tag{5.16}$$

Experimental demonstration of this spatial beat concept, eqn.(5.5), is given in section 5.5.2 by exciting two 'conventional' modes in a prism coupled arrangement.

5.5.2 Experimental observation

Experimental observation of the spatial beat effect, eqn.(5.15), was performed as suggested in section 5.5.1 by simultaneously exciting two modes in a PWG arrangement. The initial intension was to employ the DMD PWG structure and make use of the symmetric and antisymmetric SPW modes due to the theoretical strong field intensity of such modes, Figure 5.11. However, the excitation of the two SPWs in the PWG of Figure 5.2c was not distinct, Figure 5.10. In addition, the IR wavelength emission of the SLD (λ_o = 980nm) did not allow easy alignment of the system. As a consequence, the PWG structure with the 'conventional' modes of section 5.4 was chosen. Because two modes needed to be simultaneously excited in that case. The experimental arrangement of section 5.4 had to be slightly modified to allow the simultaneous excitation of the two modes. The new experimental arrangement is shown in Figure 5.17.

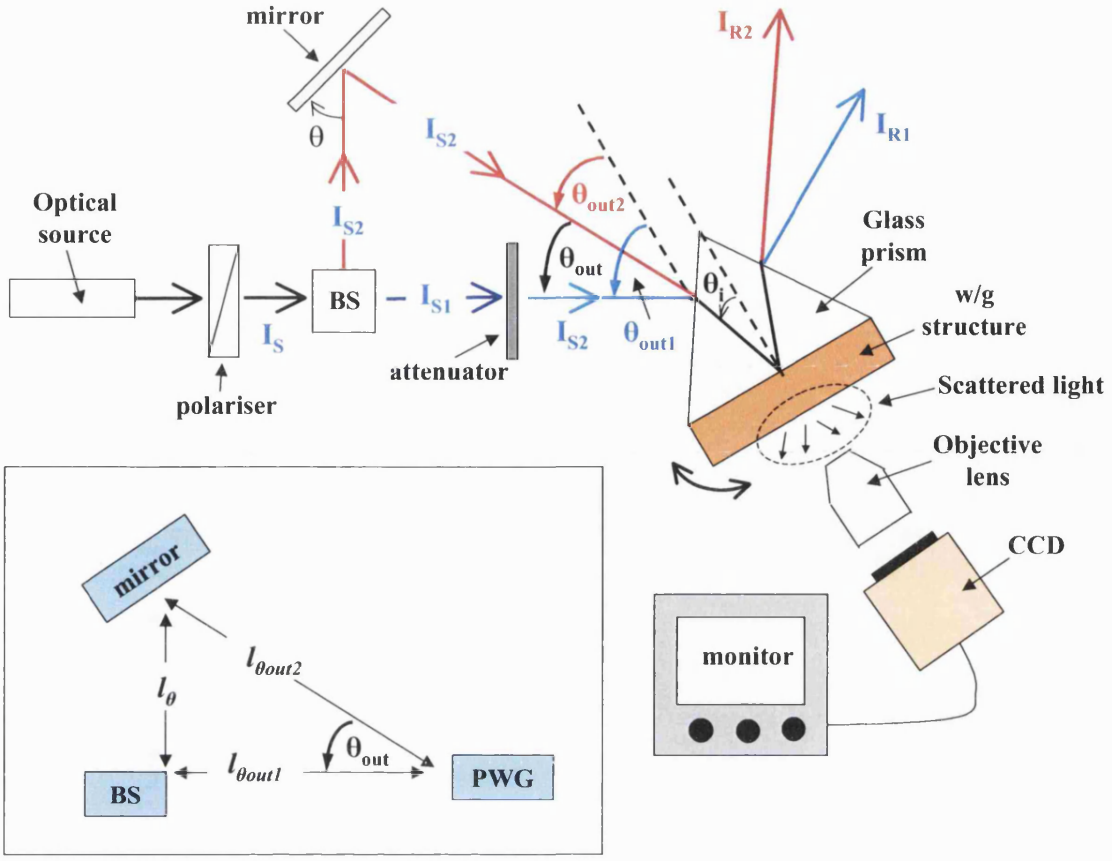

Figure 5.17. Experimental arrangement for producing the spatial mode beat effect.

With reference to the experimental arrangement of Figure 5.17, in the present case a beam splitter (BS) is introduced after the polariser to produce a second beam with intensity I_{S2} needed for the excitation of the second mode. This beam will be referred to as 'indirect', and it is incident onto the PWG through a mirror (M), at an external to prism wave excitation angle θ_{out2} (inside prism angle θ_{i2}). Since the intensity I_{S1} of the direct to the PWG optical beam was higher than I_{S2} , an attenuator was used between the BS and the PWG to ensure that $I_{S1} = I_{S2}$. The direct beam was then incident onto the PWG at an external angle θ_{out1} (internal angle θ_{i1}).

The next stage of the experimental process was to ensure the simultaneous excitation of the two modes. This was performed in three steps. Initially, the indirect beam was blocked ($I_{S2} = 0$), while the direct ($I_{S1} \neq 0$) was used to excite a mode in the PWG at $\theta_{out1} = \theta_{M1}$. The next step was to excite a second mode in the PWG with the use of the indirect beam at an angle $\theta_{out2} = \theta_{M2}$. To do so, the direct beam was blocked ($I_{S1} = 0$),

unlike the indirect which was now released ($I_{S2} \neq 0$) and impinged onto the PWG system. The excitation of the second mode was done by keeping the PWG fixed at $\theta_{out1} = \theta_{M1}$ and placing the mirror at an angle θ with respect to the incident beam coming from the BS, so to satisfy the angle $\theta_{out} = \theta_{out2} - \theta_{out1}$ in the triangle formed by the mirror, the BS and the PWG, inset of Figure 5.17. The sides of the triangle had length l_θ, $l_{\theta out1}$ and $l_{\theta out2}$ which correspond to the distances between the BS and the mirror, the BS and the PWG, and the mirror and the PWG. The final step was then to use both beams ($I_{s1} \neq 0$, $I_{s2} \neq 0$) and align their spots to overlap onto the prism - Au interface, so the excited modes are at the same place along z direction, as required by eqn.(5.15).

The spatial beat effect was then expected to be observed at the SiO_2 - air interface of the PWG system, Figure 5.2c. Hence, a combination of an objective microscope lens with 10 times magnification and a CCD camera, giving a total magnification of 1100 times, imaged the interface onto a monitor. The peaks and the troughs of the envelope of eqn.(5.15) were then expected to be observed at the SiO_2 - air interface as a result of scattered light due to surface defects or dust particles.

Experimental demonstration of the phenomenon was performed by choosing $\theta_{i1} = 72^o$ and $\theta_{i2} = 67^o$ which corresponded to $\beta_1 = 14.22\mu m^{-1}$ and $\beta_2 = 13.77\mu m^{-1}$, eqn.(4.2), respectively, Figure 5.18a. This β combination could produce the longest $\lambda_{env} \approx 14\mu m$, eqn.(5.16), among the six β of the excited modes.

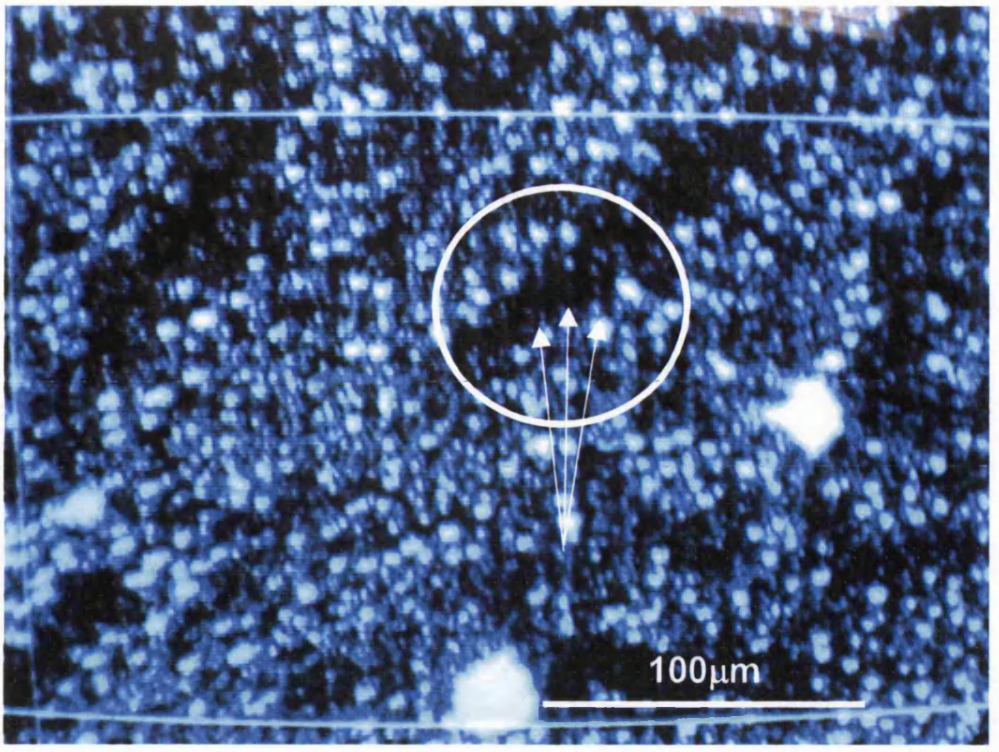

(a)

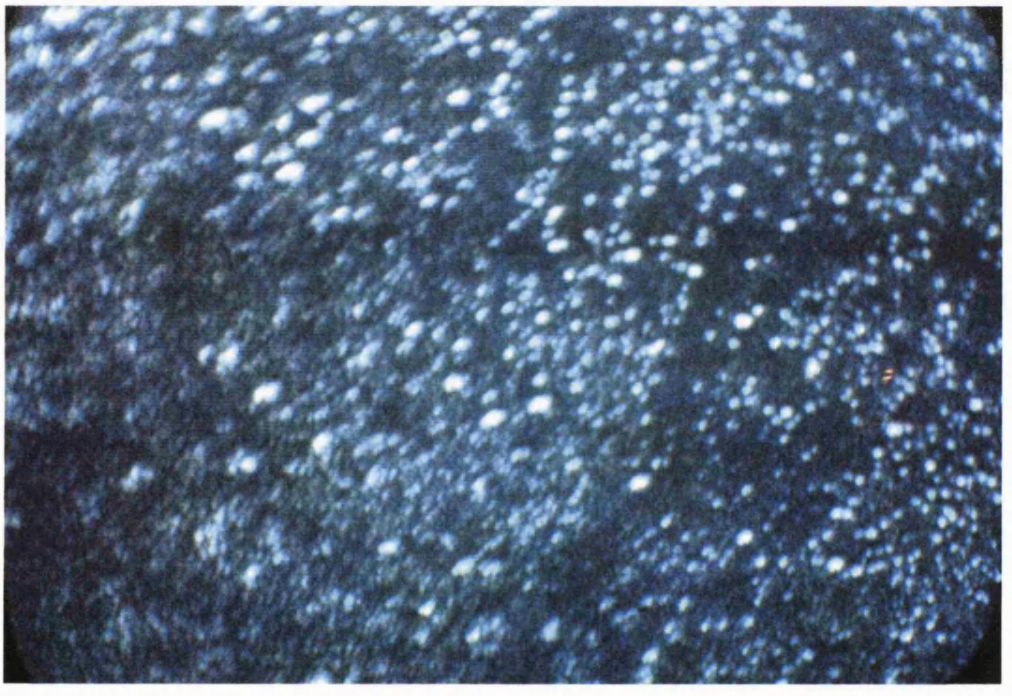

(b)

Figure 5.18. a) Simultaneous excitation of two modes in the PWG of Figure 5.2c, producing a spatial mode effect, where $\varepsilon_p = 2.25$, $\varepsilon_s = 1$, $\varepsilon_{SiO_2} \approx 2.1$, $d_1 = d_3 = 3nm$, $d_m = 36nm$, $d_4 = 2.1\mu m$, $\epsilon_{cr} = -1.096 - j\ 20.7868$, $\epsilon_m = -9.89 - j\ 1.045$ and $\lambda_o = 633nm$. b) Single mode excitation does not allow a spatial mode effect to be produced.

Although the picture in Figure 5.18a is not very clear, however, periodical vertical light lines can be observed when two modes are simultaneously excited. The light lines correspond to the maxima of eqn.(5.15), and they do not appear for single mode excitation, Figure 5.18b. The experimental λ_{env} was measured to be 7μm peak to peak, which is not so close to the theoretical estimation of $\lambda_{env} \approx 14\mu m$, eqn.(5.16). this error is believed to be due to:

a) the picture being defocused
b) the angle for the mode excitation is not exact

Note here that the spatial mode beat effect can be performed for any two incident angles as shown by eqn.(5.15). However, when a mode is excited, the corresponding field intensity $|T|^2$, eqn.(4.14), is much stronger, Figure 5.14, producing more intense scattered light. By comparing the various modes of the structure, Figure 5.14, much brighter light lines could have been produced if the higher order modes (smaller angles) had been employed, but at the expense of a shorter λ_{env}, eqn.(5.16)

In addition, if the system is to be used as a sensor, any change in the relative permittivity of the dielectric substrate (air in our example) can shift the corresponding surface mode excitation angle. Hence, by considering the beam angles to be fixed, the mode excitation will not be optimum anymore. As a consequence a less intense field will be generated at the SiO_2 – dielectric substrate interface, Figure 5.14, which will reduce the intensity of the periodic bright spots. This intensity change can therefore be detected for sensing purposes. Of course it is also possible to measure λ_{env}, eqn.(5.16), for any changes in the permittivity of the substrate, but this will require continuous alignment of the two beams which is not so convenient.

5.6 SPW excitation with non-ideal optical sources

So far in this thesis, the analysis of prism coupled structures, has been done assuming an ideal collimated monochromatic source beam such as the commonly used HeNe gas laser. However, for a compact system it would be desirable to use sources such as semiconductor lasers and SLDs. The drawback however of such optical sources is that they have divergent beams and the SLD is also spectrally broad [5.10]. To delineate the requirements for semiconductor optical sources to be employed for SPW excitation, the

following section will present theoretical and experimental results for SPW excitation with a typical K-R prism coupled arrangement when such sources are employed.

Consider an optical source with beam divergent angle $\delta\psi$, spectral width $\delta\lambda$, and field intensity $\hat{I}_{in}$, incident on the K-R prism coupler of Figure 5.19 at an angle θ_i.

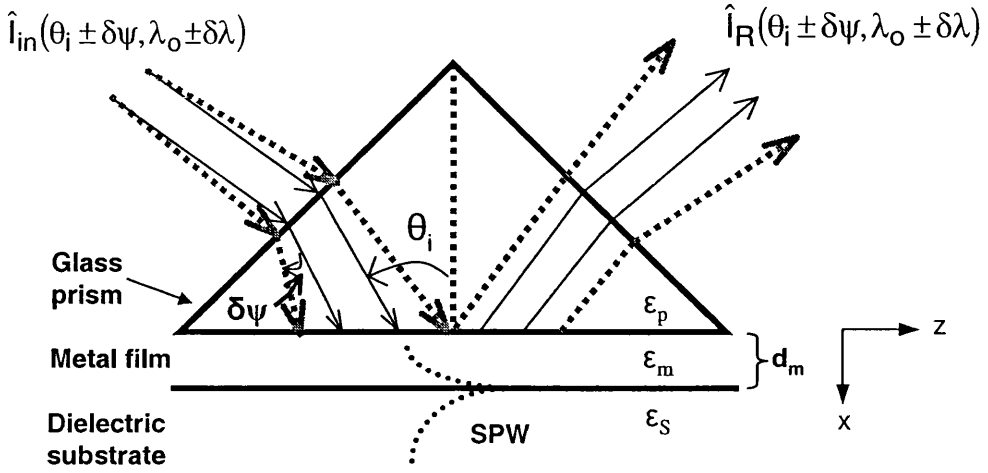

Figure 5.19. Single interface SPW excitation with a K-R prism coupled structure, employing a non-ideal optical source.

The field intensity of the reflected signal $\hat{I}_R$ can then be represented as a convolution between the intensity I_R of a reflected signal from an ideal optical source ($\delta\psi = 0$ and $\delta\lambda = 0$) and $\hat{I}_{in}$, [5.11-13],

$$\hat{I}_R(\theta_i, \lambda_o) = \int_{\theta_-}^{\theta_+} \int_{\lambda_-}^{\lambda_+} \hat{I}_{in}(\theta, \lambda) I_R(\theta_i - \theta, \lambda)\, d\theta\, d\lambda \qquad (5.17)$$

where $\theta_\pm = \theta_i \pm \delta\psi$, $\lambda_\pm = \lambda_o \pm \delta\lambda$ with $\theta_i >> \delta\psi > 0$ and $\lambda_o >> \delta\lambda > 0$. Note that I_R in eqn.(12) is theoretically described by the corresponding reflection coefficient $|\Gamma|^2$ as given by eqn.(4.13).

Since the cross sectional shape for a typical far-field irradiance and spectrum profile for an optical source approaches a Gaussian function, [Appendix G.2], the intensity of the input beam $\hat{I}_{in}$ can be written as

$$\hat{I}_{in}(\theta, \lambda) = I_o(\lambda) \exp\left[-\alpha\theta^2\right] \qquad (5.18)$$

where $I_o(\lambda)$ is the wavelength-dependent amplitude coefficient, $\alpha = [1 / (2\,\sigma_\theta)]$ and σ_θ is the standard deviation of a Gaussian profile [5.3], which here is $\sigma_\theta = \delta\psi$.

Equation (5.17) can also be modified to calculate the SPW field intensity $\hat{I}_T$ at the metal - substrate interface, by replacing I_R with the corresponding field intensity I_T ($= |T|^2$) given by eqn.(4.14),

$$\hat{I}_T(\theta_i, \lambda_o) = \int_{\lambda_-}^{\lambda_+} \int_{\theta_-}^{\theta_+} \hat{I}_{in}(\theta, \lambda) I_T(\theta_i - \theta, \lambda)\, d\theta\, d\lambda \tag{5.19}$$

Comparisons between theoretical and experimental SPW excitation with non-ideal optical sources are given in this section. Results have been obtained from a commercial LASER pointer with λ_o = 633nm and $\delta\lambda \approx$ 1nm, and the in–house fabricated semiconductor SLD used in sections 5.1.1-2 which has λ_o = 980nm and $\delta\lambda \approx$ 15nm. The reason of the two different optical sources was to investigate the influence of $\delta\lambda$ and $\delta\psi$ variation on SPW excitation at different λ_o. The PWG structure used for the experiments is that of Figure 5.2a, with parameters: $\varepsilon_p = 2.25$, $\varepsilon_s = 1$, ε_m depending on λ_o and d_m = 47nm. Note that all theoretical $\hat{I}_R$ and $\hat{I}_T$ graphs have been normalised with respect to $\hat{I}_{in}$ so that

$$R = \frac{\hat{I}_R}{\hat{I}_{in}} \tag{5.20}$$

$$G = \frac{\hat{I}_T}{\hat{I}_{in}} \tag{5.21}$$

Hence, R and G will be plotted as a function of the incident angle θ_i for different $\delta\psi$ and $\delta\lambda$.

5.6.1 Experimental apparatus

The experimental configuration used with the semiconductor optical sources for exciting SPWs was based on the system of section 5.2.2. The addition of a system of lenses between the PWG and the polariser was necessary to control $\delta\psi$ in the output beam of the optical source, Figure 5.20, [5.12-13].

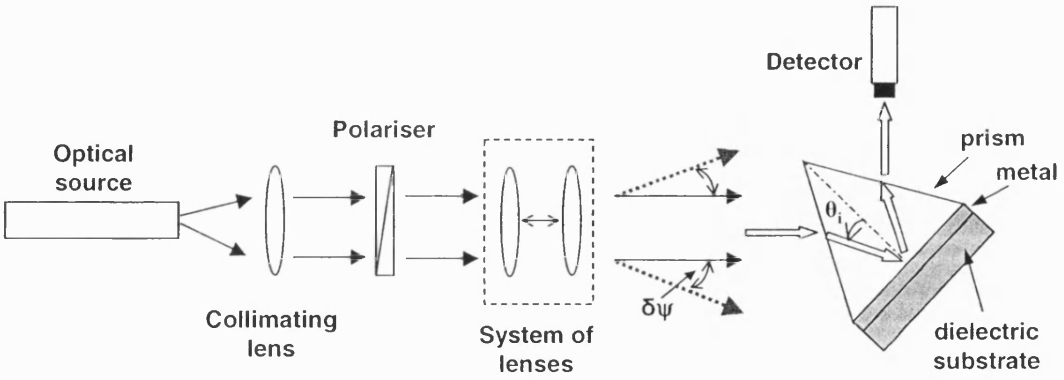

Figure 5.20. Experimental apparatus for SPW excitation with a non ideal optical source.

The measurement of $\delta\psi$ was performed by following the procedure described in section 5.1.4.

5.6.2 Results of SPW excitation with non-ideal sources

a) Laser diode

For the laser diode case, the SPW excitation parameters R, eqn.(5.20), and G, eqn.(5.21), were examined for $\delta\psi \approx 0.09^\circ$ and 1° respectively, Figures 5.21-22.

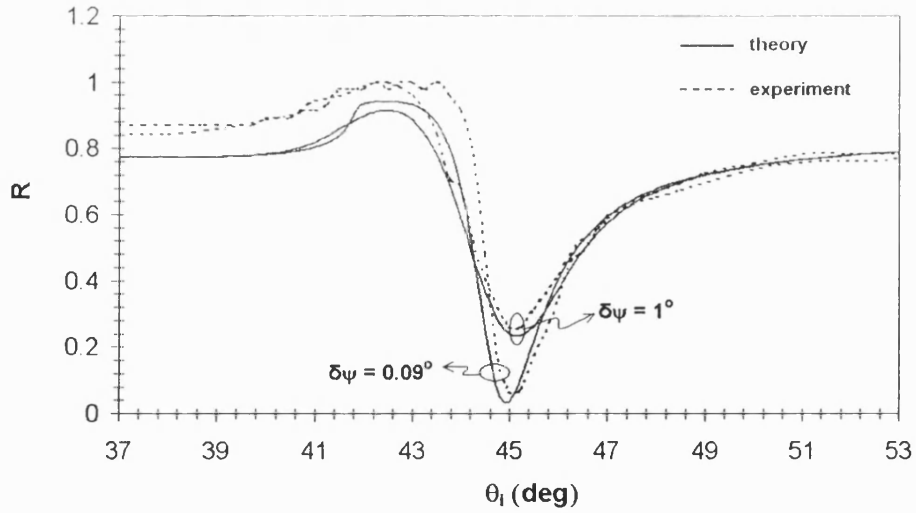

Figure 5.21. Experimental and theoretical SPW excitation at the PWG of Figure 5.2a, where $\varepsilon_p = 2.25$, $\varepsilon_{cr} = -1.096 - j\,20.7868$, $\varepsilon_m = -9.89 - j\,1.045$, $\varepsilon_s = 1$, $d_1 = 3$nm, $d_m = 47$nm, when using a laser pointer with $\lambda_o = 633$nm, $\delta\lambda = 1$nm, $\delta\psi = 0.09^\circ$ and 1°.

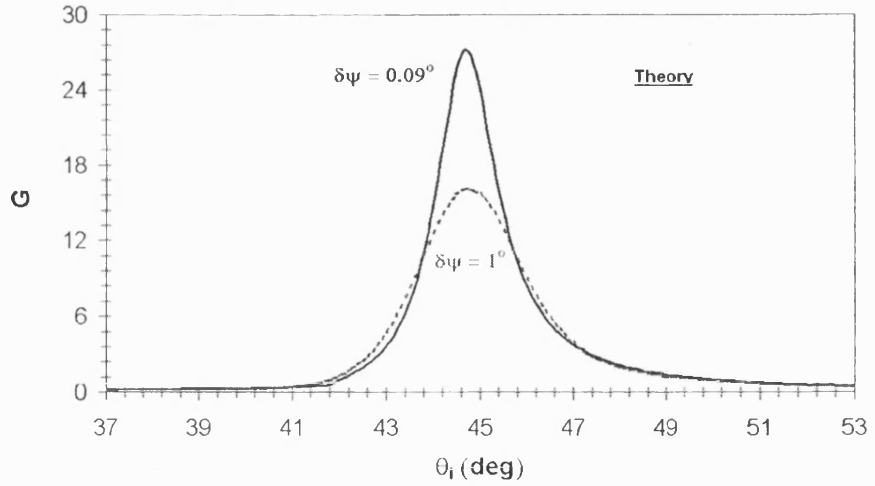

Figure 5.22. Theoretical SPW field intensity at the Au – air interface of the PWG of Figure 5.2a, where $\varepsilon_p = 2.25$, $\varepsilon_{cr} = -1.096 - j\ 20.7868$, $\varepsilon_m = -9.89 - j\ 1.045$, $\varepsilon_s = 1$, $d_1 = 3nm$, $d_m = 47nm$, when using a laser pointer with $\lambda_o = 633nm$, $\delta\lambda = 1nm$, $\delta\psi = 0.09^o$ and 1^o.

Theoretical and experimental results are in a good agreement and any discrepancies observed are due to the reasons outlined in section 5.2.1. The results show that, as intuitively expected, with increasing $\delta\psi$ the FWHM of R widens and the corresponding 'dip' becomes shallower. Similarly, G at the metal - substrate interface is reduced for an increasing $\delta\psi$. This worsening in the resolution sensitivity of the system as $\delta\psi$ becomes larger is better seen theoretically in Figure 5.23, which corresponds to a typical experiment where the SPW prism coupler acts as a sensor and is used to detect a change of 0.1% in ε_s. Clearly, as $\delta\psi$ increases the change in the position of the SPW excitation angle θ_{spw}, eqn.(4.25), becomes more difficult to resolve.

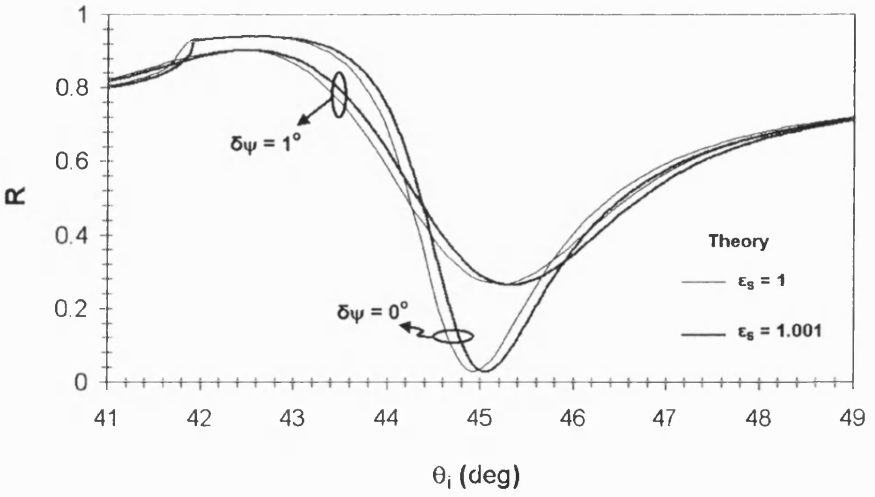

Figure 5.23. SPW resolution sensitivity employing a Laser pointer with $\lambda_o = 633nm$ and $\delta\lambda = 1nm$.

b) SLD

The use of the SLD which has a broader spectral width ($\delta\lambda$ = 15nm) compared to the HeNe laser, revealed also a good match between the theoretical and the experimental results for R when used for SPW excitation with $\delta\psi \approx 0.09^{\circ}$ and 0.64° respectively, as it is illustrated in Figure 5.24.

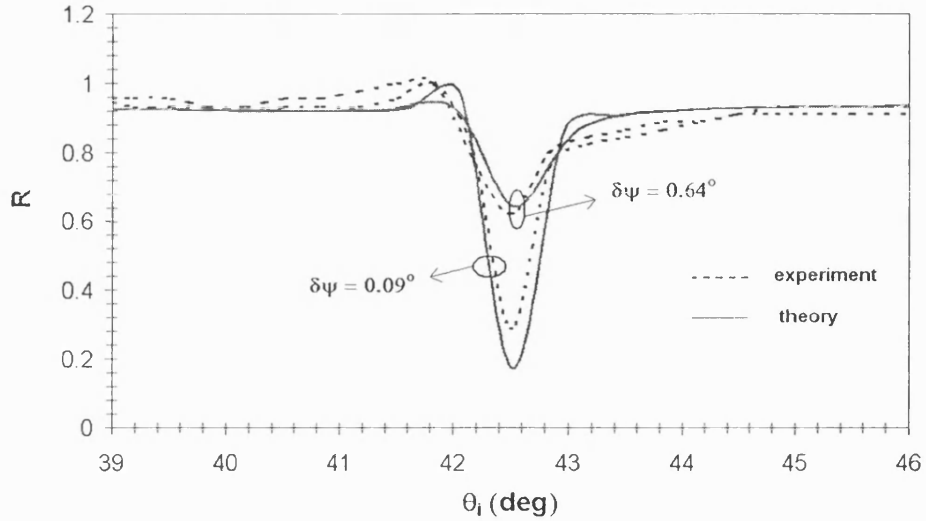

Figure 5.24. Experimental and theoretical SPW excitation at the PWG of Figure 5.2a, where ε_p = 2.25, ε_{cr} = - 1.12 – j 24.35, ε_m = - 41.8 - j 3.05, ε_s = 1, d_1 = 3nm, d_m = 47nm, when using a SLD with λ_o = 980nm, $\delta\lambda$ = 15nm, $\delta\psi = 0.09^{\circ}$ and 0.64°.

The field reflection coefficient R of the prism coupled arrangement when the SLD is used, has a narrower FWHM compared to the case with the Laser, due to the longer λ_o of the source. As a consequence, the maximum $\delta\psi$ allowed before the 'dip' in R flattens out, is now limited to around 0.6°. Beyond that value, a 0.1% change in ε_s, which corresponds to a shift of about 0.1° at θ_{spw}, eqn.(4.25), when $\delta\psi$ = 0, is very difficult to be detected as it is shown in Figure 5.25.

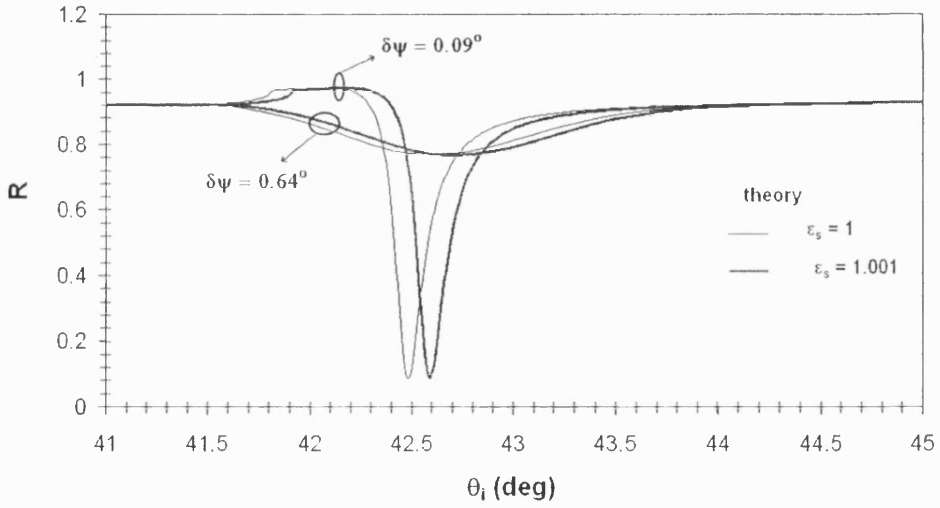

Figure 5.25. SPW resolution sensitivity employing an SLD for a 0.1% change in ε_s.

In addition, the corresponding field intensity $|T|^2$ of the structure as $\delta\psi$ increases becomes worse as it is theoretically shown in Figure 5.26.

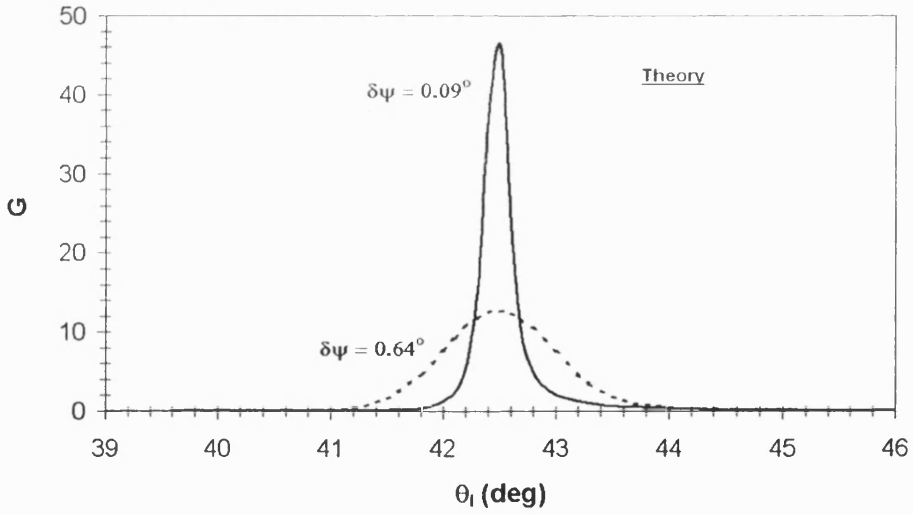

Figure 5.26. Theoretical SPW field intensity at the Au – air interface of the PWG of Figure 5.2a, where $\varepsilon_p = 2.25$, $\varepsilon_{cr} = -1.12 - j\,24.35$, $\varepsilon_m = -41.8 - j\,3.05$, $\varepsilon_s = 1$, $d_1 = 3$nm, $d_m = 47$nm, when using an SLD with $\lambda_o = 980$nm, $\delta\lambda = 15$nm, $\delta\psi = 0.09^o$ and 0.64^o.

5.6.3 Effects of non-ideal sources on SPW signal excitation parameters

Apart from the resolution sensitivity of the SPW system given by the shift of θ_{spw} for an amount of $\delta\varepsilon_s$ and the SPW field intensity G, there are also some other parameters of R when SPW excitation takes place which are affected by the divergent angle and the spectral width of the optical source. These parameters are the FWHM and the depth of

the 'dip' in R i.e. the minimum value of R , R_{min}. While θ_{spw}, eqn.(4.25), is sensitive to $\delta\varepsilon_s$, R_{min} and the FWHM can be used to evaluate the thickness of the metal and the relative permittivity of the different media of the system [5.14]. The variation of θ_{spw}, FWHM of R, R_{min}, and G as a function of $\delta\psi$ at $\theta_i = \theta_{spw}$, eqn.(4.25), is given for the two optical sources with λ_o = 633nm and 980nm, in Figures 5.27-30.

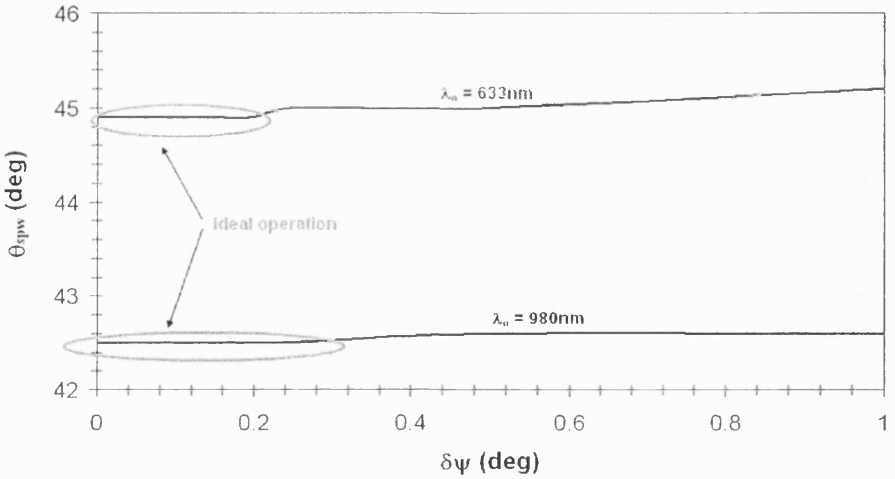

Figures 5.27. Variation of θ_{spw} as a function of $\delta\psi$ for the PWG structure of Figure 5.2a when using a SLD with λ_o = 980nm and $\delta\lambda$ = 15nm and a laser pointer with λ_o = 633nm and $\delta\lambda$ = 1nm.

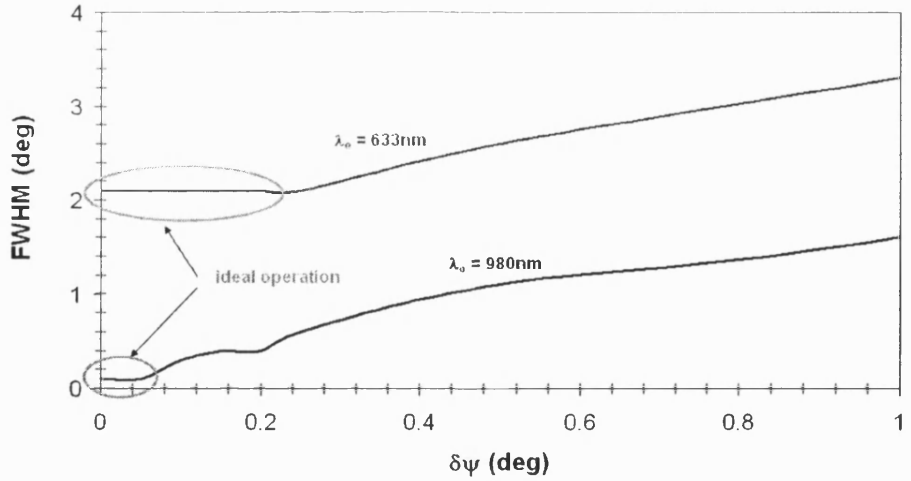

Figure 5.28. Variation of the FWHM of the 'dip' of R as a function of $\delta\psi$ for the PWG structure of Figure 5.2a when using a SLD with λ_o = 980nm and $\delta\lambda$ = 15nm and a laser pointer with λ_o = 633nm and $\delta\lambda$ = 1nm.

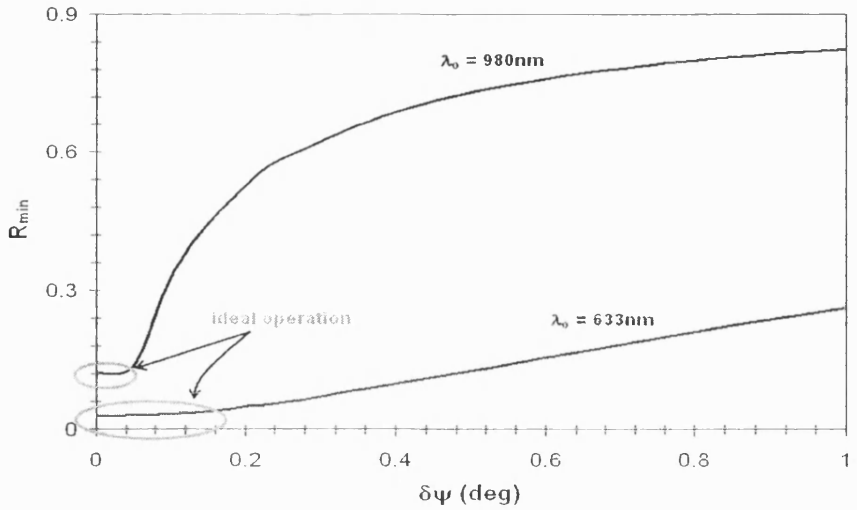

Figure 5.29. Variation of R_{min} at $\theta_i = \theta_{spw}$ as a function of $\delta\psi$ for the PWG structure of Figure 5.2a when using a SLD with λ_o = 980nm and $\delta\lambda$ = 15nm and a laser pointer with λ_o = 633nm and $\delta\lambda$ = 1nm.

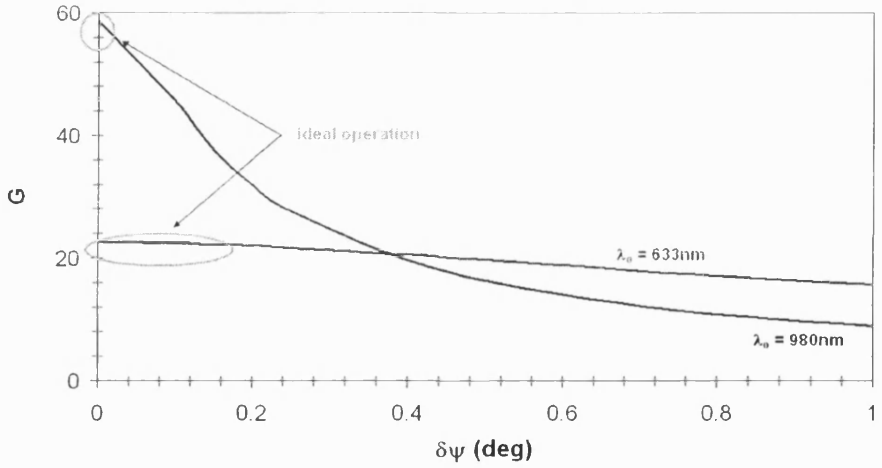

Figure 5.30. Field intensity G as a function of $\delta\psi$ at the Au - air interface of the PWG structure of Figure 5.2a when using a SLD with λ_o = 980nm and $\delta\lambda$ = 15nm and a laser pointer with λ_o = 633nm and $\delta\lambda$ = 1nm .

The results indicate that the SPW excitation is more sensitive to $\delta\psi$ variations as λ_o becomes longer. This is due to the reduced metal losses that lead to a narrower FWHM. As is shown in Figure 5.28, as long as the FWHM from an ideal source ($\delta\psi = 0$, $\delta\lambda = 0$) is larger than $\delta\psi$, then the SPW excitation remains unaffected by any $\delta\psi$ variation and keeps the 'ideal' character. Here 'ideal' condition is defined the situation when there is no parameter variation as $\delta\psi$ increases. For our experiments the allowed $\delta\psi$ for 'ideal' system operation was almost four times larger for the Laser ($\delta\psi \sim 0.2^o$) compared to the

SLD ($\delta\psi \sim 0.05^{\circ}$) in most of the SPW excitation parameters. As a consequence, the $\delta\psi$ tolerance of the optical source is reduced as the FWHM becomes narrower. For $\delta\psi$ beyond the critical values for the two sources, the SPW prism coupler if acting as a sensor will not operate properly and start to lose sensitivity.

The above study shows that it is possible even with non-ideal optical sources to achieve an 'ideal' SPW excitation. Moreover, the small and compact size and the reduced cost of the semiconductor sources can help in producing fully integrated systems with small financial cost.

5.7 Conclusions

This chapter has experimentally demonstrated SPW and 'conventional' wave excitation in prism coupled waveguide arrangements. In addition, 'conventional' excited modes were used to achieve a spatial mode beat effect which has the potential to be used in scattering or sensing measurements.

Finally, optical sources with spectrally broad and divergent output beam such as semiconductor lasers and SLDs have been theoretically and experimentally investigated for replacing the commonly used gas lasers. The results have shown that such optical sources are very strong candidates in order to be employed as the main optical source for SPW excitation. If this is achieved, then compact integrated systems with reduced cost can be obtained.

Chapter 5

[5.1]http://www.schott.com/optics_devices/english/products/flash/abbediagramm_flash.html

[5.2] http://www.cargille.com/refractivestandards.shtml [series B, 1812Y]

[5.3] E. Hecht, "Optics", Addison Wesley, 3rd edition 1998

[5.4] E. Fred Schubert, "Light-Emitting Diodes", Cambridge University Press, 2003.

[5.5] http://rswww.com [product #651-995, 303-674]

[5.6] www.luxpop.com

[5.7] E.D. Palik, "Handbook of optical constants of solids", Academic Press (1985).

[5.8] R. Syms, J. Cozens, "Optical Guided Waves and Devices", McGraw-Hill Book Company, 1992.

[5.9] H. F. Arrand, T. M. Benson, A. Loni, R. Arens-Fischer, M. Kruger, M. Thonissen, H. Luth, S. Kershaw, "Novel Liquid Sensor Based on Porous Silicon Optical Waveguides", IEEE Photonics Technology Letters, vol.10, no.10, October 1998, p.1467.

[5.10] J.Wilson, J.F.B.Hawkes, "Optoelectronics: An Introduction", Prentice-Hall International Series In Optoelectronics, 1983.

[5.11] A.Tarlis, J.Sarma, F.Causa, "Semiconductor Optical Sources for Surface Plasmon Waves", Quantum Electronics and Photonics Conference, (Institute of Physics Photon04), Glasgow Caledonian University, Glasgow, UK, 6-9 September 2004.

[5.12] A.Tarlis, J.Sarma, "Surface Plasmon Wave Detection with Semiconductor Optical Sources", SIOE'05 "Semiconductors and Integrated Optoelectronics Conference", University of Cardiff, Wales, 21-23 March 2005.

[5.13] A.Tarlis, J.Sarma, F.Causa, "Transmission Line Circuit Representation of Surface Plasmon Waves", International Conference on Nano-Material Synthesis and Integration for Sensors, Electronics, Photonics and Electro-Optics, SPIE OpticsEast 2006, Boston, USA, (Invited Oral Presentation).

[5.14] H.E. de Brujin, R.P.H. Kooyman, J. Greve, "Determination of dielectric permittivity and thickness of a metal layer from a surface plasmon resonance experiment", Applied Optics, vol.29, no.13, 1 May, 1990, p.1974.

Chapter 6

Optically active SPWs

It has been mentioned in chapter 3 that the high metal losses in a SPW structure, do not allow SPWs to exhibit subwavelength and lossless propagation properties. This chapter however, will show that the use of optically active media can compensate for the detrimental effect of the metal losses and significantly improve the SPW modal characteristics. As a consequence, the effect of such media will be studied for the SPW modes supported in the guides of chapter 3 and some of the prism coupled structures of chapter 4.

6.1 Improving SPWs modal parameters

As shown in chapter 3, the high metal losses prevent SPW lossless propagation ($\beta_I \rightarrow 0$) and subwavelength operation ($\beta_R \rightarrow \infty$, very short decay depth Δ and effective wavelength λ_{eff}). To reduce β_I, eqn.(3.13), different approaches have been reported such as:

a) the use of low refractive index media [6.1]
b) SPW excitation at long wavelengths [6.2]
c) multilayer SPW structures [6.2]
d) use of optically active media [6.3-5].

Among the four suggestions, (c) and (d) are the most promising since there are no many materials with very low refractive index and long wavelength SPW operation causes the field to spread a lot (i.e. large Δ), Figure 3.6. Although multilayer structures can significantly reduce the SPW modal losses as shown in sections 3.4.1-2, cannot however totally eliminate them. Optically active media however, have the potential to compensate for the metal losses and reduce the SPW modal losses.

In addition to the $\beta_I \rightarrow 0$ requirement, if a high β_R is desired, it is necessary to have $|\varepsilon_{mR}| \approx \varepsilon_{1R}$, eqn.(3.18), or reduce the thickness of the metal (M) or dielectric (D) film in a DMD or MDM configuration, respectively Figures 3.9-10 and 3.13-14. The problem however that now arises is that a high β_I is obtained under both procedures, which in some cases is $\beta_I \approx \beta_R$, eqn.(3.27-28). This difficulty can be overcome by introducing into the SPW structure an optically active dielectric medium with optical gain $g > 0$.

6.2 Single interface optically active SPW structure

Consider the single interface SPW structure of Figure 3.1, where the dielectric medium ($x > 0$) is now optically active with optical gain $g > 0$ and relative permittivity

$$\varepsilon_D = \varepsilon_1 + j\varepsilon_g \approx \varepsilon_1 + j\left(\sqrt{\varepsilon_1}/k_o\right)g \tag{6.1}$$

where $\varepsilon_1 >> \varepsilon_g > 0$, [Appendix H.1]. As a consequence, the SPW longitudinal propagation constant β, eqn.(3.8), is complex $\beta = \beta_R - j\beta_I$, where it is derived that, [Appendix H.2],

$$\beta_R \approx k_o \frac{\sqrt{2}}{2} \frac{\left[\varepsilon_1 \varepsilon_{mR}^2 - |\varepsilon_{mR}|\varepsilon_1^2 + \sqrt{\left(\varepsilon_1 \varepsilon_{mR}^2 - |\varepsilon_{mR}|\varepsilon_1^2\right)^2 + \left(|\varepsilon_{mI}|\varepsilon_1^2 - \varepsilon_g \varepsilon_{mR}^2\right)^2}\right]^{1/2}}{\left[\left(|\varepsilon_{mR}| - \varepsilon_1\right)^2 + \left(|\varepsilon_{mI}| - \varepsilon_g\right)^2\right]^{1/2}} \tag{6.2}$$

$$\beta_I \approx \frac{|\varepsilon_{mI}|\varepsilon_1^2 - \varepsilon_g \varepsilon_{mR}^2}{\beta_R} \tag{6.3}$$

Equation (6.3) clearly shows that lossless SPW propagation with $\beta_I \rightarrow 0$ can be realized for an amount of gain

$$g_o = k_o \frac{\varepsilon_1^{3/2}}{\varepsilon_{mR}^2} |\varepsilon_{mI}| \tag{6.4}$$

Hence, eqn.(6.4) indicates that if $g < g_o$ then $\beta_I > 0$, and the SPW remains lossy, unlike the case where $g > g_o$, which describes an exponential growing wave in the longitudinal. The physical interpretation of the $g > g_o$ condition is that the optical gain has overcompensated for the metal losses of the structure, hence resulting in an optical wave amplification [6.3].

If a low g_o is a desired design criterion for a structure, then it is proposed to use a low ε_1 or operate at long wavelengths where the metal losses are less ($|\varepsilon_{mR}| >> |\varepsilon_{mI}|$). For the single dielectric – metal interface structure of our study, g_o as a function of the wavelength λ_o for typical metals when $\epsilon_1 = 1$, is given in Figure 6.1.

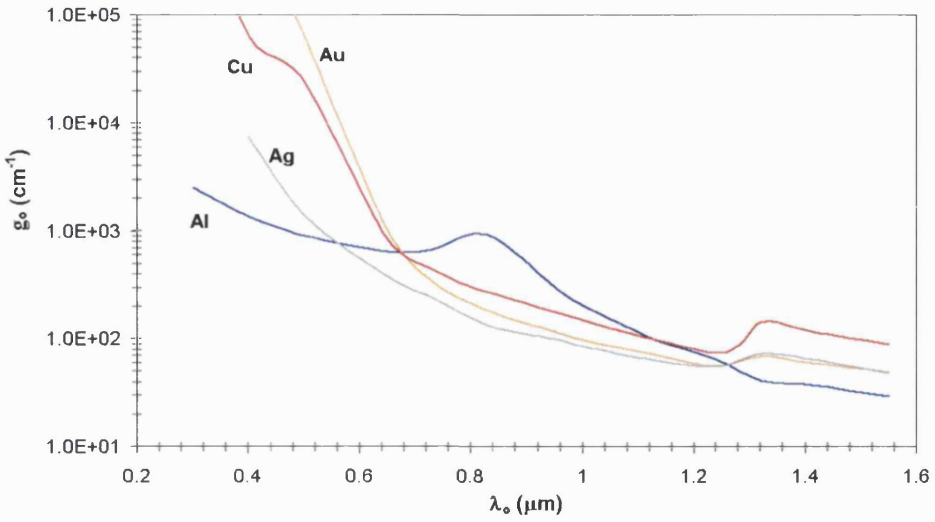

Figure 6.1. Variation of g_o as a function of λ_o for different metals; g_o is in a logarithmic scale.

Hence, Ag yields the lowest g_o for $\lambda_o > 0.6\mu m$ followed by Au, Cu and Al, whereas Al is the most suitable candidate for a low g_o when $\lambda_o < 0.6\mu m$. Note that although Al for $\lambda_o > 1.3\mu m$ exhibits the lowest g_o, however it is not recommended when it is used in prism coupled arrangements as it gives a very broad FWHM for $|\Gamma|^2$ when SPW excitation takes place. Media that can satisfy the above g_o requirements are semiconductor quantum wells (Gallium Arsenide (GaAs), Gallium Nitride (GaN)) with gain $g \approx 3 \times 10^4$ cm^{-1}, arrays of quantum dots with $g \approx 7 \times 10^4$ cm^{-1} or low molar mass dyes (thiphrene-based oligomeres) with $g \approx 2.2 \times 10^3$ cm^{-1}, [6.3].

Equation (6.2) also indicates that a high β_R can be achieved for almost the same amount of g_o, but only when $|\varepsilon_{mR}| \approx \varepsilon_1$ and $|\varepsilon_{mI}| \approx \varepsilon_g$ are satisfied simultaneously which happens at frequencies $\omega \approx \omega_p / \sqrt{\varepsilon_1 + 1}$.

From a practical point of view, both SPW subwavelength and lossless propagation operation can be achieved only in the UV wavelength region, as there are materials

which allow $|\varepsilon_{mR}| \approx \varepsilon_1$ and $\varepsilon_g \approx |\varepsilon_{mI}|$. In the visible or IR spectrum regime where $|\varepsilon_{mR}| >> \varepsilon_1$, only lossless propagation is realised.

The use of optical gain in single and multiple dielectric – metal interface SPW structures for improving the SPW modal properties in both the UV and the IR wavelength regimes will be the scope of the study in the following sections (6.2.1-6.4).

6.2.1 SPW operation in the UV region

With reference to the single optically active dielectric – metal interface described in section 6.2, consider the dielectric to be GaN with $\varepsilon_1 = 5.76$ [6.6] and the metal Ag with $\varepsilon_m = -5.78 - j0.75$ operating at λ_o = 440nm [6.7]. The SPW modal properties of the structure are then given in Figure 6.2 where β_R, eqn.(6.2), and β_I, eqn.(6.3), are studied as a function of the optical gain g.

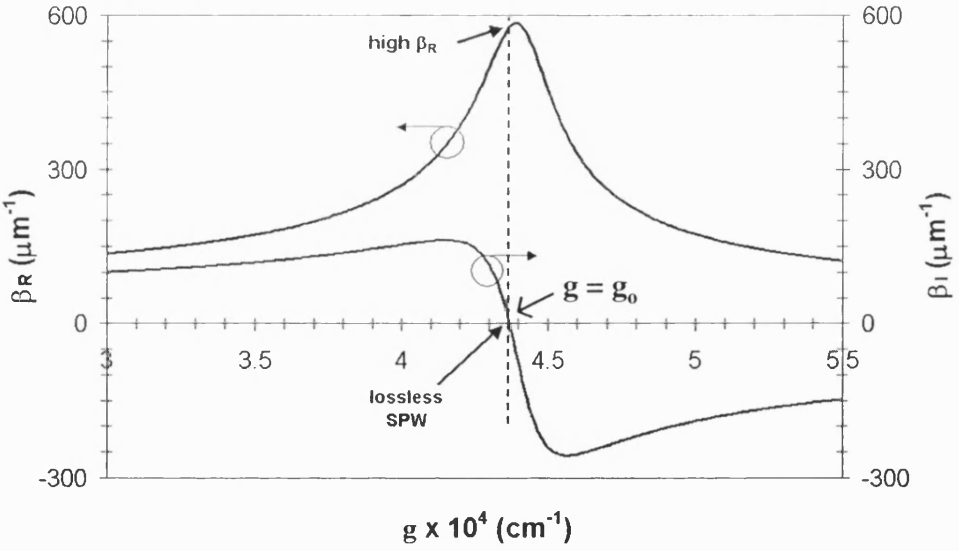

Figure 6.2. Effect of g on single interface SPW β_R and β_I for ε_1 = 5.76, ε_m = - 5.78 - j 0.75 and λ_o = 440nm.

If g = 0, then the SPW supported by the structure has $\beta_R \approx 71\mu m^{-1}$, $\beta_I \approx 57\mu m^{-1}$ which give L_z = 8nm, eqn.(3.31), $\lambda_{eff} = 47nm$, eqn.(3.24), $\Delta_1 = 15nm$, eqn.(3.20), and $U_p = 0.2 \times c$, eqn.(3.21).

When $g = g_o = 4.4 \times 10^4\ cm^{-1}$, eqn.(6.4), SPW lossless propagation and subwavelength conditions are obtained with $\beta_R \approx 595\mu m^{-1}$, $\beta_I \approx 0$, $\lambda_{eff} = 10\,nm$, eqn.(3.24), $\Delta_I \approx 1.7\,nm$, eqn.(3.20), and $U_p = 0.024 \times c$, eqn.(3.21).

For $g > g_o$ the optical gain overcompensates for the metal losses of the structure producing a longitudinally propagating and exponentially growing SPW along the positive z axis.

Hence it is clear from the above results that the use of gain can significantly increase β_R and provide the desired lossless propagation i.e. $\beta_I \approx 0$. SPW structures with such properties can be employed to improve the diffraction limited resolution given by (λ_{eff} / 2), in surface plasmon microscopy applications [6.8] or involved in the design of nanoscale photonic circuits [6.9-10].

6.2.2 SPW operation in the IR region

Let now that the optically active SPW structure of section 6.2.1 operates in the IR wavelength region and in particular at λ_o = 980nm. In that case GaN can be replaced by GaAs which has ε_1 = 12.25 [6.7], whereas the metal can still be Ag with $\varepsilon_m = -41.3 - j2.54$ [6.7], giving for g = 0: $\beta_R \approx 26.7\mu m^{-1}$, eqn.(6.2), $\beta_I \approx 0.35\mu m^{-1}$, eqn.(6.3), and $\lambda_{eff} \approx$ 235nm, eqn.(3.24), $U_p \approx$ 0.24 x c, eqn.(3.21), and $L_z \approx 1.45\mu m$, eqn.(3.31). Since at this frequency regime $\varepsilon_1 << |\varepsilon_{mR}|$, only SPW lossless propagation can be achieved and not subwavelength operation. Hence, β_R, eqn.(6.2), is constant for any g whereas β_I is strongly affected by g as discussed in section 6.2 and shown in Figure 6.3 for this example.

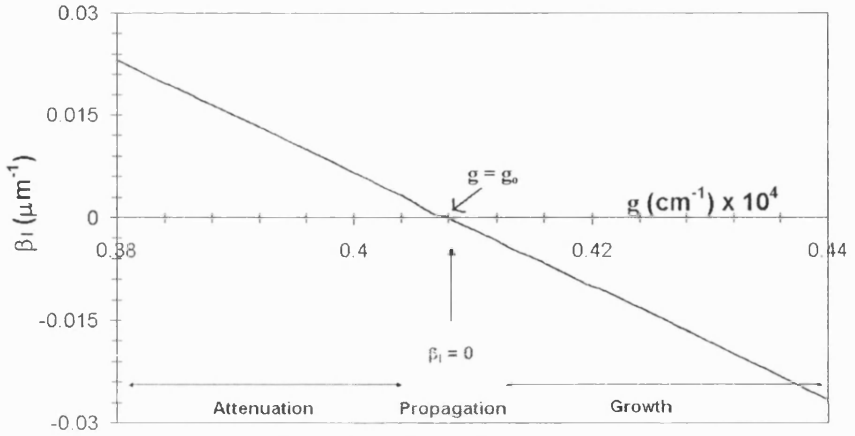

Figure 6.3. Effect of g on β_I for a single interface SPW in IR region for ε_I = 12.25, ε_m = - 41.3 - j 2.54 and λ_o = 980nm.

Unlike SPW operation in the UV region, section 6.2.1, where $g_o \approx 4.5 \times 10^4$ cm^{-1}, at λ_o = 980nm the required g_o for lossless propagation has now been reduced to 4100 cm^{-1} as a consequence of the smaller metal losses at longer wavelengths. Such optically active SPW structures have the potential to be used as components for optical circuits or long length interaction sensors.

6.3 Gain in multilayer SPW structures

The study so far in this chapter has been focused into the analysis of a single optically active dielectric – metal interface capable of supporting SPWs. For practical applications however, multiple such interfaces are more desirable for the reasons discussed in section 3.4. In this section the SPW modal properties in a MDM waveguide configuration will be studied assuming the dielectric (D) to be optically active. Examples of this study will be given for SPW excitation in the UV and IR frequency spectrum, by using the materials and parameters employed in the corresponding analysis for the single interface SPW, sections 6.2.1-2, unless otherwise explicitly indicated. The MDM waveguide configuration that is employed in the examples is that analysed in sections 3.4.2 and has been preferred over the DMD arrangement as it is closer to a heterojunction structure typically used in semiconductor optical sources such as Lasers and SLDs where the central dielectric film plays the role of the optically active medium [6.11].

The MDM configuration as described in section 3.4.2, can support a symmetric SPW and an antisymmetric with low cut-off thickness when $|\varepsilon_{mR}| > \varepsilon_1$, Figure 3.13. If $|\varepsilon_{mR}| \leq \varepsilon_1$ then only one antisymmetric SPW with an upper cut-off thickness is sustained in the structure and no symmetric mode is supported - Figure 3.14. Since the SPW modal losses in a MDM structure with $|\varepsilon_{mR}| < \varepsilon_1$ are very high and there are no easily available materials to satisfy the $|\varepsilon_{mR}| < \varepsilon_1$ condition, hence the analysis here will assume only that $|\varepsilon_{mR}| > \varepsilon_1$. Note that although there are also 'conventional' modes in the MDM structure, the study will only concentrate on the SPWs.

6.3.1 UV spectrum regime

By considering the optically active MDM structure to operate in the UV region, the corresponding β_R and β_I of the two SPW modes are studied as a function of g when the dielectric film (D) has thickness h = 10, 40 and 60nm. The results of this analysis are presented in Figure 6.4 for $\varepsilon_1 = 5.76$ and $\varepsilon_m = -5.78 - j\,0.75$ when $\lambda_o = 440$nm.

As h increases, the SPW modal losses for both the symmetric and the antisymmetric SPW are reduced leading to smaller amounts of optical gain needed to compensate for the metal losses effect in the structure. Note that for h = 10nm only the symmetric SPW is sustained in the structure as the antisymmetric yields a cut-off. Because of the parameters of the structure, the cut-off thickness of the antisymmetric SPW and the thickness at which that mode becomes degenerate with the symmetric SPW are very close to each other. When both SPWs become degenerate (h = 60nm), then the optimum amount of gain is the same as that obtained for the single interface structure i.e. $g_o \approx 4.2 \times 10^4$ cm^{-1}, Figure 6.2.

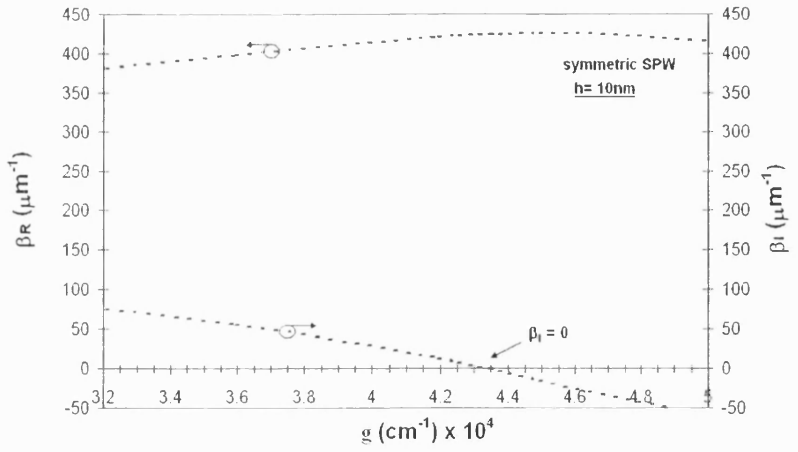

(a)

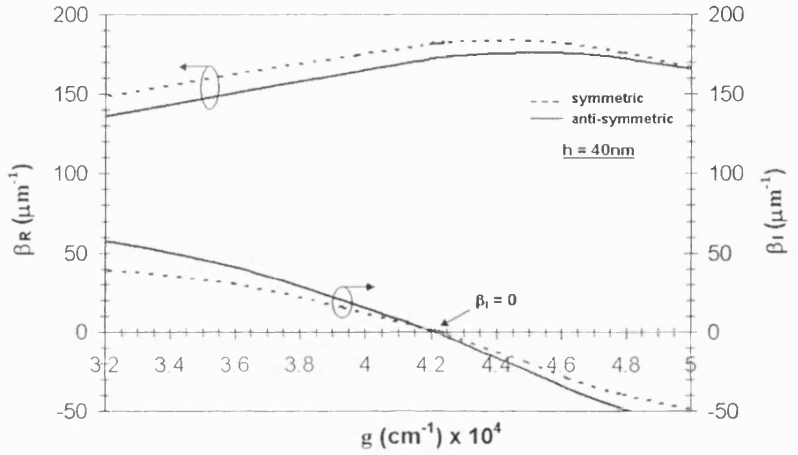

(b)

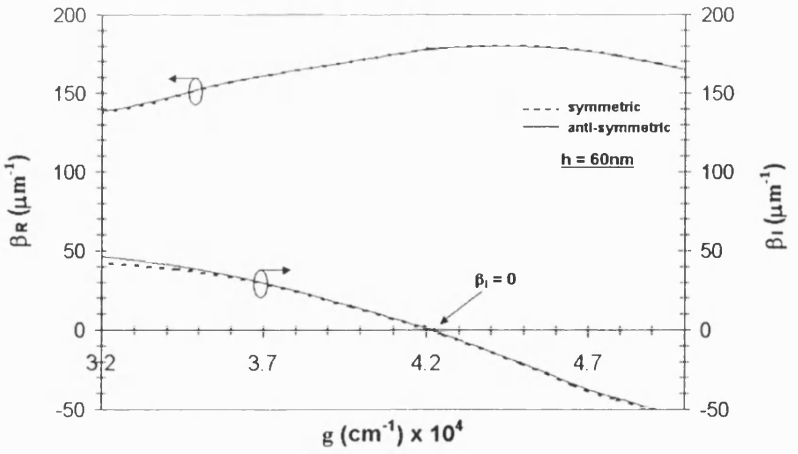

(c)

Figure 6.4. Effect of g on β_R and β_I for a symmetric (dashed line) and antisymmetric (solid line) SPW in a MDM structure at the UV regime for $\varepsilon_I = 5.76$, $\varepsilon_m = -5.78 - j\,0.75$ and $\lambda_o = 440$nm when the dielectric film thickness h is a) 10, b) 40 and c) 60nm.

6.3.2 IR spectrum regime

If the MDM structure operates in the IR wavelength regime, only β_I of the two SPWs is affected by the optical gain whereas β_R remains unaltered for the different amounts of g. Figure 6.5 presents the variation for the symmetric and antisymmetric β_I as a function of g, when h = 150 and 300nm, for $\varepsilon_l = 12.25$, $\varepsilon_m = -41.3 - j\,2.54$ and $\lambda_o = 980$nm.

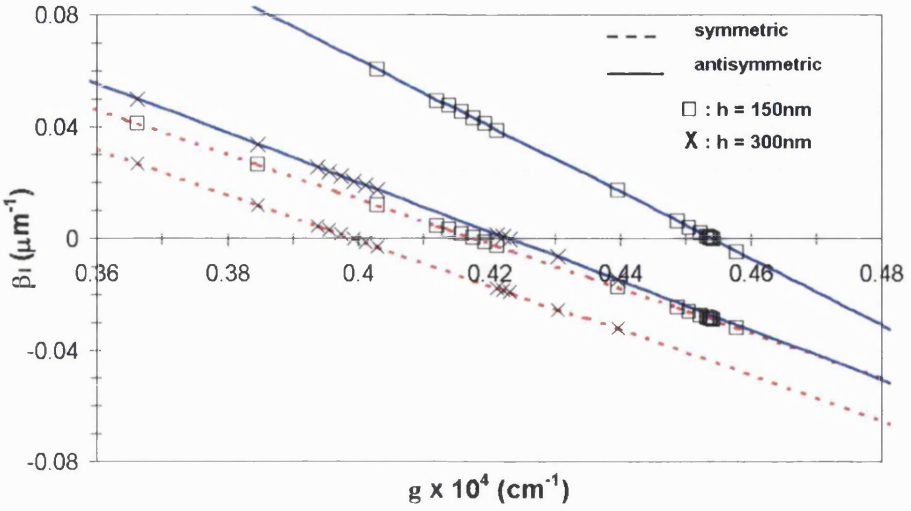

Figure 6.5. Effect of g on β_I for symmetric (dashed line) and antisymmetric (solid line) SPW in a MDM structure at IR spectrum region for $\varepsilon_l = 12.25$, $\varepsilon_m = -41.3 - j\,2.54$ and $\lambda_o = 980$nm when the dielectric film thickness h is 150 (squares) and 300nm (crosses).

The results show now that the requirement of gain for lossless SPW propagation has been almost one order of magnitude less compared to the UV example, Figure 6.4, due to the reduced metal losses. In addition the dielectric film tuning provides the potential for even smaller amounts of gain to compensate for the detrimental effect of the metal losses.

The numerical examples given in Figures 6.4 and 6.5 indicate that if lossless SPW propagation is the main design criterion of the waveguide structure, then it is better to work in the IR wavelength region using the symmetric SPW, as the required amounts of g_o are significantly less compared to the corresponding UV case. If subwavelength operation however is also necessary, then the UV regime is preferred because it allows both high β_R and $\beta_I \rightarrow 0$ conditions to be satisfied simultaneously, but unfortunately at the expense of a large g_o.

Note also that the use of multiple dielectric – metal interface structures such as the MDM configuration have the flexibility to control the required amount of gains for SPW lossless or subwavelength operation by adjusting the thickness of the dielectric film (D) or operating in different wavelength.

6.4 SPW excitation in optically active prism coupled configurations

As was theoretically discussed in chapter 4 and experimentally demonstrated in chapter 5, one method to excite SPWs is by employing a prism coupler. If however the SPW waveguide structure includes optical gain, the prism coupling technique does not allow all of the SPW modal properties to benefit by the gain features. The theoretical analysis of the prism coupled excitation as given in chapter 4 considers unattenuated longitudinal (z – directed) propagation, thus $\beta = \beta_R$, eqn.(4.2). As a consequence, the maximum β_R in a prism coupled waveguide structure is given by eqn.(4.2) when $\theta_i = 90^\circ$, i.e.,

$$\beta = \beta_R = k_o \sqrt{\varepsilon_p} \tag{6.5}$$

where ε_p is the relative permittivity of the prism. Hence, it is clearly shown from eqn.(6.5) that β_R is limited by the prism material characteristics, and therefore very short effective wavelength λ_{eff}, eqn.(3.24), and low phase velocity U_p, eqn.(3.21), are not possible. Table 6.1 shows some prism materials that are available in the market in different wavelength regimes along with the corresponding values for β_R, λ_{eff} and U_p.

λ_o (μm)	material	ε_p	max β_R (μm^{-1})	λ_{eff} (μm)	U_p
0.44	GaN	6.25 [**6.6**]	36	0.175	0.4 x c
0.63	SLFN9	3.25 [**6.12**]	18	0.35	0.55 x c
1.5	Si	14.4 [**6.13**]	16	0.392	0.26 x c
4	Ge	16 [**6.13**]	6.3	1	0.25 x c

Table 6.1. Prism materials in different wavelength regimes and corresponding values for β_R, λ_{eff} and U_p. $c \approx 3 \times 10^8$ m/s is the speed of light in free space.

If instead of a prism coupler, a grating is employed for SPW excitation, β is then given as, [6.14]:

$$\beta = \beta_R + m\frac{2\pi}{\Lambda} \tag{6.6}$$

where Λ denotes the pitch of the grating, m is an integer number corresponding to the order of the diffracted wave (m = 0, ± 1, ± 2, ± 3, etc.) and β_R is described by eqn.(4.2). Hence, eqn.(6.6) shows that a high β is possible if a proper combination of m, Λ and β_R is chosen. Avrutski et al. [6.3] have theoretically shown that the use of a diffraction grating for SPW excitation in a structure with an optically active medium can provide both subwavelength and lossless propagation SPW conditions. In addition, the reflected signal of the structure was greater than unity as a result of optical amplification when the gain overcompensated for the metal losses.

Although the use of the grating allows SPW subwavelength and lossless propagation operation, the prism coupler still remains more attractive and simple from a fabrication point of view. In addition, the effect of g on the SPW modal properties can still be realized through the reflected signal of the prism coupled arrangement.

Recently, an attempt to experimentally demonstrate the gain effect on SPW modal properties was made by employing a typical K-R prism coupled structure where the substrate dielectric was optically active [6.15], Figure 6.6.

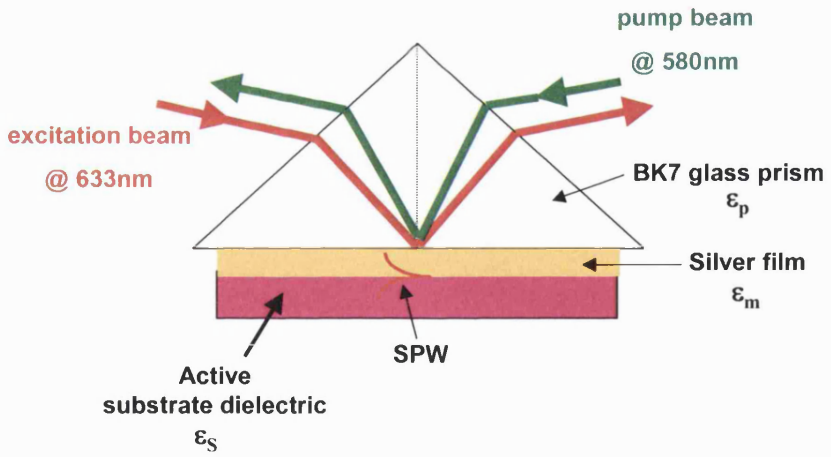

Figure 6.6. Experimental apparatus used in [6.15] for SPW excitation in an optically active prism coupled structure.

The optically active dielectric substrate was a dye solution with relative permittivity $\varepsilon_s \approx 1.85$, externally optically pumped at λ_o = 580nm to produce gain of the order of 66 x 10^{-2} cm^{-1}. SPW excitation was performed from a different optical source at wavelength λ_o = 633nm. Any gain effects on the SPW modal properties were to be

observed by examining the properties of the reflected signal from the excitation beam. The outcome of this attempt however was not so successful, as the produced optical gain from the dye was not sufficient enough to affect the SPW properties.

A different approach to the use of optical dyes for producing optical gain is to employ semiconductor structures as those utilized for providing gain for semiconductor optical sources such as Lasers and SLDs. Hence, in the following sections (6.4.1 and 6.4.2) a prism coupled SPW structure with an optically active semiconductor is proposed and theoretically analysed. Since the suggested prism coupled structure is based on the typical K-R arrangement, hence the analysis will be performed initially for such an arrangement where now the substrate dielectric is considered to be optically active, Figure 6.7a. The study will then be extended into the final configuration which can be used as a potential sensor, Figure 6.7b.

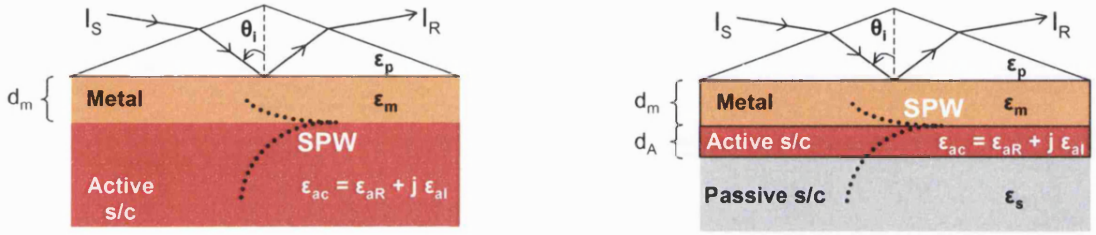

(a) (b)

Figure 6.7. a) optically active K-R prism coupled structure, b) proposed four layer optically active K-R prism coupled arrangement.

6.4.1 SPW excitation in optically active K-R structure

With reference to Figure 6.7a, consider the prism to have a real relative permittivity $\varepsilon_p > 0$ and the metal film of thickness d_m a complex one with $\varepsilon_m = -|\varepsilon_{mR}| - j|\varepsilon_{mI}|$. The substrate dielectric is assumed to be an optically active semiconductor medium with optical gain $g > 0$ and complex relative permittivity

$$\varepsilon_{ac} = \varepsilon_{aR} + j\varepsilon_{aI} = \varepsilon_{aR} + j\frac{\sqrt{\varepsilon_{aR}}}{k_o}g \qquad (6.7)$$

where $\varepsilon_p > \varepsilon_{aR} >> \varepsilon_{aI} > 0$. To model the intensity of the reflected signal I_R and therefore study the effects of the optical gain on SPW properties, the optically active K-R arrangement is represented and analysed as a T-L network where $|\Gamma|^2$, eqn.(4.13), and $|T|^2$, eqn.(4.14), of the structure are examined . Hence, with reference to Figure 4.2,

where now n = 3, $\varepsilon_1 = \varepsilon_p$, $\varepsilon_2 = \varepsilon_m$, $\varepsilon_3 = \varepsilon_{ac}$, $d_1 = d_m$, $\varphi_1 = \varphi_m$, $Z_{0x(1)} = Z_p$, $Z_{0x(2)} = Z_m$ and $Z_{0x(3)} = Z_{ac}$. If the optically active dielectric substrate is a GaAs semiconductor with $\varepsilon_{ar} = 12.25$, the metal film is Ag with $d_m = 38$nm and $\varepsilon_m = -41.3 - j\,2.54$, and $\varepsilon_p = 20.25$ at $\lambda_o = 980$nm, hence results of $|\Gamma|^2$, eqn.(4.13), and $|T|^2$, eqn.(4.14), as a function of the incident angle θ_i for different values of gain are presented in Figures 6.8 and 6.9 respectively. The large value of ε_p is needed if prism excitation of SPW is used. However, grating excitation is an alternative method that eliminates this constraint.

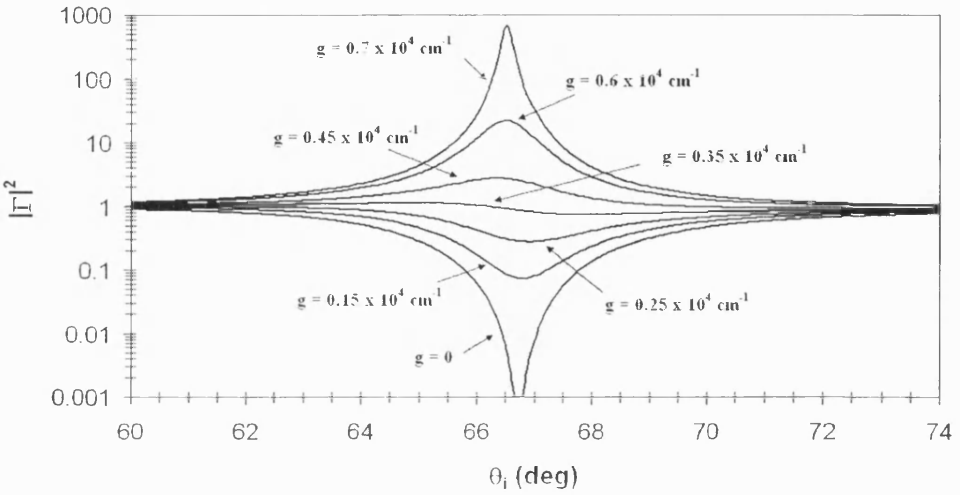

Figure 6.8. Angular variation of $|\Gamma|^2$ for different values of g, for the optically active K-R prism coupled arrangement of Figure 6.7a which used for SPW excitation, where $\varepsilon_{aR} = 12.25$, $d_m = 38$nm, $\varepsilon_m = -41.3 - j\,2.54$, $\varepsilon_p = 20.25$ and $\lambda_o = 980$nm. Note that $|\Gamma|^2$ is given in logarithmic scale.

If g = 0, then the semiconductor medium is passive and $|\Gamma|^2$, eqn.(4.13), indicates typical SPW excitation at $\theta_{spw} = 67^o$, eqn.(4.25). As however g increases, the 'dip' in $|\Gamma|^2$ becomes shallower while the corresponding FWHM is reduced. Moreover when $g > 0.35 \times 10^4$ cm^{-1}, $|\Gamma|^2$ exceeds unity which indicates that the metal losses have been counterbalanced by the optical gain and optical amplification is taking place.

Similarly to the $|\Gamma|^2$ variation, for an increasing g it is found that $|T|^2$ becomes a few orders of magnitude larger compared to the g = 0 case, as it is shown in Figure 6.9.

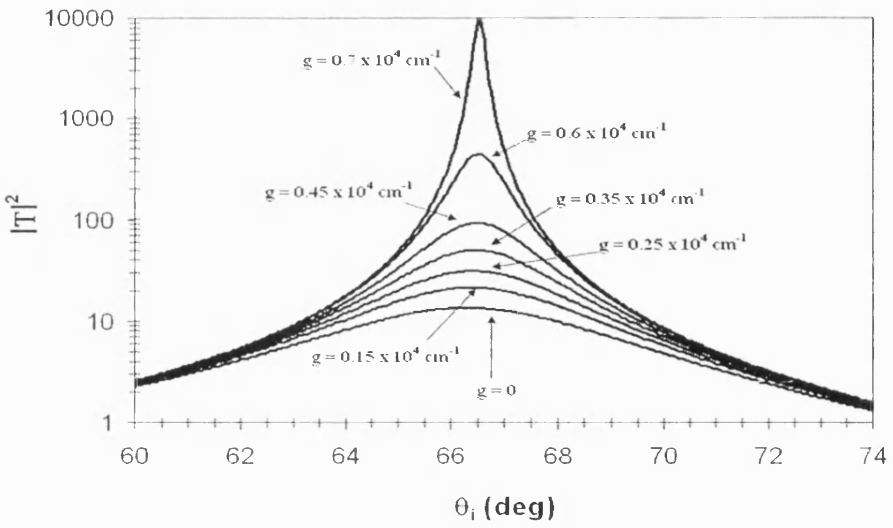

Figure 6.9. Effect of g on $|T|^2$ of the optically active K-R prism coupled arrangement of Figure 6.7a used for SPW excitation where ε_{aR} = 12.25, d_m = 38nm, ε_m = - 41.3 – j 2.54, ε_p = 20.25 and λ_o = 980nm. Note that $|T|^2$ axis is in logarithmic scale.

By adjusting the metal thickness d_m for the different values of g, it is possible to optimize the 'dip' in $|\Gamma|^2$ and obtain some interesting results as it is shown in Figure 6.10a.

The results for $|\Gamma|^2$ and $|T|^2$ in Figure 6.10 have similar behaviour with those obtained in Figure 4.14, where $\varepsilon_{mI} \rightarrow 0$. Hence, for a specific combination of g and d_m, the effect of the metal losses in SPW excitation can be significantly reduced producing a very narrow FWHM and a high SPW field intensity at the metal – semiconductor substrate compared to the g = 0 case. As a consequence, if the system is to be used as a sensor then a high sensitivity resolution is realised. Note that the shift observed at θ_{spw} in Figures 6.8-10 for the different g cases, is a consequence of the fact that θ_{spw} is a function of ε_{aI} which is proportional to g, eqn.(6.7).

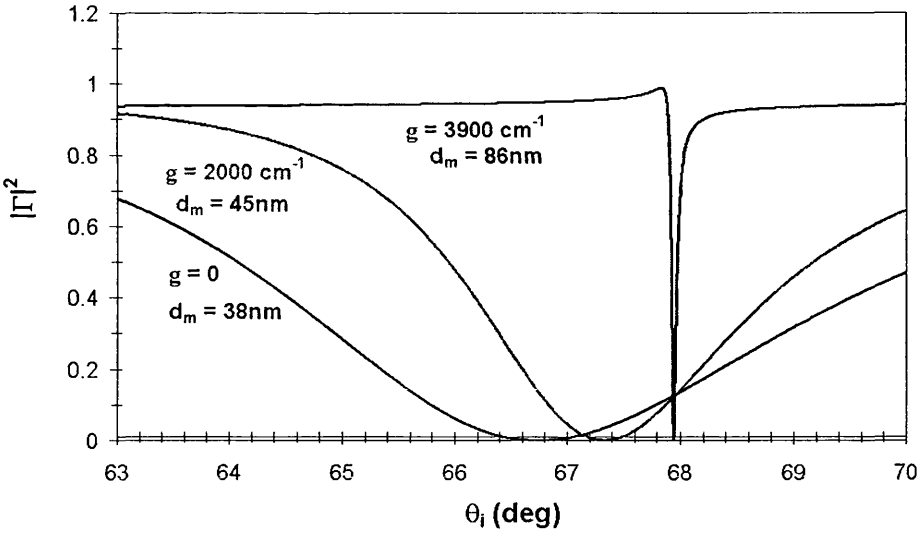

(a)

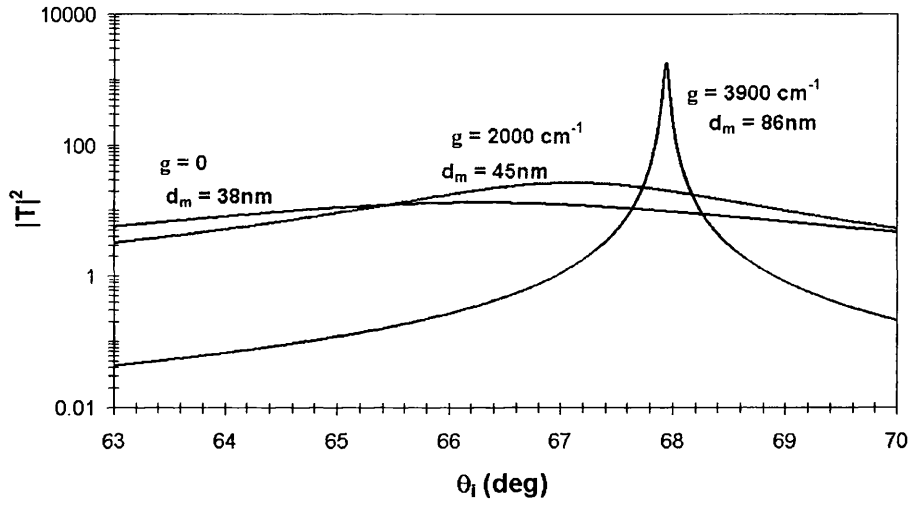

(b)

Figure 6.10. Optimum $|\Gamma|^2$, (a), and $|T|^2$, (b), of SPW excitation with different values of g in the optically active K-R prism coupled structure of Figure 6.7a where ε_{aR} = 12.25, ε_m = - 41.3 – j 2.54, ε_p = 20.25 and λ_o = 980nm. Note that $|T|^2$ axis is in logarithmic scale.

6.4.2 SPW excitation in an optically active four - layer K-R structure

In practice the optically active K-R arrangement described in section 6.5.1 cannot be used for many applications and especially for sensing purposes. This constraint is because the optically active semiconductor medium is semi-infinite hence not allowing any sample to be placed close to it and therefore probed by the SPW field.

To overcome this difficulty, the active semiconductor is considered to have a finite thickness d_A, and is now followed by a passive dielectric medium with real relative permittivity $\epsilon_s > 0$, Figure 6.7b. The metal – (active dielectric) – (passive dielectric) structure, can be thought of as a typical heterojunction configuration (e.g. passive s/c – active s/c – passive s/c) commonly used in semiconductor optical sources, where the passive dielectric can be GaAlAs and the active GaAs. The only difference is that now one of the passive s/c has been replaced by the metal. Hence, the use of the prism coupled arrangement provides SPW excitation at the metal – active dielectric interface. Because the optically active film is thin compared to the metal film and the semi-infinite passive dielectric, hence the SPW field extends inside the semi-infinite passive dielectric without any significant perturbation as it is shown in Figure 6.11.

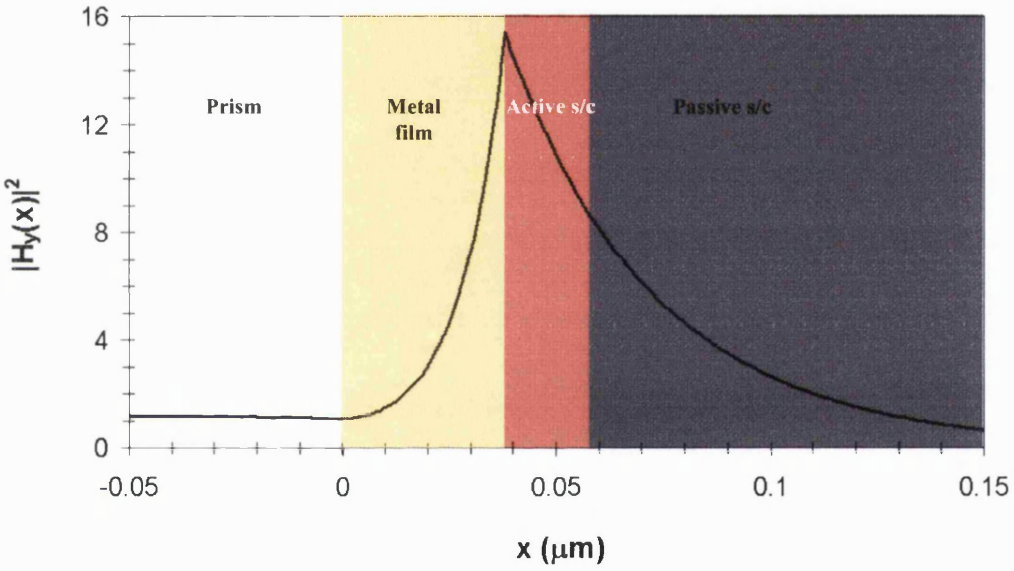

Figure 6.11. $|H_y(x)|^2$ field distribution when SPW has been excited at the metal – active s/c interface of the prism coupled structure of Figure 6.7b for the given parameters.

The properties of $|\Gamma|^2$, eqn.(4.13), and $|T|^2$, eqn.(4.14), of the structure can then be studied by analyzing the prism coupled waveguide structure of Figure 6.7b as a 4 – section T-L network. Hence, with reference to Figure 4.2, for n = 4, let $\epsilon_1 = \epsilon_p$, $\epsilon_2 = \epsilon_m$, $\epsilon_3 = \epsilon_{ac}$, $\epsilon_4 = \epsilon_s$, $d_1 = d_m$, $d_2 = d_A$, $\varphi_2 = \varphi_m$, $\varphi_3 = \varphi_{ac}$, $Z_{0x(1)} = Z_p$, $Z_{0x(2)} = Z_m$, $Z_{0x(3)} = Z_{ac}$ and $Z_{0x(4)} = Z_s$. Results of a numerical example where $|\Gamma|^2$ and $|T|^2$ of the prism coupled arrangement are studied as a function of the incident angle θ_i for different values of g are presented in Figures 6.12-13 for $\varepsilon_p = 20.25$, $\varepsilon_m = -41.3 - j\ 2.54$, $\varepsilon_{aR} = 12.25$, $\varepsilon_s = 11.22$, $d_m = 38$nm and $d_A = 20$nm at $\lambda_o = 980$nm.

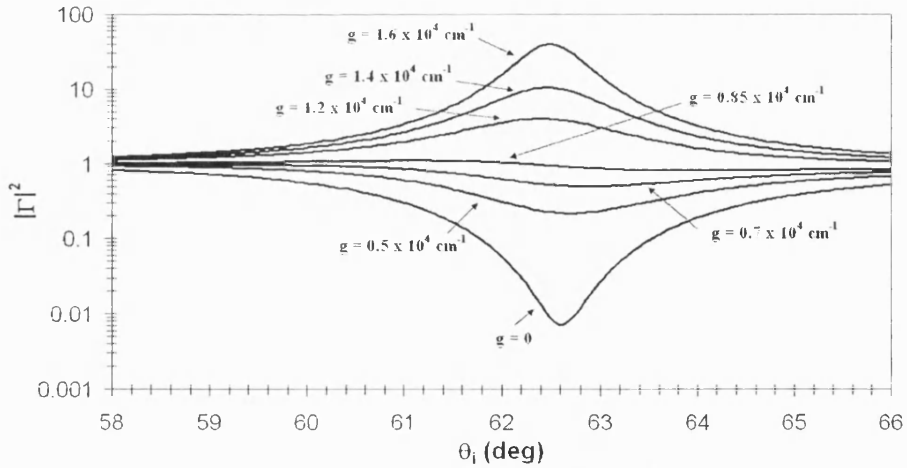

Figure 6.12. Angular variation of $|\Gamma|^2$ for different values of g, for the four layer optically active K-R prism coupled arrangement of Figure 6.7b used for SPW excitation with ε_{aR} = 12.25, d_m = 38nm, ε_m = - 41.3 – j 2.54, ε_p = 20.25, d_A = 20nm, ε_S = 11.22 and λ_o = 980nm. Note that $|\Gamma|^2$ axis is in logarithmic scale.

The results here are similar to those calculated in Figure 6.8. Hence, SPW excitation for g = 0 is observed at $\theta_i = 67.5^o$ where $|\Gamma|^2 \approx 0$, Figure 6.12. As the optical gain is increased then the FWHM of the 'dip' of $|\Gamma|^2$ becomes narrower, and $|\Gamma|^2$ exceeds unity when g > 0.8 x 10^4 cm^{-1}, where the optical gain has overcompensated for the metal losses. The SPW field intensity at the optically active – optically passive dielectric interface also increases as g increases, Figure 6.13.

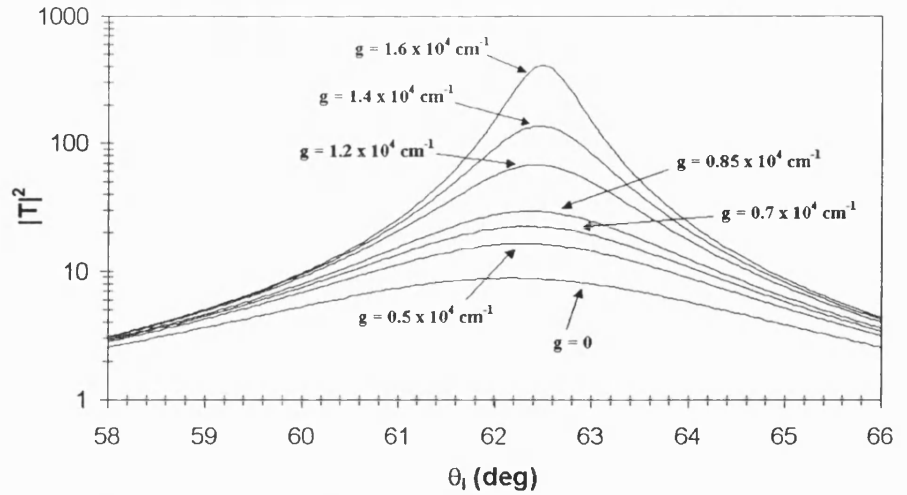

Figure 6.13. Angular variation of $|\Gamma|^2$ for different values of g, for the four layer optically active K-R prism coupled arrangement of Figure 6.7b used for SPW excitation with ε_{aR} = 12.25, d_m = 38nm, ε_m = - 41.3 – j 2.54, ε_p = 20.25, d_A = 20nm, ε_S = 11.22 and λ_o = 980nm. Note that $|T|^2$ axis is in logarithmic scale.

Note however that the corresponding $|T|^2$ of the K-R arrangement of Figure 6.7a is much higher compared to the intensity presented in Figure 6.13 for the same amount of g. This result is because the field intensity in the four layer structure, Figure 6.7b, is maximum at the metal – active dielectric interface, whereas $|T|^2$ has been evaluated for the active – passive dielectric interface where the intensity has been reduced by the factor $\exp[-2\, k_{xA} d_A]$. Note that the passive dielectric medium can serve as the probing area of sensing, hence the evaluation of $|T|^2$.

By tuning the metal film thickness d_m to achieve optimum SPW excitation for the different values of g, a significantly narrow FWHM of $|\Gamma|^2$ and enhanced $|T|^2$ can be obtained, Figure 6.14.

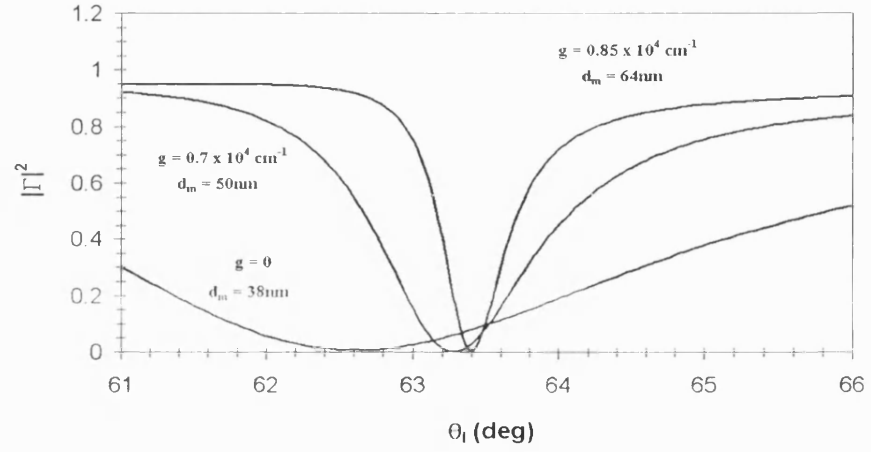

(a)

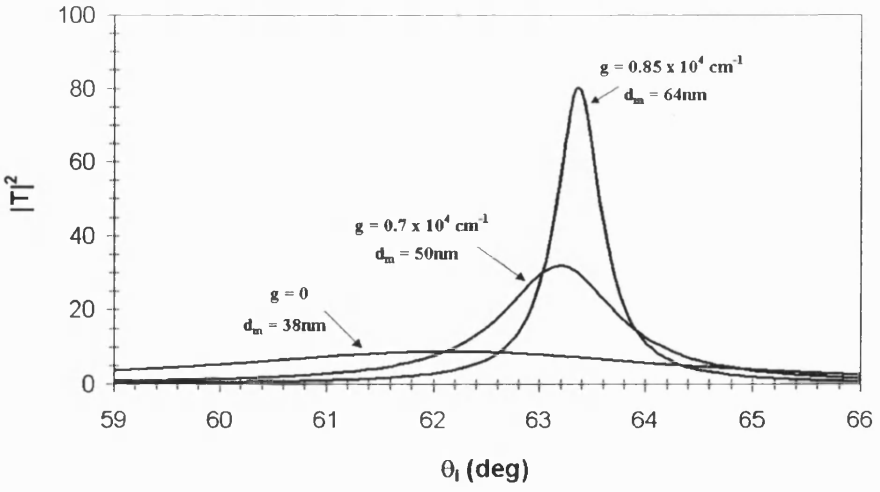

(b)

Figure 6.14. Optimum $|\Gamma|^2$, (a), and $|T|^2$, (b), of SPW excitation with different values of g in the optically active K-R prism coupled structure of Figure 6.7b with ε_{aR} = 12.25, ε_m = - 41.3 – j 2.54, ε_p = 20.25, ε_S = 11.22 and λ_o = 980nm.

Thus, the prism coupled SPW arrangement becomes more sensitive and high field intensity can be potentially used to enhance weak scattered signals from particles at the passive dielectric medium as done in SERS.

The results that have been discussed in section 6.4.2 illustrate that optically active layers with thickness similar to that for typical Quantum Well (QW) semiconductor material ($d_A \approx 20nm$) and optical gain g comparable to that used for high power edge-emitting, SLDs or Lasers, can lead to enormous improvements in SPW characteristics.

6.5 Conclusions

This chapter has theoretically shown that the use of an optically active medium in a SPW structure can provide SPW subwavelength and lossless propagation operation, as it compensates for the detrimental effect of the large metal losses. The study has found that the symmetric SPW mode in a thin MDM configuration operating in the IR spectrum regime is the most desirable option if only lossless propagation is required in terms of required amount of gain.

The analysis has also been extended in optically active prism coupled SPW arrangements where it has been shown that the use of optical gain can significantly reduce the FWHM of the 'dip' of the power reflection coefficient, make the intensity of the reflected signal exceed unity, indicating optical amplification, and in addition greatly enhance the SPW field intensity. Such a system can then potentially be employed as a biological / chemical sensor as it offers a high resolution sensitivity.

Chapter 6

[6.1] J.J. Burke, G.I. Stegeman, T. Tamir, "Surface-polariton-like waves guided by thin, lossy metal films", Phys. Rev. B, vol.33, no. 8, pp.5186-5201, 15 April 1986.

[6.2] A. Tarlis, J. Sarma, F. Causa, S.A. Maier, "Losses and Gains with Surface Plasmon Waves", presented at SIOE'2006 Conference, Cardiff, Wales, April 2006.

[6.3] I. Avrutsky, "Surface plasmons at nanoscale relief gratings between a metal and a dielectric medium with optical gain", Phys. Rev. B, vol.70, no.15, p.155416, October 2004.

[6.4] S.A. Maier, "Lossless propagation of electromagnetic energy with subwavelength confinement in surface plasmon polariton gap waveguides incorporating gain media", Opt. Commun., vol.258, pp.295-299, 15 February 2006.

[6.5] A. Tarlis, J. Sarma, "Surface Plasmon Waves in Multilayers with Loss / Gain", presented at XXVIII URSI General Assembly, New Delhi, India, October 2005.

[6.6] www.luxpop.com [GaN, λ = 440nm, temperature: 25 C^0].

[6.7] E.D. Palik, "Handbook of optical constants of solids", Academic Press (1985).

[6.8] I.I. Smolyaninov, "A far-field optical microscope with nanometre-scale resolution based on in-plane surface plasmon imaging", J. Opt. A: Pure Appl. Opt., vol.7, no.2, pp.S165–S175, February 2005.

[6.9] S.I.Bozhevolnyl, V.M.Shalaev, "Nanophotonics with Surface Plasmons – Part I", Photonics Spectra, January 2006, p.58.

[6.10] S.I.Bozhevolnyl, V.M.Shalaev, "Nanophotonics with Surface Plasmons – Part II", Photonics Spectra, February 2006, p.66.

[6.11] A. Yariv, "Optical Electronics in Modern Communications", Oxford University Press, 5th ed., 1997, p.572.

[6.12]http://www.schott.com/optics_devices/english/products/flash/abbediagramm_flash.html

[6.13] http://www.optotl.ru/PrismRaitEng.htm

[6.14] U. Schröter and D. Heitmann, "Grating couplers for surface plasmons excited on thin metal films in the Kretschmann-Raether configuration", Phys. Rev. B60, no.7-15, pp.4992–4999, August 1999.

[6.15] J. Seidel, S. Gafstrom, L. Eng, "_Stimulated Emission of Surface Plasmons at the Interface between a Silver Film and an Optically Pumped Dye Solution", Phys. Rev. Letters, vol.94, no.17, p.177401, 30 April 2005.

Chapter 7

SPW Induced Radiation

It has been mentioned in this thesis that small metallic particles capable of sustaining SPWs can significantly enhance the weak scattered signal from biological molecules. Hence, this chapter will analyse the electromagnetic mechanism of that enhancement and will show that the direction of the scattered far field radiation pattern from an array of such molecules can be controlled by the use of SPWs excited in a prism coupled waveguide configuration.

7.1 Raman Scattering

As briefly mentioned in chapter 1, section 1.2.2, the strong optical field intensity of SPWs can be utilised to improve weak scattered signals from particles or molecules such as in the Raman scattering case. The detection and interpretation of the scattered Raman signals is widely used for molecular spectroscopy or for providing chemical composition, molecular structure and molecular interactions in cells and tissues [7.1-2].

A simple description of the Raman effect can be given by considering a molecule M with dimensions much smaller than the free space (vacuum) wavelength λ_o. Assume then that an optical source with a time dependent electric field strength E_L of the form

$$E_L(t) = E_{in} \sin(2\pi f t) \tag{7.1}$$

is irradiating the molecule, where E_{in} is the field amplitude and f the frequency. The presence of E_L converts the molecule into an oscillating dipole with moment [7.1-4]

$$p(t) = \alpha E_L \tag{7.2}$$

where α is the electric polarisability which represents the average dipole moment per unit field strength [7.5], and changes if the size of the molecule changes [7.4].

If the molecule experiences some internal motion such as vibration that is not due to E_L, α can have a periodic change which can be described by [7.1-4]

$$\alpha = \alpha_o + \alpha_1 \sin(2\pi f_{vib}\, t) \tag{7.3}$$

where α_o is the equilibrium polarizability, α_1 is the rate of change of polarizability and f_{vib} the frequency of vibration. From eqns.(7.1) and (7.3), the dipole moment of the molecule, eqn.(7.2), becomes

$$p(t) = \alpha_o E_o \sin(2\pi f\, t) + \frac{1}{2}\alpha_1 E_o\{\cos[2\pi(f - f_{vib})t] - \cos[2\pi(f + f_{vib})t]\} \tag{7.4}$$

indicating that the oscillating dipole has now three frequencies f, $f - f_{vib}$ and $f + f_{vib}$.

Hence, eqn.(7.4) shows that if the molecule is regarded as a Hertzian dipole, the detailed analysis of which will be given in section 7.3.1, the corresponding scattered (radiated) electric field E_{sc} will contain the three frequencies f, $f - f_{vib}$ and $f + f_{vib}$, representing the Raman scattering concept, Figure 7.1.

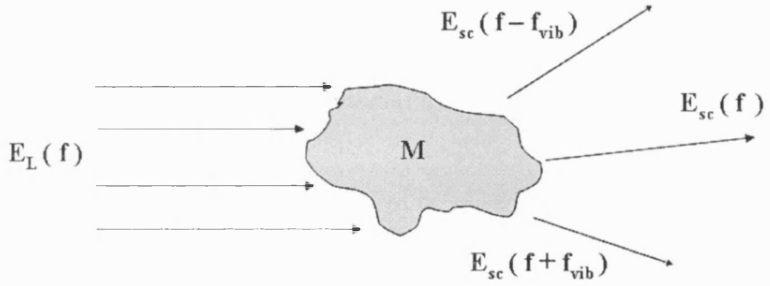

Figure 7.1. A molecule M is irradiated by an optical source with electric field strength E_L producing a scattered electric field E_{sc} which contains three different frequencies, f, f-f_{vib} and f+f_{vib}.

The high frequency component ($f + f_{vib}$) of the scattered signal indicates that during the collision between the photons (of the incident signal) and the molecule (particle), there is energy transfer into the molecule, unlike the low frequency component ($f - f_{vib}$) which shows energy lost from the molecule. Hence, the incident radiation is scattered either elastically at frequency f or inelastically at frequencies ($f \pm f_{vib}$).

Note however, that for a molecule to be capable of being Raman active, it is necessary that its internal motion (vibration or rotation) should alter the polarizability, i.e. $\alpha_1 \neq 0$, eqn.(7.3), [7.2]. If $\alpha_1 = 0$ then $\alpha = \alpha_o$, eqn.(7.3), and the molecule scatters signals containing only the incident signal frequency component f, which corresponds to the Rayleigh scattering concept [7.4].

The intensity of the scattered Raman signal however, is very weak since about only 1 in 10^7 photons scatters at different frequencies [7.6]. Stronger scattered signals can be obtained if a more powerful optical source is employed [7.6], or the molecule (particle) is placed close to a metal surface or particle. The second case corresponds to the Surface Enhanced Raman Scattering (SERS) phenomenon [7.7-8] and depending on the structure and the morphology of the metal surface can provide typical enhancement factors for the weak Raman signal of the order of 10^3 - 10^6 [7.6-9], although signal enhancement of the order of 10^{14} have also been seen [7.9].

The SERS technique has been known and widely used for the last three decades and the origin of the sometimes gigantic signal enhancement that provides, is due to an electromagnetic and a chemical mechanism. Between the two however, the electromagnetic is the dominant mechanism [7.10-11], unlike the chemical that is weak (of the order of 10^2) and associated with electron transition from the Fermi states of metal to unoccupied states of the molecule or from occupied states of the adsorbed molecule to the Fermi states of the metal [7.9, 7.12]. The electromagnetic amplification mechanism that is caused due to the metal surface (structure), is described in the following section for the simple case of a metal sphere scattering light. To simplify the calculations, the scattered signal will be considered to be Rayleigh, with frequency f.

7.2 Electrostatic analysis of single spheres

Consider a sphere with relative permittivity ε_1, diameter d_1 and radius r_1, which is located in a medium with relative permittivity ε_2 real and positive where a homogeneous field E_{in} exists, pointing in the z-direction, as it is shown in Figure 7.2.

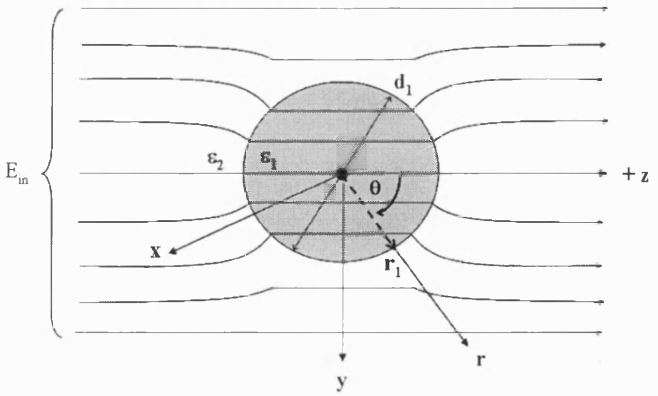

Figure 7.2. Sphere with relative permittivity ε_1, radius r_1 and diameter $d_1 = 2\ r_1$, in a parallel homogeneous field E_{in} along z, embedded in a medium with relative permittivity ε_2.

The scattering problem for an arbitrary sphere has been solved exactly by Mie [7.12]. For a clear physical insight however, the quasi-static approximation is easier to understand by assuming that the diameter of the sphere is much smaller than the wavelength λ_o. Quasi-static implies that the field is static spatially, i.e. there are no retardation effects, but temporarily it oscillates by exp[+jωt] [7.13].

Hence, with reference to the sphere of Figure 7.2 and following the quasi-static approach, consider that $d_1 << \lambda_o$. To find the electric field produced by the sphere, it is then essential to evaluate first the potential Φ of the sphere, which satisfies Laplace's equation in the spherical polar co-ordinates (r, θ, φ), [7.5, 7.14],

$$\nabla^2\Phi = 0 \tag{7.4}$$

By assuming no field variation in φ, eqn.(7.4) becomes, [Appendix A],

$$\frac{1}{r^2}\frac{\partial}{\partial r}\left(r^2\frac{\partial\Phi}{\partial r}\right)+\frac{1}{r^2\sin(\theta)}\frac{\partial}{\partial\theta}\left(\sin(\theta)\frac{\partial\Phi}{\partial\theta}\right)+\frac{1}{r^2\sin^2(\theta)}\frac{\partial^2\Phi}{\partial\phi^2}=0 \tag{7.5}$$

The solution of eqn.(7.5) can provide the potential of the sphere for $r \le r_1$, Φ_1, and outside the sphere ($r > r_1$), Φ_2, and has the form, [7.5]:

$$\Phi_q = \left(\frac{A_q}{r^2} + B_q\, r\right)\cos(\theta) \tag{7.6}$$

where q = 1,2 and A_q and B_q are unknown coefficients.

To find Φ_1 and Φ_2 it is necessary to apply the corresponding boundary conditions which are, [Appendix I], [7.5, 7.13-14]:

$$\left.\begin{aligned}\Phi_1(r,\theta) &= \Phi_2(r,\theta)\\ \varepsilon_1\frac{\partial\Phi_1(r,\theta)}{\partial r} &= \varepsilon_2\frac{\partial\Phi_2(r,\theta)}{\partial r}\end{aligned}\right\} \quad \text{at } r = r_1 \tag{7.7}$$

In addition, the potential at the center of the sphere (r = 0) should be finite:

$$\Phi_1(r,\theta) \neq 0 \tag{7.8}$$

whereas at a very large distance from the sphere ($r \to \infty$) the external field has to remain undisturbed:

$$\Phi_2(r,\theta) = -E_{in}\, r\cos(\theta) \tag{7.9}$$

Hence, the matching of eqns.(7.7-7.9) gives:

$$\Phi_1(r = r_1, \theta) = -\frac{3\varepsilon_2}{2\varepsilon_2 + \varepsilon_1} E_{in}\, z \tag{7.10}$$

$$\begin{aligned}\Phi_2(r > r_1, \theta) &= \left[\frac{\varepsilon_1 - \varepsilon_2}{\varepsilon_1 + 2\varepsilon_2}\right]\frac{r_1^3}{r^2} E_{in}\cos(\theta) - E_{in}\, r\cos(\theta) \\ &= \Phi_{sc} + \Phi_{in}\end{aligned} \tag{7.11}$$

Equation (7.11) shows that the potential outside the sphere ($r > r_1$) consists of the potential due to the optical source Φ_{in} , and the scattering potential from the sphere Φ_{sc} [7.13].

The electric field components at $r = r_1$, $\underline{E}_1$, and $r > r_1$, $\underline{E}_2$, can be found by, [7.5, 7.13-14]:

$$\underline{E}_q = -\nabla \Phi_q \tag{7.12}$$

which gives:

at $r = r_1$:

$$E_{z1} = \frac{3\varepsilon_2}{\varepsilon_1 + 2\varepsilon_2} E_{in} \tag{7.13}$$

at $r > r_1$:

$$\underline{E}_2 = \left[\left(\frac{\varepsilon_1 - \varepsilon_2}{\varepsilon_1 + 2\varepsilon_2}\right) E_{in}\frac{r_1^3}{r^3}\left(2\cos(\theta)\hat{r} + \sin(\theta)\hat{\theta}\right)\right] + E_{in}\,\hat{z} \tag{7.14}$$

where $\hat{z}$, $\hat{r}$ and $\hat{\theta}$ are unit vectors, [Appendix A]. Note that the first term of eqn.(7.14) describes the scattering fields from the sphere.

The polarization of the sphere $\underline{P}$ is then along the z direction due to the incident field E_{in} and given by, [Appendix I],

$$P_z = 3\varepsilon_2\left(\frac{\varepsilon_1 - \varepsilon_2}{\varepsilon_1 + 2\varepsilon_2}\right) E_{in} \tag{7.15}$$

As a consequence, the corresponding dipole moment $\underline{p}$, considering the sphere to be a dipole oriented along the z – axis, is [7.5, 7.13],

$$p_z = P_z\, V \tag{7.16}$$

where V is the volume of the dipole (sphere).

By using eqn.(7.15) in eqn.(7.16), p_z of the sphere becomes, eqn.(7.16),

$$p_z = 4\varepsilon_2 \left(\frac{\varepsilon_1 - \varepsilon_2}{\varepsilon_1 + 2\varepsilon_2} \right) \pi r_1^3 E_{in} = \alpha E_{in} \tag{7.17}$$

where α is the polarisability of the sphere. As a consequence, the field outside the sphere will now be, eqn.(7.14),

$$\underline{E}_2 = \left[\frac{p_z}{4\pi\varepsilon_2} \frac{\left(2\cos(\theta)\hat{r} + \sin(\theta)\hat{\theta}\right)}{r^3} \right] + E_{in}\,\hat{z} \tag{7.18}$$

which shows that the scattered field is dependent on the dipole moment of the sphere.

It is clear from the above analysis that the electric field at the surface of the sphere E_{z1}, eqn.(7.13), the scattering electric fields from the sphere, eqn.(7.14), and the dipole moment of the dipole (sphere), eqn.(7.17), can become larger than the input field E_{in} when,

$$\varepsilon_1 + 2\varepsilon_2 = 0 \tag{7.19}$$

The condition of eqn.(7.19) can only be satisfied if the sphere is an (ideal) metal which exhibits $\varepsilon_1 = -|\varepsilon_{1R}| < 0$, considering that the surrounding medium is a dielectric with $\varepsilon_2 > 0$. Since the relative permitivity of a metal is strongly wavelength dependent as was shown in chapter 2, hence as ε_2 increases the spectrum regime that will satisfy eqn.(7.19) will shift from the UV towards the visible/IR region. However, in real life metals are lossy with $\varepsilon_1 = -|\varepsilon_{1R}| - j|\varepsilon_{1I}|$ and eqn.(7.19) cannot be fully satisfied as $\varepsilon_{1I} \neq 0$. The strong induced electric fields on the surface ($r = r_1$) of such a metallic sphere when eqn.(7.19) is satisfied can be seen by calculating the corresponding field enhancement factor of eqn.(7.13) given by

$$T_S = \left| \frac{E_{z1}(r = r_1, \theta)}{E_{in}} \right|^2 = \left| \frac{3\varepsilon_2}{2\varepsilon_2 + \varepsilon_1} \right|^2 \tag{7.20}$$

The variation of T_S, eqn.(7.20), as a function of different metals and ε_2 values when eqn.(7.19) is satisfied is given in Table 7.1.

$2\,\varepsilon_2$	Metal	T_S	λ_o (nm)
2	Cu	0.374	330
	Ag	112	354
	Au	0.62	496
	Al	393	138
3.5378	Cu	0.88	430
	Ag	720	380
	Au	4.12	520
	Al	242	170
4.5	Cu	0.79	450
	Ag	47	400
	Au	4.125	520
	Al	39	184

Table 7.1. Calculated T_S for a sphere made of Ag, Au, Cu and Al when ε_2 =1 (air), 1.7686 (water) and 2.25 (glass). The values of ε_1 for Ag, Cu and Au have been taken from [7.15], whereas those for Al from [7.16].

The results of Table 7.1 show that as ε_2 increases the maximum value of T_S, eqn.(7.20), for the different metals becomes smaller as it is achieved at longer wavelengths where ε_{1I} usually becomes larger. Among the different metals, Ag and Al give the highest T_S. Note that if a dielectric sphere is used with ε_1 real and positive, the corresponding field enhancement T_S, eqn.(7.20), is then less than one and further reduces as ε_1 increases.

The high field produced by the metal spheres is a result of "localized" SPW modes which are able to radiate and can be excited directly by incident photons. These "localized" SPW modes can produce more intense optical fields compared to the SPW modes discussed up to now in this thesis which are non-radiative and tightly bound at a perfectly smooth and flat dielectric – metal interface [7.13].

Hence, the above results clearly show why the use of metal structures and especially particles has been so attractive when placed close to molecules for enhancing the weak Raman scattered signals.

7.3 Elemental dipole antenna radiation

One of the problems when dealing with light scattering measurements as mentioned before is related to the weak scattered signals as for example in Raman scattering. Another significant problem however, is the direction of these scattered signals from the molecules. For example, the fluorescent radiation from fluorophores is isotropic and it is difficult to collect more than a small fraction of the emitted photons. It has been found that collection efficiencies near 10% are possible, but at the expense of complex optics, [7.17].

To improve the scattered light collection efficiency from particles (molecules) without the use of complicated or expensive instruments, it is suggested in this chapter to employ a K-R prism coupled structure and make use of the properties of the excited SPW field such as the corresponding longitudinal SPW phase. This will allow the control of the direction of the radiation pattern from the molecules. Hence, the involvement of SPWs will not only enhance the intensity of the scattered signals due to the strong field which can become even stronger with the use of optically active films, section 6.4, but also provide an increase in the scattered light collection efficiency. Although planar interfaces do not offer such a high SPW field intensity as metal particles or rough surfaces, but have the advantage of ease of fabrication. In addition, for some biological applications if a rough metal surface is used with certain atomic level roughness, a specific charge transfer interaction and/or the electronic structure of the adspecies are responsible for large enhancement in SERS, and therefore the Raman spectra of adsorbates often contains additional bands which are not always unambiguously assigned. In contrast, the use of smooth surface for the Raman enhancement does not show these disadvantages and enhancement factors of the order of $10^2 - 10^3$ have been theoretically predicted, [7.18].

The analysis of the proposed configuration will consider that each of the molecules is placed inside a homogeneous SPW field that is excited in a K-R prism coupled arrangement. Each molecule will then scatter (radiate) light in a similar manner to a radiating elementary dipole antenna.

In section 7.2 the analysis of the sphere has ignored the field time dependency due to the assumed quasi-static approximation which gave a permanent dipole moment $\underline{p}$, eqn.(7.17). This result however is not always valid as most of the times we do not deal with such permanent moments, but with moments induced by the external field and varying with it as a periodic function of time [7.5, 7.13],

$$\underline{\tilde{p}}(t) = \underline{p}e^{+j\omega t} \tag{7.21}$$

Such an induced dipole moment $\underline{\tilde{p}}$ can then be visualized as a dipole of length d_l where the charge alternates periodically, Figure 7.3a, and can represented as an equivalent to an infinitesimal (elemental) dipole antenna traversed by current [7.5],

$$I(t) = \frac{dQ}{dt} = \frac{d}{dt}\left(\frac{\underline{\tilde{p}}}{d_l}\right) = \frac{\underline{p}}{d_l} j\omega e^{+j\omega t} = I_o e^{+j\omega t} \tag{7.22}$$

which can radiate in the free space [7.5, 7.14, 7.19-20], Figure 7.3b; Q represents charge.

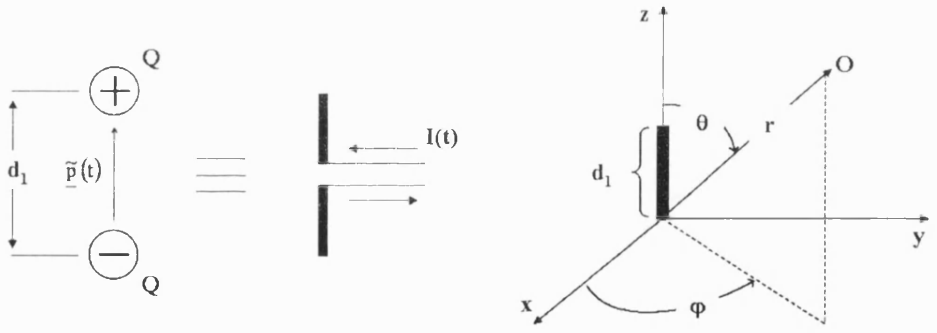

Figure 7.3. Representation of an electric dipole, (a), of length d_l, charge Q and time varying moment $\underline{\tilde{p}}(t)$, as a dipole antenna, (b), traversed by current I(t), which is located at the origin of the co-ordinate system, (c).

Consider then such an infinitesimal dipole antenna of length $d_l << \lambda_o$ positioned at the origin of the co-ordinate system and oriented along the z axis at a distance r from an observation point O as shown in Figure 7.3c.

The current I, eqn.(7.22), in the dipole antenna is assumed to be harmonic and flows only along the z direction. The corresponding harmonic time dependent electric, $\underline{E}$, and magnetic, $\underline{H}$, field components of the radiating oscillating dipole are well known and can be found in any textbook dealing with radiation, [7.5, 7.19-20]:

$$H_{\varphi}(r,\theta)=p_z\frac{\omega}{4\pi}\left[-\frac{k}{r}+\frac{j}{r^2}\right]\sin(\theta)\exp[-jkr] \tag{7.23}$$

$$E_r(r,\theta)=\frac{p_z}{2\pi\varepsilon_2}\left[j\frac{k}{r^2}+\frac{1}{r^3}\right]\cos(\theta)\exp[-jkr] \tag{7.24}$$

$$E_{\theta}(r,\theta)=\frac{p_z}{4\pi\varepsilon_2}\left[\frac{1}{r^3}+j\frac{k}{r^2}-\frac{k^2}{r}\right]\sin(\theta)\exp[-jkr] \tag{7.25}$$

where k is the propagation constant in medium ε_2 given as:

$$k=k_o\sqrt{\varepsilon_2} \tag{7.26}$$

With reference to the eqns.(7.23) – (7.25), in the near field zone of the radiating dipole ($r \ll \lambda_o$) the term [$1/r^3$] dominates, and all field components exist:

$$H_{\varphi}(r,\theta)\approx p_z\frac{\omega}{4\pi}\frac{j}{r^2}\sin(\theta)\exp[-jkr] \tag{7.27}$$

$$E_r(r,\theta)\approx\frac{p_z}{2\pi\varepsilon_2}\frac{1}{r^3}\cos(\theta)\exp[-jkr] \tag{7.28}$$

$$E_{\theta}(r,\theta)\approx\frac{p_z}{4\pi\varepsilon_2}\frac{1}{r^3}\sin(\theta)\exp[-jkr] \tag{7.29}$$

However, there are no now any Poynting vector components as the E and H fields form a standing wave instead of a traveling one, [7.19].

In contrast with the near-field components, in the far field zone ($r \gg \lambda_o$), only the term varying with [$1/r$] in eqns.(7.23)-(7.25) remain, hence $E_r \approx 0$ and E_{θ} with H_{φ} are the only non zero field components:

$$H_{\varphi}(r,\theta)\approx p_z\frac{\omega}{4\pi}\left[-\frac{k}{r}\right]\sin(\theta)\exp[-jkr] \tag{7.30}$$

$$E_{\theta}(r,\theta)\approx\frac{p_z}{4\pi\varepsilon_2}\left[-\frac{k^2}{r}\right]\sin(\theta)\exp[-jkr] \tag{7.31}$$

The corresponding Poynting vector of the dipole, eqn.(2.11), solved in spherical co-ordinates has then a component only in the r direction [7.5, 7.19-20]:

$$S_r(r,\theta)=\frac{1}{2}\mathrm{Re}\{E_\theta H_\varphi^*\}=\left(\frac{p_z}{4\pi}\right)^2\frac{\omega}{2\varepsilon_2}\frac{k^3}{r^2}\sin^2(\theta) \tag{7.32}$$

It is clearly shown from eqn.(7.32) that the intensity of the dipole's radiation pattern is zero in the direction of the dipole moment ($\theta = 0$) and becomes maximum in the direction perpendicular to the dipole ($\theta = \pi/2$) with

$$S_{r\,max}(r,\theta=\pi/2)=\left(\frac{p_z}{4\pi}\right)^2\frac{\omega}{2\varepsilon_2}\frac{k^3}{r^2} \tag{7.33}$$

as it is shown in Figure 7.4.

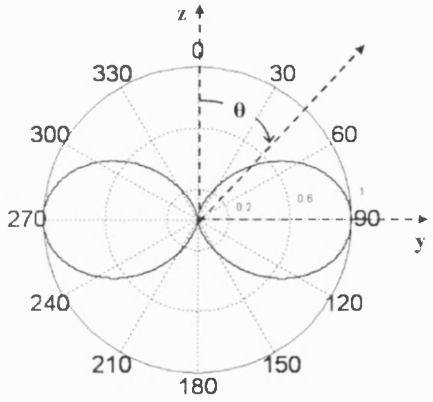

Figure 7.4. Polar plot of the normalized radiating intensity of a single elementary dipole.

Since the main scope of this study is to improve the directivity of the radiating fields and increase the scattered signal collection efficiency, as a consequence only the far field zone components of the dipole will be considered in the analysis.

7.4 Two dimensional array of particles

Since the field properties for a single spherical particle are now known, it is therefore necessary to introduce the SPW field effects. This can be achieved by employing the K-R prism coupled structure of Figure 4.3a for exciting the SPW. In most experimental cases however, we deal with a large number of particles. The particles here are considered in close vicinity to the metal film and are much smaller compared to the excitation wavelength and the SPW decaying field as it is shown in Figure 7.5a. If the particles occupy an area on the metal film with known dimensions, it is then possible to

calculate their overall far field radiation pattern. For the sake of the simplicity, it is assumed here that the particles form a rectangular array with length l_z along the z direction and width l_y along the y direction, as it is shown in Figure 7.5b, [7.21].

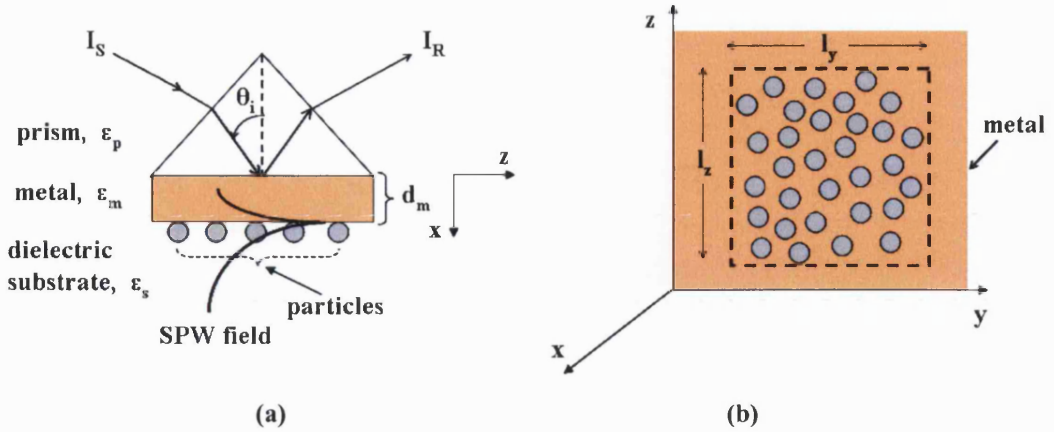

Figure 7.5. a) particles probed by SPW field excited in a K-R arrangement, b) rectangular array of particles with length l_z along the z axis and width l_y along the y axis.

The rectangular particle array can then be considered as a two dimensional (2D) array consisted of M rows with respect to the z axis and N columns with respect to the y axis as it is shown in Figure 7.6.

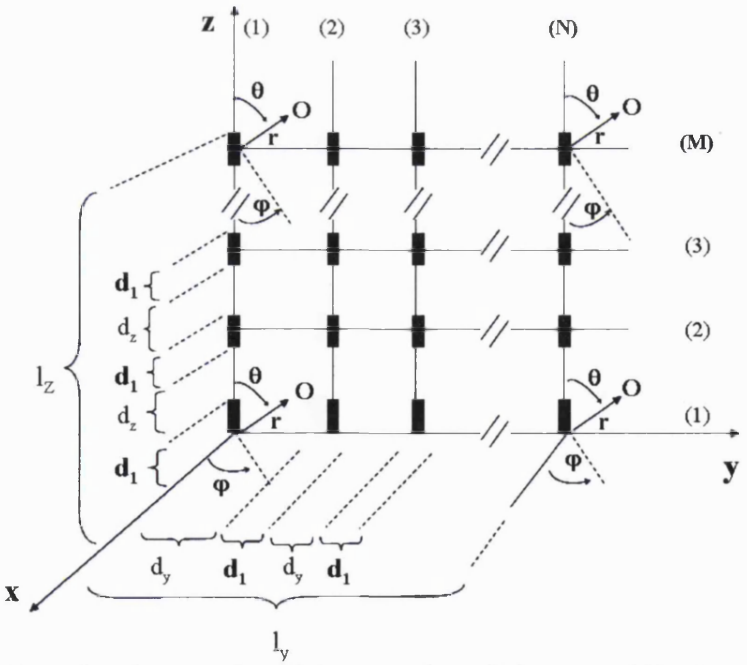

Figure 7.6. Two dimensional array of particles consisting of M rows and N columns. The particles have length d_1 and are separated by each other by a distance $d_z << d_1$ and $d_y << d_1$ along the z and y axis respectively. Total length of each column and row is l_z and l_y respectively. Note that d_1, d_y and d_z are not in scale in the picture.

Every row/column of the array is formed by a large number of particles each one acting as an elemental dipole antenna and having the far field properties described in section 7.3.1. However, since the particles are now separated by each other by a distance d_z in the z direction and d_y in the y direction, there is an introduced phase shift between them along the z, $\Delta\Phi_z$, and y axis, $\Delta\Phi_y$, as given by eqns.(7.34) and (7.35) respectively, [Appendix J.1]:

$$\Delta\Phi_z = k\,d_z\cos(\theta) \tag{7.34}$$

$$\Delta\Phi_y = k\,d_y\sin(\theta)\sin(\varphi) \tag{7.35}$$

Since SPW excitation is required, hence the analysis will consider TM polarized signals and no field variation along the y axis. As a consequence, since the dipoles are oriented along the z axis, their excitation will be done by employing the E_z field component of the K-R structure inside the dielectric substrate medium, [Appendix F.1]. For incident angles θ_i beyond the total reflection angle θ_{TR} between the prism and the substrate E_z becomes:

$$E_{z(S)} = j\frac{k_{x(s)}}{\omega\varepsilon_o\varepsilon_S}A_S\exp[-k_{x(S)}x]\exp[-j\beta z] \tag{7.36}$$

where $k_{x(S)}$ is the transverse propagation constant, eqn.(4.3), and β the longitudinal, eqn.(4.2). Because E_z, eqn.(7.36), is propagating along the z direction, hence an additional excitation phase term will have to be introduced to the dipole field calculations but only along z. The electric and magnetic far field components for a single dipole along the z axis will now be, eqn.(7.30)-(7.31):

$$E_{\theta(z)}(r,\theta) \approx A_\theta\frac{\sin(\theta)}{r}\exp[-jkr]\exp[+j(k\cos(\theta)+\beta)d_z] \tag{7.37}$$

$$H_{\varphi(z)}(r,\theta) \approx A_\varphi\frac{\sin(\theta)}{r}\exp[-jkr]\exp[+j(k\cos(\theta)+\beta)d_z] \tag{7.38}$$

whereas these for the dipoles along the y axis are:

$$E_{\theta(y)}(r,\theta) \approx A_\theta\frac{\sin(\theta)}{r}\exp[-jkr]\exp[+jk\sin(\theta)\sin(\varphi)d_y] \tag{7.39}$$

$$H_{\varphi(y)}(r,\theta) \approx A_\varphi\frac{\sin(\theta)}{r}\exp[-jkr]\exp[+jk\sin(\theta)\sin(\varphi)d_y] \tag{7.40}$$

where

$$A_\theta = -\frac{k^2}{4\pi\varepsilon_S} p_z \tag{7.41}$$

$$A_\varphi = -\frac{k\omega}{4\pi} p_z \tag{7.42}$$

Note that all the dipoles are dielectric spheres with relative permittivity ε_1 and radiate inside the dielectric substrate region, hence in k, eqn.(7.26), and p_z, eqn.(7.17), consider $\varepsilon_2 = \varepsilon_S$ real and positive.

Since the diemeter d_1 of each radiating dipole, Figure 7.3a, is assumed to be much bigger than the separations d_z and d_y , hence each row/column of the array can be thought of being homogeneous. As a consequence this implies that the particles are very close to each other so that d_z = z, eqns.(7.37)-(7.38), and d_y = y, eqns.(7.39)-(7.40), forming a continuous linear array along z and y. Hence, the total electric $E_{\theta(T)}$ and magnetic $H_{\varphi(T)}$ field components along the z and y direction can be calculated by integrating eqns.(7.37)-(7.40) over the entire length l_z and l_y respectively, [Appendix J]:

along z:

$$E_{\theta(zT)}(r,\theta) \approx A_\theta \frac{\sin(\theta)}{r} \exp[-jkr] AF_z \tag{7.43}$$

$$H_{\varphi(zT)}(r,\theta) \approx A_\varphi \frac{\sin(\theta)}{r} \exp[-jkr] AF_z \tag{7.44}$$

along y:

$$E_{\theta(yT)}(r,\theta) \approx A_\theta \frac{\sin(\theta)}{r} \exp[-jkr] AF_y \tag{7.45}$$

$$H_{\varphi(yT)}(r,\theta) \approx A_\varphi \frac{\sin(\theta)}{r} \exp[-jkr] AF_y \tag{7.46}$$

where

$$AF_z = \frac{\sin\left(\frac{u_z l_z}{2}\right)}{u_z} \tag{7.47}$$

$$u_z = k\cos(\theta) + \beta \tag{7.48}$$

$$AF_y = \frac{\sin\left(\frac{u_y l_y}{2}\right)}{u_y} \tag{7.49}$$

$$u_y = k\sin(\theta)\sin(\varphi) \tag{7.50}$$

The term $\frac{\sin(\theta)}{r}\exp[-jkr]$ in eqns.(7.43)-(7.46) describes a single radiating dipole, whereas AF_z and AF_y are referred to as the array factors and represent the influence of the linear array (column) along the z and y direction on the dipole radiation. As a consequence, the fields of the rectangular array of dipoles can be found by multiplying the single radiating dipole term with the corresponding array factors along the z and y directions:

$$E_{\theta(T)}(r,\theta) \approx A_\theta \frac{\sin(\theta)}{r}\exp[-jkr]AF_z\, AF_y \tag{7.51}$$

$$H_{\varphi(T)}(r,\theta) \approx A_\varphi \frac{\sin(\theta)}{r}\exp[-jkr]AF_z\, AF_y \tag{7.52}$$

giving a Poynting vector, eqn.(7.32):

$$S_{r\,(T)}(r,\theta) = 2A_\varphi\, A_\theta\left[\frac{\sin(\theta)}{r}\right]^2 [AF_z\, AF_y]^2 \tag{7.53}$$

7.5 Array far field radiation results

With reference to Figure 7.5a, let the K-R prism coupled arrangement to have the following parameters: $\varepsilon_p = 2.25$, $\varepsilon_s = 1$, and the metal film of thickness $d_m = 30$nm is silver with $\varepsilon_m = -48.8 - j\,3.16$ at $\lambda_o = 1\mu$m. Following the analysis given in chapter 4, from the power reflection coefficient $|\Gamma|^2$, eqn.(4.17), of the structure the SPW excitation angle $\theta_i = \theta_{spw}$ is now found at 42.4°, eqn.(4.25). In addition the excited SPW field has peak intensity at the metal – dielectric substrate interface given by $|T|^2 = 65$, eqn.(4.18), whereas at $\theta_i = \theta_{spw}$, the SPW field inside the dielectric substrate region has a decay depth $\Delta \approx 0.7\mu$m, eqn.(3.20). Both $|\Gamma|^2$ and $|T|^2$ of the prism coupled structure are given as a function of the incident angle θ_i in Figure 7.7.

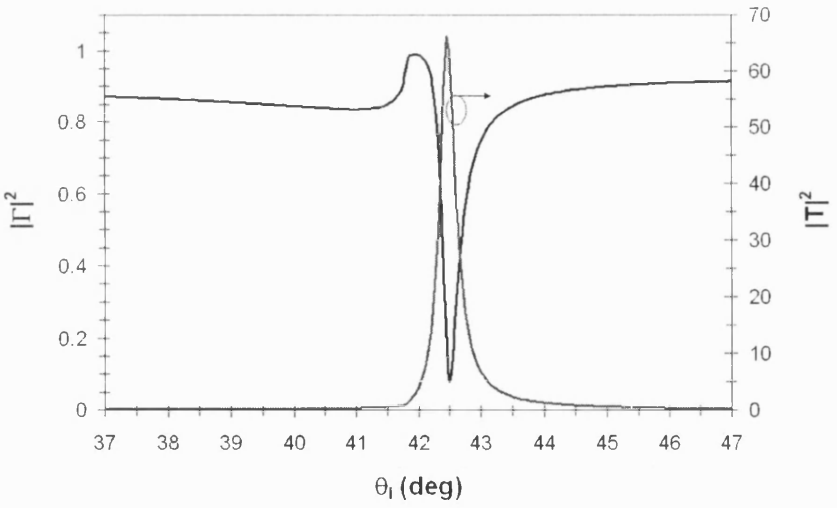

Figure 7.7. Calculated $|\Gamma|^2$ and $|T|^2$ as a function of the incident angle θ_i for a K-R prism coupled structure with $\varepsilon_p = 2.25$, $\varepsilon_s = 1$, $d_m = 30nm$, $\varepsilon_m = -48.8 - j\,3.16$ and $\lambda_o = 1\mu m$.

With reference to Figure 7.5b, assume that an array of dielectric spherical particles with diameter d_1 and relative permittivity ε_1 is then formed in a close vicinity to the dielectric substrate side of the metal, and has width l_y and length l_z along the y and z direction respectively. If each of the particles is considered much smaller than the incident wavelength ($d_1 << \lambda_o = 1\mu m$) and placed inside the SPW field which is considered to be homogeneous, hence the analysis given in section 7.5 can be applied to estimate the radiation far field emission pattern of the whole particle array. Note that the particles are experiencing an excitation phase only along the z direction, which is, [7.21]:

$$\Delta\Psi_z = \int_{-lz/2}^{+lz/2} \beta\, dz = \beta l_z = k_o \sqrt{\varepsilon_p}\, \sin\left(\theta_{spw}\right) l_z \qquad (7.54)$$

The intensity S_r of the far field pattern of the array is then given by eqn.(7.53) and its corresponding normalized quantity for $\phi = 0$, is plotted as a function of θ for various array dimensions in Table 7.2, with and without the excitation SPW phase $\Delta\Psi_z$.

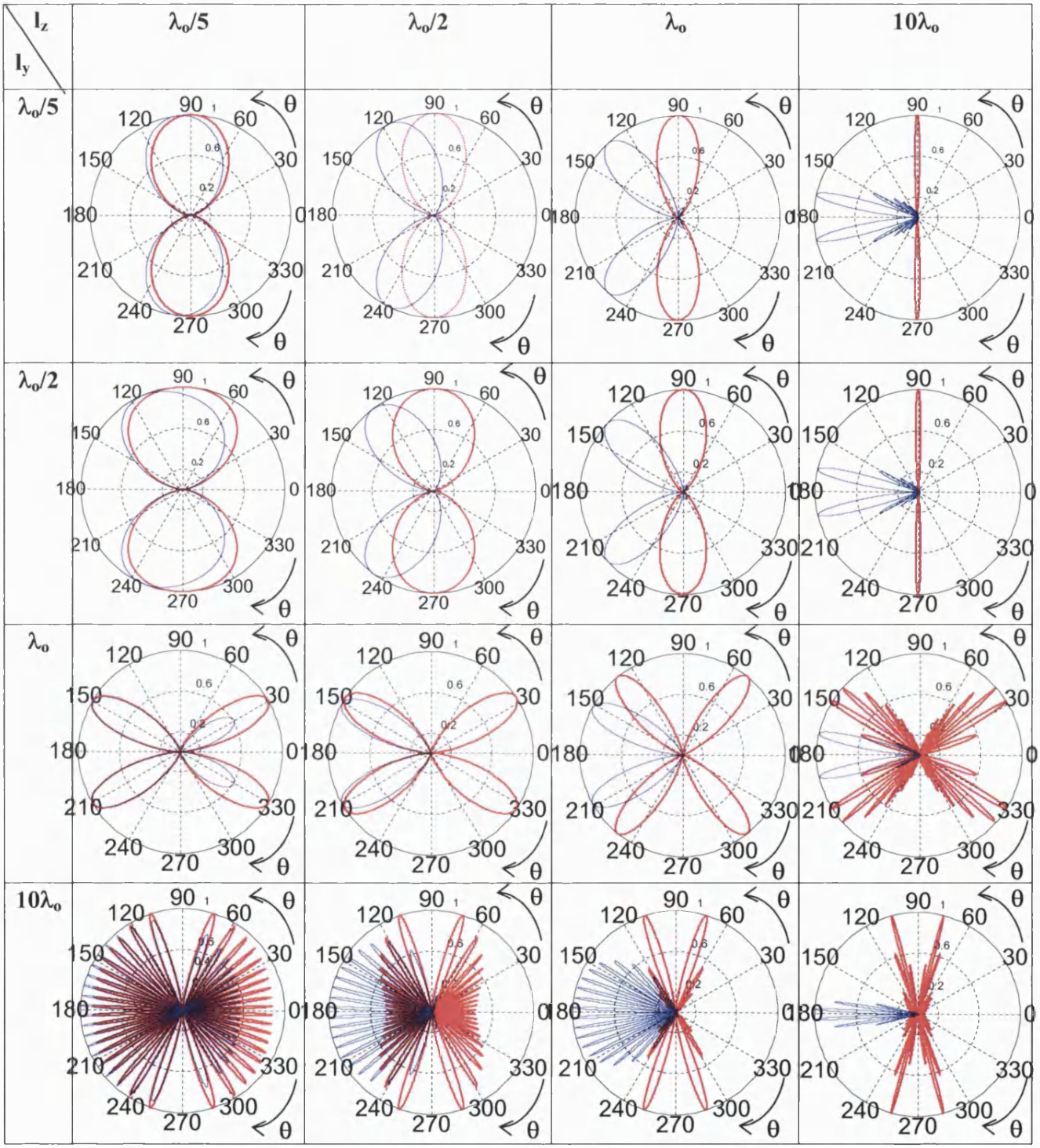

Table 7.2. Polar plots of the normalised intensity S_r of the far field radiation pattern from the array of particles as a function of θ for different array dimensions when $\phi = 0$. The solid (blue) line patterns include the SPW excitation phase, whereas the dotted (red) line plots are without.

Note that in the plots of Table 7.2, with reference to Figure 7.5b, the $0 - 180^0$ and the $90 - 270^0$ axes correspond to the z and y axis respectively. The results of Table 7.2 clearly show that as the l_z length increases the radiation pattern becomes more narrow (i.e. directive) compared to the corresponding increase of l_y which produces a broader emission pattern. When $l_y > \lambda_o$, this broad far field pattern splits into many lobes which in the absence of the excitation phase are symmetric with respect to the $90 - 270^0$ axis. If the excitation phase along z is not zero, then the emission pattern becomes very directive and points towards 180^0. The fact that the far field radiation becomes very narrow and in some cases significantly directive is due to the fact that as l_z increases the overall effect of the excitation (SPW) phase becomes more significant as also the phase $\Delta\Psi_z$, eqn.(7.54), increases, Table 7.3.

l_z (μm)	$\Delta\Psi_z$ (rads)
0.2	$0.4\,\pi$
0.5	π
1	$2\,\pi$
10	$20\,\pi$

Table 7.3. Total excitation phase along z as a function of the length l_z.

On the other hand, when both l_y and l_z become smaller, the far field pattern of the array approaches that of a single elementary dipole, Figure 7.4. The far field radiation of the array varies similarly when $\phi = \frac{\pi}{4}$ as it is shown in Appendix J.

An alternative method to change the far field radiation pattern and make it more directive is by varying the excitation shift $\Delta\Psi_z$, eqn.(7.54), for a particular array dimensions. This change in $\Delta\Psi_z$ can easily be achieved by using different incident angles θ_i inside the prism coupler. Figure 7.8 shows an example of how the intensity S_r, eqn.(7.53), of the far field radiation pattern from the array of Table 7.3 with $l_y = l_z = \lambda_o$ varies when $\Delta\Psi_z = 0.03\,\pi$, $0.3\,\pi$, $2\,\pi$ and $3\,\pi$ (rads).

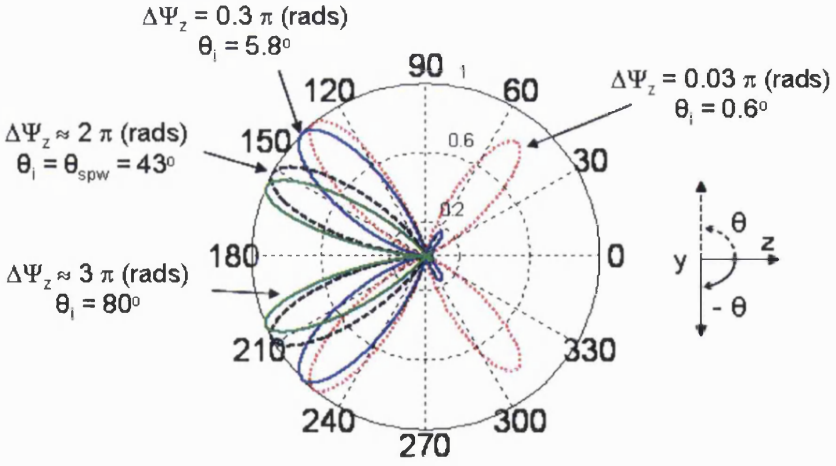

Figure 7.8. Polar plot of the normalised far field intensity radiation S_r for a two dimensional array of particles with $l_y = l_z = \lambda_o$ calculated for excitation phase $\Delta\Psi_z$ = 0.03 π, 0.3 π, 2 π and 3 π (rads).

It is clearly illustrated in Figure 7.8 that the larger the excitation phase $\Delta\Psi_z$ (larger θ_i), the more directive the far field pattern becomes and the less lobes exist. However, only the phase $\Delta\Psi_z$ that corresponds to the SPW excitation is of interest ($\Delta\Psi_z \approx 2\ \pi$), as it is followed by the high SPW field intensity SPW which makes the radiation fields from the particles very strong. In addition, as it is shown for this example, the effect of $\Delta\Psi_z$ on the radiation pattern for $\theta_i > \theta_{spw}$ is not so strong.

Hence, it is possible to steer the far field radiation from an array of particles and also make it more directive by either changing the dimensions of the array or varying the external excitation phase through the incident prism angle θ_i.

7.6 Far Field radiation pattern measurement techniques

Unfortunately we did not experimentally measure the far field radiation pattern of any of the theoretically analysed dipole arrays of section 7.5. However, we present here two experimental configurations that can be employed to complete the work in the future. The two experimental arrangements are presented in Figures 7.9 and 7.10 respectively. Both structures, Figures 7.9-7.10, are based on the K-R prism coupled configuration of Figure 7.5a, where SPW excitation is achieved at the metal – substrate interface when the field intensity of the reflected signal I_R vanishes at $\theta_i = \theta_{spw}$, eqn.(4.25). The optical source is followed by a collimating lens to ensure minimum divergence angle for the

source output beam, and a polariser to allow only the TM polarized signals with intensity I_S to impinge onto the prism. The particles are dielectric with relative permittivity $\varepsilon_1 > 0$ and properties as given in section 7.4, and are placed at the metal - substrate interface to form the required array. Note importantly that in some particles such as fluorescent molecules, the radiation is significantly affected by the presence of the metal, hence the use of a 5nm to 10nm SiO_2 film between the two media [7.13]. The array of particles at the metal – substrate dielectric is then radiating with the use of the excited SPW mode in the K-R arrangement.

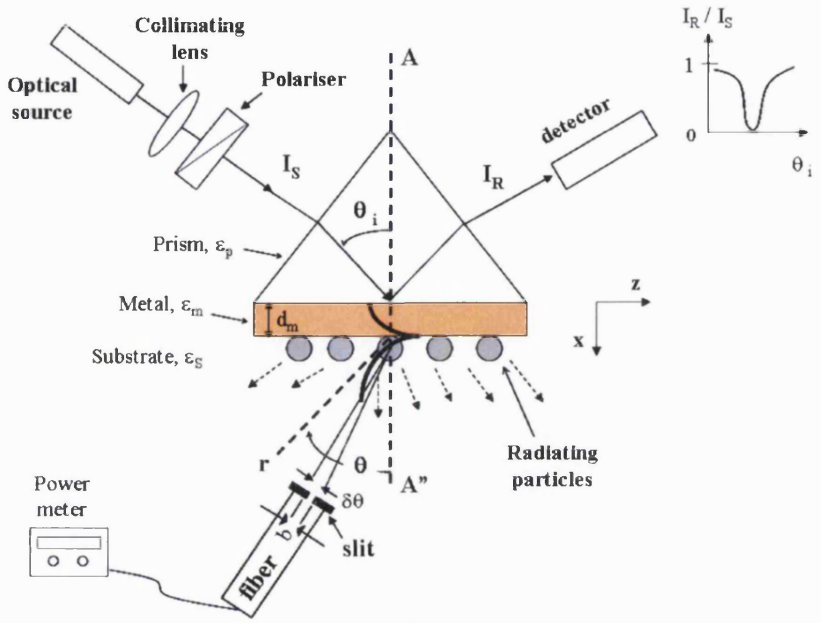

Figure 7.9. Arrangement for measuring the far field profile from an array of particles in a K-R configuration using a fiber. Dotted arrows indicate radiation from the particles.

With reference to Figure 7.9, the measurement concept of the far field radiation pattern of the excited array of particles is based on a direct angular scanning with the use of a fiber. In that case, a fiber can be placed at a distance r in front of the particle array and connected to a very sensitive power meter for measuring the scattered signals. The measurement of the array far field is then performed by rotating the fiber at an angle θ with respect to the optical axis AA". A slit with an aperture width b can also be placed on the detecting facet of the fiber to increase the angular detection resolution $\delta\theta$,

$$\delta\theta \approx \frac{b}{r} \tag{7.55}$$

which is measured in radians.

It is suggested here though, that before the final measurement of the far field radiation profile of the array of particles that a reference measurement has to be taken from the metal surface without the presence of the array. By this way any damages on the metal film which may allow more light to transmit inside the substrate region and affect the radiation profile of the array are avoided.

The advantage of this technique is that the far field profile from the array can be obtained directly and in real time. The drawbacks however are that there may be mechanical vibrations due to the rotation of the fiber. In addition, single mode fibers which have small diameter and provide high rotating flexibility are difficult to couple light whereas high numerical aperture (NA) fibers are larger and more cumbersome to rotate or bend. A suggestion to overcome the fiber problem could be the direct use of the power meter but in that case a small enough detector has to be used at close distances from the sample.

The technique employed in the arrangement of Figure 7.10 can measure the far field radiation pattern with the use of a lens.

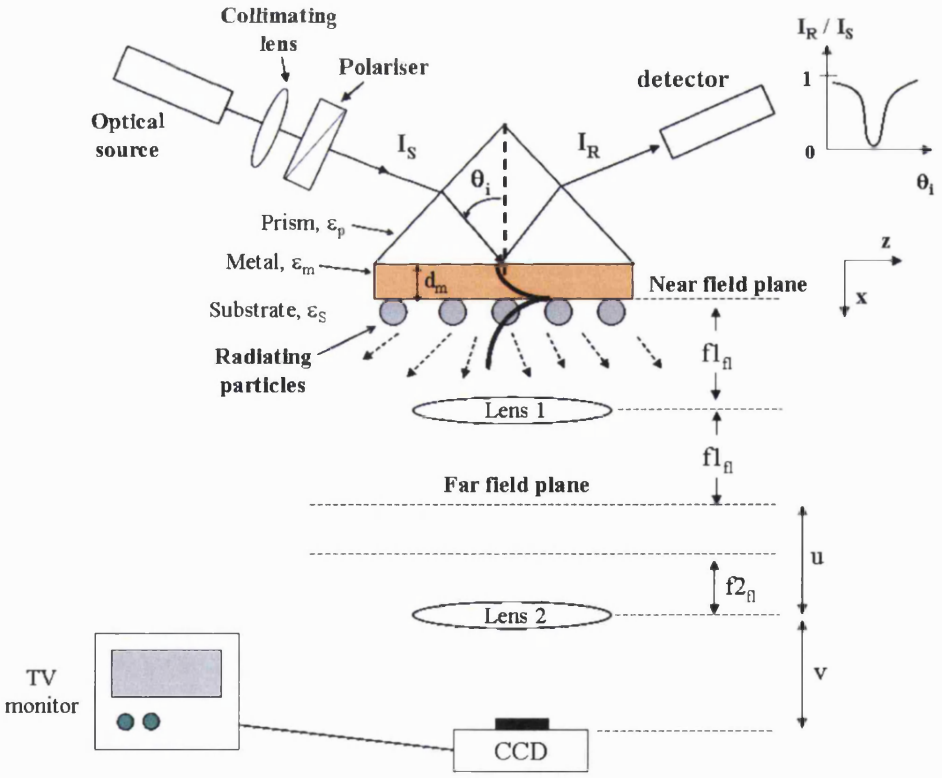

Figure 7.10. Arrangement for measuring the far field profile from an array of particles in a K-R configuration using a set of lenses. Dotted arrows indicate radiation from the particles.

The main concept of the measurement is based on the ability of the lenses to perform instant Fourier transform on a signal, [7.22-23]. Is it also well known that the Fourier transform of the near field radiation produces the corresponding far field profile [7.24]. As a consequence, in the arrangement of Figure 7.10 it is suggested that a biconvex lens (Lens 1) with focal length $f1_{fl}$ is placed at distance $x = x_L \approx f1_{fl}$ from the particles to image their near field profile. Note here that x_L cannot be exactly equal to $f1_{fl}$ as then the near field image will be formed at infinity following the thin les formula calculations, [7.22]. As a consequence, at a distance $x \approx 2f1_{fl}$ from the particles, which for our arrangement corresponds to the front focal length $f1_{fl}$ of the Lens 1, the Fourier transform plane of the lens exists where the far field radiation profile of the array of particles is expected to be formed. A CCD camera connected to a TV monitor can then be placed at the Fourier transform plane to capture the far field profile image, which is seen now as an intensity profile along the z axis. Depending on the dimensions of the array the capture image may be small and outside the resolution capabilities of the CCD. Hence, a second biconvex lens (Lens 2) with focal length $f2_{fl}$ can be placed at a distance u from the far field plane. By applying the thin lens formula where, [7.22],

$$\frac{1}{f2_{fl}} = \frac{1}{u} + \frac{1}{v} \tag{7.56}$$

it is then expected that at a distance v from Lens 2 an image of the far field profile will be formed magnified by a factor, [7.22],

$$M_{IM} = \frac{v}{u} \tag{7.57}$$

and can then be captured by the CCD. It is important here to mention that the maximum magnification, eqn.(7.57), is limited by the area of the CCD chip. Similarly to the measurement with the fiber, Figure 7.9, a reference measurement without the presence of the particle array is recommended.

The advantage of the lens arrangement, Figure 7.10, compared to the use of the fiber, Figure 7.9, is that the lenses offer stability to the system as there are no mechanical movements (e.g. fiber rotation). In addition, a large working distance lens will allow the measurement of the far field radiation profile at a safe distance from the particles. Examination of a particular site on the particle array is also feasible with the lens. A real time measurement is also provided.

The lens technique however, measures the far field intensity profile along the z axis and not as it is usually done as an angular variation. In addition, depending on the dimensions of the particle array and the strength of the scattered signals, a high sensitivity and high resolution CCD camera may be required which can increase the cost of the system.

To prove that the lens concept works, an example of measuring the far field radiation profile from a beam coming out from a slit with dimensions less that the beam's diameter, is given in Appendix K.

The use of fluorescent materials for imaging the far field radiation pattern from particles excited by SPWs has also been reported in the literature, [7.25]. The structure consists of a rough silver film of 70nm thickness that has been deposited on a glass slide and coated by 1/100 monolayer of the Rhodamin 6G fluorescent molecules. As fluorescent molecules are completely quenched when they are in direct contact with metals, a 10nm thick film of SiO_2 was used between the two media. On the top of the monolayer, silver particles with different dimensions were positioned. SPW excitation was achieved by focusing a laser beam with a wavelength λ_o = 515nm onto the rough silver film, Figure 7.11.

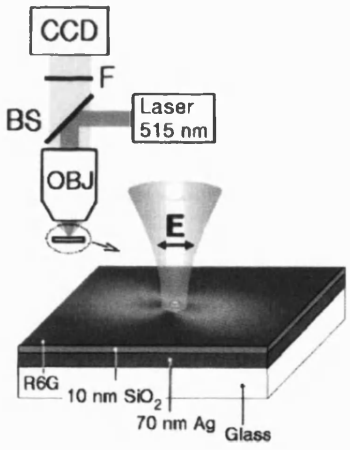

Figure 7.11. Experimental configuration employed for imaging radiation from particles as it is given in [7.25]. BS: beam splitter, OBJ: microscope objective lens, F: filter, CCD: camera, E: electric field.

The focused light on the structure allows SPW excitation, and also makes the molecules fluoresce but at a different wavelength from the source. The silver particles on the

fluorescent layer are excited by the SPWs and their radiation pattern is imaged by a CCD camera. Since the lifetime of the fluorescent molecules is very short, it is necessary to employ a CCD camera with exposure times of few seconds, [7.25]. In addition, the intensity of the excitation source needs to be kept low as this can cause bleaching (decomposition) of the molecules. In that case a CCD camera sensitive to low light levels is required. The laser excitation wavelength is blocked from the CCD with a long pass filter. Typical results of the radiation pattern from the silver particles as observed in [7.25] are given in Figure 7.12.

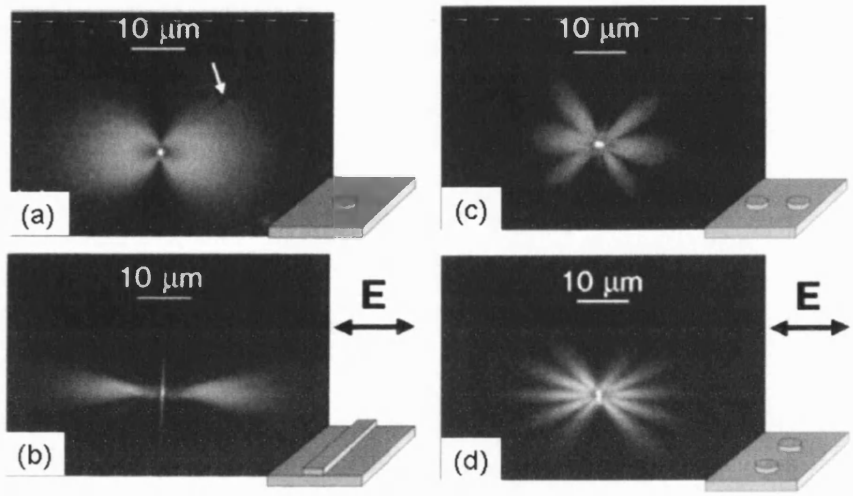

Figure 7.12. Results of particle radiation with the use of SPWs as obtained in [7.25]. a) silver particle with dimensions: 200nm diameter, 60nm height ; b) silver wire: 200nm width, 60nm height, 20μm length; c) two silver particles positioned parallel to the excitation field E: 200nm diameter, 60nm height, 1.5μm separation; d) two silver particles positioned normal to the excitation field E: 200nm diameter, 60nm height, 2μm separation.

The results of Figure 7.12 do not follow the traveling wave antenna radiation pattern that was observed in Table 7.2. Instead, the particle radiation pattern is similar to that for long linear antennae with standing-wave sinusoidal current distributions, [7.26], which is believed to be due the way SPWs were excited. As a consequence, the particle now has a bi-directional radiation pattern which becomes narrower as the length of the particle increases, Figures 7.12a-b. In addition, when two particles are used, more lobes in the radiation pattern are observed, Figures 7.12c-d.

Hence, the above described technique has the potential to be employed for imaging the radiation pattern from particles excited by a traveling SPW, [section 7.4].

7.7 Conclusions

It has been shown in this chapter that the intensity of scattered signals from particles with dimensions smaller that the wavelength of the excitation source can be significantly enhanced with the use of metal structures such as spheres. The analysis has been performed by assuming that such particles act as elementary dipole antennas. It has also been presented that if an array of such particles is formed, it is then possible that the use of SPWs can not only provide an intensity enhancement for the scattered signals, which significantly increase with optically active media, but can also control the far field radiation profile from the array by introducing an excitation phase term and make the radiating beam significantly directive. Finally, two far field measurement techniques and the corresponding experimental arrangements have been suggested and described.

Chapter 7

[7.1] D.A. Long, "Raman spectroscopy", 1977.

[7.2] C.N. Banwell, "Fundamentals of molecular spectroscopy", McGraw-Hill, 1966.

[7.3] M. Born, "Atomic Physics", Blackie & Son Limited, 4th edition 1946.

[7.4] F.H. Read, "Electromagnetic Radiation", Johnn Wiley & Sons, 1980.

[7.5] A.R. Von Hippel, "Dielectrics and Waves", Hohn Wiley & Sons, 1954.

[7.6] "Surface-enhanced Raman effect", Physics Today, April 1980, p.18.

[7.7] Martin Moskovits, "Surface-Enhanced Spectroscopy", Reviews of Modern Physics, Vol. 57, No. 3, Part I, July 1985.

[7.8] P. Halevi, "Photonic Probes of Surfaces", Electromagnetic Waves: Recent Developments in Research, vol.2, Elsevier, 1995.

[7.9] K. Kneipp1, H. Kneipp, I. Itzkan, R.R. Dasari, M.S. Feld, "Surface-enhanced Raman scattering and biophysics", J. Phys.: Condens. Matter 14 (2002) p.R597–R624.

[7.10] G.C. Schatz, R.P. Van Duyne, "Electromagnetic Mechanism of Surface Enhanced Spectroscopy", reproduced from "Handbook of Vibrational Spectroscopy", J. M. Chalmers and P. R. Griffiths (editors), John Wiley & Sons Ltd, Chichester, 2002.

[7.11] H. Metiu, P. Das, "The Electromagnetic Theory of Surface Enhanced Spectroscopy", Ann. Rev. Phys. Chem., vol.35 (1984), p.507.

[7.12] S. Kruszewski, " Surface enhanced Raman scattering phenomenon", Cryst. Res. Technol. 41, 2006, no.6, p.562.

[7.13] S. Kawata, "Near-Field Optics and Surface Plasmon Polaritons", Topics in Applied Physics vol.81, Springer, 2001.

[7.14] J.A. Stratton, "Electromagnetic Theory", McGraw-Hill Book Company, 1941.

[7.15] P.B. Johnson, R.W. Christy, "Optical Constants of the Noble Metals", Physical Review B, vol.6, no.12, 15 December 1972, p.4370.

[7.16] E.D. Palik, "Handbook of optical constants of solids", Academic Press (1985).

[7.17] J.R. Lakowicz, "Rdiative decay engineering 3. Surface Plasmon-coupled directional emission", Anal. Bioch., vol.324, (2004), p.153.

[7.18] M. Futamata, "Surface-Plasmon-Polariton-Enhanced Raman Scattering from Self-Assembled Monolayers of p-Nitrothiophenol and p-Aminothiophenol on Silver", J. Phys. Chem. 1995, vol. 99, pp.11901-11908.

[7.19] C.A. Balanis, "Antenna Theory Analysis and Design", Harper & Row Publishers New York, 1982.

[7.20] S.R. Pennock, "Microwave engineering : with wireless applications", Macmillan, 1998.

[7.21] A.Tarlis, J.Sarma, F.Causa, "SPW Enhanced Optical Scattering", SIOE'07 "Semiconductors and Integrated Optoelectronics Conference", University of Cardiff, Wales, 1-3 April 2007.

[7.22] E. Hecht, "Optics", Addison Wesley, 3rd edition 1998.

[7.23] A. Ghatak, "Optics", Tata McGraw-Hill Publishing Company Limited New Delhi, 2nd Edition, 1993.

[7.24] G.P. Agrawal, N.K. Dutta, "Semiconductor Lasers", Van Nostrand Reinhold New York, 2nd edition, 1993.

[7.25] H. Ditlbacher, J.R. Krenn, N. Felidj, B. Lamprecht, G. Schider, M. Salermo, A. Leitner, F.R. Aussenegg, "Fluorescence imaging of surface plasmon fields", Applied Physics Letters, vol.80, no.3, 21 January 2002, p.404.

[7.26] J.A. Stratton, "Electromagnetic Theory", McGraw-Hill Book Company, 1941.

Chapter 8

Conclusions and Future work

8.1 Conclusions

A systematic study of the modal properties of Surface Plasmon Waves (SPWs) has been given in this thesis. It has been shown that SPWs can be supported at a single interface structure formed by a dielectric with positive relative permittivity $\varepsilon_d > 0$ and an ideal metal with a negative relative permittivity $\varepsilon_m = - |\varepsilon_{mR}| < 0$, if $\varepsilon_d < |\varepsilon_{mR}|$. For a lossless metal, if $|\varepsilon_{mR}| \approx \varepsilon_d$ then SPWs yield a very large longitudinal propagation constant providing an extremely short field decay depth and modal wavelength making SPWs very attractive for subwavelength applications. In realistic situations however, the metal losses limit the SPWs longitudinal propagation. This detrimental metal effect can be overcome when operating at long wavelengths, but then the SPW field has a large decay depth and a reduced field intensity. It has been shown that a more effective method is the use of multiple dielectric – metal interface structures capable of supporting symmetric and antisymmetric – like SPWs such as the dielectric cladding metal guide (DMD) structure and the metal cladding dielectric guide configuration (MDM). By adjusting the dielectric (D) or metal (M) film thickness, the SPWs can yield subwavelength operation and a significantly extended propagation compared to the single interface case. Interestingly, if $\varepsilon_d > |\varepsilon_{mR}|$ the SPWs can exhibit a negative group velocity and negative total poynting vector.

SPW excitation in prism coupled waveguides is very popular as it allows mode selectivity and ease of fabrication compared to gratings or rough surfaces. The well established for describing electromagnetic wave propagation Transmission Line (T-L) theory has been utilized here over the commonly employed plane wave cascade matrix analysis to study SPW excitation in a Kretschman-Raether (K-R) prism coupled structure. The T-L has the advantage of reducing any intricate multilayer prism coupled structure into a two section T-L circuit which is characterized by the corresponding transverse impedance of each section. Hence, a better physical insight is obtained of the

nature of the contribution by each of the layers to the overall electromagnetic phenomenon. The analysis has shown that the SPW excitation seen as a 'dip' in the power reflection coefficient of the structure corresponds to an impedance matching between the input and the load of the two section T-L circuit, which is a result of transverse resonance. This matching however occurs only if the metal is lossy, as for ideal (lossless) situations the load impedance of the T-L network is purely reactive giving unity power reflection coefficient. The T-L concept has also been successfully applied to model SPW excitation in DMD and MDM prism coupled waveguides where not only SPWs are supported but also "conventional" waves.

Experimental SPW and "conventional" wave excitation in prism coupled waveguide structures has also been demonstrated, and the results were close to the theoretical predictions. Simultaneous excitation of two "conventional" surface waves having the same frequency has shown that a spatial wave beat effect can be produced which corresponds to a time varying high frequency travelling wave enclosed in a low frequency envelope.

The effect of semiconductor optical sources with spectrally broad and divergent output beam on SPW excitation in prism coupled arrangements has also been studied. The analysis studies the field reflection coefficient by performing a numerical convolution between the non-ideal input beam and the corresponding reflected field intensity of the structure calculated considering an ideal source. The input beam profile was assumed to be Gaussian as it was best fitting to the beam shape of typical semiconductor optical sources. Experimental demonstration of the above analysis has been performed by using a Laser diode with emission wavelength in the visible (λ_o = 633nm) and a narrow spectral width ($\delta\lambda \approx$ 1nm), and a SLD with λ_o = 980nm and broad $\delta\lambda$ ($\approx$ 15nm), to excite SPW in a K-R arrangement for different output beam divergent angles for the two sources. Experimental results were in a good agreement with theory and showed that SPW excitation at long wavelengths is more susceptible to the characteristics of the optical source compared to the short wavelength excitation. Hence, such sources have the potential to replace the gas lasers traditionally used for this type of experiment.

A different approach to reduce or even eliminate the effect of the metal losses on the SPW modal properties has been the use of optically active media with optical gain.

When such media are employed in SPW structures, the optical gain can compensate for the metal losses and allow SPW lossless propagation and subwavelength operation. If minimum amount of gain is required then it has been suggested to operate in the IR, use silver, dielectric media with small relative permittivity and employ DMD or MDM structures.

SPW excitation in an optically active prism coupled structure with optically active dielectric films having thickness and amounts of optical gain similar to those employed in semiconductor optical sources has also been analysed. The study has shown that as the gain increases, the "dip" at the power reflection coefficient at the SPW excitation angle becomes shallower and exceeds unity. This result indicates that the metal losses have been overcompensated by the gain and optical amplification takes place. In addition, the corresponding FWHM of the "dip" becomes narrower allowing the system to have a high sensitivity if it is to be used as sensor.

Finally, it has been shown that SPWs excited in prism coupled structures, apart from enhancing weak scattered signals from particles (molecules), can also be employed to control and narrow the far field radiation from those particles. The analysis assumes that an array of such particles is excited and radiates by the use of the SPW field from the prism arrangement. The far field radiation pattern from the array has been evaluated by considering that each one of the particles that form the array is radiating as a dipole antenna. Hence, it has been found that by making use of the longitudinal phase of the excited SPW, the radiation from the array of particles becomes very distinct and directive. Furthermore, this effect becomes more dominant by adjusting the dimensions of the array and especially by increasing the side of the array that coincides with the longitudinal direction of the SPW, producing a larger phase and an end-fire scattered radiation from the particles. If the prism coupled structure where the SPW is excited is also optically active, then much more enhanced scattered signals will be produced which in addition to the use of the SPW phase, a significantly increased collection of those signals can be realised.

8.2 Future Work

The work carried out so far has demonstrated the significant potential of SPWs for being employed in various applications such as a biosensing, subwavelength probing and the design of nanoscale structures. The analyses and experimental results for some of the structures of this thesis show however that further improvements are needed to for achieving a functional SPW device with the required properties.

Chapter 5 has shown that a spatial beat effect can be produced with the use of two simultaneously excited surface modes in a prism coupled arrangement. However, this phenomenon has been demonstrated only with the use of "conventional" surface modes. Since it was shown that SPWs exhibit high field intensity, it would be very interesting to modify the prism coupled DMD structure of Figure 5.2b for optimum symmetric and antisymmetric SPW excitation. As one of the main problems for not achieving optimum SPW excitation seems to be the presence of the cromium film, hence it is suggested to fabricate some structures where the gold film is directly deposited on the SiO_2 and then repeat the experiment. The same process can also be performed for a structure operating in the visible spectrum regime where alignment of the full system becomes easier compared to the corresponding operation in the infrared frequency region.

To complete the investigation of the use of non-ideal optical sources for SPW excitation, it is recommended that the existing model covering the effect of the divergence angle and spectral width of the output beam, is extended to include also any polarisation effects from the source. Experimental demonstration of this concept could be performed by employing a circularly (50% TE – 50% TM) polarised source followed by a polariser to control the degree of polarisation. An alternative approach is to use a linearly (single) polarised source which could be then rotated with respect to the optical axis of the SPW prism coupled structure for introducing the polarisation effect without the use of optical polarisers.

The use of optically active media in SPW structures has shown that lossless SPW propagation and subwavelength operation can be obtained. In practice however there are still some problems that need to be tackled before such structure becomes functional. One of the main problems is whether a metal film adjacent to an optically active dielectric can deteriorate the performance of the latter. In that case it is necessary to

study the effects of the metal – active region interaction. It has also been discussed in chapter 6 that SPWs can be excited in an optically active waveguide structure by employing a prism coupler. According to our knowledge however, there are no practically easily available prism materials with higher refractive index than the optically active dielectric medium so to allow SPW excitation. To overcome this problem it is recommended that a grating instead of a prism is employed. Hence, with reference to the structure of Figure 6.7b it is suggested that the periodicity of such a grating can be formed on the top side of the metal film while the bottom flat side will be in contact with the active medium. In that case the structure could be a heterostructure commonly employed in semiconductor Lasers and SLDs where the top cladding layer has been replaced by a metal contact will have also the grating formed.

The analysis of the radiating dipole array performed in chapter 7 has considered that the particles are placed far away from the metal film hence there are no reflected signals from the metal that affect their radiation. However, in practice this is not the case as the particles are usually situated on the metal or on a dielectric film and are affected by reflected signals (Sommerfeld effect [8.1]). As a consequence, it would be necessary to modify our model describing the far field radiation from an array so to include the effect of these reflected signals from the metal (dielectric) film.

The experimental demonstration of the far field profile from an array of radiating dipoles (particles) excited by a SPW supported in a prism coupled structure has also to be performed. As a suggested in chapter 7, a lens system can be employed to monitor the far field radiation pattern from the particle array, which can be formed of SiO_2 or TiO_2 particles.

Finally, a different approach to increase the intensity of the far field radiation from the array of particle and alter the direction of the radiation could be to produce a standing (rather than the commonly used travelling) wave SPW for exciting the particles (dipoles) (similar to that employed, for example, in phased-array antennae [8.2]).

Hence, it is suggested to study and excite such a standing wave in a prism coupler configuration using two counter-propagating external beams for excitation. The formed standing wave SPW will then (Rayleigh) scatter from the particles on the air side of the

metal surface. The field variation along the direction of propagation, z-axis, for the standing wave will be of the form $\sin(\beta z)$ or $\cos(\beta z)$ where, for typical glass prism, metal, and air (bottom) substrate, the value of β is, in general, nearly the same as k_o, the wavenumber for plane wave propagation in (air) free-space.

Under this assumption ($\beta \approx k_o$), the dipoles will radiate in the free space, with patterns similar to those for very long linear antennae with standing-wave sinusoidal current distributions [8.3]. Hence, a highly collimated bi-directional radiation along the positive/negative longitudinal, z-axis will be produced instead of a radiation pattern tilted towards the direction of propagation but with a quite wide angular distribution generated by travelling SPWs.

References

[8.1] C.A. Balanis, "Antenna Theory Analysis and Design", Harper & Row Publishers New York, 1982.

[8.2] E.C. Jordan, K.G. Balman, "Electromagnetic Waves and Radiating Systems", Prentice-Hall Publications, 2nd edition 1968.

[8.3] J.A. Stratton, "Electromagnetic Theory", McGraw-Hill Book Company, edition 1941.

Appendix A

Maxwell's equations and Vector Relations

A.1. Vector Transformations

ψ is a scalar variable

$\underline{A}$ is a vector

$$\nabla \times (\nabla \times \underline{A}) = \nabla \nabla \cdot \underline{A} - \nabla^2 \underline{A} \tag{A.1}$$

$$\nabla \times (\psi \underline{A}) = \nabla \psi \times \underline{A} + \psi \nabla \times \underline{A} \tag{A.2}$$

$$\nabla \cdot (\nabla \psi) = \nabla^2 \psi \tag{A.3}$$

$$\nabla \cdot (\nabla \times \underline{A}) = 0 \tag{A.4}$$

$$\nabla \times \nabla \psi = 0 \tag{A.5}$$

Co-ordinate systems

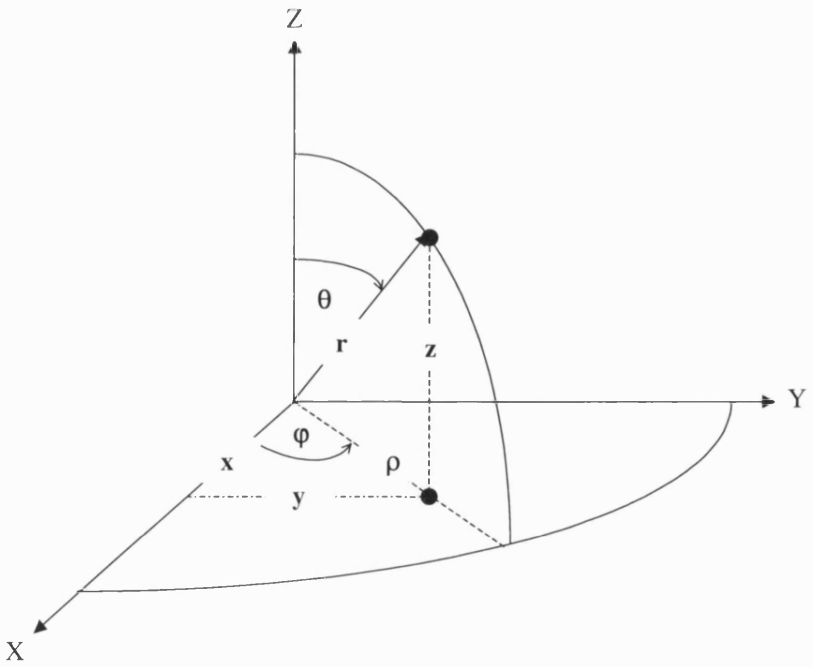

Figure A.1. Relationship between cartesian, cylindrical and spherical co-ordinate systems.

With reference to the co-ordinate systems shown in Figure A.1, the following properties are applying:

Co-ordinate systems variables

Cartesian	x	y	z
Cylindrical	ρ	φ	z
Spherical	r	φ	θ

Table A.1. Co-ordinate systems variables.

Geometrical relations between co-ordinate systems

Cartesian => Cylindrical	Cartesian => Spherical	Cylindrical => Spherical
$x = \rho \cos(\varphi)$	$x = r \sin(\theta) \cos(\varphi)$	$\rho = r \sin(\theta)$
$y = \rho \sin(\varphi)$	$y = r \sin(\theta) \sin(\varphi)$	$z = r \cos(\theta)$
$z = z$	$z = r \cos(\theta)$	$\varphi = \varphi$

Table A.2. Geometrical relations between co-ordinate systems.

Vector $\underline{A}$ in different co-ordinate systems

Cartesian: $$\underline{A} = \hat{x} A_x + \hat{y} A_y + \hat{z} A_z \tag{A.6}$$

Cylindrical: $$\underline{A} = \hat{\rho} A_\rho + \hat{\varphi} A_\varphi + \hat{z} A_z \tag{A.7}$$

Spherical: $$\underline{A} = \hat{r} A_r + \hat{\varphi} A_\varphi + \hat{\theta} A_\theta \tag{A.8}$$

Gradient of scalar ($\nabla\psi$)

Cartesian: $$\nabla\psi = \hat{x} \frac{\partial \psi}{\partial x} + \hat{y} \frac{\partial \psi}{\partial y} + \hat{z} \frac{\partial \psi}{\partial z} \tag{A.9}$$

Cylindrical: $$\nabla\psi = \hat{\rho} \frac{\partial \psi}{\partial \rho} + \hat{\varphi} \frac{1}{\rho} \frac{\partial \psi}{\partial \varphi} + \hat{z} \frac{\partial \psi}{\partial z} \tag{A.10}$$

Spherical: $$\nabla\psi = \hat{r} \frac{\partial \psi}{\partial r} + \hat{\theta} \frac{1}{r} \frac{\partial \psi}{\partial \theta} + \hat{\varphi} \frac{1}{r \sin(\theta)} \frac{\partial \psi}{\partial \varphi} \tag{A.11}$$

Divergence of a vector ($\nabla \cdot \underline{A}$)

Cartesian:
$$\nabla \cdot \underline{A} = \frac{\partial A_x}{\partial x} + \frac{\partial A_y}{\partial y} + \frac{\partial A_z}{\partial z} \tag{A.12}$$

Cylindrical:
$$\nabla \cdot \underline{A} = \frac{1}{\rho}\frac{\partial}{\partial \rho}\left(\rho A_\rho\right) + \frac{1}{\rho}\frac{\partial A_\varphi}{\partial \varphi} + \frac{\partial A_z}{\partial z} \tag{A.13}$$

Spherical:
$$\nabla \cdot \underline{A} = \frac{1}{r^2}\frac{\partial}{\partial r}\left(r^2 A_r\right) + \frac{1}{r\sin(\theta)}\frac{\partial}{\partial \theta}\left(\sin(\theta) A_\theta\right) + \frac{1}{r\sin(\theta)}\frac{\partial A_\varphi}{\partial \varphi} \tag{A.14}$$

Curl of a vector ($\nabla \times \underline{A}$)

Cartesian:
$$\nabla \times \underline{A} = \hat{x}\left[\frac{\partial A_z}{\partial z} - \frac{\partial A_y}{\partial y}\right] + \hat{y}\left[\frac{\partial A_x}{\partial x} - \frac{\partial A_z}{\partial z}\right] + \hat{z}\left[\frac{\partial A_y}{\partial y} - \frac{\partial A_x}{\partial x}\right] \tag{A.15}$$

Cylindrical:
$$\nabla \times \underline{A} = \hat{\rho}\left[\frac{1}{\rho}\frac{\partial A_z}{\partial \varphi} - \frac{\partial A_\varphi}{\partial z}\right] + \hat{\varphi}\left[\frac{\partial A_\rho}{\partial z} - \frac{\partial A_z}{\partial \rho}\right] + \hat{z}\left[\frac{1}{\rho}\frac{\partial}{\partial \rho}\left(\rho A_\varphi\right) - \frac{1}{\rho}\frac{\partial A_\rho}{\partial \varphi}\right] \tag{A.16}$$

Spherical:
$$\begin{aligned}\nabla \times \underline{A} = {} & \hat{r}\frac{1}{r\sin(\theta)}\left[\frac{\partial}{\partial \theta}\left(\sin(\theta) A_\varphi\right) - \frac{\partial A_\theta}{\partial \varphi}\right] \\ & + \hat{\theta}\frac{1}{r}\left[\frac{1}{\sin(\theta)}\frac{\partial A_r}{\partial \varphi} - \frac{\partial}{\partial r}\left(r A_\varphi\right)\right] \\ & + \hat{\varphi}\frac{1}{r}\left[\frac{\partial}{\partial r}\left(r A_\theta - \frac{\partial A_r}{\partial \theta}\right)\right]\end{aligned} \tag{A.17}$$

Laplacian of a scalar ($\nabla^2\psi$)

Cartesian:
$$\nabla^2 \psi = \frac{\partial^2 \psi}{\partial x^2} + \frac{\partial^2 \psi}{\partial y^2} + \frac{\partial^2 \psi}{\partial z^2} \tag{A.18}$$

Cylindrical:
$$\nabla^2 \psi = \frac{1}{\rho}\frac{\partial}{\partial \rho}\left(\rho \frac{\partial \psi}{\partial \rho}\right) + \frac{1}{\rho^2}\frac{\partial^2 \psi}{\partial \varphi^2} + \frac{\partial^2 \psi}{\partial z^2} \tag{A.19}$$

Spherical:
$$\nabla^2 \psi = \frac{1}{r^2}\frac{\partial}{\partial r}\left(r^2 \frac{\partial \psi}{\partial r}\right) + \frac{1}{r^2 \sin(\theta)}\frac{\partial}{\partial \theta}\left(\sin(\theta)\frac{\partial \psi}{\partial \theta}\right) + \frac{1}{r^2 \sin^2(\theta)}\frac{\partial^2 \psi}{\partial \varphi^2} \tag{A.20}$$

A.2. Maxwell's equations

Charge free, ρ, source free, $\underline{J} = 0$, non-magnetic medium, $\mu = 1$, and harmonic time dependence, $\exp[+j\omega t]$ with ω and t both real and positive, are assumed.

Cartesian co-ordinates

$$\partial_x \varepsilon E_x + \partial_y \varepsilon E_y + \partial_z \varepsilon E_z = 0 \tag{A.21}$$

$$\partial_x H_x + \partial_y H_y + \partial_z H_z = 0 \tag{A.22}$$

$$-j\omega\mu_o H_x = \partial_y E_z - \partial_z E_y \tag{A.23}$$

$$-j\omega\mu_o H_y = \partial_z E_x - \partial_x E_z \tag{A.24}$$

$$-j\omega\mu_o H_z = \partial_x E_y - \partial_y E_x \tag{A.25}$$

$$j\omega\varepsilon_o \varepsilon E_x = \partial_z H_y - \partial_y H_z \tag{A.26}$$

$$j\omega\varepsilon_o \varepsilon E_y = \partial_x H_z - \partial_z H_x \tag{A.27}$$

$$j\omega\varepsilon_o \varepsilon E_z = \partial_y H_x - \partial_x H_y \tag{A.28}$$

Cylindrical co-ordinates

$$\frac{1}{\rho}\partial_\rho \rho\varepsilon E_\rho + \frac{1}{\rho}\partial_\varphi \varepsilon E_\varphi + \partial_z \varepsilon E_z = 0 \tag{A.29}$$

$$\frac{1}{\rho}\partial_\rho \rho H_\rho + \frac{1}{\rho}\partial_\varphi H_\varphi + \partial_z H_z = 0 \tag{A.30}$$

$$-j\omega\mu_o H_\rho = \frac{1}{\rho}\partial_\varphi E_z - \partial_z E_\varphi \tag{A.31}$$

$$-j\omega\mu_o H_\varphi = \partial_z E_\rho - \partial_\rho E_z \tag{A.32}$$

$$-j\omega\mu_o H_z = \frac{1}{\rho}\partial_\rho (\rho E_\varphi) - \frac{1}{\rho}\partial_\varphi E_\rho \tag{A.33}$$

$$j\omega\varepsilon_o \varepsilon E_\rho = \partial_z H_\varphi - \frac{1}{\rho}\partial_\varphi H_z \tag{A.34}$$

$$j\omega\varepsilon_o \varepsilon E_\varphi = \partial_\rho H_z - \partial_z H_\rho \tag{A.35}$$

$$j\omega\varepsilon_o \varepsilon E_z = \frac{1}{\rho}\partial_\varphi H_\rho - \frac{1}{\rho}\partial_\rho (\rho H_\varphi) \tag{A.36}$$

Appendix B

Single Interface Waveguide Properties

B.1. Single interface TE field components

With reference to Figure 3.1, consider transverse electric (TE) wave propagation. Such propagating waves are best described by their electric field component which for the structure of Figure 3.1 is of the form

$$E_y(x,z) = F(x)e^{-j\beta z} \tag{B.1}$$

assuming no field variation along y and harmonic time dependency which for the sake of the simplicity has been omitted. Hence, the transverse field variation F(x) is given by

$$F(x) = \begin{cases} A_1 e^{-k_1 x}, & x \geq 0 \\ A_2 e^{+k_2 x}, & x \leq 0 \end{cases} \tag{B.2}$$

where k_1, k_2, A_1 and A_2 are defined in section 3.1. From Maxwell's equations, eqn.(2.1), the rest non-zero TE field components are $H_x(x,z)$ and $H_z(x,z)$, described by

$$H_x = -j\frac{1}{\omega\mu_o}\frac{\partial E_y}{\partial z} \tag{B.3}$$

$$H_z = +j\frac{1}{\omega\mu_o}\frac{\partial E_y}{\partial x} \tag{B.4}$$

Hence, the fields in the two media have the following variation:

$\Rightarrow x \geq 0$

$$E_y(x,z) = A_1 e^{-k_1 x} e^{-j\beta z} \tag{B.5}$$

$$H_x = -\frac{\beta}{\omega\mu_o}E_y \tag{B.6}$$

$$H_z = -j\frac{k_1}{\omega\mu_o}E_y \tag{B.7}$$

$\Rightarrow x \leq 0$

$$E_y(x,z) = A_2 e^{-k_2 x} e^{-j\beta z} \tag{B.8}$$

$$H_x = -\frac{\beta}{\omega\mu_o} E_y \tag{B.9}$$

$$H_z = +j\frac{k_2}{\omega\mu_o} E_y \tag{B.10}$$

B.2. Single interface longitudinal propagation constant

With reference to the single interface structure of Figure 3.1 and assuming TM wave propagation, the longitudinal propagation constant β, eqn.(3.8), of the surface electromagnetic wave with field components as given by eqns.(3.5) - (3.6) is studied for different ε_1 and ε_2 combinations for obtaining confined (bound) propagation. In the following sections, the analysis will accept solutions which satisfy confined wave propagation when β is of the form $\beta = \beta_R - j\,\beta_I$, where $\beta_R > 0$ and $\beta_I > 0$.

From eqn.(3.8),

$$\beta^2 = k_o^2 \frac{\varepsilon_1 \varepsilon_2}{\varepsilon_1 + \varepsilon_2} = k_o^2 \varepsilon_1 \frac{\varepsilon_2}{\varepsilon_1 + \varepsilon_2} \tag{B.11}$$

1) If $\varepsilon_1 = \varepsilon_{1R} > 0$ and $\varepsilon_2 = \varepsilon_{2R} > 0$ then eqn.(B.11) gives

$$\beta^2 = k_o^2 \varepsilon_1 \frac{\varepsilon_2}{\varepsilon_1 + \varepsilon_2} < k_o^2 \varepsilon_1 \tag{B.12}$$

which indicates that bound propagation cannot be sustained in the structure as $k_{x1}^2 < 0$, eqn.(3.3), hence oscillating solutions exist and not exponentially decaying.

2) If $\varepsilon_1 = \varepsilon_{1R} > 0$ and $\varepsilon_2 = -|\varepsilon_{2R}| < 0$ then eqn.(3.8) becomes

$$\beta^2 = k_o^2 \varepsilon_1 \frac{-|\varepsilon_{2R}|}{\varepsilon_1 - |\varepsilon_{2R}|} > k_o^2 \varepsilon_1 \tag{B.13}$$

which allows bound modes to be obtained only if $|\varepsilon_{2R}| > \varepsilon_{1R}$.

3) If $\varepsilon_2 = \varepsilon_{2R} - j\varepsilon_{2I}$ and $\varepsilon_1 = \varepsilon_{1R} > 0$ with $\varepsilon_{2R} > 0$, $\varepsilon_{2I} > 0$, and $\varepsilon_{2R} >> \varepsilon_{2I}$, then eqn.(3.8) takes the form:

$$\beta^2 = k_o^2 \varepsilon_{1R} \frac{\varepsilon_{2R} - j\varepsilon_{2I}}{\varepsilon_{2R} + \varepsilon_{1R} - j\varepsilon_{2I}} = k_o^2 \varepsilon_{1R} \left[1 - \frac{\varepsilon_{1R}(\varepsilon_{2R} + \varepsilon_{1R})}{(\varepsilon_{1R} + \varepsilon_{2R})^2 + \varepsilon_{2I}^2} - j\frac{\varepsilon_{1R}\varepsilon_{2I}}{(\varepsilon_{1R} + \varepsilon_{2R})^2 + \varepsilon_{2I}^2} \right] \tag{B.14}$$

Hence,

$$\begin{aligned} \beta &= \pm k_o \sqrt{\varepsilon_{1R}} \left[1 - \frac{\varepsilon_{1R}(\varepsilon_{2R} + \varepsilon_{1R})}{(\varepsilon_{1R} + \varepsilon_{2R})^2 + \varepsilon_{2I}^2} - j\frac{\varepsilon_{1R}\varepsilon_{2I}}{(\varepsilon_{1R} + \varepsilon_{2R})^2 + \varepsilon_{2I}^2} \right]^{1/2} = \\ &= \pm k_o \sqrt{\varepsilon_{1R}} \left[1 - \frac{\varepsilon_{1R}(\varepsilon_{1R} + \varepsilon_{2R})}{(\varepsilon_{1R} + \varepsilon_{2R})^2 + \varepsilon_{2I}^2} \right]^{1/2} \left[1 - j\frac{\varepsilon_{2I}\varepsilon_{1R}}{\varepsilon_{2R}^2 + \varepsilon_{1R}\varepsilon_{2R} + \varepsilon_{2I}^2} \right]^{1/2} \end{aligned} \tag{B.15}$$

with a real part given as

$$\beta_R \approx k_o \sqrt{\varepsilon_{1R}} \left(1 - \frac{\varepsilon_{1R}(\varepsilon_{1R} + \varepsilon_{2R})}{(\varepsilon_{1R} + \varepsilon_{2R})^2 + \varepsilon_{2I}^2} \right)^{1/2} < k_o \sqrt{\varepsilon_{1R}} \tag{B.16}$$

and an imaginary as

$$\beta_I \approx \frac{k_o}{2} \left[\frac{\varepsilon_{2I}\varepsilon_{1R}^{3/2}}{\left[\varepsilon_{2R}^2 + \varepsilon_{1R}\varepsilon_{2R} + \varepsilon_{2I}^2\right]^{1/2}} \frac{1}{\left[(\varepsilon_{1R} + \varepsilon_{2R})^2 + \varepsilon_{2I}^2\right]^{1/2}} \right] > 0 \tag{B.17}$$

Since eqns.(A.15) and (A.16) are both positive, hence a propagating wave which is attenuated along the positive z direction is possible to be obtained.

4) If $\varepsilon_1 = \varepsilon_{1R}$ and $\varepsilon_2 = -|\varepsilon_{2R}| - j|\varepsilon_{2I}|$ with $\varepsilon_{1R} > 0$ and $|\varepsilon_{2R}| >> |\varepsilon_{2I}|$, then eqn.(3.8) takes the form

$$\begin{aligned} \beta^2 &= k_o^2 \varepsilon_{1R} \frac{-|\varepsilon_{2R}| - j|\varepsilon_{2I}|}{-|\varepsilon_{2R}| - j|\varepsilon_{2I}| + \varepsilon_{1R}} \\ &= k_o^2 \varepsilon_{1R} \left[1 + \frac{(|\varepsilon_{2R}| - \varepsilon_{1R})\varepsilon_{1R}}{(|\varepsilon_{2R}| - \varepsilon_{1R})^2 + |\varepsilon_{2I}|^2} \right] \left[1 - j\frac{|\varepsilon_{2I}|\varepsilon_{1R}}{|\varepsilon_{2I}|^2 - |\varepsilon_{2I}|\varepsilon_{1R} + |\varepsilon_{2I}|^2} \right] \end{aligned} \tag{B.18}$$

and gives

$$\beta \approx \pm k_o \sqrt{\varepsilon_{1R}} \left[1 + \frac{(|\varepsilon_{2R}| - \varepsilon_{1R})\varepsilon_{1R}}{(|\varepsilon_{2R}| - \varepsilon_{1R})^2 + |\varepsilon_{2I}|^2} \right]^{1/2} \left[1 - \frac{j}{2} \frac{|\varepsilon_{2I}|\varepsilon_{1R}}{|\varepsilon_{2I}|^2 - |\varepsilon_{2I}|\varepsilon_{1R} + |\varepsilon_{2I}|^2} \right] \tag{B.19}$$

with a real part given by

$$\beta_R \approx k_o\sqrt{\varepsilon_{1R}}\left[1+\frac{\left(|\varepsilon_{2R}|-\varepsilon_{1R}\right)\varepsilon_{1R}}{\left(|\varepsilon_{2R}|-\varepsilon_{1R}\right)^2+|\varepsilon_{2I}|^2}\right]^{1/2} > k_o\sqrt{\varepsilon_{1R}} \qquad \text{(B.20)}$$

and an imaginary by

$$\beta_I \approx \frac{k_o}{2}\frac{1}{\left[\left(|\varepsilon_{2R}|-\varepsilon_{1R}\right)^2+|\varepsilon_{2I}|^2\right]^{1/2}}\left[\frac{|\varepsilon_{2I}|\varepsilon_{1R}^{3/2}}{\left[|\varepsilon_{2R}|^2-|\varepsilon_{2I}|\varepsilon_{1R}+|\varepsilon_{2I}|^2\right]^{1/2}}\right] > 0 \qquad \text{(B.21)}$$

Both eqns.(B.20) and (B.21) are positive and $\beta_R > k_o\sqrt{\varepsilon_{1R}}$ for $|\varepsilon_{2R}| >> \varepsilon_{1R}$, allowing bound wave propagation. This type of electromagnetic surface wave corresponds to the Surface Plasmon Waves.

5) If $\varepsilon_1 = \varepsilon_{1R}$ and $\varepsilon_2 = -j|\varepsilon_{2I}|$ with $\varepsilon_{1R} > 0$, eqn.(3.8) becomes

$$\beta^2 = k_o^2\frac{\varepsilon_{1R}|\varepsilon_{2I}|}{\varepsilon_{1R}^2+|\varepsilon_{2I}|^2}\left[|\varepsilon_{2I}|-j\varepsilon_{1R}\right] \qquad \text{(B.22)}$$

and therefore

$$\beta = \pm k_o\left[\frac{\varepsilon_{1R}|\varepsilon_{2I}|}{\varepsilon_{1R}^2+|\varepsilon_{2I}|^2}\right]^{1/2}\left[|\varepsilon_{2I}|-j\varepsilon_{1R}\right]^{1/2} \qquad \text{(B.23)}$$

a) If $|\varepsilon_{2I}| > \varepsilon_{1R}$ then eqn.(B.23) gives

$$\begin{aligned}\beta &= \pm k_o\left[\frac{\varepsilon_{1R}|\varepsilon_{2I}|}{\varepsilon_{1R}^2+|\varepsilon_{2I}|^2}\right]^{1/2}\sqrt{|\varepsilon_{2I}|}\left[1-j\frac{\varepsilon_{1R}}{|\varepsilon_{2I}|}\right]^{1/2} \\ &\approx \pm k_o\left[\frac{\varepsilon_{1R}|\varepsilon_{2I}|}{\varepsilon_{1R}^2+|\varepsilon_{2I}|^2}\right]^{1/2}\sqrt{|\varepsilon_{2I}|}\left[1-\frac{j}{2}\frac{\varepsilon_{1R}}{|\varepsilon_{2I}|}\right]\end{aligned} \qquad \text{(B.24)}$$

Hence,

$$\beta_R \approx k_o\left[\frac{\varepsilon_{1R}\varepsilon_{2I}^2}{\varepsilon_{1R}^2+\varepsilon_{2I}^2}\right]^{1/2} \qquad \text{(B.25)}$$

$$\beta_I \approx \frac{k_o}{2}\frac{\varepsilon_{1R}^{3/2}}{\left[\varepsilon_{1R}^2+\varepsilon_{2I}^2\right]^{1/2}} > 0 \qquad \text{(B.26)}$$

This case of surface wave represents Zenneck waves supported between a lossless dielectric with real permittivity $\varepsilon_1 = \varepsilon_{1R} > 0$ and a high conducting medium with $\varepsilon_2 = -j|\varepsilon_{2I}|$ at radio frequencies.

b) If $|\varepsilon_{2I}| < \varepsilon_{1R}$ then eqn.(B.23) gives

$$\begin{aligned}\beta &= \pm k_o \left[\frac{\varepsilon_{1R}|\varepsilon_{2I}|}{\varepsilon_{1R}^2 + |\varepsilon_{2I}|^2}\right]^{1/2} \sqrt{\varepsilon_{1R}}\sqrt{j}\left[-j\frac{|\varepsilon_{2I}|}{\varepsilon_{1R}} - 1\right]^{1/2} \\ &\approx \pm k_o \left[\frac{\varepsilon_{1R}|\varepsilon_{2I}|}{\varepsilon_{1R}^2 + |\varepsilon_{2I}|^2}\right]^{1/2} \sqrt{\varepsilon_{1R}}\sqrt{j}\left[-1 - \frac{j}{2}\frac{|\varepsilon_{2I}|}{\varepsilon_{1R}}\right]\end{aligned} \tag{B.27}$$

By considering that

$$\sqrt{j} = \pm\frac{\sqrt{2}}{2}(1+j) \tag{B.28}$$

eqn.(B.27) becomes

$$\beta \approx \pm k_o \left[\frac{\varepsilon_{1R}|\varepsilon_{2I}|}{\varepsilon_{1R}^2 + |\varepsilon_{2I}|^2}\right]^{1/2} \sqrt{\varepsilon_{1R}}\frac{\sqrt{2}}{2}(1+j)\left[-1 - \frac{j}{2}\frac{|\varepsilon_{2I}|}{\varepsilon_{1R}}\right] \tag{B.29}$$

which can be rewritten as

$$\beta \approx \pm\frac{\sqrt{2}}{2} k_o \sqrt{\varepsilon_{1R}}\left[\frac{\varepsilon_{1R}|\varepsilon_{2I}|}{\varepsilon_{1R}^2 + |\varepsilon_{2I}|^2}\right]^{1/2} \left[-\frac{\varepsilon_{1R} - |\varepsilon_{2I}|}{\varepsilon_{1R}} - j\frac{2\varepsilon_{1R} + |\varepsilon_{2I}|}{2\varepsilon_{1R}}\right] \tag{B.30}$$

The real part of eqn.(B.30) is

$$\beta_R \approx \frac{\sqrt{2}}{2} k_o \sqrt{\varepsilon_{1R}}\left[\frac{\varepsilon_{1R}|\varepsilon_{2I}|}{\varepsilon_{1R}^2 + |\varepsilon_{2I}|^2}\right]^{1/2} \frac{\varepsilon_{1R} - |\varepsilon_{2I}|}{\varepsilon_{1R}} \tag{B.31}$$

and the imaginary

$$\beta_I \approx -\frac{\sqrt{2}}{4} k_o \left[\frac{|\varepsilon_{2I}|}{\varepsilon_{1R}^2 + |\varepsilon_{2I}|^2}\right]^{1/2} \left[2\varepsilon_{1R} + |\varepsilon_{2I}|\right] < 0 \tag{B.32}$$

Since eqn.(B.32) gives $\beta_I < 0$, hence if $|\varepsilon_{2I}| < \varepsilon_{1R}$ when $\varepsilon_1 = \varepsilon_{1R}$ and $\varepsilon_2 = -j|\varepsilon_{2I}|$ with $\varepsilon_{1R} > 0$, it is not possible to allow bound wave propagation.

B.3. Single Interface SPW group velocity

With reference to eqn.(3.8), the longitudinal propagation constant β for a SPW travelling at the single interface of Figure 3.1 which is formed by a lossless dielectric and an ideal metal with relative permittivities $\varepsilon_1 > 0$ and $\varepsilon_2 = -|\varepsilon_2|$ respectively is

$$\beta = k_o \sqrt{\frac{\varepsilon_1 |\varepsilon_2|}{|\varepsilon_2| - \varepsilon_1}} \tag{B.33}$$

From Drude's model, $|\varepsilon_2|$ can be written as, eqn.(**2.30**),

$$|\varepsilon_2| = \left(\frac{\omega_p}{\omega}\right)^2 - 1 \tag{B.34}$$

and the group velocity U_g of the SPW wave can be found by

$$U_g = \frac{\partial \omega}{\partial \beta} = \frac{1}{\frac{\partial \beta}{\partial \omega}} \tag{B.35}$$

where

$$\frac{\partial \beta}{\partial \omega} = \frac{\partial\left[\frac{\omega}{c}\sqrt{\frac{\varepsilon_1|\varepsilon_2|}{|\varepsilon_2|-\varepsilon_1}}\right]}{\partial \omega} = \frac{1}{c}\left\{\sqrt{\frac{\varepsilon_1|\varepsilon_2|}{|\varepsilon_2|-\varepsilon_1}} + \omega\frac{\partial\left[\sqrt{\frac{\varepsilon_1|\varepsilon_2|}{|\varepsilon_2|-\varepsilon_1}}\right]}{\partial \omega}\right\} \tag{B.36}$$

$$\frac{\partial\left[\sqrt{\frac{\varepsilon_1|\varepsilon_2|}{|\varepsilon_2|-\varepsilon_1}}\right]}{\partial \omega} = -\frac{1}{2\sqrt{\frac{\varepsilon_1|\varepsilon_2|}{|\varepsilon_2|-\varepsilon_1}}}\frac{\varepsilon_1^2}{(|\varepsilon_2|-\varepsilon_1)^2}\frac{\partial|\varepsilon_2|}{\partial \omega} \tag{B.37}$$

$$\frac{\partial|\varepsilon_2|}{\partial \omega} = -2\frac{\omega_p^2}{\omega^3} \tag{B.38}$$

From eqn.(B.38), eqn.(B.37) becomes

$$\frac{\partial\left[\sqrt{\frac{\varepsilon_1|\varepsilon_2|}{|\varepsilon_2|-\varepsilon_1}}\right]}{\partial \omega} = \frac{1}{\sqrt{\frac{\varepsilon_1|\varepsilon_2|}{|\varepsilon_2|-\varepsilon_1}}}\frac{\varepsilon_1^2}{(|\varepsilon_2|-\varepsilon_1)^2}\frac{\omega_p^2}{\omega^3} \tag{B.39}$$

giving

$$\frac{\partial\beta}{\partial\omega}=\frac{1}{c}\left\{\sqrt{\frac{\varepsilon_1|\varepsilon_2|}{|\varepsilon_2|-\varepsilon_1}}+\omega\frac{1}{\sqrt{\frac{\varepsilon_1|\varepsilon_2|}{|\varepsilon_2|-\varepsilon_1}}}\frac{\varepsilon_1^2}{(|\varepsilon_2|-\varepsilon_1)^2}\frac{\omega_p^2}{\omega^3}\right\} \qquad (B.40)$$

$$=\frac{\varepsilon_1^{1/2}}{c}\left\{\frac{\sqrt{|\varepsilon_2|}\,(|\varepsilon_2|-\varepsilon_1)\,\omega^2+\varepsilon_1\,\omega_p^2}{(|\varepsilon_2|-\varepsilon_1)^{3/2}\omega^2}\right\}$$

Therefore the SPW group velocity becomes, eqn.(B.35),

$$U_g=\frac{\partial\omega}{\partial\beta}=\frac{c}{\varepsilon_1^{1/2}}\left\{\frac{(|\varepsilon_2|-\varepsilon_1)^{3/2}\omega^2}{\sqrt{|\varepsilon_2|}\,(|\varepsilon_2|-\varepsilon_1)\,\omega^2+\varepsilon_1\,\omega_p^2}\right\}>0 \qquad (B.41)$$

which is positive as long as a propagating SPW mode exist, i.e. $|\varepsilon_2| > \varepsilon_1$. If however, $|\varepsilon_2|=\varepsilon_1$ then it is clear that $U_g=0$, eqn.(B.41).

Appendix C

Dielectric Waveguides

One of the fundamental applications of the total reflection phenomenon is found in the operation of optical waveguides [C.1]. The most well known and simplest waveguide structure is the three-layer slab as it is shown in Figure C.1, [C.1]. It is constituted of a lossless dielectric layer (core) of finite thickness h = 2b, $-b \leq x \leq +b$, and real refractive index $n_2 > 0$ sandwiched between two semi-infinite lossless dielectric media (cladding), with real refractive index $n_1 > 0$, $x > +b$, and $n_2 > 0$, $x < -b$, respectively. Since optical signals need to be confined inside the core to allow propagation, the use of total reflection phenomenon requires that $n_2 > n_1 \geq n_3 > 0$ (for a symmetric guide $n_1 = n_3$), [C.1]. The relative permittivity for each medium is $\varepsilon_1 = n_1^2$, $\varepsilon_2 = n_2^2$ and $\varepsilon_3 = n_3^2$.

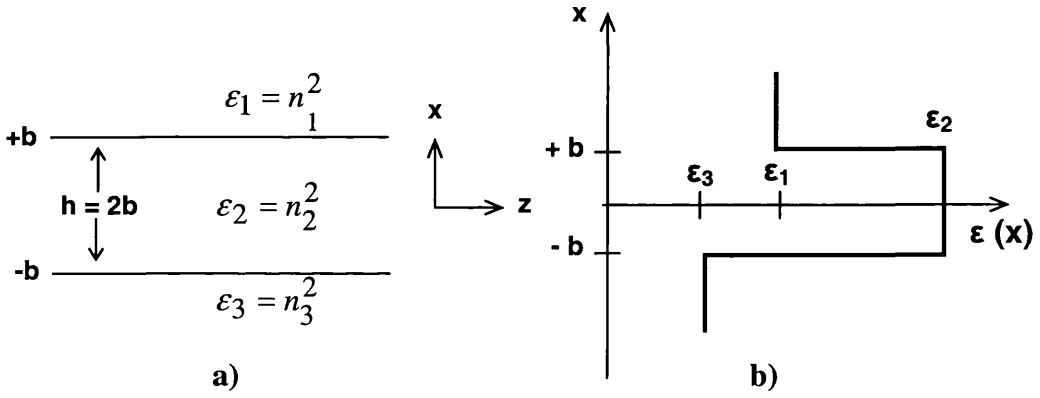

Figure C.1. a) Three layer slab optical waveguide structure and b) corresponding relative permittivity profile.

With reference to Figure C.1, guided electromagnetic waves can be classified as either Transverse Electric (TE) polarized (also known as s-polarised wave) where the electric field is normal to the plane of incidence (poi) (x-z) or Transverse Magnetic (TM) polarized (also known as p-polarised wave) where the magnetic field is normal to the poi [C.1]. Hence, this appendix will study the properties of both TE and TM guided waves supported in the three layer slab dielectric waveguide arrangement of Figure C.1.

Note that the analysis in the following sections will be done for the optical waveguide structure of Figure C.1, by considering that $\varepsilon_1 = \varepsilon_3$.

C.1. TE surface waves

The analysis of TE electromagnetic waves can be best performed by considering the normal to the poi electric field component which with reference to Figure C.1 is $\tilde{E}_y$. By assuming no field variation along y, $\tilde{E}_y$ is of the form

$$\tilde{E}_y(x,z,t) = E_y(x)\exp[+j(\omega t - \beta z)] \qquad (C.1)$$

where β is the longitudinal propagation constant, $\exp[+j\omega t]$ denotes time dependency and ω, t are both real and positive representing angular frequency and time respectively. $E_y(x)$ represents the transverse field variation along x direction and can be found by solving the wave equation, eqn.(2.7), in every region.

By assuming no field variation along y, $\partial y \equiv 0$, the wave equation becomes, eqn.(2.7),

$$\left[\frac{d^2}{dx^2} + \left(k_o^2\varepsilon_q - \beta^2\right)\right]E_y(x) = 0 \qquad (C.2)$$

giving

$$E_y(x) = A_q \exp\left[-jk_{x(q)}x\right] + B_q \exp\left[+jk_{x(q)}x\right] \qquad (C.3)$$

where q = 1, 2 denotes region 1 and 2 respectively, A_q and B_q are the corresponding field amplitudes and $k_{x(q)}$ is the transverse propagation constant in the q^{th} medium which is of the form

$$k_{x(q)} = \sqrt{k_o^2\varepsilon_q - \beta^2} \qquad (C.4)$$

For confined propagation it is necessary that the field amplitudes in medium 1, $x \geq +b$ and $x \leq -b$, tend to zero as $x \rightarrow \pm\infty$, which can be achieved only if decaying E_y field solutions exist in eqn.(C.3). This result can be achieved if $k_{x(1)}$ is imaginary

$$k_{x(1)} = \pm j\left|k_{x(1)}\right| = \pm j\sqrt{\beta^2 - k_o^2\varepsilon_1} \qquad (C.5)$$

which needs a β in the range

$$k_o^2\varepsilon_1 < \beta^2 < k_o^2\varepsilon_2 \qquad (C.6)$$

If $\beta^2 > k_o^2 \varepsilon_2$ then the waveguide structure cannot support any type of waves, whereas for $\beta^2 < k_o^2 \varepsilon_1$, non-confined electromagnetic waves can be obtained [C.2]. In that case the fields in the cladding, $x \geq +b$ and $x \leq -b$, are oscillatory since $k_{x(1)}$, eqn.(C.4), is real and positive. A summary of the available field types in the waveguide structure for various β values is given in Figure C.2.

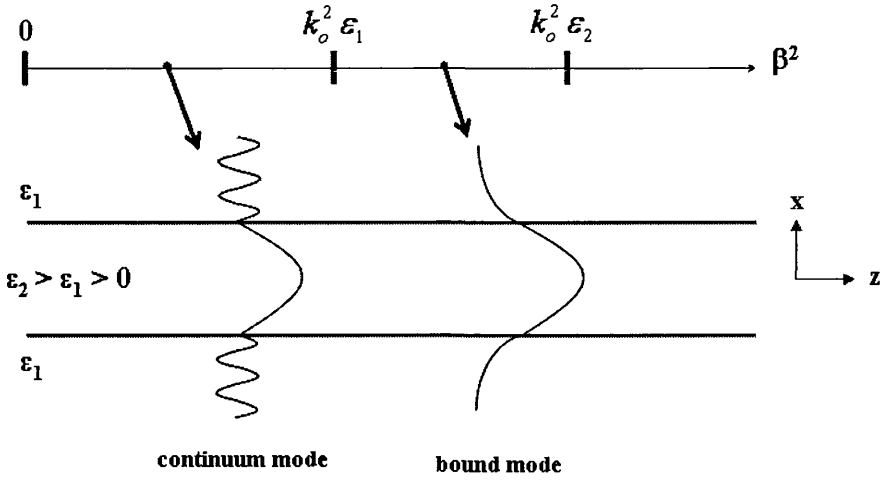

Figure C.2. Pictorial representation of the different modes for different β ranges if $\varepsilon_2 > \varepsilon_1 > \varepsilon_3$.

As a consequence, E_y for confined propagation will have the form

$$E_y(x) = \begin{cases} A_1 \exp\left[-|k_{x(1)}|\, x\right], & x > +b \\ A_2 \cos\left(k_{x(2)}\, x\right) + B_2 \sin\left(k_{x(2)}\, x\right), & -b < x < +b \\ B_1 \exp\left[+|k_{x(1)}|\, x\right], & x < -b \end{cases} \qquad \text{(C.7)}$$

From Maxwell's equations, eqn.(2.2), the rest non-zero electric and magnetic field components are $\tilde{H}_z$ and $\tilde{H}_x$ having transverse field variation found from

$$H_z = \frac{j}{\omega \mu_o} \frac{\partial E_y}{\partial x} \qquad \text{(C.8)}$$

$$H_x = -\frac{\beta}{\omega \mu_o} E_y \qquad \text{(C.9)}$$

The continuity of the tangential fields $\tilde{E}_y$ and $\tilde{H}_z$ at the interfaces x = ± b yields the dispersion equation of the structure which provides the allowed values of β *(modes)* for confined propagation [C.3]

$$\tan(u) = \frac{2vu}{u^2 - v^2} \tag{C.10}$$

where $v = b\left|k_{x(1)}\right|$ and $u = b\,k_{x(2)}$.

The dispersion equation can split into

$$v = u\tan(u) \tag{C.11}$$

$$v = -u\cot(u) \tag{C.12}$$

representing symmetric, eqn.(C.11), and antisymmetric, eqn.(C.12), field solutions respectively. By combining $\left|k_{x(1)}\right|$, eqn.(C.5), and $k_{x(2)}$, eqn.(C.4), it is possible to eliminate β and obtain the normalized frequency w of the waveguide structure,

$$v^2 + u^2 = b^2 k_o^2 [\varepsilon_2 - \varepsilon_1] = w^2 \tag{C.13}$$

which represents a circle with radius w.

To find β for confined wave propagation, it is necessary to solve eqs.(C.10) and (C.13) numerically with the use of computer algorithms [C.3] or in the simplest case of a three layer slab guide graphically. With reference to the structure of Figure C.1, the TE guided modes can be obtained by plotting w, eqn.(C.13), and the corresponding symmetric, eqn.(C.11), or antisymmetric, eqn.(C.12), dispersion equation as a function of u and v. Any intersection between the two functions will correspond to a guided TE wave. A typical schematic for graphically obtaining β is presented in Figure C.3.

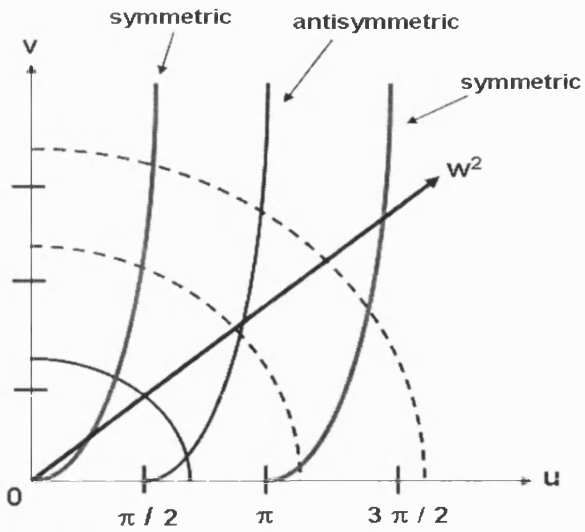

Figure C.3. Dispersion plot for TE surface wave propagation.

It is clear from the graph of Figure C.3 that the number of confined TE modes depends on the value of w. For $0 < w < \pi/2$ only a symmetric mode is obtained, whereas when $w > \pi/2$ an antisymmetric can in addition appears. As w increases, confined modes appear successively, first of one category (symmetric) and then of the other (antisymmetric). As a consequence the support or not of a mode in a waveguide structure depends on the thickness h of the guide, the vacuum (free space) wavelength λ_o and the relative permittivity step between the core and the cladding $[\varepsilon_2 - \varepsilon_1]$. A typical schematic of the first symmetric and antisymmetric E_y transverse field wave pattern is given in Figure C.4.

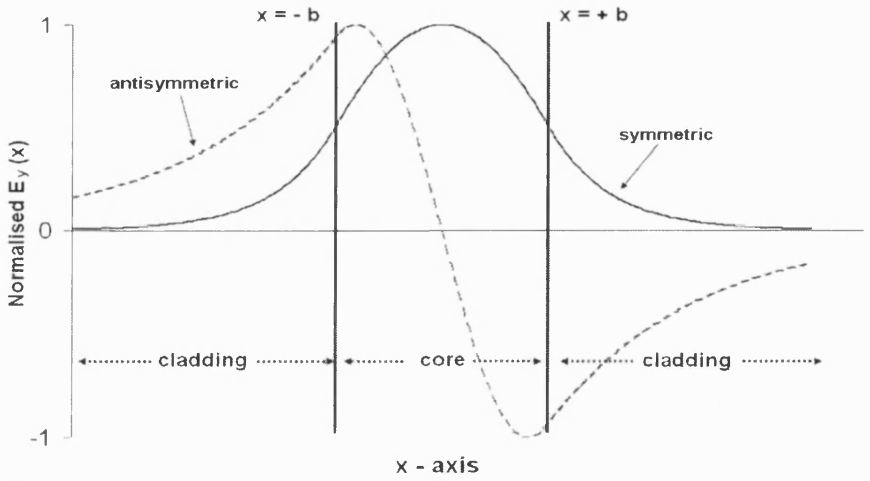

Figure C.4. Symmetric and antisymmetric $E_y(x)$ field distribution.

The Poynting vector $\underline{S}$, eqn.(2.11), of the structure is only along the direction of the wave propagation z and is given as

$$S_z(x,z) = \frac{\beta}{2\omega\mu_o}\left|E_y(x)\right|^2 \tag{C.14}$$

C.2 TM surface waves

A similar to the TE wave propagation analysis can be performed also for the TM wave propagation in the structure of Figure C.1. The only difference is that $\tilde{H}_y$ is now the starting field component which has the same form as $\tilde{E}_y$ for confined propagation, eqn.(C.7). The other non-zero field components are $\tilde{E}_x$ and $\tilde{E}_z$ which are having a transverse field variation obtained by

$$E_z = -\frac{j}{\omega\varepsilon_o\varepsilon_q}\frac{\partial H_y}{\partial x} \tag{C.15}$$

$$E_x = \frac{\beta}{\omega\varepsilon_o\varepsilon_q}H_y \tag{C.16}$$

From the continuity of the tangential field components $\tilde{H}_y$ and $\tilde{E}_z$ at x = ± b, the TM wave dispersion equation for obtaining symmetric, eqn.(C.17), and antisymmetric, eqn.(C.18), wave solutions are

$$v = \frac{\varepsilon_1}{\varepsilon_2}u\tan(u) \tag{C.17}$$

$$v = -\frac{\varepsilon_1}{\varepsilon_2}u\cot(u) \tag{C.18}$$

whereas the normalised frequency w of the structure is described by eqn.(C.13).

Similarly to the TE case, section C.1, the guided modes of the structure can obtained graphically or numerically, having non-zero $\underline{S}$ components, eqn.(2.11), only along the longitudinal direction of the wave propagation (z),

$$S_z(x,z) = \frac{\beta}{2\omega\varepsilon_o\varepsilon_q}\left|H_y(x)\right|^2 \tag{C.19}$$

References

[C.1] C.A. Balanis, "Advanced Engineering Electromagnetics", John Wiley & Sons, ed.1989.

[C.2] R. Syms, J. Cozens, "Optical Guided Waves and Devices", McGraw-Hill Book Company, 1992.

[C.3] P. Yeh, "Optical Waves in Layered Media", John Wiley & Sons, 1988.

Appendix D

SPW Modal Properties in DMD Waveguides

D.1. SPW dispersion equations

With reference to the DMD structure of section 3.4.1 and by considering an ideal metal with $\varepsilon_{mI} = 0$, it is given that the symmetric SPW mode of the arrangement can be found by solving eqns.(D.1) and (D.2)

$$\tanh(u) = \frac{|\varepsilon_{mR}|}{\varepsilon_1}\frac{v}{u} \tag{D.1}$$

$$u^2 - v^2 = d^2 k_o^2 \left(\varepsilon_1 + |\varepsilon_{mR}|\right) \tag{D.2}$$

whereas the antisymmetric SPW is obtained by eqns.(D.3) and (D.2)

$$\tanh(u) = \frac{\varepsilon_1}{|\varepsilon_{mR}|}\frac{v}{u} \tag{D.3}$$

where

$$u = d\left(\beta^2 + k_o^2 |\varepsilon_{mR}|\right)^{1/2} \tag{D.4}$$

$$v = d\left(\beta^2 - k_o^2 \varepsilon_1\right)^{1/2} \tag{D.5}$$

Hence, the combination of eqns.(D.1) and (D.2) gives for the symmetric SPW:

$$u^2\left[1 - \left(\frac{\varepsilon_1}{|\varepsilon_{mR}|}\right)^2 \tanh^2(u)\right] = d^2 k_o^2 \left(\varepsilon_1 + |\varepsilon_{mR}|\right) \tag{D.6}$$

and that of eqns.(D.2) and (D.3) for the antisymmetric SPW:

$$u^2\left[1-\left(\frac{\varepsilon_1}{|\varepsilon_{mR}|}\right)^2\coth^2(u)\right]=d^2\,k_o^2\left(\varepsilon_1+|\varepsilon_{mR}|\right) \qquad (D.7)$$

D.2. Symmetric SPW modal properties

The study of eqns.(D.1) and (D.7) can reveal whether a symmetric SPW can be sustained in the DMD arrangement. Hence,

a) If $\varepsilon_1 < |\varepsilon_{mR}|$ then:

⇨ for $h \to 0$, $\tanh(u) \to 0$, in eqn.(D.1), thus a symmetric SPW exists for:

$$\beta^2 \to k_o^2\,\varepsilon_1 \qquad (D.8)$$

⇨ For $h \to \infty$, $\tanh(u) \to 1$ and eqn.(D.1) is satisfied for:

$$\beta^2 \to k_o^2\left[\frac{\varepsilon_1|\varepsilon_{mR}|}{|\varepsilon_{mR}|-\varepsilon_1}\right] \qquad (D.9)$$

b) If $\varepsilon_1 \geq |\varepsilon_{mR}|$ then:

⇨ for $h \to 0$, eqn.(C.1) can be satisfied for:

$$\beta^2 \to k_o^2\,\varepsilon_1 \qquad (D.10)$$

⇨ for $h \to \infty$, eqn.(D.1) can be satisfied up to a cut-off thickness

$$h = h_{CO} = \log_e\left[\frac{\varepsilon_1+|\varepsilon_{mR}|}{\varepsilon_1-|\varepsilon_{mR}|}\right]\left[k_o\left(\varepsilon_1+|\varepsilon_{mR}|\right)^{1/2}\right]^{-1} \qquad (D.11)$$

which is obtained when $\beta^2 = k_o^2\,\varepsilon_1$ in eqn.(D.1).

D.3. Antisymmetric SPW modal properties

The modal properties for an antisymmetric SPW mode in the DMD structure can be examined through eqns.(D.3) and (D.7).

a) If $\varepsilon_1 < |\varepsilon_{mR}|$ then:

- ⇨ for $h \to 0$, $\tanh(u) \to 0$ and eqn.(D.3) is satisfied for:

$$\beta^2 \to \infty \tag{D.12}$$

- ⇨ for $h \to \infty$, $\tanh(u) \to 1$ which satisfies eqn.(D.3) for:

$$\beta^2 \to k_o^2 \left[\frac{\varepsilon_1 |\varepsilon_{mR}|}{|\varepsilon_{mR}| - \varepsilon_1} \right] \tag{D.13}$$

b) If $\varepsilon_1 \geq |\varepsilon_{mR}|$ then:

- ⇨ for $h \to 0$, eqn.(D.7) cannot be satisfied for any combination of h , ε_1 and $|\varepsilon_2|$.
- ⇨ for $h \to \infty$, no modes can be supported in the structure.

Appendix E

Multilayer Waveguide Mode Solving Program

The results obtained from the in-house developed program in section 3.6 to calculate complex β, $\beta = \beta_R - j\,\beta_I$, in multilayer waveguide structures including media with complex ε, are compared in this appendix with results obtained in [E.1]. This comparison is presented in Table E.1, and the studied waveguide structure is a three layer asymmetric slab analysed for both TE and TM wave propagation.

structure	thickness (μm)	Mode	(β_R / k_o)	(β_R / k_o) [E.1]	(β_I / k_o) x 10^{-7}	(β_I / k_o) x 10^{-7} [E.1]
A-P-Ag	**5.9**	TE	1.587	1.588	0.95	0.9
		TE	1.584	1.583	3.822	3.5
		TE	1.580	1.580	8.626	8
		TM	1.715	1.726	5.054×10^{4}	5×10^{4}
		TM	1.587	1.588	11.1	8
	2.6	TE	1.583	1.583	10.46	11
		TE	1.570	1.569	42.22	45
		TE	1.548	1.550	96.4	100
		TM	1.715	1.718	5.2×10^{4}	5×10^{4}
		TM	1.5828	1.582	136	110
		TM	1.567	1.568	492	400
	1.0	TE	1.562	1.56	155	150
		TE	1.4815	1.48	652	700
		TM	1.715	1.73	5.29×10^{4}	5×10^{4}
		TM	1.547	1.55	2.36×10^{3}	2×10^{3}
		TM	1.430	1.47	5.64×10^{3}	5×10^{3}
Ag-P-G	**5.9**	TM	1.715	1.726	5.46×10^{4}	5×10^{4}
A-P-Au	**7.2**	TE	1.587	1.588	1.5	2
		TE	1.585	1.585	6.02	8
		TE	1.582	1.582	13.5	18
		TM	1.807	1.825	1.87×10^{4}	3×10^{5}
		TM	1.587	1.587	7.34	13
		TM	1.585	-	29.3	-
		TM	1.582	1.582	65.5	50
A-P-Al	**5.9**	TE	1.587	1.588	6.86	7
		TE	1.584	1.583	27.5	30
		TE	1.580	1.580	62.02	70
		TM	1.616	1.634	3.9×10^{4}	2×10^{5}
		TM	1.587	1.587	152	190
		TM	1.584	1.581	564	630

Table E.1. Comparison between the modal solutions of the structures of [E.1] obtained from [E.1] and the 'in-house' developed model.

For the above analysed waveguide structure: A = air, P = polymer, G = glass, Au = gold, Ag = silver, Al = aluminium with refractive indices as given in [E.1].

The results are quite similar between those obtained with the 'in-house' developed program and [E.1]. Any discrepancies observed are due to the different algorithms employed for solving the corresponding dispersion equation of each of the waveguide structures. However, it seems that for the structures of [E.1], our model has found one more extra mode in A-P-Au that is not reported in [E.1]. In addition, in the structures A-P-Au and A-P-Al the solutions for β_I obtained from our program and [E.1] are very different which is believed to be due to the different algorithms and accuracy employed in the two techniques.

The 'in-house' developed program of section 3.6 has also been compared with [E.2]. The results of this comparison are given in Tables E.2 and E.3. Table E.2 presents results for a three layer symmetric slab where the cladding is Ag and the core Polysterene with 1.8μm thickness, whereas Table E.2 has results for a three layer Ag cladded Polymer core waveguide of 1 μm thickness.

Mode	(β_R / k_o) [E.2]	(β_R / k_o)	$(\beta_I / k_o) \times 10^{-4}$ [E.2]	$(\beta_I / k_o) \times 10^{-4}$
TE	1.574863	1.5748578	0.029746	0.029773
TE	1.548692	1.548671251	0.121010	0.12112
TE	1.504169	1.504121	0.280294	0.28055
TE	1.439795	1.439706	0.520016	0.520511
TE	1.353140	1.3529933	0.861391	0.86224
TE	1.240454	1.24022	1.338221	1.339603
TE	1.096752	1.0964218	1.971468	1.97336

Table E.2. Comparison between the modal solutions of the structures of [E.2] obtained from [E.2] and the 'in-house' developed model for 1.8μm guide thickness.

Mode	(β_R / k_o) [E.2]	(β_R / k_o)	$(\beta_I / k_o) \times 10^{-4}$ [E.2]	$(\beta_I / k_o) \times 10^{-4}$
TE	1.5623445	1.5623236	0.152794	0.15298
TE	1.4832057	1.4831186	0.640422	0.6412304
TE	1.3432613	1.34305	1.564895	1.56696
TE	1.1286310	1.1282237	3.072778	3.07655

Table E.3. Comparison between the modal solutions of the structures of [E.2] obtained from [E.2] and the 'in-house' developed model for 1μm guide thickness.

Hence, the results obtained from [E.2] and the program of section 3.6 which are presented in Tables E.2 and E.3, are very similar as they become different after the third decimal digit.

To conclude, the comparison of the results obtained with the 'in-house' developed program and those from [E.1] and [E.2] are very similar. This observation verifies the correct operation of the program developed in section 3.6 for solving multilayer waveguide structures consisted of media with complex relative permittivies ε which result into a complex $\beta = \beta_R - j\,\beta_I$.

References

[E.1] I.P. Kaminow, M.L. Mammel, H.P. Weber, "Metal-Clad Optical Waveguides: Analytical and Experimental Study", Applied Optics, vol.13, no.2, February 1974, p.396.

[E.2] E. Anemogiannis, E. Glytsis, "Multilayer Waveguides: Efficient Numerical Analysis of General Structures", Journal of Lightwave Technology, vol.10, no.10, October 1992, p.1344.

Appendix F

Cascade Matrix Analysis for Multilayer Structures

F.1. TM polarised signals

One of the most commonly used techniques for analysing multilayer structures is the Cascade Matrix Analysis (CMA). Consider the multilayer configuration of Figure F.1 which has the electric field $\underline{E}$ parallel to the plane of incident x – z and the magnetic $\underline{H}$ normal to it, hence representing TM polarised signals.

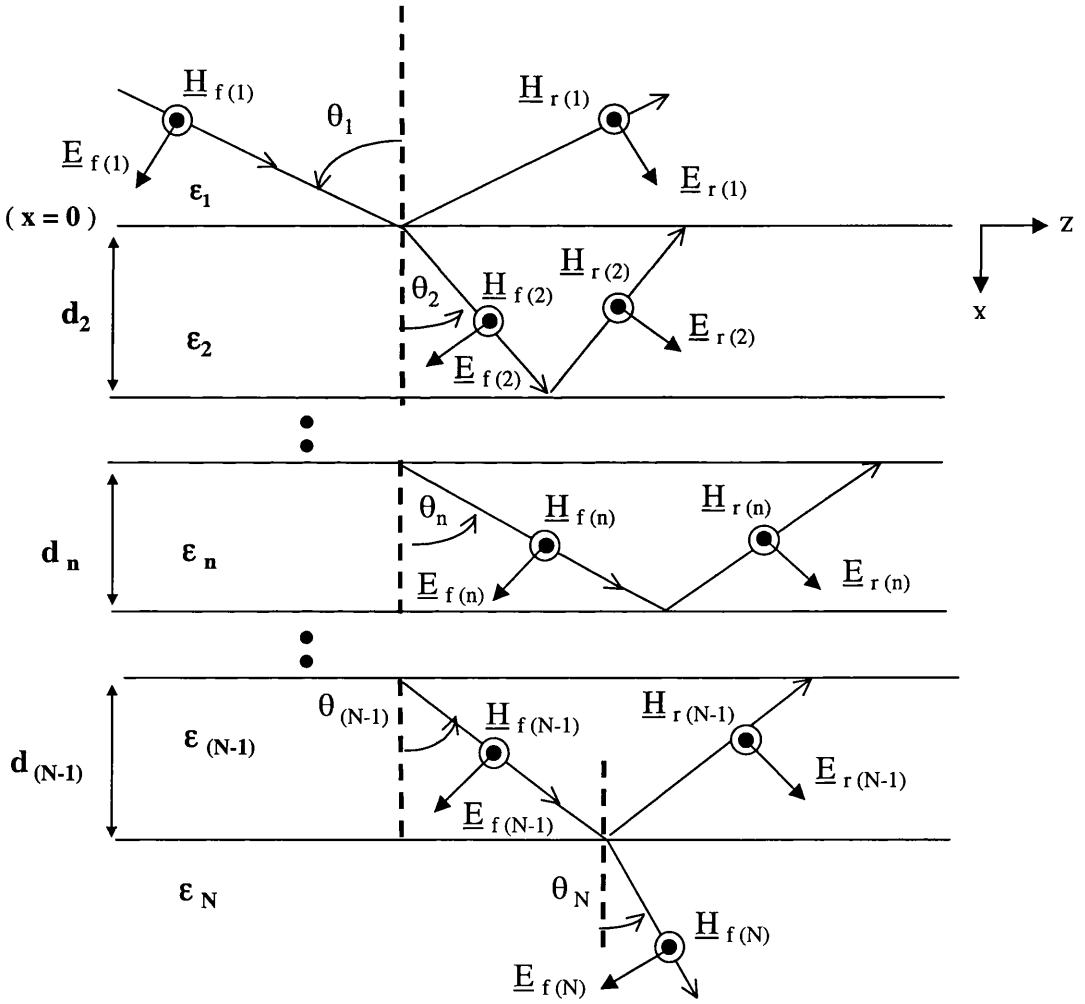

Figure F.1. TM polarised signals in a multilayer structure. The subscripts f and r in the magnetic and electric field vectors $\underline{H}$ and $\underline{E}$ describe forward and reverse travelling wave in each layer. θ_n is the angle of the n^{th} forward travelling wave with respect to the x axis, while ε_n and d_n are the corresponding relative permittivity and thickness of the n^{th} medium.

The multilayer structure described in Figure F.1 is consisted of n layers where n = 1, 2, 3, ..., N. The n^{th} layer has a relative permittivity ε_n and is of finite thickness d_n. Note that the layers n = 1 and n = N are semi-infinite since they represent the input and output sections of the multilayer structure. It is assumed that there is no field variation in the y direction and the total field in the n^{th} medium is of the form

$$\tilde{\underline{F}}_{T(n)}(x,z,t) = \underline{F}_{T(n)}(x,z)\exp[+j\omega t] \tag{F.1}$$

where

$$\underline{F}_{T(n)}(x,z) = \underline{F}_{f(n)}(x,z) + \underline{F}_{r(n)}(x,z) \tag{F.2}$$

and $\exp[+j\omega t]$ describes time dependent fields where ω and t are the angular frequency and time respectively, both being real and positive. Subscripts T, f and r describe total, forward and reverse travelling wave respectively.

If TM polarised signals are considered as shown in Figure F.1, then the analysis of the structure can be done by starting with the magnetic field vector $\underline{H}$. There is only $\underline{H}$ field component along the y direction, hence the total magnetic field in the n^{th} layer is

$$H_{yT(n)}(x,z) = H_{yf(n)}(x,z) + H_{yr(n)}(x,z) \tag{F.3}$$

where

$$H_{yf(n)} = A_n \exp\left[-j\left(k_{x(n)}x + k_{z(n)}z\right)\right] = A_n \exp[-\gamma_n x]\exp\left[-jk_{z(n)}z\right] \tag{F.4}$$

$$H_{yr(n)} = B_n \exp\left[-j\left(-k_{x(n)}x + k_{z(n)}z\right)\right] = B_n \exp[+\gamma_n]\exp\left[-jk_{z(n)}z\right] \tag{F.5}$$

and

$$\gamma_n = +jk_{x(n)} \tag{F.6}$$

From Maxwell's equations, eqns.(2.2), the rest of the non zero field components are E_z and E_x. The total E_z and E_x in the n^{th} medium are

$$E_{zT(n)} = -\frac{k_{x(n)}}{\omega\varepsilon_o\varepsilon_n}\left[A_n \exp\left[-j\left(k_{x(n)}x + k_{z(n)}z\right)\right] - B_n \exp\left[-j\left(-k_{x(n)}x + k_{z(n)}z\right)\right]\right] \tag{F.7}$$

$$E_{xT(n)} = +\frac{k_{z(n)}}{\omega\varepsilon_o\varepsilon_n}\left[A_n \exp\left[-j\left(k_{x(n)}x + k_{z(n)}z\right)\right] + B_n \exp\left[-j\left(-k_{x(n)}x + k_{z(n)}z\right)\right]\right] \tag{F.8}$$

where A_n and B_n are the field amplitude of the forward and reverse travelling waves respectively, and ε_o is the free space (vacuum) permittivity. The longitudinal and transverse propagation constants $k_{z(n)}$ and $k_{x(n)}$ are related with the n^{th} angle θ_n as

$$k_{z(n)}^2 = k_o^2 \varepsilon_n \sin^2 \theta_n \tag{F.9}$$

$$k_{x(n)}^2 = k_o^2 \varepsilon_n - k_{z(n)}^2 \tag{F.10}$$

Since the tangential total field components of E_z , eqn.(F.7), and H_y , eqn.(F.4) – (F.5), have to be continuous at every interface along x for all z, therefore

$$k_{z(n)} = k_{z(n-1)} = \beta = k_o \sqrt{\varepsilon_1} \sin \theta_1 \tag{F.11}$$

Note that since an unattenuated infinite plane wave is assumed in medium 1, hence β, eqn.(F.11), is considered real whereas $k_{x(n)}$, eqn.(F.10), may be complex. In addition, to represent experimental conditions, ε_1 is also real and positive in our calculations.

As a consequence, the corresponding transverse (characteristic) impedance for a forward travelling TM polarised wave can then be evaluated by

$$Z_{0x(n)} = \frac{E_{zf(n)}}{-H_{yf(n)}} = Z_{vac} \frac{k_{x(n)}}{k_o \varepsilon_n} \tag{F.12}$$

where $Z_{vac} = \sqrt{\mu_o / \varepsilon_o} \approx 377\,\Omega$. The negative sign of $H_{yf(n)}$ in eqn.(F.12) assumes a positive power flow in the transverse direction x for $x > 0$, and follows the right-hand screw rule for the given co-ordinate system.

By matching the tangential total field components of E_z , eqn.(F.7), and H_y , eqn.(F.4) – (F.5), at the interface between the n^{th} and the $(n+1)^{th}$ layers, the following relationship between the field amplitudes A_n, $A_{(n+1)}$, B_n and $B_{(n+1)}$ is obtained

$$\begin{bmatrix} A_{(n+1)} \\ B_{(n+1)} \end{bmatrix} = K_n \begin{bmatrix} A_n \\ B_n \end{bmatrix} \tag{F.13}$$

where

$$K_n = \frac{1}{2} \begin{bmatrix} K_{11(n)} & K_{12(n)} \\ K_{21(n)} & K_{22(n)} \end{bmatrix} \tag{F.14}$$

and

$$K_{11(n)} = \exp[-jk_{x(n)}d_{(n)}] + \frac{\varepsilon_{(n+1)}}{\varepsilon_n}\frac{k_{x(n)}}{k_{x(n+1)}}\exp[-jk_{x(n)}d_{(n)}] \quad \text{(F.15)}$$

$$K_{12(n)} = \exp[+jk_{x(n)}d_{(n)}] - \frac{\varepsilon_{(n+1)}}{\varepsilon_n}\frac{k_{x(n)}}{k_{x(n+1)}}\exp[+jk_{x(n)}d_{(n)}] \quad \text{(F.16)}$$

$$K_{21(n)} = \exp[-jk_{x(n)}d_{(n)}] - \frac{\varepsilon_{(n+1)}}{\varepsilon_n}\frac{k_{x(n)}}{k_{x(n+1)}}\exp[-jk_{x(n)}d_{(n)}] \quad \text{(F.17)}$$

$$K_{22(n)} = \exp[+jk_{x(n)}d_{(n)}] + \frac{\varepsilon_{(n+1)}}{\varepsilon_n}\frac{k_{x(n)}}{k_{x(n+1)}}\exp[+jk_{x(n)}d_{(n)}] \quad \text{(F.18)}$$

A relationship between A_1, B_1 and A_N, B_N can then be derived

$$\begin{bmatrix} A_{(N)} \\ B_{(N)} \end{bmatrix} = \Pi_{(N-1)} \begin{bmatrix} A_1 \\ B_1 \end{bmatrix} \quad \text{(F.19)}$$

where

$$\Pi_{(N-1)} = \begin{bmatrix} \Lambda_{11} & \Lambda_{12} \\ \Lambda_{21} & \Lambda_{22} \end{bmatrix} \quad \text{(F.20)}$$

which can be evaluated as

$$\Pi_{(N-1)} = \Pi_{(N-2)} K_{(N-1)} \quad \text{(F.21)}$$

with $\Pi_1 = K_1$ and $d_1 = 0$.

Note that $B_N = 0$ and therefore the field reflection coefficient Γ of the multilayer structure can be evaluated from eqns.(F.19) – (F.20),

$$\Gamma = \frac{B_1}{A_1} = -\frac{\Lambda_{21}}{\Lambda_{22}} \quad \text{(F.22)}$$

whereas the field transmission coefficient T is given from eqns.(F.19) – (F.20) as

$$T = \frac{A_N}{A_1} = \Lambda_{11} - \Lambda_{12}\frac{\Lambda_{21}}{\Lambda_{22}} \quad \text{(F.23)}$$

F.2. TE polarised signals

The CMA analysis can equally be applied to obtain the reflection and transmission coefficients for TE polarised signals by following the procedure of section F.1, hence it will not be given here. The only difference is that with reference to Figure F.1, the electric field vector $\underline{E}$ is normal to the plane of incidence whereas $\underline{H}$ is parallel and the analysis starts with the electric field E_y instead of the H_y for the TM signals. The non-zero field components are E_y, H_z and H_x, and can be obtained from eqns.(2.2) assuming total electric field

$$E_{yT(n)}(x,z) = E_{yf(n)}(x,z) + E_{yr(n)}(x,z) \tag{F.24}$$

where

$$E_{yf(n)} = A_n \exp\left[-j\left(k_{x(n)}x + k_{z(n)}z\right)\right] = A_n \exp[-\gamma_n x]\exp\left[-jk_{z(n)}z\right] \tag{F.25}$$

$$E_{yr(n)} = B_n \exp\left[-j\left(-k_{x(n)}x + k_{z(n)}z\right)\right] = B_n \exp[+\gamma_n]\exp\left[-jk_{z(n)}z\right] \tag{F.26}$$

F.3. Transverse Propagation Constant Characteristics

The characteristics of the transverse propagation constant $k_{x(n)}$, eqn.(F.10), of the n^{th} layer due to the corresponding relative permittivity ε_n, are presented in this section. The study assumes that ε_n is in general complex of the form

$$\varepsilon_n = \varepsilon_{nR} - j\,\varepsilon_{nI} \tag{F.27}$$

In that case $k_{x(n)}$, eqn.(F.10), can also be assumed in general complex of the form

$$k_{x(n)} = k_{x(n)R} - jk_{x(n)I} \tag{F.28}$$

i) $\varepsilon_{nR} > 0$, $\varepsilon_{nI} > 0$

In that case $k_{x(n)}$, eqn.(F.28), will be

$$k_{x(n)} = \left|k_{x(n)R}\right| - j\left|k_{x(n)I}\right| \tag{F.29}$$

where $\left|k_{x(n)R}\right|$ is the real part describing wave propagation and $\left|k_{x(n)I}\right|$ the imaginary representing attenuation (decay) rate. The signs of $k_{x(n)R}$ and $k_{x(n)I}$ have been chosen to follow the forward travelling and exponentially decaying field requirements for $x > 0$, as given by eqn.(F.4). As a consequence, γ, eqn.(F.6), will now be

$$\gamma_n = \left|k_{x(n)R}\right| + j\left|k_{x(n)I}\right| \tag{F.30}$$

ii) $\varepsilon_{nR} > 0$, $\varepsilon_{nI} < 0$

If the dielectric is optically active, i.e. $\varepsilon_{nI} < 0$, $k_{x(n)}$, eqn.(F.10), becomes

$$k_{x(n)} = \left| k_{x(n)R} \right| + j \left| k_{x(n)I} \right| \tag{F.31}$$

where $\left| k_{x(n)R} \right|$ represents wave propagation and $\left| k_{x(n)I} \right|$ growth rate for $x > 0$. Thus γ_n, eqn.(F.6), becomes

$$\gamma_n = -\left| k_{x(n)I} \right| + j \left| k_{x(n)R} \right| \tag{F.32}$$

iii) $\varepsilon_{nR} > 0$, $\varepsilon_{nI} = 0$

For a wave travelling in a lossless dielectric ($\varepsilon_{nI} = 0$) with $\varepsilon_{nR} > 0$, two cases exist:

a) If $k_{z(n)}^2 < k_o^2 \varepsilon_n$, eqns.(F.10) and (F.6) become

$$k_{x(n)} = + \left| k_{x(n)R} \right| \tag{F.33}$$

$$\gamma_n = j \left| k_{x(n)R} \right| \tag{F.34}$$

representing a forward travelling wave for $x > 0$.

b) If $k_{z(n)}^2 > k_o^2 \varepsilon_n$, eqns.(F.10) and (F.6) are taking the form

$$k_{x(n)} = - j \left| k_{x(n)I} \right| \tag{F.35}$$

$$\gamma_n = \left| k_{x(n)I} \right| \tag{F.36}$$

The sign of $k_{x(n)}$ in eqn.(F.35) has been chosen so that $H_{y\,f(n)}$, eqn.(F.4), describes an exponentially decaying field for $x > 0$.

iv) $\varepsilon_{nR} < 0$, $\varepsilon_{nI} = 0$

For a wave travelling in a medium with $\varepsilon_{nR} < 0$ and $\varepsilon_{mI} = 0$ such as an ideal (lossless) metal, then $k_{x(n)}$, eqn.(F.10), is always

$$k_{x(n)} = - j \left| k_{x(n)I} \right| \tag{F.37}$$

defining an exponentially decaying field for $x > 0$, which makes eqn.(F.6) to be

$$\gamma_n = \left| k_{x(n)I} \right| \tag{F.38}$$

v) $\varepsilon_{nR} < 0$, $\varepsilon_{nI} > 0$

If the electromagnetic wave is travelling inside a lossy metal ($\varepsilon_{nI} > 0$), $k_{x(n)}$, eqn.(F.10), becomes

$$k_{x(n)} = |k_{x\,(n)\,R}| - j\,|k_{x\,(n)\,I}| \tag{F.39}$$

and γ_n, eqn.(F.4),

$$\gamma_n = \left| k_{x(n)\,I} \right| + j \left| k_{x(n)\,R} \right| \tag{F.40}$$

Appendix G

Optical sources and Detectors

G.1. Relationship between input and output prism angles

Consider an input signal incident on a right angle glass prism with relative permittivity ϵ_p at an angle θ_{out} . The prism is embedded in a dielectric with relative permittivity $\epsilon_a > 0$. To approach experimental conditions $\epsilon_a = 1 < \epsilon_p$. The relationship between the external prism angle θ_{out} and the internal prism angle θ_i can then be derived by studying the schematic of Figure G.1.

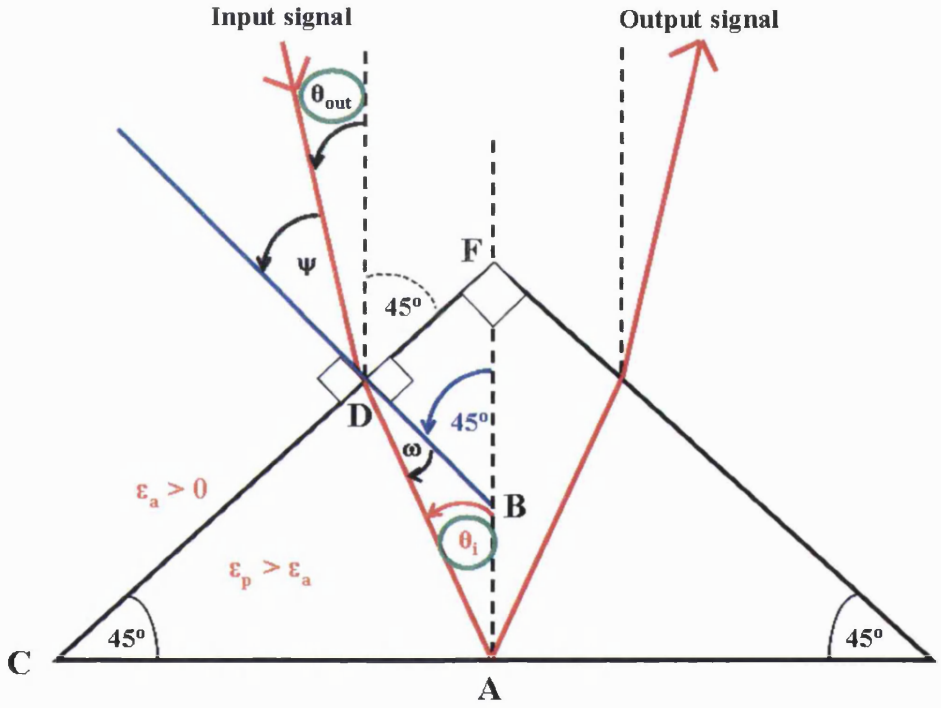

Figure G.1. Schematic diagram for relating input and output prism angles θ_i and θ_{out}.

With reference to Figure G.1, the dashed lines represent the reference level of our measurements at which $\theta_{out} = 0^o$ and $\theta_i = 0^o$, whereas the solid red line indicates the input signal from the optical source.

The implementation of Snell's law at the CF interface formed between the air and the prism gives,

$$\sqrt{\varepsilon_a}\sin\psi = \sqrt{\varepsilon_p}\sin\omega \tag{G.1}$$

$$\sin(45-\theta_{out}) = \sqrt{\varepsilon_p}\sin\omega \tag{G.2}$$

From the triangle ADB it is found that

$$\omega + \theta_i + 135 = 180 \tag{G.3}$$

and then eqn.(G.2) becomes

$$\sin(45-\theta_{out}) = \sqrt{\varepsilon_p}\sin(45-\theta_i) \tag{G.4}$$

As a consequence,

$$\theta_i = 45 - \sin^{-1}\left[\frac{1}{\sqrt{\varepsilon_p}}(45-\theta_{out})\right] \tag{G.5}$$

G.2. SLD Characteristics

The SLD used in chapter 5 as the optical source for exciting guided waves (SPWs and 'conventional' dielectric waves) in various prism coupled waveguide structures, was a straight stripe (SS) edge emitting SLD with length L = 1mm, width W = 100μm and consisted of three quantum wells (QW). The amount of optical power emitted by the SLD for various injected currents and the corresponding normalised emission spectra and far-field profile of the device are presented in Figures G.2 – G.4. Note that all the measurements of the SLD characteristics have been performed under pulsed operation with a pulse width of 1μs and pulse period of 1ms.

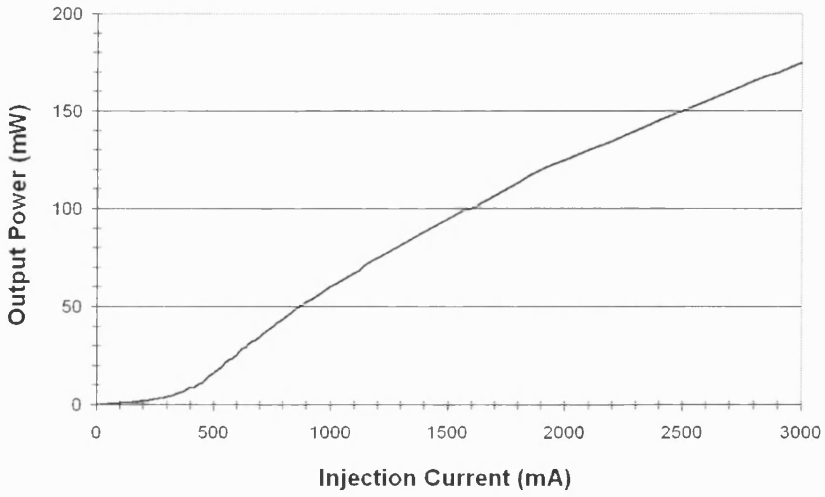

Figure G.2. SLD optical power as a function of the injected current.

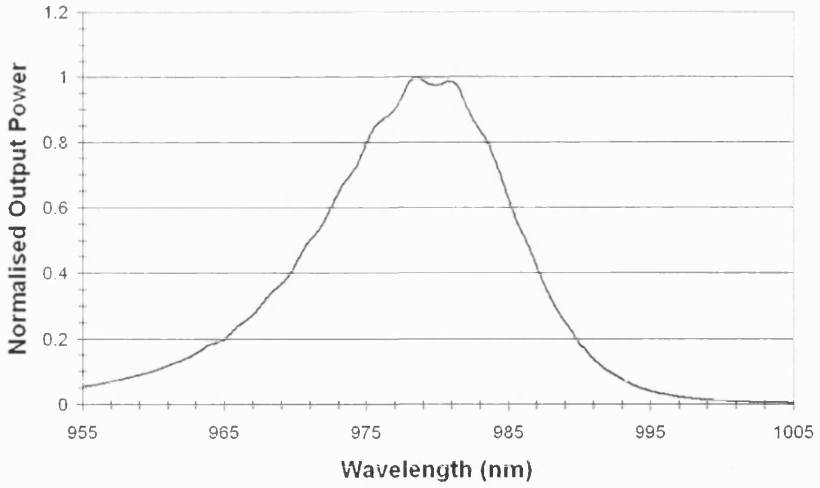

Figure G.3. Normalised emission spectrum of the SLD for 2A of injected current.

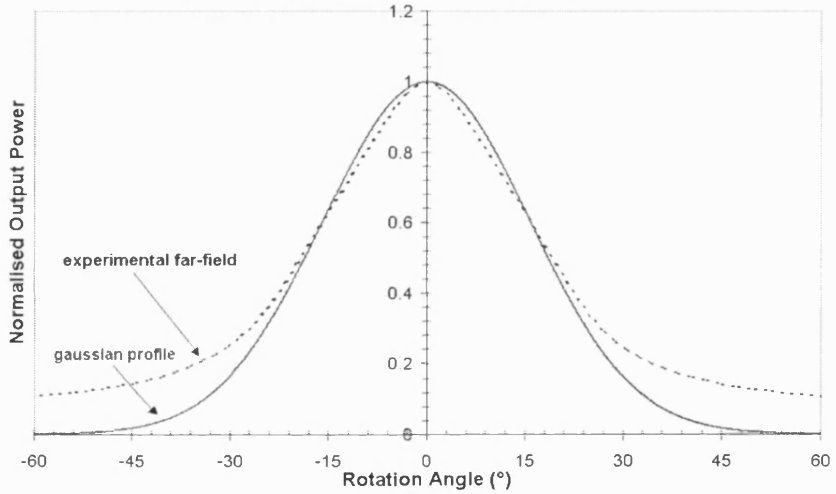

Figure G.4. Far-field profile of the SLD output beam. Note that it has similar behaviour to a gaussian function.

G.3. Detector Circuits

Two types of photodetectors were employed for the experiments of chapter 5 depending on the optical source used. A continuous wave (cw) photodetector was used with the HeNe laser and a pulsed one with the SLD. The corresponding circuit diagrams of the two detectors are shown in Figures G.5 – G.6.

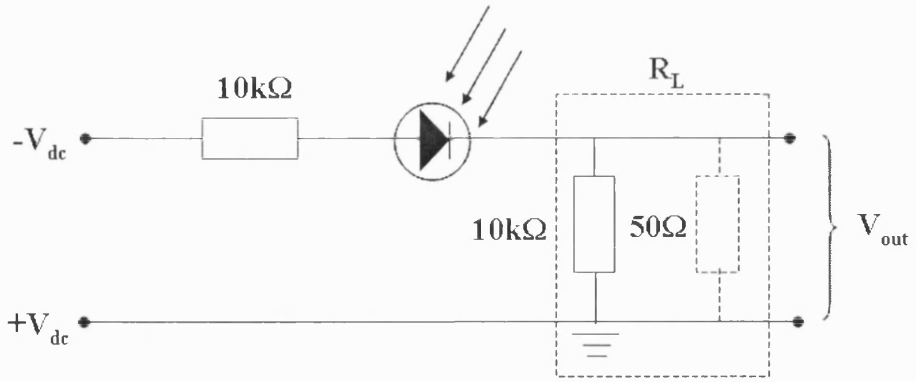

Figure G.5 Circuit diagram of the cw detector.

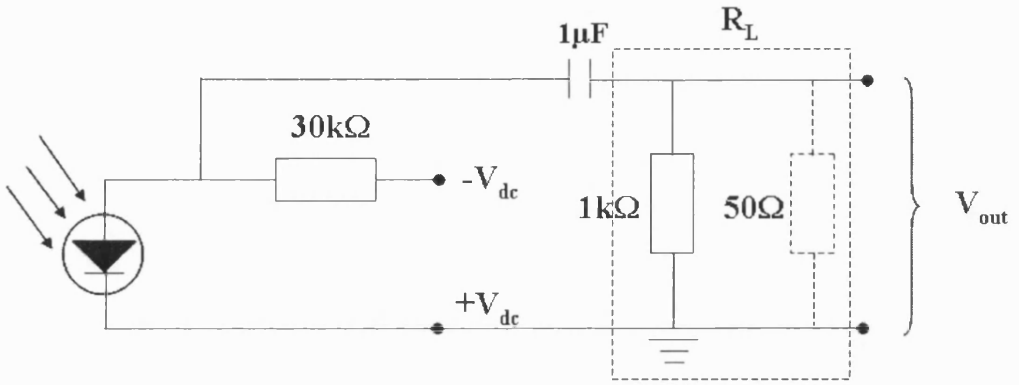

Figure G.6. Circuit diagram of the pulsed operating detector.

Note that for both the photodetectors, the biased voltage was V_{dc} = 25V. The output voltage V_{out} was measured in a digital multimeter for the cw detector and an oscilloscope for the pulsed one. The optical power P measured from the detectors was then evaluated as

$$P = \frac{V_{out}}{\rho R_L} \tag{G.6}$$

where ρ is the responsivity of the corresponding photodiode measured in (A/W) and R_L is the load resistor of the photodetector ciruit. Note that in some cases a 50Ω resistor was used on the oscilloscope which made $R_L \approx 50\Omega$. The use of the 50Ω resistor was to increase the response time of the detector

$$\tau = R_L C \tag{G.7}$$

where C is the capacitor of the photodiode. The disadvantage of such low resistor value is however the reduced detection sensitivity of the system. In this thesis, as there was no need for fast detector responses but for high detection sensitivity, the 50Ω resistor has been omitted during the measurements.

Appendix H

Gain effect on SPW modal properties

H.1. Permittivity of a gain medium

As discussed in section 2.2, eqn.(2.8), the refractive index n of a medium is in general complex and can be written as

$$n = n_R - jn_I \tag{H.1}$$

which gives a relative permittivity ε of the form,

$$\varepsilon = n^2 = \left(n_R^2 - n_I^2\right) - j2n_R\, n_I \tag{H.2}$$

If the medium is a dielectric with $n_R > n_I > 0$ and contains optical gain $g > 0$, where g is

$$g = -2k_o\, n_I \tag{H.3}$$

when $n_I < 0$, eqn.(H.1) then becomes

$$n = n_R + j\frac{g}{2k_o} \tag{H.4}$$

and therefore ε, eqn.(H.2), can be written as

$$\varepsilon = n^2 \approx n_R^2 - jn_R\frac{g}{k_o} = \varepsilon_R + j\varepsilon_I \tag{H.5}$$

where $\varepsilon_R > \varepsilon_I > 0$ representing an optically active dielectric medium.

H.2. Optical gain and SPW propagation constant

From eqn.(3.10) the longitudinal propagation constant of a SPW at a single interface formed between a metal and a dielectric with relative permittivies $\varepsilon_m = -|\varepsilon_{mR}| - j\,|\varepsilon_{mI}|$ and $\varepsilon_D = \varepsilon_1 + j\,\varepsilon_g$ respectively and $|\varepsilon_{mR}| >> |\varepsilon_{mI}|$ and $|\varepsilon_{mR}| > \varepsilon_1 > \varepsilon_g > 0$ is

$$\beta = k_o\left[\frac{\varepsilon_m\,\varepsilon_D}{\varepsilon_m + \varepsilon_D}\right]^{1/2} \tag{H.6}$$

which can be rewritten as

$$\beta = k_o \left[\frac{\left(-|\varepsilon_{mR}| - j|\varepsilon_{mI}|\right)\left(\varepsilon_1 + j\varepsilon_g\right)}{\left(-|\varepsilon_{mR}| + \varepsilon_1\right) + j\left(-|\varepsilon_{mI}| + \varepsilon_g\right)} \right]^{1/2} =$$

$$= k_o \left[\frac{\varepsilon_1\left(\varepsilon_{mR}^2 + \varepsilon_{mI}^2\right) - |\varepsilon_{mR}|\left(\varepsilon_1^2 + \varepsilon_g^2\right)}{\left(|\varepsilon_{mR}| - \varepsilon_1\right)^2 + \left(|\varepsilon_{mI}| - \varepsilon_g\right)^2} + j\frac{\varepsilon_g\left(\varepsilon_{mR}^2 + \varepsilon_{mI}^2\right) - |\varepsilon_{mR}|\left(\varepsilon_1^2 + \varepsilon_g^2\right)}{\left(|\varepsilon_{mR}| - \varepsilon_1\right)^2 + \left(|\varepsilon_{mI}| - \varepsilon_g\right)^2} \right]^{1/2} \tag{H.7}$$

If the metal is lossy ($\varepsilon_{mI} \neq 0$) and the dielectric optically active ($\varepsilon_g > 0$) then β should be complex and of the form

$$\beta = \beta_R - j\,\beta_I \tag{H.8}$$

where β_R , $\beta_I > 0$ to comply with a forward traveling and exponentially decaying field for z > 0. Equation (H.7) can then be solved as

$$(\beta_R - j\beta_I)^2 = k_o \left[\frac{\varepsilon_1\left(\varepsilon_{mR}^2 + \varepsilon_{mI}^2\right) - |\varepsilon_{mR}|\left(\varepsilon_1^2 + \varepsilon_g^2\right)}{\left(|\varepsilon_{mR}| - \varepsilon_1\right)^2 + \left(|\varepsilon_{mI}| - \varepsilon_g\right)^2} + j\frac{\varepsilon_g\left(\varepsilon_{mR}^2 + \varepsilon_{mI}^2\right) - |\varepsilon_{mR}|\left(\varepsilon_1^2 + \varepsilon_g^2\right)}{\left(|\varepsilon_{mR}| - \varepsilon_1\right)^2 + \left(|\varepsilon_{mI}| - \varepsilon_g\right)^2} \right] =$$

$$= \alpha - jb \tag{H.9}$$

where α and b are both positive. Equation (H.9) then gives

$$4\beta_R^4 - 4\beta_R^2\,\alpha - b^2 = 0 \tag{H.10}$$

$$\beta_I = \frac{b}{2\beta_R} \tag{H.11}$$

from which

$$\beta_R \approx k_o \frac{\sqrt{2}}{2} \frac{\left[\varepsilon_1\,\varepsilon_{mR}^2 - |\varepsilon_{mR}|\varepsilon_1^2 + \sqrt{\left(\varepsilon_1\varepsilon_{mR}^2 - |\varepsilon_{mR}|\varepsilon_1^2\right)^2 + \left(|\varepsilon_{mI}|\varepsilon_1^2 - \varepsilon_g\varepsilon_{mR}^2\right)^2} \right]^{1/2}}{\left[\left(|\varepsilon_{mR}| - \varepsilon_1\right)^2 + \left(|\varepsilon_{mI}| - \varepsilon_g\right)^2\right]^{1/2}} \tag{H.12}$$

$$\beta_I \approx \frac{|\varepsilon_{mI}|\varepsilon_1^2 - \varepsilon_g\varepsilon_{mR}^2}{\beta_R} \tag{H.13}$$

Equation (H.13) clearly shows that $\beta_I \rightarrow 0$ when

$$\varepsilon_g = \varepsilon_1^2 \frac{|\varepsilon_{mI}|}{\varepsilon_{mR}^2} \tag{H.14}$$

or if eqns.(H.14) and (H.5) are combined then

$$g \approx k_o\,\varepsilon_1^{3/2} \frac{|\varepsilon_{mI}|}{\varepsilon_{mR}^2} \tag{H.15}$$

For an amount of gain g close to that obtained from eqn.(H.15) it is also possible to obtain a very high β_R.

Appendix I

Electrostatic Dipole Properties

With reference to the sphere described in Figure 7.2, it is possible to find the potential Φ of the sphere by solving the Laplace's equation

$$\nabla^2\Phi = 0 \tag{I.1}$$

in spherical co-ordinates, [Appendix A],

$$\frac{1}{r^2}\frac{\partial}{\partial r}\left(r^2\frac{\partial\Phi}{\partial r}\right)+\frac{1}{r^2\sin\theta}\frac{\partial}{\partial\theta}\left(\sin\theta\frac{\partial\Phi}{\partial\theta}\right)+\frac{1}{r^2\sin^2\theta}\frac{\partial^2\Phi}{\partial\phi^2}=0 \tag{I.2}$$

Equation (I.2) assumes that the sphere is symmetrical to the z-axis hence independent of the angle φ.

The potential inside and outside the sphere Φ_1 and Φ_2 respectively, is the solution of eqn.(I.2), [I.1],

$$\Phi_1 = \left(\frac{A}{r^2}+Br\right)\cos(\theta) \tag{I.3}$$

$$\Phi_2 = \left(\frac{C}{r^2}+Fr\right)\cos(\theta) \tag{I.4}$$

where A, B, C, D are unknown coefficients, which can be found by applying boundary conditions at $r = r_1$ and $r \rightarrow \infty$. Hence, it is required that at $r = r_1$

$$\Phi_1(r,\theta) = \Phi_2(r,\theta) \tag{I.5}$$

$$\varepsilon_1\frac{\partial\Phi_1(r,\theta)}{\partial r} = \varepsilon_2\frac{\partial\Phi_2(r,\theta)}{\partial r} \tag{I.6}$$

In addition, the potential at the center of the sphere remains finite,

$$\Phi_1(r = 0, \theta) \neq 0 \tag{I.7}$$

and the external field remains undisturbed at large distances from the sphere

$$\Phi_2(r = +\infty, \theta) = -E_{in}\cos(\theta) \tag{I.8}$$

From eqns.(I.5) – (I.8) it is then found that,

$$\begin{aligned}\Phi_1(r,\theta) &= -\frac{3\varepsilon_2}{\varepsilon_1+2\varepsilon_2}E_{in}\,r\cos(\theta)\\ &= -\frac{3\varepsilon_2}{2\varepsilon_2+\varepsilon_1}E_{in}\,z\end{aligned} \tag{I.9}$$

$$\begin{aligned}\Phi_2(r>r_1,\theta) &= \left[\frac{\varepsilon_1-\varepsilon_2}{\varepsilon_1+2\varepsilon_2}\right]\frac{r_1^3}{r^2}E_{in}\cos(\theta)-E_{in}\,r\cos(\theta)\\ &= \Phi_{sc}+\Phi_{in}\end{aligned} \tag{I.10}$$

where Φ_{in} is the applied external potential of the optical source, and Φ_{sc} is known as the scattering potential [I.2].

The electric field components inside, $\underline{E}_1$, and outside, $\underline{E}_2$, of the sphere are found from [I.1],

$$\underline{E}_q = -\nabla\Phi_q \tag{I.11}$$

$$\underline{E}_q = \hat{r}\frac{\partial\Phi_q}{\partial r}+\hat{\theta}\frac{1}{r}\frac{\partial\Phi_q}{\partial\theta} \tag{I.12}$$

where q = 1, 2, refer to the corresponding medium.

Hence, the fields are:

at $r = r_1$:

$$\begin{aligned}E_{z1}(z) &= -\frac{\partial\Phi_1}{\partial z}\\ &= \frac{3\varepsilon_2}{\varepsilon_1+2\varepsilon_2}E_{in}\end{aligned} \tag{I.13}$$

at $r > r_1$:

$$\underline{E}_2 = \left[\left(\frac{\varepsilon_1-\varepsilon_2}{\varepsilon_1+2\varepsilon_2}\right)E_{in}\frac{r_1^3}{r^3}\left(2\cos(\theta)\hat{r}+\sin(\theta)\hat{\theta}\right)\right]+E_{in}\,\hat{z} \tag{I.14}$$

where

$$E_{r2} = \left(\frac{\varepsilon_1-\varepsilon_2}{\varepsilon_1+2\varepsilon_2}\right)E_{in}\frac{r_1^3}{r^3}2\cos(\theta) \tag{I.15}$$

$$E_{\theta 2} = \left(\frac{\varepsilon_1-\varepsilon_2}{\varepsilon_1+2\varepsilon_2}\right)E_{in}\frac{r_1^3}{r^3}\sin(\theta) \tag{I.16}$$

$$E_{z2} = E_{in} \tag{I.17}$$

Since the applied electric field on the sphere is along the z direction, hence the polarization of the dipole is then given by [I.1-3],

$$\begin{aligned} P_z &= D_z - \varepsilon_1 E_{z1} \\ &= \varepsilon_1 E_{z1} - \varepsilon_2 E_{z1} \\ &= (\varepsilon_1 - \varepsilon_2)\left[\frac{3\varepsilon_2}{2\varepsilon_2 + \varepsilon_1}\right] E_{in} \end{aligned} \tag{I.18}$$

which gives a dipole moment

$$\begin{aligned} p_z &= P_z V \\ &= 4(\varepsilon_1 - \varepsilon_2)\left[\frac{\varepsilon_2}{2\varepsilon_2 + \varepsilon_1}\right] \pi r_1^3 E_{in} \\ &= \alpha E_{in} \end{aligned} \tag{I.19}$$

where V is the volume of the sphere and α is the corresponding polarisability which describes average dipole moment per unit field strength [I.1].

Finally, the dielectric polarisation P_z, eqn.(I.13), modifies the field within the sphere by a depolarising factor M [I.3]:

$$E_{z1} = E_{in} - M P_z \tag{I.20}$$

$$M = \frac{E_{z1} - E_{in}}{P_z} = \frac{1}{3\varepsilon_2} \tag{I.21}$$

References

[I.1] A.R. Von Hippel, "Dielectrics and Waves", Hohn Wiley & Sons, 1954.

[I.2] S. Kawata, "Near-Field Optics and Surface Plasmon Polaritons", Topics in Applied Physics vol.81, Springer, 2001.

[I.3] J.A. Stratton, "Electromagnetic Theory", McGraw-Hill Book Company, 1941.

Appendix J

Far Field Dipole Radiation

J.1. Phase due to dipole separation

Consider two elementary dipoles of length d_l placed along the z axis and separated by each other by a distance d_z, as it is shown in Figure J.1.

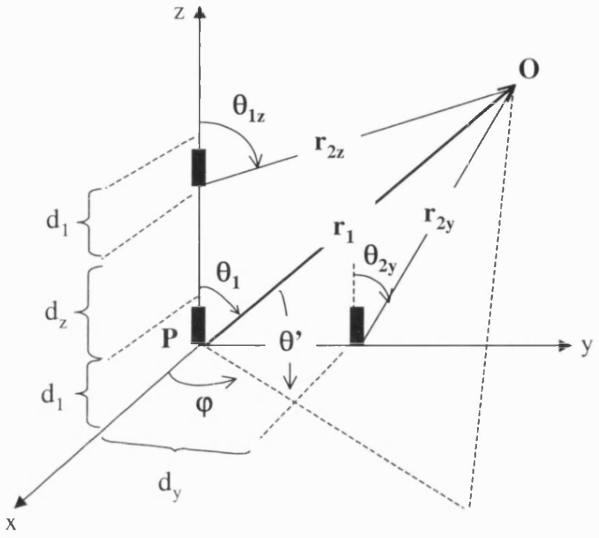

Figure J.1. Geometry of elementary dipoles located along the z and y axis.

The first dipole is oriented at the origin of the co-ordinate system P and radiates at an angle θ_1 with respect to z axis. At the far field observation point O which is at a distance r_1 from the dipole, the electric far field component of that dipole is, eqn.(7.33),

$$E_{\theta 1}(r_1,\theta_1) \approx A_\theta \left[-\frac{k^2}{r_1}\right] \sin(\theta_1) \exp[-jk r_1] \qquad (J.1)$$

where A_θ is the field amplitude given by eqn.(7.40).

Similarly, the second dipole radiates at an angle θ_{2z} with respect to z axis and at the observation point O, which is now located at a distance r_{2z} from the dipole, has an electric far field component, eqn.(7.33),

$$E_{\theta 2z}(r_{2z},\theta_{2z}) \approx A_\theta \left[-\frac{k^2}{r_{2z}}\right] \sin(\theta_{2z}) \exp[-jk r_{2z}] \qquad (J.2)$$

At the far field it can be assumed that

$$\theta_1 \approx \theta_{2z} = \theta \tag{J.3}$$

$$r_1 \approx r_{2z} = r \tag{J.4}$$

Note however, that eqn.(J.4) is only valid for the amplitude variations of the field and not for the corresponding phase variations which for the case of the two dipoles is due to their separation d_z. Hence, r_{2z} can be written in terms of r1 to include the field phase effect in the second dipole:

$$r_{2z}^2 = r_1^2 + d_z^2 - 2 r_1 d_z \cos(\theta_1) \tag{J.5}$$

$$\begin{aligned} r_{2z} &\approx r_1 \left[1 - 2\frac{d_z}{r_1}\cos(\theta_1)\right]^{1/2} \approx r_1 - d_z\cos(\theta_1) \\ &\approx r - d_z\cos(\theta) \end{aligned} \tag{J.6}$$

As a consequence the electric field components of the two dipoles will now be, eqn.(J.1-2),

$$E_{\theta 1}(r,\theta) \approx A_\theta \left[-\frac{k^2}{r}\right] \sin(\theta)\exp[-jkr] \tag{J.7}$$

$$E_{\theta 2z}(r,\theta) \approx A_\theta \left[-\frac{k^2}{r}\right] \sin(\theta)\exp[-jkr]\exp[-j\Delta\Phi_z] \tag{J.8}$$

where

$$\Delta\Phi_z = k d_z \cos(\theta) \tag{J.9}$$

is the phase introduced in the second dipole due to separation d_z.

Hence, the total electric field at O is:

$$E_{\theta(T)}(r,\theta) = E_{\theta 1} + E_{\theta 2z} \approx A_\theta \left[-\frac{k^2}{r}\right] \sin(\theta)\exp[-jkr][1+\exp[-j\Delta\Phi_z]] \tag{J.10}$$

Similarly the far field magnetic field component for the two dipoles is, eqn.(7.32):

$$H_{\varphi 1}(r,\theta) \approx A_\varphi \frac{\sin(\theta)}{r}\exp[-jkr] \tag{J.11}$$

$$H_{\varphi 2z}(r,\theta) \approx A_\varphi \frac{\sin(\theta)}{r}\exp[-jkr]\exp[+j\Delta\Phi_z] \tag{J.12}$$

where A_φ, eqn.(7.41), is the field amplitude. The total magnetic field at O is then:

$$H_{\theta(T)}(r,\theta) = H_{\theta 1} + H_{\theta 2z} \approx A_{\varphi}\left[-\frac{k^2}{r}\right]\sin(\theta)\exp[-jkr][1+\exp[-j\Delta\Phi_z]] \quad (J.13)$$

Consider now the two dipoles to be located along the y axis and separated by each other by a distance d_y, as it is shown in Figure J.1. The dipole that is oriented at the origin of the co-ordinate system has a radiating angle θ_1 with respect to z axis and is at a distance r_1 from the observation point O. The second dipole radiates at an angle θ_{2y} with respect to z axis and is placed at a distance r_{2y} from the observation point. The electric far field components for the two dipoles can be obtained in the same process as the ones for the dipoles along the z axis. Thus, at far field:

$$\theta_1 \approx \theta_{2y} = \theta \quad (J.14)$$

$$r_1 \approx r_{2y} = r \quad (J.15)$$

where

$$r_{2y}^2 = r_1^2 + d_y^2 - 2r_1 d_y \cos(\theta') \quad (J.16)$$

$$r_{2y} \approx r_1\left[1 - 2\frac{d_y}{r_1}\cos(\theta')\right]^{1/2} \approx r_1 - d_y\cos(\theta') \quad (J.17)$$

But

$$\cos(\theta') = \hat{y}\cdot\hat{r} = \hat{z}[\hat{x}\sin(\theta)\cos(\varphi) + \hat{y}\sin(\theta)\sin(\varphi) + \hat{z}\cos(\theta)] = \sin(\theta)\sin(\varphi) \quad (J.18)$$

$$\cos(\theta') = \sin(\theta)\sin(\varphi) \quad (J.19)$$

As a consequence,

$$r_{2y} \approx r - d_y\sin(\theta)\sin(\varphi) \quad (J.20)$$

The corresponding electric far field components for the two dipoles are now:

$$E_{\theta 1}(r,\theta) \approx A_{\theta}\left[-\frac{k^2}{r}\right]\sin(\theta)\exp[-jkr] \quad (J.21)$$

$$E_{\theta 2y}(r,\theta) \approx A_{\theta}\left[-\frac{k^2}{r}\right]\sin(\theta)\exp[-jkr]\exp[+j\Delta\Phi_y] \quad (J.22)$$

where

$$\Delta\Phi_y = k d_y \sin(\theta)\sin(\varphi) \quad (J.23)$$

is the phase in the second dipole due to d_y.

The total electric field at O is then:

$$E_{\theta(T)}(r,\theta) = E_{\theta 1} + E_{\theta 2y} \approx A_\theta \left[-\frac{k^2}{r} \right] \sin(\theta) \exp[-jkr][1 + \exp[+j\Delta\Phi_y]] \quad (J.24)$$

The corresponding magnetic field components are then, eqn.(7.32):

$$H_{\varphi 1}(r,\theta) \approx A_\varphi \frac{\sin(\theta)}{r} \exp[-jkr] \quad (J.25)$$

$$H_{\varphi 2y}(r,\theta) \approx A_\varphi \frac{\sin(\theta)}{r} \exp[-jkr] \exp[+jk\sin(\theta)\sin(\varphi)d_y] \quad (J.26)$$

giving a total magnetic field at O:

$$H_{\varphi(T)}(r,\theta) = H_{\varphi 1} + H_{\varphi 2y} \approx A_\varphi \left[-\frac{k^2}{r} \right] \sin(\theta) \exp[-jkr][1 + \exp[+j\Delta\Phi_y]] \quad (J.27)$$

J.2. Linear array along the z axis

Consider a large number of the dipoles discussed in section J.1 to form a linear array of length l_z along the z axis, as it is shown in Figure J.2.

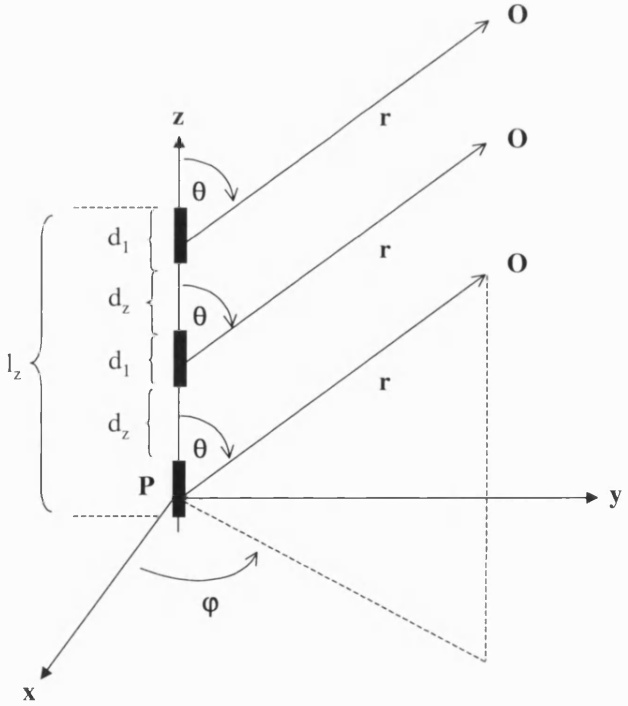

Figure J.2. Geometry of a linear array of dipoles along the z axis.

Following the analysis given in section J.1, the far field components for each of the radiating dipoles with respect to the origin of the co-ordinate system are, eqn.(J.8):

$$E_{\theta(m)}(r,\theta) \approx A_\theta \frac{\sin(\theta)}{r} \exp[-jkr]\exp[+j(k\cos(\theta)+Q_z)md_z] \quad (J.28)$$

$$H_{\varphi(m)}(r,\theta) \approx A_\varphi \frac{\sin(\theta)}{r} \exp[-jkr]\exp[+j(k\cos(\theta)+Q_z)md_z] \quad (J.29)$$

where m = 1, 2, .., M and Q_z is an extra excitation phase term due to an incident field.

By assuming that the dipoles are very close to each other, hence forming a homogeneous linear array, it is possible to find the total electric, $E_{\theta(T)}$, and magnetic field, $H_{\varphi(T)}$, of the array by integrating eqns.(J.28-29) along z for the length of the array l_z. Hence,

$$E_{\theta(T)}(r,\theta) \approx A_\theta \frac{\sin(\theta)}{r} \exp[-jkr] \int_{-lz/2}^{lz/2} \{\exp[+j(k\cos(\theta)+Q_z)z]\} dz$$

$$\approx A_\theta \frac{\sin(\theta)}{r} \exp[-jkr] 2 \frac{\sin\left(\frac{u_z l_z}{2}\right)}{u_z} \quad (J.30)$$

$$= A_\theta \frac{\sin(\theta)}{r} \exp[-jkr] AF_z$$

$$H_{\varphi(T)}(r,\theta) \approx A_\varphi \frac{\sin(\theta)}{r} \exp[-jkr] \int_{-lz/2}^{lz/2} \{\exp[+j(k\cos(\theta)+Q_z)z]\} dz$$

$$\approx A_\varphi \frac{\sin(\theta)}{r} \exp[-jkr] 2 \frac{\sin\left(\frac{u_z l_z}{2}\right)}{u_z} \quad (J.31)$$

$$= A_\varphi \frac{\sin(\theta)}{r} \exp[-jkr] AF_z$$

where

$$u_z = k\cos(\theta) + Q_z \quad (J.32)$$

The term $\frac{\sin(\theta)}{r}\exp[-jkr]$ in eqns.(J.30-31) describes a single radiating dipole, whereas AF_z is referred to as the array factor. As a consequence, the radiating intensity is then, eqn.(7.28),

$$S_{r(T)}(r,\theta) = 2A_\varphi A_\theta \left[\frac{\sin(\theta)}{r}\right]^2 [AF_z]^2 \quad (J.33)$$

J.3. Linear array along the y axis

Consider now the case where the linear array is formed along the y axis and has length l_y as it is shown in Figure J.3.

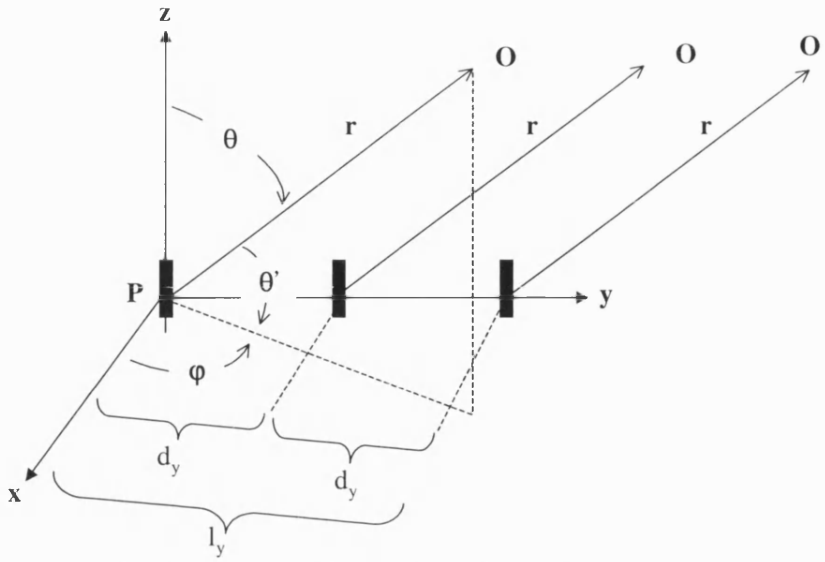

Figure J.3. Geometry of a linear array of dipoles along the y axis.

The far field components for each one of the dipoles of the array with respect to the origin of the co-ordinate system can be written as, eqn.(J.24):

$$E_{\theta(n)}(r,\theta) \approx A_\theta \frac{\sin(\theta)}{r} \exp[-jkr]\exp[+j(k\sin(\theta)\sin(\varphi)+Q_y)n d_y] \qquad (J.34)$$

$$H_{\varphi(n)}(r,\theta) \approx A_\varphi \frac{\sin(\theta)}{r} \exp[-jkr]\exp[+j(k\sin(\theta)\sin(\varphi)+Q_y)n d_y] \qquad (J.35)$$

where n = 0, 1, 2,..,N and Q_y is the phase introduced by an excitation wave along the y axis.

As a consequence, the total electric, $E_{\theta(T)}$, and magnetic field, $H_{\varphi(T)}$, components of the array can be obtained by integrating eqns.(J.34-35) along y for the length of the array l_y, as it was performed in section J.2, which gives

$$E_{\theta(T)}(r,\theta) \approx A_\theta \frac{\sin(\theta)}{r}\exp[-jkr]2\frac{\sin\left(\frac{u_y l_y}{2}\right)}{u_y} = A_\theta \frac{\sin(\theta)}{r}\exp[-jkr]AF_y \tag{J.36}$$

$$H_{\varphi(T)}(r,\theta) \approx A_\varphi \frac{\sin(\theta)}{r}\exp[-jkr]2\frac{\sin\left(\frac{u_y l_y}{2}\right)}{u_y} = A_\varphi \frac{\sin(\theta)}{r}\exp[-jkr]AF_y \tag{J.37}$$

where AF_y is the array factor of the linear array along the y direction and

$$u_y = k\sin(\theta)\sin(\varphi) + Q_y \tag{J.38}$$

The total field intensity is then

$$S_{r(T)}(r,\theta) = 2A_\varphi A_\theta\left[\frac{\sin(\theta)}{r}\right]^2[AF_y]^2 \tag{J.39}$$

J.4. Two dimensional planar dipole array

Consider now that the linear arrays of sections J.2 and J.3 form a planar, two dimension (2D), array of M rows and N columns, as it is shown in Figure J.4.

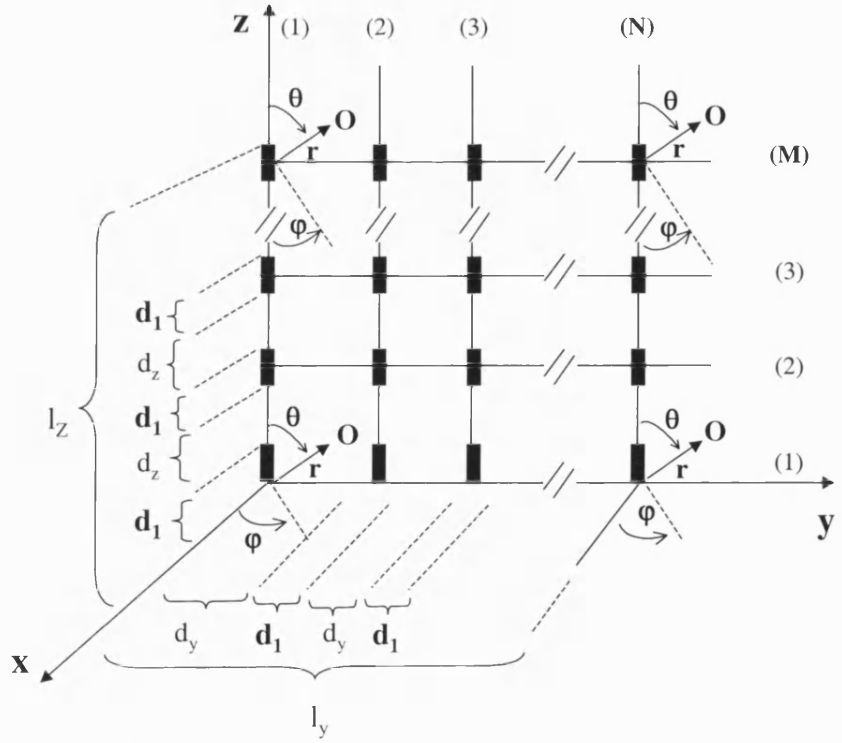

Figure J.4. Geometry of a planar array of dipoles along the z-y plane.

The far field components of the 2D array can then easily be found by evaluating the product of the field from a single dipole with the array factors of the linear arrays along the z and y axis.

Hence, by eqns.(J.30) and (J.36), and eqn.(J.31) and (J.37), the total electric and magnetic field components of the array are:

$$E_{\theta(T)}(r,\theta) \approx A_{\theta} \frac{\sin(\theta)}{r} \exp[-jkr] AF_z \, AF_y \qquad (J.40)$$

$$H_{\varphi(T)}(r,\theta) \approx A_{\varphi} \frac{\sin(\theta)}{r} \exp[-jkr] AF_z \, AF_y \qquad (J.41)$$

The corresponding field intensity of the array is then found from eqns.(J.33) and (J.36):

$$S_{r(T)}(r,\theta) = 2 A_{\varphi} \, A_{\theta} \left[\frac{\sin(\theta)}{r}\right]^2 [AF_z \, AF_y]^2 \qquad (J.42)$$

J.5. far field radiation pattern results

With reference to the numerical example of section 7.5, the far field radiation pattern of the array of dipoles for various l_z and l_y when $\varphi = \pi/4$ is given in Table J.1.

The results for the various array dimensions follow the same pattern as for the case with $\varphi = 0$, Table 7.2, for the same reasons given in section 7.5.

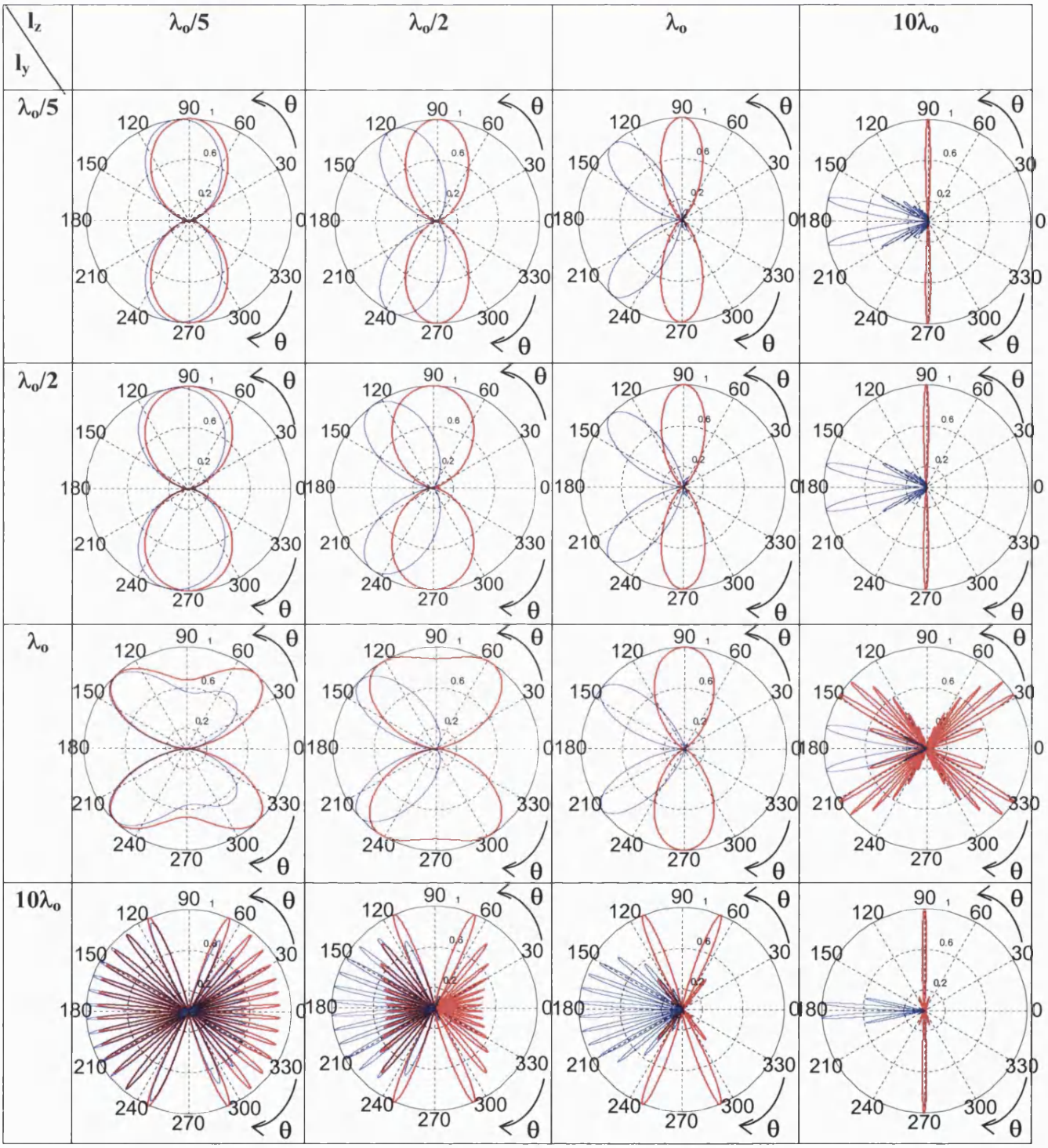

Table J.1. Polar plots of the normalised intensity S_r of the far field radiation pattern from an array of particles as a function of θ for different array dimensions when $\phi = \pi / 4$. The solid (blue) line patterns include the SPW excitation phase $Q_z \approx 2\pi$ (μm^{-1}), whereas the dotted (red) line plots have $Q_z = 0$.

Appendix K

Far field measurement

The measurement of the far field profile from a radiating source using a lens is described in this appendix. Consider a HeNe gas laser with emission wavelength λ_o = 630nm producing a collimated output beam of diameter d_b = 2mm, which passes through a slit with width b = 0.25mm, as it is shown in Figure K.1.

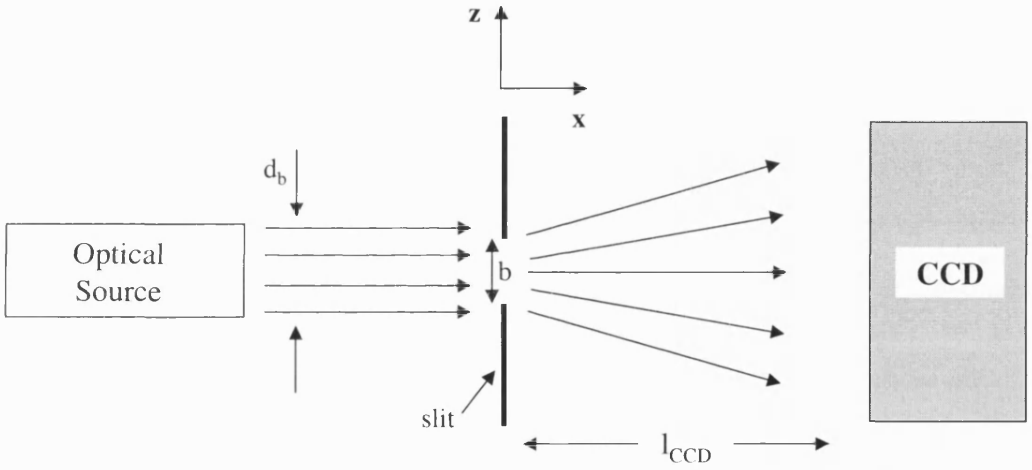

Figure K.1. Schematic of parallel beam with diameter d_b passing through a slit of width b. The optical components of the system given in the schematic are not in scale.

Since d_b >> b, the beam diffracts at the slit and produces a far field intensity profile I along the z direction which is captured at a distance x ≈ 24mm by a CCD camera, Figure K.2.

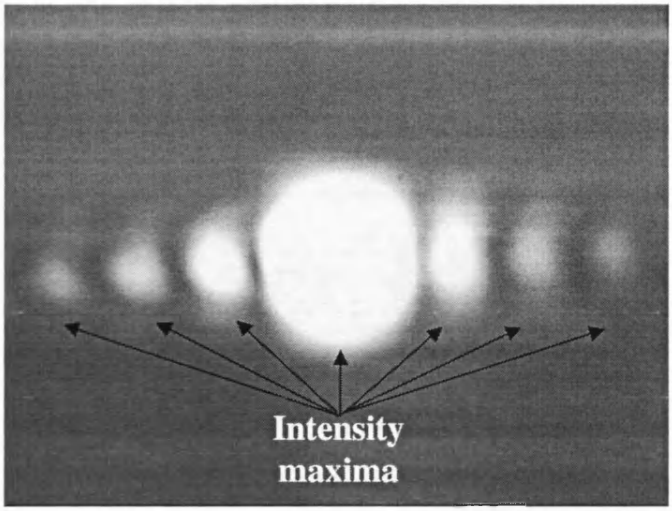

Figure K.2. Far field profile of the diffracted from the slit beam.

The results for I are following the well known expression for a diffracted beam produced by a slit, Figure K.3, given by [K.1-2],

$$I = I_o \frac{\sin^2 \chi}{\chi^2} \tag{K.1}$$

where

$$\chi = \frac{\pi b \sin\theta}{\lambda_o} \tag{K.2}$$

θ is the diffraction angle and I_o is the field intensity at $\theta = 0$.

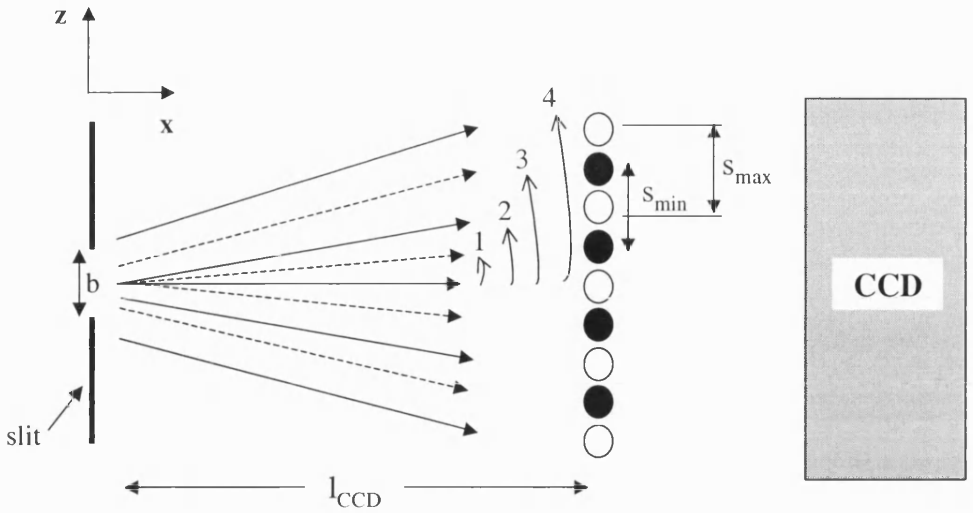

Figure K.3. Schematic of a diffracted beam from a slit. The white circles correspond to the maxima of the far field intensity distribution and the black circles to the minima. Dashed lines indicate minimum in intensity whereas solid lines show maximum. Arrow 1 corresponds to $\theta_{min(1)}$, arrow 2 to $\theta_{max(1)}$, arrow 3 to $\theta_{min(2)}$ and arrow 2 to $\theta_{max(1)}$, where θ_{min} represents a diffracted minimum intensity angle and θ_{max} a diffracted maximum intensity angle. s_{min} and s_{max} correspond to distance between two minima and two maxima respectively.

With reference to Figure K.3, the distance between two far field intensity minima can then be found by calculating first the corresponding θ_{min} angles given by [K.2]:

$$\sin\theta_{min(q)} = q\frac{\lambda_o}{b} \tag{K.3}$$

where q = ±1, ±2, .., ±Q correspond to the different number of minima with respect to the central beam (θ = 0). Since θ_{min} is considered very small, thus $\sin\theta_{min(q)} \approx \theta_{min(q)}$ (measured in radians). Hence by assuming that the slit is at distance r from the CCD camera where I is captured, the distance s_{min} between the first two intensity minima (q = 1, 2) is:

$$s_{min} = \left|\theta_{max(q+1)} - \theta_{max(q)}\right| r \tag{K.4}$$

Consequently, the intensity maxima are found for diffracted angles $\theta_{max(q)}$ by [K.2]:

$$\sin\theta_{max(q)} = 1.43q\frac{\lambda_o}{b} \tag{K.5}$$

Hence, the corresponding distance between the first two maxima s_{max}, (q = 1, 2), assuming that $\theta_{max(q)} \approx 1.43q\frac{\lambda_o}{b}$ is:

$$s_{max} = \left[\theta_{max(q+)1} - \theta_{max(q)}\right]r \qquad (K.6)$$

A different way to produce the far field profile from the slit can be done by imaging the near field intensity distribution across the slit with the use of a lens. It is well known that a lens performs a Fourier transform and therefore can be used to convert the near field intensity distribution into a far field [K.3]. To verify that concept, in the experimental arrangement of Figure K.1 a set of lenses is introduced between the slit and the CCD camera as it is shown in Figure K.4.

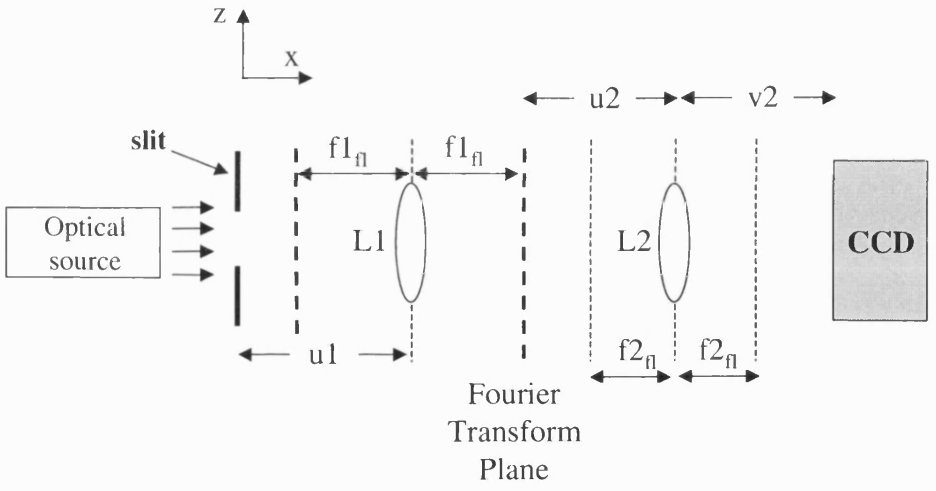

Figure K.4. Schematic of converting a near field intensity distribution into a far field with the use of lenses.

A biconvex lens L1 with focal length $f1_{fl}$ = 32mm is placed at a distance u1 ≈ 37mm from the slit, in order to image the near field intensity distribution across the slit at a distance v1 ≈ 237mm from L1. The imaged near field is then captured by a CCD camera and shown in Figure K.5.

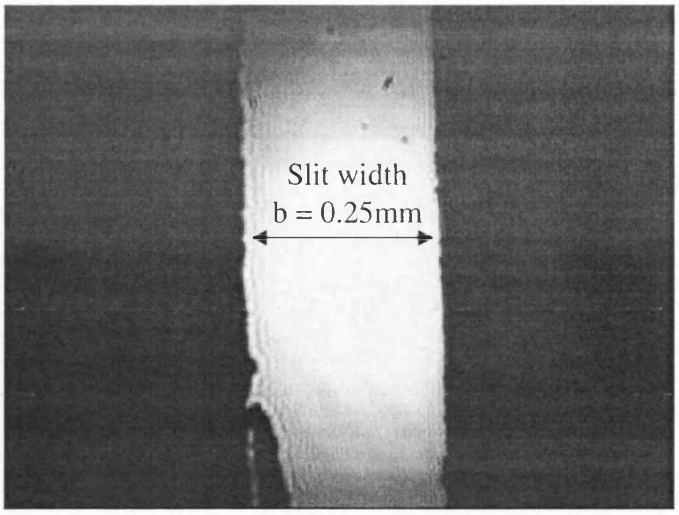

Figure K.5. Near field image of the illuminating slit.

The front focal length of the lens at $x = 2\ f1_{fl}$, corresponds to the Fourier transform plane of the lens, thus where the far field intensity profile from the slit takes place [K.1-2]. If a second biconvex lens L2 with focal length $f2_{fl} \approx 14$mm is introduced at a distance u2 = 15mm from the Fourier transform plane of L1, then the far field intensity distribution across the slit produced by L1 will then be projected at a distance $v2 \approx 210$mm from L2 and magnified by a factor

$$M_{IM} = \frac{v2}{u2} \tag{K.7}$$

The far field intensity distribution from the slit as it is produced with the use of the lenses is shown in Figure K.6.

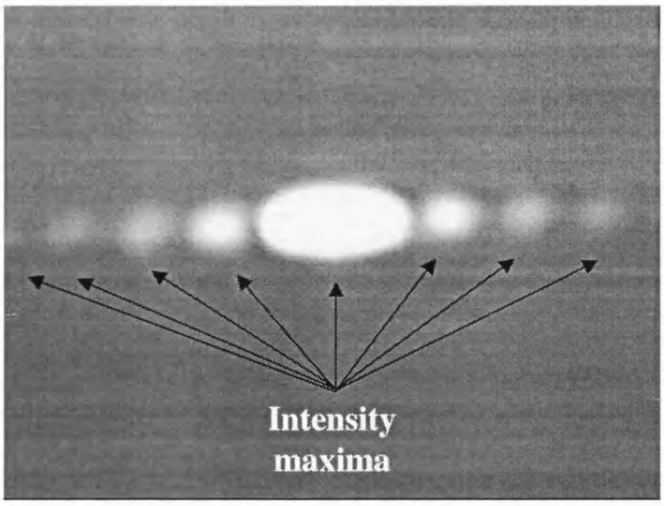

Figure K.6. Far field profile of the field intensity across the slit, obtained with the use of lenses.

The maxima and minima of the far field intensity can then be found by eqns.(K.1-6).

References

[K.1] E.Hecht, "Optics", Addison Wesley, 3rd edition, 1998, p.130.

[K.2] A. Ghatak, "Optics", Tata McGraw-Hill Publishing Company Limited New Delhi, 2nd Edition, 1993.

[K.3] G.P. Agrawal, N.K. Dutta, "Semiconductor Lasers", Van Nostrand Reinhold New York, 2nd edition, 1993.

List of Publications obtained from this Thesis

[1] "Making Sense of Surface Plasmon Waves", A.Tarlis, J.Sarma, F.Causa, SIOE'03 "Semiconductors and Integrated Optoelectronics Conference", University of Cardiff, Wales, April 2003.

[2] "Transmission Line Analysis of Surface Plasmon Resonance", A.Tarlis, J.Sarma, SIOE'04 "Semiconductors and Integrated Optoelectronics Conference", University of Cardiff, Wales, 5-7 April 2004.

[3] "Study of Optical Surface Waves – bio-chemical medical applications", A.Tarlis, J.Sarma, F.Causa, UK National URSI Symposium, University of Bath, UK, 5-6 July 2004.

[4] "Semiconductor Optical Sources for Surface Plasmon Waves", A.Tarlis, J.Sarma, F.Causa, Quantum Electronics and Photonics Conference, (Institute of Physics Photon04), Glasgow Caledonian University, Glasgow, UK, 6-9 September 2004.

[5] "Investigating the Sensitivity of Surface Plasmon Waves", A.Tarlis, J.Sarma, F.Causa, Opticks'04 (Institute of Physics), The Royal Society, London, UK, 9 December 2004.

[6] "Surface Plasmon Wave Detection with Semiconductor Optical Sources", A.Tarlis, J.Sarma, SIOE'05 "Semiconductors and Integrated Optoelectronics Conference", University of Cardiff, Wales, 21-23 March 2005.

[7] "Surface Plasmon Waves and Sensors in a Transmission Line Context", A.Tarlis, J.Sarma, Physics 2005 – A Century After Einstein Conference (Institute of Physics), University of Warwick, UK, 10-14 April 2005.

[8] "Surface Plasmon Waves in Multilayers with Loss / Gain", A.Tarlis, J.Sarma, XXVIII URSI General Assembly, New Delhi, India, 23-29 October 2005.

[9] "Losses and Gains with Surface Plasmon Waves", A.Tarlis, J.Sarma, F.Causa, S.Maier, SIOE'06 "Semiconductors and Integrated Optoelectronics Conference", University of Cardiff, Wales, 21-23 March 2006.

[10] "Transmission Line Circuit Representation of Surface Plasmon Waves", A.Tarlis, J.Sarma, F.Causa, International Conference on Nano-Material Synthesis and Integration for Sensors, Electronics, Photonics and Electro-Optics, SPIE OpticsEast 2006, Boston, USA, (Invited Oral Presentation).

[11] "SPW Enhanced Optical Scattering", A.Tarlis, J.Sarma, F.Causa, SIOE'07 "Semiconductors and Integrated Optoelectronics Conference", University of Cardiff, Wales, 1-3 April 2007.

List of Figures

List of Tables